Sound Propagation and Quantum-Limited Damping in an Ultracold Two-Dimensional Fermi Gas

Markus Bohlen

Markus Bohlen. Sound Propagation and Quantum-Limited Damping in an Ultracold Two-Dimensional Fermi Gas. Physics [physics]. PSL Research University; École Normale Supérieure, 2020. English. NNT : . tel-03150908

HAL Id: tel-03150908
https://hal.science/tel-03150908

Submitted on 24 Feb 2021

PSL
UNIVERSITÉ PARIS

THÈSE DE DOCTORAT
DE L'UNIVERSITÉ PSL

Préparée à l'École Normale Supérieure Paris
et à l'Université de Hambourg

Sound Propagation and Quantum-Limited Damping in an Ultracold Two-Dimensional Fermi Gas

Soutenue par
Markus BOHLEN
Le 27/11/2020

École doctorale nº564
Physique en Île-de-France

Spécialité
Physique Quantique

Composition du jury :

Mme Hélène PERRIN CNRS	*Présidente du jury*
M Stefano GIORGINI Università di Trento	*Rapporteur*
M Chris VALE Swinburne University of Technology	*Rapporteur*
M Jean-Philippe BRANTUT EPFL	*Examinateur*
M Matteo ZACCANTI CNR-INO, LENS	*Examinateur*
M Henning MORITZ Universität Hamburg	*Co-encadrant*
M Frédéric CHEVY ENS	*Directeur de thèse*

ENS | PSL

Résumé

Les systèmes bi-dimensionnels fortement corrélés sont captivants. À cause de la dimensionnalité réduite, des fluctuations thermiques empêchent un vrai ordre à longue portée et devraient donc entraver des phénomènes comme la condensation Bose-Einstein ou la superfluidité. Malgré cela, la superfluditié et la supraconductivité semblent particulièrement robustes en 2D : Dans presque tous les supraconducteurs à haute température critique les structures 2D ainsi que le couplage en onde d semblent jouer un rôle central. Dans cette thèse, nous utilisons des gaz de lithium 6 ultrafroids et homogènes avec des interactions ajustables pour effectuer des simulations quantiques explorant certaines propriétés de ces systèmes fascinants.

Comme résultat principal, je présente les premières mesures de la vitesse et de l'atténuation du son dans un gaz de Fermi 2D ultrafroid, que nous utilisons pour étudier des propriétés thermodynamiques et les coefficients de transport du gaz. La vitesse du son nous permet d'extraire la compressibilité du gaz et nous obtenons un accord raisonnable avec la valeur mesurée indépendamment dans un système statique ou calculée à partir de simulations Monte-Carlo quantiques. L'atténuation des ondes sonores est déterminée par la viscosité et la conductivité thermique du gaz, et approche un minimum dans le régime fortement corrélé. Ce minimum correspond à une limite quantique universelle $\hbar/m$ pour la diffusivité du son. Le gaz de Fermi 2D fortement corrélé représente donc un fluide quasi-parfait.

En outre, je rends compte de deux autres expériences qui ont été réalisées dans le cadre de cette thèse, menées principalement par mes collègues N. Luick et L. Sobirey. Premièrement, nous réalisons une jonction de Josephson en séparant le gaz en deux réservoirs à l'aide d'un laser induisant une fine barrière de potentiel répulsive. Nous observons des oscillations de Josephson entre les deux réservoirs démontrant la cohérence de phase du gaz de Fermi 2D. En réduisant la hauteur de la barrière, ces oscillations sont progressivement transformées en ondes sonores. Dans la deuxième expérience, nous déplaçons un réseau optique à travers le gaz à des vitesses ajustables. Nous observons une vitesse critique pour la création d'excitations, prouvant que le gaz de Fermi 2D est superfluide. La vitesse critique est déterminée par la vitesse du son sur un grand domaine d'interactions.

Finalement, je présente la caractérisation d'une nouvelle résonance Feshbach en onde d dans du potassium 40 ultrafroid, un projet qui a été mené principalement par mon collègue T. Reimann. Nous mesurons le taux de pertes inélastiques $L^{(2)}$ et l'évolution des populations de spins et nous les comparons à des prédictions théoriques. Nous trouvons un bon accord entre théorie et expérience pour le taux de pertes. L'évolution des populations des spins est compatible avec le comportement prédit par la théorie.

Abstract

Strongly correlated two-dimensional (2D) systems are a fascinating field of study. The reduced dimensionality should in principle impede phenomena such as Bose-Einstein condensation or superfluidity. Yet, evidence suggests that superfluidity and superconductivity are especially robust in 2D: In almost all known high T_c-supercondcutors, strongly correlated 2D structures and higher-partial-wave coupling seem to play a crucial role. In this thesis, we use ultracold homogeneous gases of lithium 6 with tunable interactions to perform analog quantum simulation of these captivating systems.

As the main result of this thesis, I present the first measurements of the speed and attenuation of sound waves in ultracold 2D Fermi gases, which we use to probe the thermodynamic and transport properties of the gas. From the speed of sound, we extract the compressibility equation of state and compare it both to an independent static measurement and to quantum Monte Carlo calculations and find reasonable agreement between the three. The damping of the sound waves, which is determined by the shear and bulk viscosities as well as the thermal conductivity of the gas, exhibits a minimum in the strongly correlated regime. Here, the sound diffusivity approaches a universal quantum bound $\hbar/m$ and the strongly correlated 2D Fermi gas thus realizes a nearly perfect fluid.

In addition, I report on further related measurements performed in the course of this thesis, which were led by my coworkers N. Luick and L. Sobirey. We show that the 2D Fermi gas is phase coherent by realizing a Josephson junction in the homogeneous gas and observing Josephson oscillations between two reservoirs separated by a thin barrier. When the barrier height is reduced to zero, these oscillations transform smoothly into sound waves. By dragging a lattice though the homogeneous system at variable velocities, we observe a critical velocity for the creation of excitations, proving that the system is superfluid. Here, the sound velocity determines the critical velocity for a large range of interaction strengths.

Finally, I present the characterization of a novel d-wave Feshbach resonance in ultracold potassium 40 via measurements of the inelastic loss rate $L^{(2)}$ and via the dynamics of spin populations, led by my coworker T. Reimann. The experimental results are compared to theoretical predictions and we observe good agreement between the theoretical and experimental loss rates. The evolution of the spin populations is found to be consistent with the expected behavior for the theoretically predicted exit channel.

Contents

List of Figures

Bibliography

1. Introduction

Strongly correlated two-dimensional systems are a captivating field of study. The reduced dimensionality of these systems alters their physical properties in exciting ways compared to materials in three-dimensional configurations. For instance, thermal fluctuations in a two-dimensional system are enhanced with respect to a three-dimensional system. Indeed the Mermin-Wagner-Hohenberg theorem [1, 2] prohibits phenomena like Bose-Einstein condensation and superfluidity in two-dimensional materials in principle[1]. On the other hand, novel phenomena such as the Berezinskii-Kosterlitz-Thouless (BKT) transition [3–5] allow a weaker type of ordering, so-called quasi-long-range order, to be established. Below a critical temperature, previously unbound vortices form pairs, causing the order parameter to decay algebraically instead of exponentially fast. The BKT-transition is heralded by a universal jump in the superfluid phase space density $n_s\lambda_{\mathrm{dB}}^2$ from 0 to 4 and enables phenomena like superfluidity to exist in two-dimensional systems of finite size.

The weaker type of ordering found in 2D systems suggests that phenomena relying on phase coherence, in particular superfluidity, superconductivity or Bose-Einstein condensation, should be suppressed in low-dimensional materials with respect to three-dimensional materials. Yet in fact, superfluidity and superconductivity seem to be most robust in 2D. Evidence shows that the ratio between the critical temperature and the Fermi temperature T_c/T_{F} is systematically highest in materials with two-dimensional structures, from cuprates [6] over iron-based superconductors [7] to magic-angle bilayer graphene [8]. A second ingredient that seems to play a major role is unconventional (non-s-wave) pairing, i.e. pairing between particles with an anisotropic order parameter [6–9].

Achieving a better understanding of strongly correlated 2D systems is of high interest on a fundamental and technological level[2]. However, despite extensive research efforts, strongly correlated systems remain one of the most challenging problems in the field of quantum many-body physics. The interactions between the particles are strong and cannot be treated perturbatively, which complicates theoretical approaches. The enhanced fluctuations make mean-field approaches less reliable and in addition, the numerical analysis of fermionic systems, for instance using quantum Monte-Carlo methods, encounters difficulties from the so-called fermion sign problem [10–12], which originates in the necessary anti-symmetrization of the wave function.

To approach these fascinating systems in an experimental way, we here perform analog quantum simulations of strongly correlated two-dimensional BKT superfluids. More concretely, we create atomic gases of ^{6}Li in homogeneous two-dimensional potentials with variable interac-

[1] To be precise, the Mermin-Wagner-Hohenberg theorem states that there can be no spontaneously broken continuous symmetry in a system with less than three dimensions and short-range interactions at nonzero temperature.

[2] The 'holy grail' of 2D-physics would be to uncover the mechanism for high-T_c superconductivity and its connection to the dimensionality of the material. Such an achievement could open the door to revolutionary technologies with far-reaching consequences.

tions and study their response to a short perturbation by measuring the propagation and the damping of sound waves in the gas.

Quantum simulation with ultracold atoms

The general concept of quantum simulation is to build a system that is analog to the problem at hand, i.e. an apparatus which can emulate the Hamiltonian underlying the problem in a clean and controlled way, such that the answer to the question at hand can be measured instead of calculated[3]. This idea has been popularized among others by R. Feynman. To borrow his words:

> "[...] it does seem to be true that all the various field theories have the same *kind* of behavior, and can be simulated in every way, apparently, with little latticeworks of spins and other things. [...] I therefore believe it's true that with a suitable class of quantum machines you could imitate any quantum system, including the physical world."[a]
>
> ---
>
> [a] R. P. Feynman: Simulating Physics with Computers [14]

Ultracold atoms are an ideal platform for such experiments, since they allow us to create a wide range of nearly defect-free model systems and to tune parameters that are often inaccessible in real-world materials, such as the interaction strength between the particles. After the development of optical laser cooling and trapping techniques [15–19], the use of evaporative cooling techniques has quickly led to the realization of the first Bose-Einstein condensates in 1995 [20, 21] as well as the first degenerate Fermi gases in 1999 [22]. Since then, the field of ultracold atoms has developed explosively and with it an entire toolkit of techniques for the controlled manipulation of the quantum states of atoms in various settings [13, 23–26]. Today, ultracold atoms are used to simulate and study a broad range of diverse fields: A non-exhaustive list of examples includes atoms in optical lattices [27] and topological systems with artificial gauge fields [28]. Homogeneous [29, 30] as well as strongly disordered systems [31] have been created. Tailored optical potentials are used for studying quantum transport phenomena [32]. Finally, systems incorporating impurities such as polarons [33, 34], ions [35] or Rydberg atoms [36] are investigated as well.

For the last decade, ultracold atomic gases have also been used to study the fascinating physics of 2D Fermi gases. A particularly close analog to solid state systems is realized by simulators implementing the repulsive Fermi-Hubbard model [37–40]. Two-dimensional bulk gases with balanced and imbalanced spin populations have been produced [41–44]. Experiments on fermionic pairing [45–48] have been performed and both pair condensation and the Berezinskii-Kosterlitz-Thouless transition have been observed [49, 50]. Furthermore, Fermi polarons [51, 52] and Fermi liquids [53] have been investigated. In close relation to the work carried out in this thesis are the measurements of the equation of

---

[3] This approach is not an entirely new idea: Classical systems have been modeled with automata for long times. One may think for instance about astrolabes, built since the classical era, or medieval astronomical clocks, which are able to simulate the motion of celestial bodies [13].

state of fermionic gases [54–56] as well as measurements of viscosity [57] and spin diffusion in bulk 2D Fermi gases [58, 59].

Sound waves in a homogeneous 2D Fermi gas

A common feature in the experiments performed on two-dimensional Fermi gases in the past is the use of harmonic trapping potentials. While such traps are well understood, the resulting inhomogeneous density profiles "hinder the observation of critical phenomena with a diverging correlation length and exotic phases such as the Fulde-Ferell-Larkin-Ovchinnikov (FFLO) state" [60]. Furthermore, the nonlocal quantities, such as correlation functions or momentum distributions can only be extracted as trap-averaged quantities [60]. In our group, a homogeneous box potential has been realized by my predecessors K. Hueck et al. [60], providing a perfect platform for the study of phase coherence and superfluidity in a two-dimensional system. In this thesis, I present joint work with N. Luick and L. Sobirey as lead authors, which demonstrates phase coherence and superfluidity in the system via the observation of Josephson oscillations and a critical velocity for the creation of excitations in the system.

Another fundamental question that we address in this thesis is how a homogeneous two-dimensional superfluid reacts when it is brought out of equilibrium and how perturbations propagate through the system. More precisely, we investigate the fundamental excitations of the gas and their decay back towards the ground state by performing the first measurements of the propagation and damping of sound waves in a homogeneous two-dimensional Fermi gas. Sound waves are simultaneous oscillations in several thermodynamic quantities, which are related to each other via the equation of state of the gas. From the sound velocity, we thus extract the compressibility equation of state of the gas. The damping rate of the sound waves is related to the transport coefficients of the gas, in particular to the heat conductivity and viscosity.

In these measurements, we make use of the important 'tool' of Feshbach resonances [61, 62]. These enable us to access regimes of different interaction strengths and to vary the character of the gas from weakly interacting fermions via a strongly correlated gas to strongly bound bosonic dimers across the so-called BEC-BCS crossover [63, 64]. This continuous transition links Bardeen-Cooper-Schrieffer type superfluids to Bose-Einstein condensates. We observe that the viscosity of the gas is minimal in the regime where the particles interact most with each other. This is surprising, since one would naïvely expect strong interactions between the particles to lead to fast equilibration and consequently to a fast decay of oscillations. However, we can understand this behavior as a minimum of momentum and energy transport in the gas. This minimum is caused by a corresponding minimum in the mean free path between the particles, which limits the diffusion of the energy in the sound waves to a lower limit set by fundamental quantum mechanical quantities. The viscosity of the gas similarly approaches a lower bound and hence, the strongly interacting 2D Fermi gas constitutes a 'nearly perfect' fluid [65].

These findings constitute the main results of this thesis. The experimental data we provide characterize a system that is challenging to approach theoretically and may serve as benchmarks for future theories.

Organization of this thesis

This manuscript is organized as follows:

- In chapter 2, I introduce ultracold quantum gases and some key parameters that can be used to control their properties. I discuss the spectra of their fundamental excitations in the weakly interacting limits and introduce the concepts of Feshbach resonances and scattering length. Finally, I will touch on the role of the dimensionality and on the differences between the physics of two-dimensional gases and their experimental realizations.

- This thesis was executed in a collaboration between the Ultracold Fermi Gases group of ENS Paris under the supervision of Frédéric Chevy and Christophe Salomon and the Quantum Matter group of Hamburg University under the supervision of Henning Moritz. During the first years of my thesis, I therefore worked on the Fermix experiment at ENS Paris. Chapter 3 introduces this experiment and chapter 4 presents the characterization of a d-wave Feshbach resonance between two hyperfine states of fermionic potassium. These measurements were led by Thomas Reimann as senior PhD student.

- We then transition to two-dimensional gases. Chapter 5 gives a short introduction to the 2D-lithium experiment in Hamburg and touches on the experimental realization of two-dimensional Fermi gases.

- Chapter 6 presents the main results of this thesis. After an introduction to the theory of sound waves in the hydrodynamic framework, our measurements on sound propagation and damping across the BEC-BCS crossover are presented. The compressibility equation of state and the sound diffusivity are extracted in the different interaction regimes.

- Finally, chapter 7 shows further results obtained in the course of this thesis. I report on the realization of a Josephson junction in a 2D geometry and on the observation of Josephson oscillations, which were carried out with Niclas Luick as lead author, clearly demonstrating phase coherence in the gas. Finally I give an overview over the first measurements of the critical velocity in 2D Fermi gases, obtained with Lennart Sobirey as lead author, which unambiguously prove superfluidity in the two-dimensional gas.

2. Ultracold Quantum Gases

This chapter introduces ultracold quantum gases and their main features and drawbacks in order to give an overview over the system under investigation. We present the key parameters used to characterize and control ultracold Fermi gases and discuss Feshbach resonances as the main experimental tool to access the BEC-BCS crossover, in which the character of the gas can be continuously tuned from a system of weakly bound Cooper pairs to an ensemble of tightly bound molecules. We also touch upon the role of the dimensionality in the system and upon the key differences between three-dimensional, two-dimensional and quasi-two-dimensional gases.

2.1. Ultracold dilute gases

Since the realization of the first atomic Bose-Einstein condensate in 1995 [20, 21] and the first degenerate Fermi gas in 1999 [22], ultracold quantum gases have provided a versatile platform for studying many-body physics with a high degree of control over many system parameters. Today, a large toolkit of techniques is routinely used to engineer quantum gas systems and exploit their sensitivity on atomic scales for precision measurements, or to emulate complex condensed-matter systems in order to investigate their behavior in a clean and well-controlled model environment [23, 24, 26, 66].

Many of these applications require degenerate quantum gases. In a degenerate gas, the particles exhibit their character as fermions or bosons instead of showing a classical behavior. This regime is reached when the interparticle distance is comparable to the extent of the particle wavefunctions, which is given by the thermal deBroglie wavelength $\lambda_{\mathrm{dB}} = \sqrt{2\pi\hbar^2/mk_{\mathrm{B}}T}$. Starting out from a classical ensemble of atoms, one can thus either increase the density of the system or strongly reduce the temperature. When cooled down at high densities, most elements and molecules would form a solid before quantum degeneracy is reached. The density of the sample must therefore be kept low in order to limit the likelihood for particles to be in close proximity to each other and to suppress the formation of deeply bound dimers or trimers. Hence for quantum gases of alkali atoms, typical interparticle distances of $d \sim 0.1-1\,\mu\mathrm{m}$ are used. Compared to solid state systems, with typical atomic distances of the order of 1 Å, ultracold quantum gases are very dilute. At such low densities, the temperatures required to reach the degenerate regime are of the order of tens of nK to a few µK, depending on the species, which requires extreme cooling methods. Since atoms at room temperature carry thermal energies orders of magnitude larger

λ_{dB} : Thermal deBroglie wavelength
$\hbar$: Reduced Planck constant
m : Particle mass
k_{B} : Boltzmann constant
T : Temperature

d : Interparticle distance

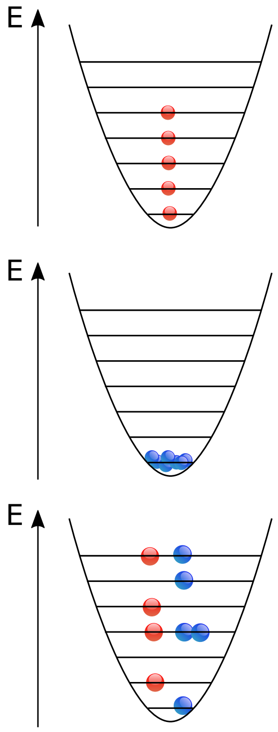

Figure 2.1. – The distribution of fermions (top) and bosons (middle) at zero temperature. Two identical fermions never occupy the same quantum state, while bosons condense to a BEC in the ground state of the potential. At high temperature (bottom), both bosons and fermions behave as classical particles and are described by the Maxwell-Boltzmann distribution. (see also section 2.3.)

than the typical energy of an atom in the ultracold gas, single collisions with thermal atoms are enough to expel particles from the gas. In order to ensure long lifetimes compared to the atomic timescales, the number of collisions with background atoms needs to be reduced as much as possible. Atomic quantum gases are thus produced within ultrahigh vacua at pressures below 10^{-11} mbar, yielding typical lifetimes of up to a few minutes.

The high sensitivity to the environment makes ultracold atoms a perfect candidate for precision measurements, yet it is also a drawback. Many experimental parameters must be controlled to a very high degree. In addition, all measurement processes used in the experiments presented in this thesis are destructive processes. In order to generate enough statistics, the capability to reliably generate many samples with similar properties is necessary.

Ultracold atomic gases have been produced with various species [67], including alkali atoms as some of the first due to their relatively simple atomic structure. But also alkaline earth metals [68, 69] and several more complex elements, such as chromium [70] or lanthanides like erbium [71] or ytterbium [72], have been brought to quantum degeneracy. Depending on the element (or the isotope), the ultracold gas exhibits fundamentally different properties, due to the different masses or magnetic momenta, the level structure or due to the different quantum statistics.

This thesis reports on experiments on ultracold two-dimensional gases of lithium 6 and on three-dimensional gases of potassium 40. Both species are fermionic, which means that the wave function of two atoms must acquire a negative sign under exchange of the two particles. A profound consequence of this property is the Pauli exclusion principle, which states that two identical fermions can never occupy the same quantum state. Bosons conversely have an enhanced probability to be found in the same state. Bose gases thus exhibit phenomena such as Bose-Einstein condensation, where a macroscopic number of particles assemble in the ground state of the system at low temperatures, whereas the fermions of a non-interacting Fermi gas neatly occupy every accessible state, filling up a Fermi sea (compare Fig. 2.1). With increasing temperature, the likelihood of finding two particles in the same single-particle state decreases and the distinction between bosons and fermions becomes less pronounced until both species can be treated as classical particles.

2.2. Key parameters of ultracold Fermi gases

The main properties and features of degenerate Fermi gases can be described with only a few key parameters. In an ideal Fermi gas at zero temperature, a Fermi sea is formed as a consequence of the Pauli exclusion principle. The available single-particle states of the system are occupied up to a given energy, the Fermi energy E_F. Since the states are filled up one by one from the lowest-lying state, the Fermi energy is only dependent on the density of states, which is determined by the system geometry, and on the density of particles n. Similarly, the kinetic and

E_F : Fermi energy
n : Particle density

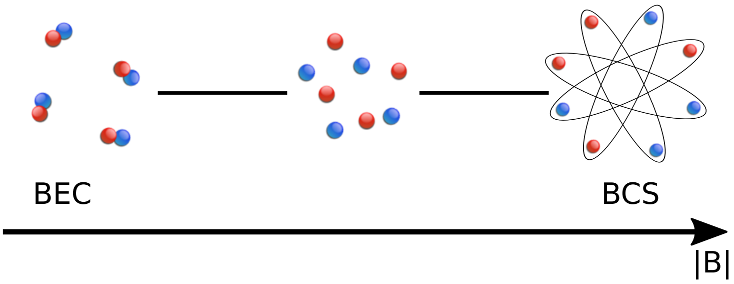

Figure 2.2. – Illustration of the BEC-BCS crossover. In the BEC regime, the strong attraction between the fermions allows them to pair up to tightly bound bosonic molecules which interact weakly with each other. In the BCS regime, the weakly attractive fermions pair up in momentum space to form a BCS-gas. In between the two regimes, the particles interact strongly and the gas is strongly correlated. Red and blue colors correspond to particles with opposite spin.

potential energies in a non-interacting gas depend only on the particle density and the system geometry. A number of related quantities can be defined from the Fermi energy. The momentum which corresponds to the Fermi energy is called the Fermi momentum $p_\mathrm{F} = \hbar k_\mathrm{F} = \sqrt{2mE_\mathrm{F}}$. The Fermi temperature $T_\mathrm{F} = E_\mathrm{F}/k_\mathrm{B}$ is the temperature scale associated with the Fermi energy and the Fermi time $\tau_\mathrm{F} = h/E_\mathrm{F}$ is the typical time scale at which the dynamics occurs in a Fermi gas. In this thesis, the Fermi velocity $v_\mathrm{F} = p_\mathrm{F}/m$ will be important, representing the velocity scale at which a disturbance can propagate through the Fermi gas[1].

p_F :	Fermi momentum
k_F :	Fermi wave vector
T_F :	Fermi temperature
τ_F :	Fermi time
$(\hbar)h$:	(Reduced) Planck constant
v_F :	Fermi velocity

In an interacting gas, the interaction strength between the particles and the density determine the interaction energy. Neutral atoms interact with each other via a van-der-Waals potential, which can often be approximated by a short-range or even a contact interaction potential[2]. At ultralow temperatures, the interaction properties can in this case be parameterized using one single parameter, the scattering length (compare section 2.4.3). If the gas features a so-called Feshbach resonance, this scattering length is experimentally tunable by adjusting a magnetic bias field. Feshbach resonances thus give the possibility to vary the interaction strength to access weakly and strongly attractive regimes and are a valuable tool for quantum simulation experiments.

In the case of a fermionic gas such as lithium 6 or potassium 40, the transition between weak and strong attractions can even be used to effectively change the character of the gas from fermionic to bosonic, which has enabled the observation of pair condensation of fermions in 2004 [76, 77]. This transition between bosonic and fermionic regimes is called the BEC-BCS crossover, since it smoothly transforms Bose-Einstein condensates (BEC) into gases of Cooper pairs described by BCS theory [78] (after Bardeen, Cooper and Shrieffer). A schematic picture of the BEC-BCS crossover is shown in Figure 2.2. At weakly attractive interactions, Cooper pairs are formed in momentum space and the gas behaves like a gas of fermions. At strong attractions, the particles can form tightly bound pairs which are bosonic in nature. Now, the system is described by a weakly interacting gas of bosonic dimers, as long as the energy scales involved are low enough that the pairs are not

[1] Our experiments with ^{6}Li 2D gases are performed at about $n \approx 1\,\mu\mathrm{m}^{-2}$. Then $E_\mathrm{F} \approx h \cdot 10\,\mathrm{kHz}$, corresponding to $T_\mathrm{F} \approx 0.5\,\mu\mathrm{K}$ and $v_\mathrm{F} \approx 40\,\mathrm{mm\,s}^{-1}$. The typical resulting timescales for the dynamics are therefore on the order of microseconds and lifetimes of minutes are largely enough to carry out the experiments.

[2] Systems with long-range interactions can be created as well by using the electric or magnetic dipole interaction, for instance using gases of polar molecules [73], Rydberg atoms [74] or atoms with high magnetic momenta such as erbium or dysprosium [75].

broken apart. These two regimes are connected by a strongly correlated regime, in which a theoretical description is challenging and where the lack of small parameters prevent the use of perturbative techniques. Here, experiments can provide valuable insight into the physics of such a strongly correlated regime. Directly on the resonance, the scattering length diverges. In this so-called unitary regime, the thermodynamic properties of 3D systems do not depend on the specific form of the interaction, but are determined only by the density and the deBroglie wavelength [79]. At diverging scattering length, systems that appear radically different, such as ultracold fermionic gases, electrons in a metal or even neutron stars, should therefore behave in a similar way.

In reduced dimensions, the physical properties of the gas change dramatically. In a one-dimensional Fermi gas, any excitation must affect the entirety of the particles, creating a Tomonaga-Luttinger-type system [80–82]. Furthermore, it is strictly speaking not possible to describe the scattering physics of a two-dimensional gas with a single parameter, in contrast to 3D, where the scattering length is sufficient, as we will see. The number of dimensions also determines whether a Bose gas can undergo Bose-Einstein condensation [83]. Quantum fluctuations play an important role in 2D, making uniform 2D gases the marginal case for the existence of a BEC.

Experimentally, true two-dimensional systems, in which there exists no third dimension, cannot be achieved. Instead, one can realize a so-called quasi-2D geometry [84], in which the motion of the particles along the third direction is frozen out by a strongly confining potential. Although the motion of the particles is restricted to 2D, scattering processes and bound states can still be sensitive to the third dimension, since the characteristic length scales involved here are much smaller than the typical length scale of an experimentally achievable confinement. This leads to some subtleties which we will explore later in this chapter (sections 2.4.3, 2.4.4).

To summarize, the three main experimental knobs to adjust the properties of the Fermi gas are the particle density, the interaction strength and the dimensionality. In solid state physics, it can be difficult to change these parameters over a broad range. Ultracold atoms in contrast offer the possibility to precisely control these parameters over large ranges. This freedom allows physicists to engineer Hamiltonians that are difficult to study with 'real' materials, or to simulate known systems and investigate their physics in a clean and controlled environment. Finally the easy access to the geometry and interaction of the systems and the relatively slow intrinsic time scales also enable experiments on systems in which these parameters vary over time.

2.3. From Bose-Einstein condensates to BCS superfluids

In this thesis, we will investigate the low-energy excitations of strongly correlated Fermi gases. Since the BEC-BCS crossover smoothly connects this regime to both weakly interacting Bose and Fermi gases, let us spend a few lines here on the ground state and the excitation spectra of degenerate Bose and Fermi gases.

2.3.1. Non-interacting gases

The key difference between bosons and fermions is that fermionic wave functions are antisymmetric under particle exchange, whereas bosonic wave functions must be symmetric. This leads to the Fermi-Dirac and Bose-Einstein distributions for the probability to find a non-interacting fermion or a boson in a state with a given energy ε:

$$f_{\mathrm{FD/BE}}(\varepsilon) = \frac{1}{e^{(\varepsilon-\mu)/k_B T} \pm 1}, \tag{2.1}$$

where μ is the chemical potential, which determines the energy cost of adding a single particle to the system. The $+/-$ signs are valid in the case of fermions and bosons, respectively. At high temperature, both distributions reduce to the Maxwell-Boltzmann distribution

$$f_{\mathrm{MB}}(\varepsilon) = \frac{1}{e^{(\varepsilon-\mu)/k_B T}}, \tag{2.2}$$

and the particles behave classically.

ε : Energy of the single-particle state
μ : Chemical potential
$f_{\mathrm{FD}}(\varepsilon)$: Fermi-Dirac dist.
$f_{\mathrm{BE}}(\varepsilon)$: Bose-Einstein dist.
$f_{\mathrm{MB}}(\varepsilon)$: Maxwell-Boltzmann dist.

In bosonic gases, there exists an upper limit for the chemical potential, namely $\mu < \varepsilon_0$, where ε_0 is the energy of the ground state. This can be seen in the Bose-Einstein distribution, which would diverge if the chemical potential is not smaller than the ground state energy of the system. In 3D, this fact limits the number of atoms allowed in the excited states of the potential [83]. At any nonzero temperature, there is therefore a critical number of atoms above which all additional atoms have to occupy the ground state, leading to a macroscopic occupation of the ground-state wavefunction and to the formation a Bose-Einstein condensate (BEC). Conversely, for a system with a given number of particles, there exists a critical temperature T_{BEC}, below which the system will start to condense a macroscopic amount of atoms into the ground state. This Bose-Einstein condensate is characterized by a common wave function whose phase can be regarded as a long-range order parameter [85].

ε_0 : Ground state energy
T_{BEC} : Critical temperature for Bose-Einstein cond.

The number of atoms that can be accommodated in the excited states depends on the density of states, which in turn depends on the trapping potential and the dimensionality. In 2D, bosonic systems in harmonic traps show Bose-Einstein condensation, whereas a homogeneous 2D Bose gas cannot condense at any nonzero temperature [83]. The absence of condensation can also be understood in terms of the thermal fluctuations, which prevent the establishment of a long-range ordered phase such as a Bose-Einstein condensate. Indeed, the Mermin-Wagner-Hohenberg theorem [1, 2] forbids long-range order in any dimensions smaller than three. In 2D, quasi-long-range order is established instead, as shown by Berezinskii, Kosterlitz and Thouless (BKT) [3–5]. In this weaker type of order, the order parameter decays algebraically with distance. Despite the decay of the order parameter in the BKT state, the spatial extents of the systems produced in cold atom experiments are typically small enough that significant phase coherence can still be established. For an extensive review of the physics of bosonic 2D gases, in particular of BKT physics, I refer the reader to [83].

For non-interacting fermions, the restriction on the number of occupied excited states does not exist and the Pauli principle forbids condensation of multiple atoms into one single state. The physical properties of the gas are then determined by the energy of the highest occupied level. In spin-polarized homogeneous 2D gases for instance, the Fermi energy and Fermi momentum are given by the expressions:

$$E_\mathrm{F} = \frac{\hbar^2 k_\mathrm{F}^2}{2m} \qquad \text{and} \qquad k_\mathrm{F} = \sqrt{4\pi n}. \tag{2.3}$$

E_FG : Total energy of a homogeneous Fermi gas.

Since the density of states is constant in 2D, the total energy E_FG of the homogeneous ideal Fermi gas is given by

$$E_\mathrm{FG} = \frac{N}{2} E_\mathrm{F}. \tag{2.4}$$

In a 2D gas, each particle hence carries in average half of the Fermi energy[3].

2.3.2. Weakly interacting gases

In order to proceed beyond the non-interacting case, we now allow for the presence of interactions. In the following, I will present the main aspects of the low-temperature excitation spectra of weakly interacting bosonic and fermionic gases in the BEC- and BCS limits. To anticipate the results, Fig. 2.3 shows a summary of the excitation spectra of a Fermi gas in the weakly interacting extremes of the BEC-BCS crossover. Since the BEC-limit of a Fermi gas is a gas of bosonic dimers, the spectrum of a weakly interacting bosonic gas can be seen in 2.3 (a) as well (blue curve).

Both in bosonic and in fermionic gases, collective modes arise as low-energy excitations of the interacting system. These collective excitations have a linear onset for small wavenumbers, whose slope determines the propagation velocity of the excitation. This velocity can also be derived as the speed of sound in the system using thermodynamic relations and the modes can therefore be identified with sound waves propagating through the gas. At higher energies, the dispersion relation of the collective mode in the bosonic regime transitions into a quadratic single-particle-like dispersion.

In addition, there exist single-particle excitations at higher energies. To create these excitations, a fermion pair has to be broken, which opens a gap in the spectrum for these modes. Both single-particle and collective modes exist in the crossover region as well, since the properties of the gas change smoothly from the fermionic to the bosonic regime. However, a theoretical description is even more challenging in this case. Since the collective mode can be identified as the sound mode of the gas, the experimental study of sound excitations allows one to gain insight into the many-body excitations of a strongly correlated quantum gas.

---

[3] At $T = 0$, E_F and E_FG can be calculated by considering the number of states with a momentum smaller than k. It is given by the area of the circle with radius k divided by the area occupied by one quantum state: $N_\mathrm{states} = \pi k^2/(2\pi/L)^2$, where L^2 is the system area.
This leads to a constant density of states of $D(\varepsilon) = mL^2/2\pi\hbar^2$.
E_F and E_FG then follow from $N_{T=0} = \int_0^{E_\mathrm{F}} D(\varepsilon)\, d\varepsilon$ and $E_\mathrm{FG} = \int_0^{E_\mathrm{F}} \varepsilon D(\varepsilon)\, d\varepsilon$.

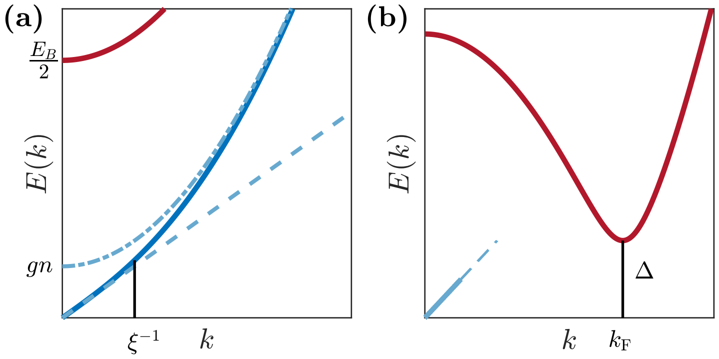

Figure 2.3. – Dispersion of a Fermi gas in the weakly interacting BEC and BCS limits. Blue curves show collective modes, red curves display single-particle excitations. (a): The collective spectrum in the BEC limit consists of a Bogoliubov mode with a linear onset for $k \ll \xi^{-1}$ and a parabolic shape at high momenta. The initial slope is proportional to the sound velocity $c = \sqrt{gn/m}$. The offset of $gn = \mu$ of the parabola shows that the free particles are interacting with the condensate. The single-particle excitations have the parabolic dispersion of a free particle, which is offset by the binding energy $E_B/2$. (b): In the BCS limit, the dispersion of the single particles is given by BCS theory. An energy cost of Δ can be associated to breaking a Cooper pair, which opens a gap in the spectrum. For momenta below k_{F}, the excitation is hole-like. For momenta above k_{F}, it is particle-like. The collective mode is the Bogoliubov-Anderson mode, which has a linear onset at low k. This sound-like excitation propagates at a speed of $v_{\mathrm{F}}/\sqrt{3}$.

Weakly interacting Bose gases

Let us consider a gas of N bosons in a potential $V(\mathbf{r})$, interacting via a contact potential $g\delta(\mathbf{r}_1 - \mathbf{r}_2)$ of strength g. The Hamiltonian of this system is given by

N :	Particle number
$\hat{\mathbf{p}}$:	momentum operator
$V(\vec{r})$:	External potential
g :	Interaction strength
$\psi(\mathbf{r},t)$:	Ground state wave function

$$\hat{H} = \sum_{i=1}^{N} \frac{\hat{\mathbf{p}}_i^2}{2m} + V(\hat{\mathbf{r}}_i) + \frac{1}{2} \sum_{i,j\neq i} g\delta(\hat{\mathbf{r}}_i - \hat{\mathbf{r}}_j). \tag{2.5}$$

The ground state obeys the Gross-Pitaevskii equation [86, 87][4]

$$i\hbar\frac{\partial}{\partial t}\psi(\mathbf{r},t) = \left(-\frac{\hbar^2}{2m}\Delta + V(\mathbf{r}) + g|\psi(\mathbf{r},t)|^2\right)\psi(\mathbf{r},t). \tag{2.6}$$

In 2D systems, dimensional arguments suggest that the interaction strength g may be written as $g = \tilde{g}\hbar^2/m$ with a dimensionless parameter $\tilde{g}$ [83].

$\tilde{g}$: Dimensionless interaction parameter in 2D

In a uniform system, $V(\mathbf{r}) = 0$, the solution to the Gross-Pitaevskii equation reads $\psi_0(t) = \sqrt{n}\exp(-i\mu t/\hbar)$, where the chemical potential is given by

$$\mu = \frac{\partial E}{\partial N} = gn. \tag{2.7}$$

To obtain the excitation spectrum of the Hamiltonian 2.5, one considers small deviations from the equilibrium wave function of the form $\psi(\mathbf{r},t) = \psi_0(t) + \exp(-i\mu t/\hbar)\delta\psi(\mathbf{r},t)$. Inserting $\psi(\mathbf{r},t)$ and $\psi^*(\mathbf{r},t)$ into the Gross-Pitaevskii equation[5] yields coupled equations for $\delta\psi(\mathbf{r},t)$ and

---

[4] This equation can be derived from eq. 2.5 using a variational method by minimizing the quantity $\langle\psi|\hat{H}|\psi\rangle$ under the condition $|\langle\psi|\psi\rangle|^2 = N$, or alternatively by writing the Heisenberg equation of motion for the field operator $\hat{\psi}(\mathbf{r},t)$ and approximating the field operator as a c-number $\psi(\mathbf{r},t)$.

[5] Note that one could also derive the dispersion relation using the density variations and phase variations as conjugate variables as done in [83], or by expanding the field operator in the Heisenberg picture up to linear order in a small non-condensed part.

its complex conjugate $\delta\psi^*(\mathbf{r},t)$. This system is diagonalized using a Bogoliubov transformation [88], and one obtains the elementary excitations of the system. These are Bogoliubov quasiparticles whose dispersion relation is given by

$$E(k) = \sqrt{\frac{\hbar^2 k^2}{2m}\left(\frac{\hbar^2 k^2}{2m} + 2gn\right)}. \tag{2.8}$$

This spectrum is shown as the blue curve in figure 2.3 (a). The character of the Bogoliubov quasiparticles is determined by the relation between their wavelength and the length scale $\xi = \hbar/\sqrt{mgn}$ defined by the interaction strength of the system. ξ is called the healing length, since it is the typical distance over which perturbations in the order parameter smooth out. Long-range perturbations (i.e. at low k) that are large with respect to the healing length, can be smoothed out by the gas. In this case, the excitation is a collective excitation, and the dispersion relation has a linear onset $E(k) \approx \hbar ck$ with $c = \sqrt{gn/m}$. The low-energy quasiparticles therefore correspond to phonon-like excitations propagating at a group velocity of c, which can be seen as the speed of sound of the system. In the case of perturbations at large k or on small scales with respect to the healing length, the gas cannot resolve the size of the perturbation. Only few particles are affected and the excitations are particle-like in nature with a quadratic dispersion relation.

ξ : Healing length

The lifetime of the low-momentum phononic quasiparticles is limited by the interaction between the quasiparticles [89]. At finite temperatures, a phonon can interact with thermal excitations, a process known as Landau damping. The Landau damping rate tends to zero with the temperature and at very low temperatures, the dominant mechanism is Beliaev damping, in which a phonon of momentum q decays into two energetically lower phonons. In the case of a concave dispersion relation, both processes are forbidden and the dominant process is so-called Landau-Khalatnikov damping, which involves interactions between four phonons [90].

Weakly interacting Fermi gases

For the description of weakly interacting fermionic gases, we follow the arguments given by Meera Parish in [64]. The standard framework for the treatment of such systems is BCS theory, which was developed by Bardeen, Cooper and Shrieffer in 1957 [78]. The key point underlying their theory is that the Fermi surface is unstable in the presence of a weak attractive interaction between the particles. In a small region around the Fermi surface, fermions of opposite spin and momentum can pair up to Cooper pairs, which are bosonic in nature and can condense into a new ground state which lies energetically lower than the Fermi sea.

The Hamiltonian of this system is given by [64]

$$\hat{H}_{\mathrm{BCS}} = \sum_{\mathbf{k}\sigma} \varepsilon_{\mathbf{k}} \hat{c}^\dagger_{\mathbf{k}\sigma}\hat{c}_{\mathbf{k}\sigma} + \frac{U}{V}\sum_{\mathbf{k},\mathbf{k}',\mathbf{q}} \hat{c}^\dagger_{\mathbf{k}\uparrow}\hat{c}^\dagger_{\mathbf{k}'\downarrow}\hat{c}_{\mathbf{k}'+\mathbf{q}\downarrow}\hat{c}_{\mathbf{k}-\mathbf{q}\uparrow}, \tag{2.9}$$

where $U < 0$ is the strength of the attractive contact interaction, V the system volume and $\varepsilon_{\mathbf{k}} = \hbar^2 k^2/2m$ the kinetic energy of a free fermion with momentum $\hbar\mathbf{k}$. The operators $\hat{c}_{\mathbf{k}\sigma}$ and $\hat{c}^{\dagger}_{\mathbf{k}\sigma}$ annihilate and create a fermion with spin σ in the momentum state $|\mathbf{k}\rangle$.

U :	Interaction strength
V :	Volume
$\varepsilon_{\mathbf{k}}$:	Kinetic energy of a particle with momentum $\hbar\mathbf{k}$
σ :	Spin
$\hat{c}^{(\dagger)}_{\mathbf{k}\sigma}$:	Fermion annihilation (creation) operator
$\|\psi_{\mathrm{BCS}}\rangle$:	BCS ground state
$\|0\rangle$:	Vacuum state

One assumes that the ground state has the form

$$|\psi_{\mathrm{BCS}}\rangle = \Pi_{\mathbf{k}}(u_{\mathbf{k}} + v_{\mathbf{k}}\hat{c}^{\dagger}_{\mathbf{k}\uparrow}\hat{c}^{\dagger}_{-\mathbf{k}\downarrow})\,|0\rangle\,, \tag{2.10}$$

where $|0\rangle$ is the vacuum state and $|u_{\mathbf{k}}|^2$ and $|v_{\mathbf{k}}|^2$ determine the probabilities of finding a particle or hole state unoccupied or occupied, respectively. Minimizing the quantity $\langle\psi_{\mathrm{BCS}}|\hat{H}_{\mathrm{BCS}}|\psi_{\mathrm{BCS}}\rangle$ under the condition $|u_{\mathbf{k}}|^2 + |v_{\mathbf{k}}|^2 = 1$ yields the following system of equations [64]:

$$\Delta := \frac{U}{V}\sum_{\mathbf{k}} u_{\mathbf{k}} = -\frac{U}{V}\sum_{\mathbf{k}} \frac{\Delta}{2E_{\mathbf{k}}}, \tag{2.11}$$

$$N = \sum_{\mathbf{k}} v_{\mathbf{k}}^2 = \frac{1}{2}\sum_{\mathbf{k}}\left(1 - \frac{\varepsilon_{\mathbf{k}} - \mu}{E_{\mathbf{k}}}\right) \tag{2.12}$$

$$E_{\mathbf{k}} = \sqrt{(\varepsilon_{\mathbf{k}} - \mu)^2 + \Delta^2}. \tag{2.13}$$

Equations 2.11 and 2.12 are called the gap and number equations. Equation 2.13 gives the energy needed to add a single particle excitation in a state $|\mathbf{k}\rangle$. In the BCS limit, it corresponds to the dispersion relation shown in red in Fig. 2.3(b), with a minimum roughly around the Fermi wave vector k_{F} and with an energy gap Δ, which can be interpreted as the energy cost of dissociating a Cooper pair and bringing the excited fermion back to the Fermi surface.

Δ :	BCS pair-breaking gap

In contrast to the Bogoliubov excitations in a bosonic gas, these excitations are single-particle excitations in nature. As can be shown with considerable effort, the system also supports a collective mode, the so-called Bogoliubov-Anderson mode, which was first derived by Anderson within the random phase approximation [91]. This mode is a sound-like collective center-of-mass oscillation of the fermion pairs and exhibits a linear dispersion for low momenta of the form $E(k) = \hbar k v_{\mathrm{F}}/\sqrt{3}$ in 3D and of $E(k) = \hbar k v_{\mathrm{F}}/\sqrt{2}$ in 2D. It is displayed as the blue line in Fig. 2.3 (b).

Strongly attractive Fermi gases

If the attractive interactions in a Fermi gas are increased, for instance using a Feshbach resonance, the particles in a Fermi gas can pair up to form strongly bound molecules whose size becomes much smaller than the interparticle distance. Far enough in the BEC regime, the bound dimers can be treated as weakly interacting pointlike bosonic particles. Nevertheless, this system can also be modeled with the BCS Ansatz [25], as can be seen by the following arguments, also presented in [64]. The ground state wave function of the gas of weakly interacting dimers can be written as a coherent state $|\Psi\rangle = \mathcal{N}\exp(\lambda\hat{b}_0^{\dagger})\,|0\rangle$, where $\hat{b}_0^{\dagger}$ creates a boson in the state $|k = 0\rangle$, $\mathcal{N}$ is a normalization constant and $\lambda = \langle\Psi|b_0|\Psi\rangle$ the condensate order parameter, given by the condensate

$\|\Psi\rangle$:	Ground state of a strongly attractive Fermi gas
$\mathcal{N}$:	Normalization constant
$\hat{b}_0^{\dagger}$:	Boson creation operator
λ :	Condensate order parameter
n_c :	Condensate density
$\varphi_{\mathbf{k}}$:	Two-body wave function

density $n_c = |\lambda|^2/V$. This coherent state does not conserve particle number but corresponds instead to a condensate state with a well defined phase [64]. Since every boson is made up of two fermions, we write $\hat{b}^\dagger_{\mathbf{q}} = \sum_{\mathbf{k}} \varphi_{\mathbf{k}} \hat{c}^\dagger_{\mathbf{k}\uparrow} \hat{c}^\dagger_{\mathbf{q}-\mathbf{k}\downarrow}$, where $\varphi_{\mathbf{k}}$ is the relative two-body wave function in momentum space. After inserting this into the expression for the ground state and using $v_{\mathbf{k}}/u_{\mathbf{k}} = \lambda\varphi_{\mathbf{k}}$ and $\mathcal{N} = \Pi_{\mathbf{k}} u_{\mathbf{k}}$, one can show [64] that:

$$|\Psi\rangle = \mathcal{N} \exp(\lambda \hat{b}^\dagger_0) |0\rangle = \Pi_{\mathbf{k}} (u_{\mathbf{k}} + v_{\mathbf{k}} \hat{c}^\dagger_{\mathbf{k}\uparrow} \hat{c}^\dagger_{-\mathbf{k}\downarrow}) |0\rangle \,. \tag{2.14}$$

This is the same state as the BCS ground state 2.10, which highlights the close link between the two systems.

We thus see that a Fermi gas far in the BEC regime can indeed be described by a weakly interacting bosonic theory and thus the same low-energy Bogoliubov excitation spectrum is found for a gas of fermion dimers. Due to the composite nature of the particles, however, we also expect that the single-particle excitation branch present in BCS theory exists in the bosonic regime as well. Indeed it is possible to create single fermionic excitations by breaking the strongly bound dimers, when an energy of half of the binding energy is available per particle. The single-particle dispersion thus has an offset of $E_{\mathrm{B}}/2$ and continues on quadratically.

2.4. Controlling the key parameters of ultracold gases

After having given an impression how changing the interaction strength in a Fermi gas might change the physical properties of the gas, we will now take a closer look on how the density, dimensionality and interaction parameters are adjusted in an experiment.

2.4.1. Controlling the density

Tuning the density of a quantum gas is relatively straightforward and can be achieved either by adjusting the particle number N at fixed system geometry or by changing the dimensions of the trapping potentials at constant particle number. The maximum achievable density is limited by inelastic three-body losses, whereas the detection sensitivity of the imaging cameras set the minimum densities which can reasonably be worked with.

The most common traps used in the final stages of a cold atom experiment are optical dipole traps [92] generated by focused laser beams, which can be interfered to form optical lattices, or shaped to form homogeneous box-shaped traps created using axicons, light sheets or digital micromirror devices (DMDs). The final stages of cooling are typically performed in these traps using evaporative cooling techniques, in which the particles with the highest energy are expelled from the trap, while the remaining particles then thermalize to a lower temperature. The potential height at the end of the final evaporation can be used to adjust the number of atoms left in the system. In the case of dipole traps or optical lattices, the trap can be recompressed after evaporation to adjust the density at constant atom number. Since the density and temperature of the gas are coupled in a harmonic trap, however, it is sometimes preferable to use a DMD or axicon setup to create a homogeneous trap. In this case, the shape of the trapping potential can additionally be varied by displaying different sets of images or by moving a lens within the optical setup.

2.4.2. Controlling the dimensionality

The trapping potentials also determine the dimensionality of the system. Two-dimensional geometries are usually experimentally created by freezing out one motional degree of freedom. In order to achieve this, the atoms are trapped in a very tight harmonic potential along one direction, such that all relevant energy scales are smaller than the level spacing of the confining potential, i.e., $\mu, E_\mathrm{F}, k_\mathrm{B}T, ... \ll \hbar\omega_z$. This confines the atoms to the motional ground state of the confining potential. Although the motion of the atoms may be restricted to 2D, there can nevertheless be other length scales, which remain smaller than the harmonic oscillator length l_z. These could be the size of the tightly bound fermion pairs in the BEC-limit of the BEC-BCS crossover or the energy of intermediate states during scattering events. These additional scales lead to deviations from the pure 2D physics. We will come back to this point after introducing the scattering amplitude and Feshbach resonances in a three-dimensional geometry.

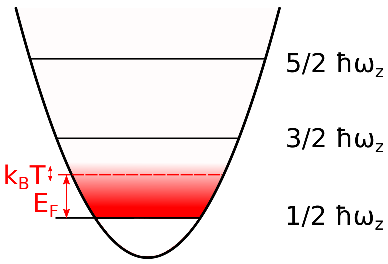

Figure 2.4. – Energy diagram of a two-dimensional gas. A gas is in a quasi-two-dimensional configuration if the level spacing of the strongly confining potential is larger than all other relevant energy scales, such as the thermal energy $k_\mathrm{B}T$ or the Fermi energy E_F. In this case, the atoms occupy the motional ground state in the direction of strong confinement.

2.4.3. Controlling interactions

In order to describe interactions in ultracold gases, we first have to introduce the scattering length and Feshbach resonances in greater detail. We will first introduce these concepts in a three-dimensional setting and then focus on the intricacies that a two-dimensional setting introduces into the problem. In the following, we assume a short-range interaction, such that the particles far away from the scattering potential are described as free particles.

The 3D scattering length

As in classical physics the scattering problem between two particles is solved by using center-of-mass and relative coordinates. The Schrödinger equation for the relative coordinates is given by

$$\left[-\frac{\hbar^2}{2m_r}\Delta_\mathbf{r} + V(\mathbf{r})\right]\Psi(\mathbf{r}) = E\Psi(\mathbf{r}). \tag{2.15}$$

Here, $m_r = m_1 m_2/(m_1 + m_2)$ is the reduced mass of the system, $\mathbf{r} = (m_1\mathbf{r}_1 - m_2\mathbf{r}_2)/m_r$ the relative coordinate, Δ_r the Laplace operator with respect to the relative coordinate and $V(\mathbf{r})$ the interaction potential between the particles.

$\Delta_\mathbf{r}$:	Laplace operator with respect to the relative coordinate
m_r :	Reduced mass
$V(\mathbf{r})$:	Interaction potential

The solution to the Schrödinger equation has the form of an incoming plane wave $e^{i\mathbf{kr}}$ and an outgoing scattered spherical wave e^{ikr} [24]

$$\Psi(\mathbf{r}) \simeq e^{i\mathbf{kr}} + f(\mathbf{k}', \mathbf{k}) \frac{e^{ikr}}{r}, \tag{2.16}$$

$f(\mathbf{k}', \mathbf{k})$: Scattering amplitude

where $f(\mathbf{k}', \mathbf{k})$ is the scattering amplitude for scattering the incoming plane wave into the direction given by $\mathbf{k}' = k\mathbf{r}/r$.

One can now decompose the incoming and outgoing waves into spherical harmonics using the Legendre polynomials $P_l(\cos\theta)$ and the Bessel functions $j_l(x)$. Here θ denotes the angle between incoming wave and the direction of scattering. We assume a radially symmetric potential $V(r)$. Using the expansions

$$f(\mathbf{k}', \mathbf{k}) = \sum_{l=0}^{\infty} (2l+1) a_l(k) P_l(\cos\theta), \text{ and} \tag{2.17}$$

$$e^{ikz} = \sum_{l=0}^{\infty} (2l+1) i^l j_l(kr) P_l(\cos\theta), \tag{2.18}$$

where the $a_l(k)$ are complex expansion coefficients, as well as the asymptotic behavior of the Bessel functions, $j_l(kr) \to (1/2kr)(i^{-(l+1)}e^{ikr} + i^{l+1}e^{-ikr})$ for $kr \gg 1$, one obtains the scattering wave function as the sum of incoming and outgoing spherical waves:

$$\Psi(\mathbf{r}) \simeq \frac{1}{2ikr} \sum_{l=0}^{\infty} (2l+1) P_l(\cos\theta) \times \\ \times \left[(2ika_l(k) + 1) e^{ikr} + (-1)^{l+1} e^{-ikr} \right]. \tag{2.19}$$

Since the total particle number has to be conserved, the coefficients of incident and scattered waves must obey $|2ika_l(k) + 1|^2 = |(-1)^{l+1}|^2 = 1$, which is fulfilled under the condition that $2ika_l(k) + 1 = e^{2i\delta_l(k)}$. This relation introduces the so-called scattering phase shifts $\delta_l(k)$, which are the phase differences between incoming and outgoing partial waves, acquired during the interaction between the particles.

$\delta_l(k)$: Scattering phase shifts

At ultralow temperatures, scattering at high angular momenta $l > 0$ is suppressed due to the occurrence of centrifugal potential barriers in those channels and only the s-wave channel contributes to the scattering process. For this channel, the scattering amplitude is

$f_0(k)$: S-wave scattering amplitude

$$f_0(k) = \frac{1}{2ik}(e^{2i\delta_0(k)} - 1) = \frac{1}{k \cot\delta_0(k) - ik}. \tag{2.20}$$

Time reversal symmetry implies that $k \cot\delta_0$ is an even function of momentum [24], and we can thus expand it to second order around $k = 0$, which yields $k \cot\delta_0 \approx -1/a + \mathcal{O}(k^2)$. This results in

$$f_0(k) \approx \frac{1}{-\frac{1}{a} - ik + \mathcal{O}(k^2)}. \tag{2.21}$$

One finds that the scattering amplitude becomes independent of θ and depends only on k and a parameter a with dimension length. This defines the 3D scattering length

$$a_{\mathrm{3D}} := a = -\lim_{k\to 0} f_0(k). \tag{2.22}$$

To give the scattering length more intuitive significance, we can note that at ultralow energies, i.e., for $ka \ll 1$, the full cross section of the ultracold scattering process is given by

$$\sigma_{\mathrm{tot}} = \int d\Omega |f(\theta)|^2 = 4\pi a_{\mathrm{3D}}^2, \tag{2.23}$$

which is the same cross section as for scattering of classical hard spheres with a radius a_{3D}.

a_{3D}:	Scattering length
a_{bg} :	Background scattering length
ΔB :	Resonance width
B_0 :	Resonance position
$\hat{H}_{\mathrm{int}}$:	Interaction Hamiltonian of the colliding atoms

Feshbach resonances

At ultralow temperatures, the interactions in an ultracold Fermi gas can be described by a single parameter, the scattering length a_{3D}. Feshbach resonances allow us to tune the scattering length of the gas by adjusting the value of a magnetic bias field. The typical dependency of the 3D s-wave scattering length on the magnetic field can be modeled as [25, 62]

$$a_{\mathrm{3D}}(B) = a_{\mathrm{bg}}\left(1 - \frac{\Delta B}{B - B_0}\right), \tag{2.24}$$

where a_{bg} is the background scattering length and ΔB and B_0 the width and position of the resonance.

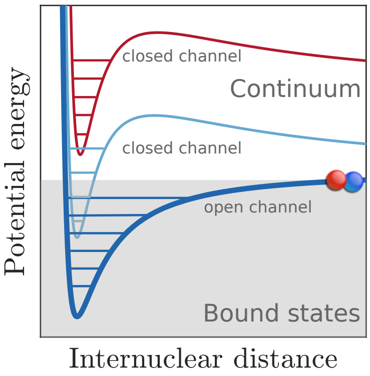

Figure 2.5. – Schematic representation of a Feshbach resonance. Two atoms are colliding in the continuum of an open channel (dark blue). The interaction between the spins admixes contributions of different spin wavefunctions. These are subject to different interaction potentials (light blue, red). Due to the different magnetic momenta of these different spin configurations, the energy difference between the potentials can be tuned. When the energy of abound state becomes resonant with the energy of the colliding atoms, the scattering amplitude becomes strongly enhanced. Since the atoms could not escape to infinite distance in the light blue and red potentials, these channels are said to be closed.

For information on the mathematical treatment of Feshbach resonances, I would like to refer the reader to [62]. Here, I will only outline the qualitative discussion presented in this reference. In short, a Feshbach resonance leads to a resonant enhancement of the scattering cross section between two particles due to the presence of bound states at an energy close to that of the scattering partners. At a fixed magnetic field, the two-body Hamiltonian takes the form

$$\hat{H}_{\mathrm{int}} = \frac{\hat{\mathbf{p}}^2}{2m} + \sum_{j=1}^{2}(\hat{V}_j^{\mathrm{hf}} + \hat{V}_j^{\mathrm{Z}}) + \hat{V}^{\mathrm{cen}} + \hat{V}^{\mathrm{dd}}. \tag{2.25}$$

Here the first term describes the relative kinetic energy between the particles. The next two terms are the single-particle hyperfine interaction $\hat{V}_j^{\mathrm{hf}} = (a_j^{\mathrm{hf}}/\hbar^2)\hat{\mathbf{s}}_j \cdot \hat{\boldsymbol{\imath}}_j$ and the Zeeman energy $\hat{V}_j^{\mathrm{Z}} = (\gamma_e \hat{\mathbf{s}}_j - \gamma_N \hat{\boldsymbol{\imath}}_j) \cdot \mathbf{B}$, where a_j^{hf} is the hyperfine splitting, $\mathbf{s}$ and $\boldsymbol{\imath}$ the electron and nuclear spins and γ_e and γ_N the corresponding gyromagnetic ratios. $\hat{V}^{\mathrm{cen}}$ is the central interaction which is given as the sum of van-der-Waals and exchange interactions $\hat{V}^{\mathrm{cen}}(r) = \hat{V}_{\mathrm{vdW}}(r) - (-1)^S \hat{V}_{\mathrm{ex}}(r)$. This contribution gives rise to different potentials depending on the atoms occupying a singlet ($S = 0$) or triplet ($S = 1$) state. Finally the spins of the atoms interact with each other via the dipole-dipole interaction

$$\hat{V}^{\mathrm{dd}} = \frac{\mu^2}{4\pi\mu_0^{-1} r^3} \cdot [\hat{\sigma}_1 \cdot \hat{\sigma}_2 - 3(\hat{\sigma}_1 \cdot \hat{\mathbf{r}})(\hat{\sigma}_2 \cdot \hat{\mathbf{r}})], \tag{2.26}$$

$\hat{V}^{\mathrm{dd}}$: Magnetic dipole-dipole interaction
μ : Electron magnetic dipole moment
σ_i : Pauli matrix of spin i
μ_0 : Vacuum permeability

where μ is the electronic magnetic dipole moment, σ_i the Pauli matrix corresponding to the spin of atom i and μ_0 the magnetic permeability. Two colliding atoms are therefore subject to different interaction potentials depending on the spin configurations and their relative angular momentum. Schematic examples for these potentials are shown in Figure 2.5.

The collision process can now be visualized as follows. Initially, the two scattering atoms are far apart and feel a negligible interaction potential. The atoms occupy a state with energy E in the continuum of this interaction potential defined by the unperturbed atomic states $|F, m_F\rangle$. Such a state is referred to as an 'open channel', since the atoms can escape to infinite distance. Upon approaching each other, additional hyperfine states are mixed in by the interactions. This admixture gives rise to coupling to different interaction potentials, which can be either open or closed channels with respect to the scattering atoms. Since the different hyperfine states have different magnetic momenta, the interaction potentials can be shifted with respect to each other via the Zeeman effect. Varying the magnetic field, one can therefore tune a closed channel bound state in close proximity to the energy of the incoming particles, which causes the a resonant enhancement of the scattering amplitude in the open channel.

The 3D scattering length across the BEC-BCS crossover

For small negative values of the scattering length, $-1/k_{\mathrm{F}}a_{\mathrm{3D}} \to \infty$, the interaction between the atoms is weak and attractive. Here, the fermions form Cooper pairs and a BCS-type system is realized. When the interaction strength is increased, the scattering length becomes more and more negative. Beyond a threshold interaction strength, a true bound state of two atoms becomes possible. The appearance of this bound state is marked with a divergence of the scattering length, which turns positive. The energy of this bound state can be calculated from the poles of the scattering amplitude. These occur at $1/a_{\mathrm{3D}} = -ik$. Squaring and multiplying both sides by $\hbar^2/2m_r$, where $m_r = m/2$ is the reduced mass of the system, yields

$E_{\mathrm{B}}^{(\mathrm{3D})}$: Bound state energy

$$E_{\mathrm{B}}^{(\mathrm{3D})} = -\frac{\hbar^2}{m a_{\mathrm{3D}}^2}. \tag{2.27}$$

Upon further increase of the attraction, the newly formed dimers become more deeply bound, the scattering length decreases again towards small but positive values and the system crosses over in the BEC-regime for $-1/k_{\mathrm{F}}a_{\mathrm{3D}} \to -\infty$. The fact that the scattering length becomes positive although the interaction between the atoms remains attractive is counter-intuitive. To see this, we note that a short-range interaction can also be modeled as a contact interaction by setting $g = 4\pi\hbar^2 a_{\mathrm{3D}}/m$. A positive scattering length would correspond to a repulsive contact interaction, which would contradict the existence of a bound state. The sign of the scattering length is therefore not in direct correspondence with the sign of the interaction.

In the case of a Fermi gas, one might instead see the positive scattering length on the BEC-side of the resonance as describing an effective repulsive interaction between the dimers. Indeed there is a simple relation between the 3D-scattering length and the effective scattering length of the dimers $a_{\mathrm{dd}} \approx 0.6 a_{3\mathrm{D}}$ [93]. However, this intuitive picture fails in different settings (for example for a bosonic gas).

a_{dd} : Dimer-dimer scattering length

2.4.4. The role of the dimensionality

2D case

For scattering at ultralow energies in two dimensions, the role of the scattering length is taken on by the quantity [84]

$$\ln(k a_{2\mathrm{D}}). \tag{2.28}$$

In principle, the derivation of the scattering length in 2D follows a similar path as in the 3D case. It is detailed for instance in [25] and [94]. The solution to the Schrödinger equation is again written as a sum of an incoming plane wave and an outgoing circular wave,

$$\psi(\mathbf{r}) = e^{ikx} - f(\mathbf{k}) \sqrt{\frac{i}{8\pi k r}} e^{ikr}, \tag{2.29}$$

where k is the wavevector of the incident wave and $\mathbf{k} = k\mathbf{r}/r$ is defined by the direction of the scattered wave. The scattering amplitude can be expanded in the partial waves

$$f(\mathbf{k}) = \sum_{l=0}^{\infty} (2 - \delta_{l0}) \cos(l\theta) a_l(k), \tag{2.30}$$

where δ_{l0} is the Kronecker symbol and the $a_l(k)$ are again complex coefficients (different from those in the 3D case). The relation between the scattering amplitude and the scattering phase shifts now take the form $a_l(k) = -4/(\cot \delta_l(k) - i)$.

The low-energy s-wave phase shift can be written as $\cot \delta_0(k) = -(2/\pi) \ln(1/k a_{2\mathrm{D}}) + \mathcal{O}(k^2)$ [94, 95], with $a_{2\mathrm{D}} > 0$ a parameter with dimension of length, from which we get

$$f_0(k) = a_0(k) = \frac{-2\pi}{\ln(k a_{2\mathrm{D}}) - i\frac{\pi}{2}}. \tag{2.31}$$

The form of this equation seems similar to equation 2.22, however the logarithm diverges at $k \to 0$ for any nonzero scattering length. This in turn signifies that the scattering amplitude tends to zero for ultralow energies, which is different from the 3D result, where the zero-energy scattering amplitude was determined by a constant $f_0 \to -a_{3\mathrm{D}}$. Clearly, the scattering amplitude at ultralow energies depends on momentum and we cannot use $a_{2\mathrm{D}}$ as a single parameter to describe the ultracold scattering properties in 2D. Instead, the composite parameter $\ln(ka_{2\mathrm{D}})$ must be used.

In a two-dimensional setting, we can again look at the poles of eq. 2.31 to find the energy of the bound state and we find

$E_{\mathrm{B}}^{(2\mathrm{D})}$: 2D Bound state energy

$$E_B^{(2\mathrm{D})} = -\frac{\hbar^2}{ma_{2\mathrm{D}}^2}. \tag{2.32}$$

Quasi-2D regime

In real experiments, it is not possible to eliminate the third direction altogether. Low-dimensional systems are instead produced by restricting the particles to the motional ground state of a strongly confining potential Comparing the length scales, the harmonic oscillator length l_z is then smaller than both the interparticle spacing $n^{-1/2}$ and the thermal wavelength of the particles λ_{dB}. However, the range of the interaction between the particles is still smaller than the oscillator length, such that the physics of the collisions are relatively unaffected by the confinement [94]. The scattering itself is still a 3D process and the confining potential only influences the incoming and outgoing wave functions. This affects both the scattering length and the bound state energy, which we will discuss now.

Scattering length

Petrov and Shlyapnikov [84] have been able to relate the 2D scattering amplitude $a_{2\mathrm{D}}$ to the 3D parameter $a_{3\mathrm{D}}$ in the limit that the energy of the scattering particles is much smaller than the spacing of the energy levels due to the confinement potential $E \ll \hbar\omega_z$. This regime is called the quasi-2D regime. According to [84], the s-wave contribution to the scattering amplitude is given by

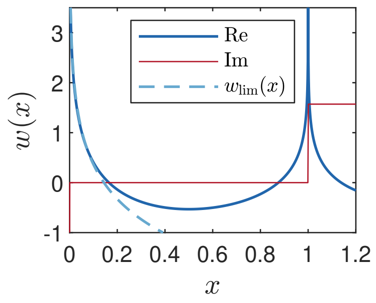

Figure 2.6. – Real and imaginary parts of the function $w(x)$ defined by 2.34. The range of validity $x < 0.1$ of the approximation $w_{\mathrm{lim}}(x)$ (light blue) defines the quasi-2D regime.

$$f_0(k) = \frac{2\sqrt{2\pi}}{\frac{l_z}{a_{3\mathrm{D}}} + \frac{1}{\sqrt{2\pi}} w\left(\frac{\varepsilon}{\hbar\omega_z}\right)}, \tag{2.33}$$

where $w(x)$ is a rather complex function given by

$$w(x) = \lim_{J\to\infty}\left[\sqrt{\frac{4J}{\pi}}\ln\frac{J}{e^2} - \sum_{j=0}^{J}\frac{(2j-1)!!}{(2j)!!}\ln(j - x - i0)\right]. \tag{2.34}$$

It is $w_{\mathrm{lim}}(x) = \lim_{x\to 0} w(x) = -\ln(2\pi x/A) + i\pi$, where $A = 0.905$ is a numerical constant. This approximation holds up to energies $\varepsilon/\hbar\omega_z \approx 0.1$ (compare Fig. 2.6). Consequently in the low energy limit, the scattering amplitude can be cast into the form of the pure 2D scattering formula by identifying $a_{2\mathrm{D}}$ with the quasi-2D scattering length [84]

$a_{\mathrm{q2D}}^{(0)}$: quasi-2D scattering length

$$a_{\mathrm{q2D}}^{(0)} = \sqrt{\frac{\pi}{A}}\, l_z \exp\left(-\sqrt{\frac{\pi}{2}}\frac{l_z}{a_{3\mathrm{D}}}\right). \tag{2.35}$$

This quasi-2D scattering length is dependent on the 3D scattering length and on the strength of the harmonic confinement, which underlines again that scattering in 2D cannot be described with the help of one single parameter.

Equation 2.35 has been derived for the low-energy limit $E \ll \hbar\omega_z$. We expect this relation to hold in the BEC regime, where the particles form a condensate and the kinetic energy of most particles is low. In the BCS regime however, the mean energy of the atoms is larger, since the Pauli principle leads to the formation of a Fermi sea. Since the Fermi energy is usually a substantial fraction of $\hbar\omega_z$, both low- and high energy collisions should occur. In the analysis of the measurements presented in thesis, we will make one central assumption and suppose that the typical collision energy is given by the chemical potential. Following [56] we may then apply a 'correction' factor to the scattering length to extend the range of validity of $a^{(0)}_{\mathrm{q2D}}$ towards higher collision energies. This yields a modified quasi-2D scattering length

$$a_{\mathrm{q2D}} = a^{(0)}_{\mathrm{q2D}} \exp\left(-\frac{1}{2}\Delta w\left(\frac{\mu}{\hbar\omega_z}\right)\right), \tag{2.36}$$

where the function $\Delta w(x)$ is defined as $\Delta w(x) = w(x) - w_{\mathrm{lim}}(x)$ [56].

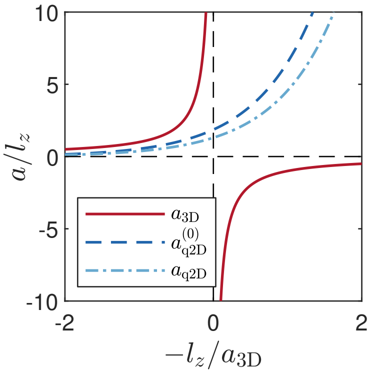

Figure 2.7. – Scattering lengths across the BEC-BCS crossover. The BEC-regime is located on the left hand side, the BCS-regime is reached on the right hand side of the graph. The 3D-scattering length (dark red) diverges on resonance, whereas the 2D-scattering length (light red) is positive across the entire range. Across the resonance, the chemical potential of the gas increases from gn on the Bose side to essentially E_{F} on the Fermi side. The correction to the scattering length for higher chemical potential therefore becomes more and more pronounced when going towards the fermionic side.

Figure 2.7 shows the 3D scattering length (red) as a function of the parameter $-l_z/a_{3\mathrm{D}}$, as well as a comparison between the bare quasi-2D scattering length $a^{(0)}_{\mathrm{q2D}}$ (dark blue) and the modified scattering length a_{q2D} for $\mu/\hbar\omega_z = 0.4$. In the Bose regime, the bare and modified quasi-2D scattering lengths approach each other. In the BCS regime, however, the deviations become important, since the average momentum of the scattering particles increases.

In the remainder of this thesis, we will use a_{q2D} and the typical momentum of the scatterers $k \approx k_{\mathrm{F}}$ to parametrize the interaction axis of the quasi-2D Fermi gas with $\ln(k_{\mathrm{F}} a_{\mathrm{q2D}})$, in analogy to the parameter existing for the true 2D gas. In addition, following the naming habits in the experimental community, we will often omit the prefix 'quasi-' and speak in short of 2D gases. Whenever we treat an experimental system, however, that true two-dimensional systems do not exist in the laboratory.

$\Delta w(\mu/\hbar\omega_z)$: Function extending a_{q2D} toward higher scattering energies

a_{q2D} : quasi-2D scattering length, modified for $\varepsilon > 0.1\hbar\omega_z$

Bound state

In Figure 2.7, we can see that the quasi-two-dimensional scattering length is always positive, signaling the existence of a bound state over the entire BEC-BCS crossover, which competes with the BCS pairing mechanism on the BCS side of the resonance [96].

The character of this bound state and its energy $E_B^{(\mathrm{q2D})}$ are strongly influenced by the size of the bound state relative to the scale set by the tight confinement. In the fermionic regime, the attractive interaction between the atoms is weak. Consequently, the pairs are weakly bound and the pair size is large compared to the oscillator length. We thus have pairs which live in the 2D plane and whose binding energy will tend to that of a true 2D pair: $E_{\mathrm{B}}^{(2\mathrm{D})} = -\hbar^2/ma^2_{\mathrm{q2D}}$ [6]. For increasing interactions, the dimer size is reduced. Once the dimers become much smaller than the oscillator length, they can be seen as are almost unperturbed with respect to the 3D scenario and their binding energy must approach

$E_B^{(\mathrm{q2D})}$: Energy of the bound state in the quasi-2D geometry.

---

[6] Note that we still have to use the quasi-2D scattering length to calculate the binding energy in the BCS-limit.

the binding energy set by the 3D scattering length $E_{\mathrm{B}}^{(3\mathrm{D})} = -\hbar^2/ma_{3\mathrm{D}}^2$. Directly on the resonance of the 3D scattering length, the energy of the quasi-2D bound state reaches a universal value only dependent on the harmonic confinement $E_{\mathrm{B}} = -0.244\hbar\omega_z$ [94].

We therefore cannot use the formula $E_{\mathrm{B}} = -\hbar^2/ma_{\mathrm{q2D}}^2$ to express the energy of the bound state over the entire crossover in terms of a single scattering length. Instead the bound state energy in the quasi-2D geometry must be calculated numerically as the solution of the integral equation [94]

$$\frac{l_z}{a_{3\mathrm{D}}} = \int_0^\infty \frac{du}{\sqrt{4\pi u^3}} \left(1 - \frac{\exp(-E_{\mathrm{B}}^{(\mathrm{q2D})} u/\hbar\omega_z)}{\sqrt{(1-\exp(-2u))/(2u)}}\right). \tag{2.37}$$

We see that like the quasi-2D scattering length, it depends on the ratio between the confinement and the three-dimensional scattering length. Figure 2.8 shows the numerical solution of this formula (blue) as well as the limits $E_{\mathrm{B}}^{(3\mathrm{D})} = \hbar^2/ma_{3\mathrm{D}}$ valid in the BEC-regime and $E_{\mathrm{B}}^{(2\mathrm{D})}(a_{\mathrm{q2D}}) = \hbar^2/ma_{\mathrm{q2D}}$, valid in the BCS-regime.

As a final point, I would like to note that we will compare the measurements taken with our system to predictions for true 2D systems, ignoring the dependency on the oscillator length of the confining potential. While this is in principle a comparison between two different systems, it is of high interest, since it shows how close a quasi-2D system can come to a true 2D system. In addition, eventual discrepancies between the two highlight, that the third dimension cannot be ignored in all parameter ranges. In order to completely understand fascinating phenomena related to two-dimensional geometries, these intricacies must then be taken into account.

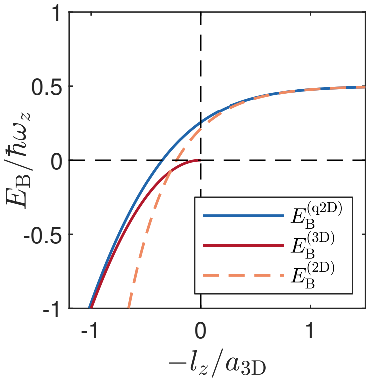

Figure 2.8. – Binding energies across the BEC-BCS crossover. In 3D there is a bound state only for positive values of $a_{3\mathrm{D}}$, in the BEC regime (red). In 2D, a bound state exists over the entire range, whose energy smoothly transitions from an energy given by the quasi-2D scattering length in the BCS regime to an energy given by the 3D scattering length in the BEC regime. Equation 2.37 [94] (blue) interpolates the binding energies across the crossover. In the BCS regime, the expression $\hbar^2/ma_{\mathrm{q2D}}^{(0)2}$ yields a good approximation (orange), which starts to deviate around $l_z/a_{3\mathrm{D}} \approx 0$.

Part I.

Characterizing a D-wave Feshbach Resonance in Ultracold ^{40}K

3. Creating Ultracold Potassium: The Fermix Experiment

Before treating the phenomenon of sound in ultracold two-dimensional Fermi gases, I would like to take time to present part of the work done in the Ultracold Fermi Gases group of Laboratoire Kastler Brossel, during the first half of my PhD. The project consisted in the characterization of a new d-wave Feshbach resonance in fermionic potassium. I will first introduce the Fermix experiment. For this, a quite general overview over the general scheme to produce ultracold Fermi gases in the experiment will be given. I will then focus on some key steps of the experimental sequence that are particular to the Fermix experiment in the following sections. Finally, I will present the setup around the science cell in particular. The experimental setup was built by my PhD predecessors Armin Ridinger, Thomas Salez, Franz Sievers, Diogo Rio Fernandes and Norman Kretzschmar, Daniel Suchet, Mihail Rabinovic, Thomas Reimann and Cédric Enesa, in whose theses more details on the setup can be found [97–105].

Roadmap for creating an ultracold atomic gas

Many cold atom experiments follow similar schemes to create ultracold Fermi gases in the laboratory. Cooling down atomic gases to temperatures of several tens of nK above absolute zero requires background pressures of the order of 10^{-11} mbar or below in order to minimize background collisions with thermal atoms and reach sample lifetimes of the order of minutes. The experiment is therefore carried out in an ultrahigh vacuum system. At the same time, generating the atomic gas from a solid sample of lithium or potassium requires to heat the source region of the vacuum chamber to high temperatures, which incurs elevated vapor pressures and increased outgassing from the walls of the steel chamber. To separate regions of high and low pressure, the vacuum systems of most experiments consist of multiple functional parts, which are connected to each other with differential pumping stages. The vacuum is maintained by an ensemble of vacuum pumps[1]. As an example of such an apparatus, the vacuum system of the Fermix experiment is shown in Figure 3.1. The experiment has been designed as a dual-species experiment, with the goal of producing quantum degenerate mixtures of ^{6}Li and ^{40}K, both fermionic alkali elements. It therefore allows me to introduce the typical implementations for both species at the same time.

An atomic source, consisting of a macroscopic block of the respective material located in a dedicated source region of the vacuum system, is

---

[1] These can be ion pumps, getter pumps or Titanium sublimation pumps for instance.

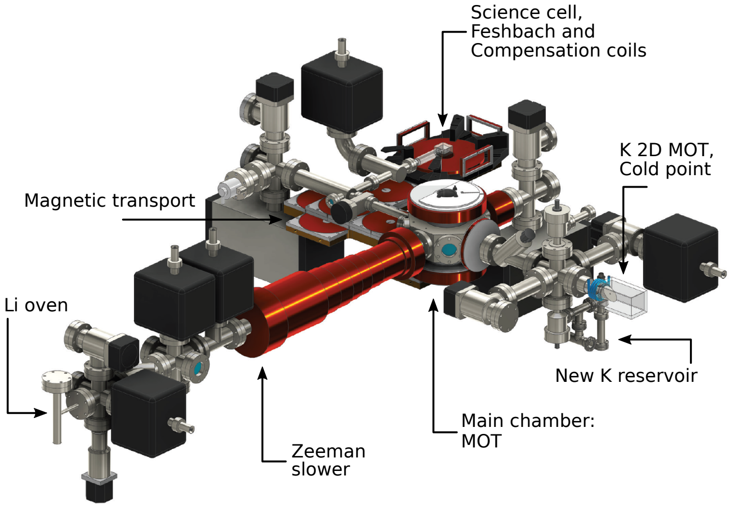

Figure 3.1. – CAD drawing of the Fermix vacuum system. The apparatus consists of two source regions, a lithium oven and a potassium 2D MOT which connect to an octagonal central cell (via a Zeeman slower in the case of lithium). Here the atoms are captured and cooled optically. In order to transfer the atoms into a region of high vacuum quality and large optical access, a magnetic transport links the main chamber to the science cell. For clarity, the top coils of the transport and the science cell region are not shown. Figure adapted from [104].

heated up in order to create a high vapor pressure. In the case of lithium, the necessary temperatures are roughly 450 °C, at which the element is in its liquid state, with a vapor pressure of roughly $8 \cdot 10^{-4}$ mbar [106]. For potassium, more reasonable temperatures of $T \approx 45\,°\mathrm{C}$ are sufficient, since the use of an enriched sample can ensure high partial pressures of ^{40}K already at lower pressures. The gases escape the oven sections through thin tubes towards the main chamber of the vacuum system, where the atoms are trapped in a magneto-optical trap (MOT) [19]. For lithium, the high oven temperature ensures a high particle flux, however the atoms exit the oven section at mean velocities of about $1500\,\mathrm{m\,s^{-1}}$. An intermediate slowing step is therefore necessary, which is typically carried out with the help of a Zeeman slower [17]. For potassium, a combination of a two-dimensional magneto-optical trap (2D-MOT) and a push beam is used at Fermix (see section 3.1.1) to accelerate the atoms towards the main chamber. The resulting velocities are low enough to allow the atoms to be trapped without additional slowing steps.

The MOT is typically located in a second vacuum chamber, which is separated from the source regions by a differential pumping stage. Its working principle relies on the repeated absorption and reemission of photons, which limits the lowest attainable temperatures in the trapped gas. For a standard MOT, this limit is given by the Doppler temperature $T_\mathrm{D} = \hbar\Gamma/2k_\mathrm{B} \approx 140\,\mu\mathrm{K}$ [107], where $\Gamma \approx 2\pi \times 6\,\mathrm{MHz}$ is the natural linewidth of the D2-line [106, 108]. While there exist optical sub-Doppler cooling schemes[2], any scheme involving absorption and reemission is limited by the release of the one-photon recoil energy $E_\mathrm{rec} = \hbar^2 k_L^2/2m$, which is still too large to reach quantum degeneracy. Here k_L is the wave number of the laser radiation.

T_D :	Doppler temperature
Γ :	Transition linewidth
E_rec :	Recoil energy
k_L :	Laser wave number

[2] One could mention Sisyphus cooling [109], Velocity-selective coherent population trapping [110], Raman cooling [111] or gray molasses cooling on the D2- or D1-lines [112, 113] to give but a few examples.

To be able to cool the gas further down, it must be loaded into conservative trapping potentials, which do not rely on absorption or emission of photons. These can be optical dipole traps (ODTs) [92] created with infrared lasers, whose large detuning with respect to the atomic transitions prevents such unwanted absorption and emission processes from occurring. Another possibility is to load the gas into magnetic traps, where the conservative trapping potential is generated by the Zeeman effect. In a succession of ODTs and magnetic traps of different geometries, the gas can be cooled down further using evaporative cooling techniques [107, 114]. These rely on the (active or passive) removal of atoms in the high-energy tail of the momentum distribution from the trap and rethermalization of the remaining particles by means of collisions. The energy carried away by the escaping atom is higher than the average particle energy and the rest of the ensemble will therefore thermalize to a lower energy and thus a lower temperature. By ramping down the potential height on a timescale slower than the thermalization time, the temperature of the trapped ensemble can be drastically reduced on the expense of the atom number (compare [107]).

In order to carry out experiments on the gas, the main chamber hosting the MOT is typically not well suited, both in terms of vacuum quality and optical access. The gas is therefore transferred from the main chamber of the vacuum system to the science cell, another dedicated part of the system with high optical access and improved vacuum. Here, the gas is brought into the desired geometry and final evaporative cooling steps bring the gas into the degenerate regime. After these preparatory steps, the experiment-specific steps of the sequence are carried out. Finally, the atoms are imaged in order to extract the density profile. The imaging method used in this thesis is absorption imaging, in which a short pulse of resonant light is shot onto the atoms and the shadow is imaged onto a camera. Since the transmission of light through the cloud is governed by the Lambert-Beer law[3], the density distribution integrated along the imaging axis can be reconstructed from a relative measurement of the light intensity with and without atoms [115].

After having introduced the main idea of the experimental sequence, let us now look at the experimental sequence in greater detail. I will concentrate on the aspects pertaining to the Fermix experiment in particular. While the experiment has been designed as a dual-species experiment, major renovation works had taken place in the building housing the experiment directly before my arrival in the group and the machine had been resting for about a year. After the construction works were finished, a decision was taken to restart the potassium parts of the experiment before reactivating the lithium parts in a later stage. I will therefore only treat the potassium part of the machine. For information of the operation of the Fermix experiment with lithium, I would refer the reader to the theses of my PhD predecessors [97–104].

[3] This is strictly only true at low intensities of the imaging light. At high intensities, the Lambert-Beer law acquires correction terms (compare [115, 116] and section 5.1.3

3.1. Experimental sequence of the Fermix experiment

3.1.1. Potassium 2D-MOT

As mentioned previously, the potassium source of the Fermix experiment consists of a 2D-MOT with additional longitudinal molasses and pushing beam. While it is possible to use an oven in conjunction with a Zeeman slower to generate atomic gases of ^{40}K[4], this setup would require very high vapor pressures to create a sufficient flux of the correct isotope, since the natural abundance of potassium 40 is only 0.012% [117]. These high pressures in turn would cause the vacuum pumps to degrade very quickly. Although considerably more expensive[5], it is therefore advantageous to use an enriched sample of potassium, containing 4% of ^{40}K and to use a 2D-MOT to produce the atomic beam. This setup is considerably less space-consuming and more efficient than a Zeeman slower in terms of the depletion rate of the atom source. At the same time, it offers a sufficiently high flux (up to $10^9\,\mathrm{s}^{-1}$) to efficiently load the MOT at moderate temperatures of only 45 °C.

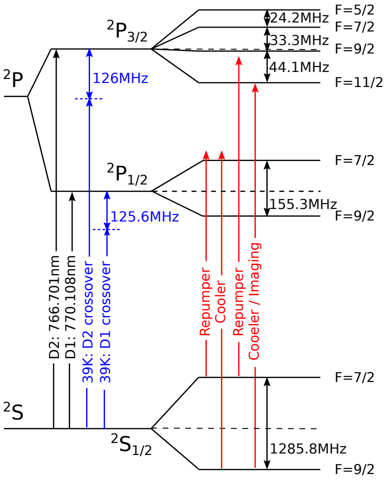

Figure 3.2. – Level scheme of fermionic potassium and of the optical transitions used at Fermix. The energy splittings are not to scale. The D1- and D2-lines between the $4^2S_{1/2}$ ground state and the $4^2P_{1/2}$ and $4^2P_{3/2}$ excited states are both used in the Fermix element. The lasers are locked onto the respective crossover lines of ^{39}K, which are offset by only about 125 MHz with respect to the lines of ^{40}K. For the MOT and the D1-molasses, bichromatic beams consisting of a cooling and repumping frequency are used, in order to prevent an unwanted accumulation of atoms in the $|F = 7/2\rangle$ ground state.

The working principle of a 2D-MOT derives from the principle of a standard three-dimensional magneto-optical trap [19]. In the 3D case, three pairs of counter-propagating laser beams are shot into the MOT chamber from orthogonal directions to intersect in the saddle point of a magnetic quadrupole field, forming the magneto-optical trap. In the center of the trap, the laser beams are red detuned with respect to an optical transition of the atoms. Once an atom leaves the center of the trap, the Zeeman effect originating from the increasing magnetic field shifts a given magnetic sublevel of the excited state into resonance with the laser beams. The six laser beams are circularly polarized and the polarization direction is chosen such that the escaping atoms absorb photons preferentially from the counter-propagating beam, which creates a net restoring force. The beams are bichromatic, consisting of a cooling and a repumping frequency, operating on the transitions of the two ground-state levels of the D2-line in order to prevent parasitic population of the $|m_F = 7/2\rangle$ ground state (compare Fig. 3.2).

The schematic setup of the 2D-MOT is shown in Figure 3.3. Here, only two of the three directions are implemented as described above, cooling and confining the hot potassium gas in the transversal directions. In the third direction, the beams are linearly polarized, creating the configuration of an optical molasses instead of a MOT-configuration. This setup increases the time the atoms spend in the transversal cooling region and thus augments the efficiency of the 2D cooling [118]. In the longitudinal direction, an aperture tube allows the central column of the gas to be coupled out in the direction of the 3D-MOT. An additional resonant push beam accelerates the transversely pre-cooled potassium atoms towards the main chamber.

The atom source itself is located in a CF-16 tube in the vicinity of the 2D-MOT chamber. This reservoir however is not used to provide the background pressure of potassium in the day-to-day operation of

---

[4] Such a setup is used for instance in the group of M. Zwierlein at MIT.

[5] The price at the time of my work at Fermix was about 10,000 € per 100 mg.

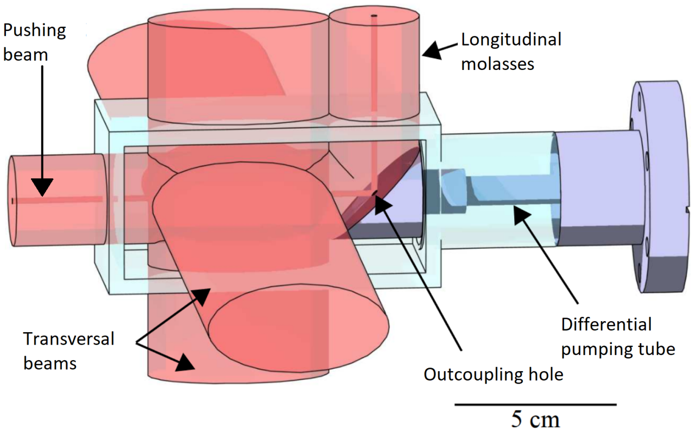

Figure 3.3. – Schematic setup of the 2D MOT. Transversal cooling of the atomic gas is ensured by two pairs of retro-reflected beams. An additional longitudinal molasses increases the efficiency. The flux of atoms escaping through the outcoupling hole in the direction of the 3D-MOT is increased considerably by the small pushing beam. The cold point (not shown here) is located directly behind the 45 ° mirror. Figure adapted from [118]

the machine. Both the metal parts in this section of the experiment as well as the glass cell of the 2D-MOT are heated to higher temperatures ($\sim 100\,^\circ$C and $60\,^\circ$C respectively) in order to avoid deposition of potassium on the outside walls of the vacuum system. Directly behind the outcoupling mirror of the 2D-MOT cell, a plastic tube (not shown in Fig. 3.3) is wrapped around the glass tube connecting the cell to the main system. Using a chiller[6], this small section of the tube is water-cooled to considerably lower temperatures than its surroundings, which serves as an efficient recycling mechanism and effectively prevents the loss of potassium atoms to different areas of the setup. When the system is not in use, the so-called 'cold point' is set to a temperature of $0\,^\circ$C. In order to operate the machine, the temperature is set to $45\,^\circ$C.

During my time at Fermix, the old potassium source was depleted, such that the operation of the 2D-MOT became unreliable. It therefore has been exchanged in cooperation with Thomas Reimann. Unfortunately, the old source was connected behind to a vacuum valve which had developed a small leak, preventing us from opening and closing the valve without degrading the vacuum of the system. This required a redesign of the source reservoir to fit behind the bottom valve of the 2D-MOT region. Since the construction of reservoir and cold point worked well in the past, it was kept in order to have a potassium reservoir in direct proximity to the 2D-MOT cell. Details on the new design and on the migration scheme to move the potassium atoms from the reservoir onto the cold point can be found in the thesis of Thomas Reimann [104].

3.1.2. Grey molasses on the D1 line

At the end of the MOT phase, a typical number of $1.5 \cdot 10^9$ atoms is trapped at temperatures of roughly $300\,\mu$K. Before proceeding to-

[6] ThermoTek T247P-30 210W, Operating range: $-5\,^\circ$C – $45\,^\circ$C.

wards the evaporative cooling stages, the gas has to be loaded from the magneto-optical trap into a far-detuned optical dipole trap or into a magnetic trap in order to avoid photon absorption and reemission processes, since these ultimately limit the final temperature of the gas due to the photon recoil. At the final temperatures reached in the MOT however, the gas is still too dilute to ensure the high collision rates necessary for evaporative cooling. One must therefore either strongly increase the density of the gas or further decrease the temperature. To do this, there are several options available in cold atom experiments. One option is to use a different optical transition with a narrower linewidth, which reduces the Doppler temperatures considerably. Since these transitions lie in the ultraviolet frequency range for Alkali atoms, this unfortunately implies technical difficulties (and increased health risks for the experimenters). Another option is to create very deep optical dipole traps using infrared lasers with powers in the range of some 100 W or using an optical resonator, as it is done in the lithium experiment in Hamburg (compare section 5.1). Finally, one can use sub-Doppler cooling methods to reduce the temperature of the gas further and then transfer the cloud into a more conservative optical or magnetic trap. This is done at the Fermix experiment using a so-called Λ-enhanced gray molasses on the D1-line.

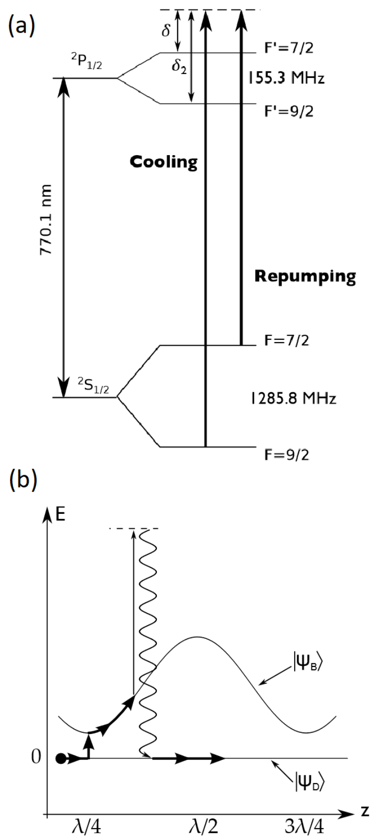

Figure 3.4. – Principle of a gray molasses. (a) Level scheme for the D1-transition of ^{40}K and transitions used for the D1 molasses. (b) Energy diagram of the resulting dark and bright eigenstates. Due to the positive detuning of the Raman beams, the energy of the bright state lies above the energy of the dark state. Atoms lose kinetic energy by moving up a potential hill. They are subsequently pumped into the dark state, whereby energy is lost to the light field. The cycle is repeated as long as the atoms have sufficient kinetic energy. The slowest atoms accumulate in the dark state. Figure adapted from [113].

The gray molasses scheme has been proposed in [119] and has been implemented on the D1 line of potassium for the first time at Fermix [113]. If an optical transition $|F\rangle \to |F' = F\rangle$ or $|F\rangle \to |F' = F - 1\rangle$ is driven, as is the case for the D1-line of Alkali metals, the eigenstates of the Hamiltonian include states that do not couple to the light field. These so-called dark states are superpositions of the ground state sublevels. When an atom occupies such a dark state, it cannot absorb or emit photons and is therefore not affected by acceleration via photon recoil. For atoms in the bright state, a polarization gradient in the laser beams gives rise to a spatially varying Zeeman shift, which translates into a periodic potential landscape for the atoms. If the detunings of the laser beams are chosen correctly, i.e., at blue detuning with respect to the Raman transition, the energy of the bright state lies above the energy of the dark state. Atoms in the dark state can transition to the bright state via motional coupling. The probability for this effect is highest for large kinetic energies and for small energy difference between the two states, i.e. at potential valleys of the bright state.

The cooling principle can be understood as a combination of Sisyphus cooling and velocity-selective population trapping: Atoms in the bright state with high (kinetic) energy move up the potential hills thereby losing kinetic energy, and are pumped back into the dark state. The energy difference between the two states is radiated away and as a result, the energy of the atoms is reduced. If the kinetic energy of the atoms is still high, the coupling to the dark state is large and they return to the bright state after some time. When their velocity becomes lower, the coupling to the bright state decreases and the lifetimes in the dark state becomes large. The cold population is therefore 'trapped' in the dark state and is unaffected by the molasses light.

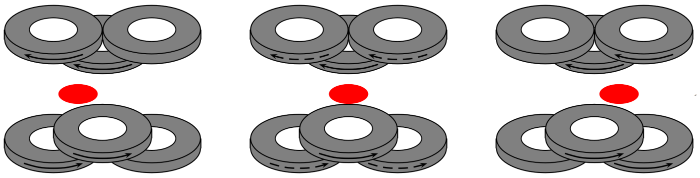

Figure 3.5. – Principle of the magnetic transport. From left to right: The center of the magnetic quadrupole field is displaced by switching the electric currents in overlapping coil pairs. At every moment, three pairs are operated to ensure smooth movement and a constant aspect ratio. The resulting magnetic field is the sum of the individual fields. Figure adapted from [98].

The use of the D1 line over the D2 line is founded in the level structure, which implements the $|F\rangle \rightarrow |F' = F\rangle$ / $|F\rangle \rightarrow |F' = F - 1\rangle$ transitions. In addition, the hyperfine levels of the excited state are further separated than the sublevels of the $^2P_{3/2}$ state and can be individually addressed more easily, which reduces off-resonant excitation of the atoms and improves cooling efficiency. Finally, the additional $\Lambda-$type level structure of the $|F = 9/2\rangle$ and $|F = 7/2\rangle$ ground states, addressed by the cooling and repumping beams, leads to additional cooling effects due to long-lived coherences between hyperfine states [120]. In the end, the D1-gray molasses reduces the temperature of over 10^9 atoms from $\sim 200\,\mu\text{K}$ to $20\,\mu\text{K}$ in about 5 ms.

3.1.3. Magnetic transport and microwave evaporation

After the D1-molasses step, the atomic cloud is cold enough to be loaded into a magnetic quadrupole trap and transferred to the science cell. Depending on the hyperfine state, potassium atoms are either high- or low-field seekers. Since Maxwell's equations forbid isolated maxima of the magnetic field, high-field seeking states can only be trapped magnetically in at most two spatial direction, whereas the potential must be anti-trapping in the third direction. This makes these states unsuitable for transport in a magnetic trap. We therefore transfer the atoms into the low-field seeking state $|m_F = 9/2\rangle$ using a short pulse of circularly polarized light that is shot through the cloud along the magnetic field direction.

After the quadrupole potential is ramped up using the MOT coils, the trap is adiabatically displaced from the MOT chamber to the science cell in about 4 s. Similar to the optical transport in the lithium experiment in Hamburg, such a transport can in principle be done by moving a single coil on a precise translation stage (see for instance [121, 122]). The Fermix setup however employs a setup of 12 overlapping pairs of static coils in anti-Helmholtz configuration whose currents are switched on and off successively using four power supplies and a complex switching circuit of insulated gate bipolar transistors (IGBTs) (a scheme developed in [123]). For a detailed description of the design and optimization process, I would like to refer the reader to the thesis of Thomas Salez [98]. At each moment in time during the transport, three pairs of coils are supplied with currents (compare fig. 3.5). The currents are optimized such as to ensure adiabatic displacement of the trap under avoidance of discontinuities in the derivatives of the trajectory. The aspect ratio of the trap is kept as constant as possible. These requirements are necessary to keep the heating of the atomic cloud during the transport to a minimum.

The main advantage of this transport setup is its physical robustness which incurs low costs in terms of maintenance time. Once optimized, it merely requires an atomic cloud fulfilling good starting conditions in terms of temperature and atom number. A second advantage is that it allows for transport along relatively complicated paths including angles, without requiring to reload the atoms into a different trap that would need to be aligned with the first. The transport path at Fermix features a 90 °-corner in order to move the atoms out of an eventual influence of eventual remaining potassium atoms exiting the 2D MOT and to offer improved optical access to the atoms in the science cell. The setup on the other hand also comes with a set of disadvantages: A minor one is that the magnetic quadrupole field has a zero crossing during the entire transport time. Here, the spin of the atoms cannot adiabatically follow the direction of the magnetic field, causing Majorana losses, i.e. some atoms flip into untrapped states. This however rarely happens since the atoms are not cold enough to spend much time close to the trap center. The main disadvantage for the day to day use at Fermix consists in the high currents used to operate the coil pairs. The dissipation of the heat load induced by these currents requires water cooled coils, which are embedded in a large metallic plate. Switching the strong magnetic fields leads to eddy currents which disturb the atoms during transport as well as at the final position inside the science cell. Another source of heating is the injection from the MOT position into the transport which has to happen fast due to the high background pressure and which is therefore not fully adiabatic. In the end, about 75% of the atoms arrive in the science cell at a temperature of $\sim 350\,\mu\mathrm{K}$, roughly a factor 2 hotter than in the magnetic trap in the MOT chamber.

Before the atoms are finally loaded into an optical dipole trap, the temperature is lowered again using microwave evaporation. In contrast to evaporative cooling in an optical trap, where the trap depth is slowly lowered to allow the energetically highest atoms to leave the trap, microwave (or radio-frequency) evaporation relies on a static magnetic trap depth and active removal of atoms from the trap. This has the advantage that the trap geometry is unaffected by the evaporation process. The atom removal is achieved by flipping the spin of the most energetic particles into an anti-trapped state, such that the magnetic field is repulsive for these atoms. Due to the spatially varying Zeeman-shift, the frequency of the microwave radiation shone into the trapped cloud can be chosen to be resonant to an outer shell of the trap only. Atoms found in this region mostly populate states of high energies. By selectively removing these atoms, the mean energy of the atom distribution is reduced and the sample thermalizes to a lower temperature. The radiation frequency is now slowly ramped towards values resonant at inner, colder shells of the trap, realizing a forced evaporation. At the end of this evaporation, the sample consists of $4 - 8 \times 10^8$ atoms at typical temperatures of 60 µK. Finally, the gas is loaded into ODTs and further evaporation steps take place, taking the cloud towards the degenerate regime.

3.1.4. Detection of spin populations

After the experimental steps, which we will discuss in the next chapter, the atoms are imaged using absorption imaging. The different spin states of the ground state manifold of ^{40}K hereby do not have the same detection probabilities with respect to the imaging light, since the scattering cross-sections are different. To circumvent this issue, a short optical pumping pulse along the magnetic field direction can be used to transfer the atoms into the stretched state $|m_F = 9/2\rangle$ prior to imaging.

For the study of the spin population dynamics in section 4.2, two spin-selective imaging methods have been developed. Firstly, a Stern-Gerlach step can be carried out to separate the different spin components. Here, a strong magnetic gradient is applied for a short time, accelerating the atoms according to their magnetic momenta, which is different for the different spin states. The different spin populations therefore separate spatially and are then pumped into the stretched state and imaged with the same detectivity.

The applicability of the Stern-Gerlach imaging procedure is limited by two constraints. Since the atoms can only separate when the trapping potentials are switched off, the atomic clouds expand during the Stern-Gerlach step, causing the separated clouds to overlap after a given time time of flight. This leads to an upper temperature limit for the use of the Stern-Gerlach procedure. Additionally, the clouds expand sufficiently at long flight times for the cameras to reach their detection limit. To reduce the separation times, stronger magnetic gradients can be used. These on the other hand are limited by factors such as the inductivities of the coils or the power supplies which are used. In addition, strong field changes lead to the rise of relatively long lived eddy currents in the metallic mounting plates of the magnetic transport, which lead to an undesired change of the imaging resonance frequencies. This change is different for the different spin populations, since the corresponding atoms are located at different positions in the chamber during the imaging pulse. Therefore the imaging frequency needs to be calibrated in dependence of the parameters of the Stern-Gerlach step. The actual sequence is a compromise between these effects. It involves currents of up to 60 A, applied during 2 ms. The resulting cloud separations limit the use of the Stern-Gerlach imaging scheme to cloud temperatures below 10 µK.

In order to implement spin-selective imaging at higher temperatures, a second scheme has been developed, relying on removing the spin population of interest from the cloud with the help of a microwave Landau-Zener sweep. The atoms are transferred from the $|F = 9/2\rangle$ manifold to the $|F = 7/2\rangle$ manifold, thereby 'hiding' them from the imaging light which is detuned by 1.285 GHz. The spin ratio is inferred from the reduction of the imaged atom number. Since the linewidth of the hyperfine transition is smaller than the Zeeman level splitting at these small fields, the spin states can be individually addressed with good accuracy. However, care must be taken for several reasons. First, some of the possible transition frequencies lie close together and radiation of a given frequency might affect more than one spin populations simultaneously. Second, the transition probability of the hiding sweep is not necessarily unity and needs to be calibrated in order to infer the correct atom numbers. Third, the different spin states are not imaged with the same detection efficiency, which can again be circumvented by an optical pumping pulse prior to imaging. In order to calibrate the efficiency of the hiding pulse, samples at low temperature have been produced. After the populations of a given different spin states has been transferred to the $|F = 7/2\rangle$ manifold, the remaining atom numbers have been measured using the Stern-Gerlach imaging procedure described above.

For further details on the imaging process, I would like to refer the reader to [104].

3.1.5. Typical performance of the machine

After having discussed the particular steps of the Fermix sequence, I will give a final overview over the performance of the machine. A total experimental sequence at Fermix takes about 60 s. First, the magneto-optical trap is loaded from the atomic beam escaping the 2D-MOT chamber. The loading rate saturates after about 30 s. At this time, a typical number of $1.5 \cdot 10^9$ atoms are trapped in the MOT. To prepare the atoms for the magnetic transport into the science cell and for the ensuing evaporative cooling stages, a few steps are carried out which have the goal to strongly reduce the temperature of the cloud and increase its density. The trap is first compressed during 5 ms by increasing the magnetic field gradients and decreasing the intensities of the cooler and repumper beams. To counteract the resulting heating of the cloud, it is then strongly cooled in a D1-gray molasses, which takes approximately 5 ms and results in a temperature of 20 µK. Finally, the atoms are optically pumped into the magnetically trappable Zeeman states $|F = 9/2\rangle$ and $|F = 7/2\rangle$ and transferred into the magnetic quadrupole trap. In order to transport the atoms the MOT chamber into the science cell, the trap is displaced over a distance of 65 cm in about 4 s, by switching currents in an ensemble of overlapping coils in anti-Helmholtz configuration.

Due to the limited efficiency of the magnetic transport, a typical number of $\sim 10^9$ atoms arrive at the science cell at temperatures of $\approx 360\,\mu\text{K}$[7]. In the following seconds, a succession of evaporative cooling steps is used to bring the gas toward degeneracy. First, a microwave evaporation is used to remove the hottest atoms from the magnetic trap in about 4 s. In an ensuing step, the atoms are loaded into an optical dipole trap, in which further evaporative cooling is carried out. The spin composition of the sample can be adjusted using radio-frequency sweeps. At the end of this step, typically $\sim 10^6$ atoms are left at temperatures of about $\sim 0.7\,\mu\text{K}$, which corresponds to $T/T_\text{F} \approx 2.5$. This is

---

[7] While this may seem like a large loss compared to the temperatures after the gray molasses, a large part of the temperature increase is due to strong compression of the trap during transport.

the starting point of the experiments presented in this thesis.

If so desired, it is possible to reduce the temperature of the sample further. To do so, the atoms are also transferred in the energetically lowest Zeeman states $|m_F = -9/2\rangle$ and $|m_F = -7/2\rangle$ using an adiabatic Landau-Zener radio-frequency sweep. This transfer also allows us to access the Feshbach resonance of potassium at 202 G. In addition, a second, crossed dipole trap is added, increasing the density and the collision rates between the particles. The magnetic field is ramped successively closer to the Feshbach resonance and two slow final evaporation are carried out during $\sim 10\,\mathrm{s}$. The lowest temperatures that were achieved with this sequence were $T/T_\mathrm{F} \approx 0.1$ with 10^4 atoms.

After the preparation of the sample, the experimental steps are carried out and finally, the gas can be imaged using standard absorption imaging using CCD cameras[8] or using a high-magnification path with a highly sensitive low-noise CCD camera[9].

3.2. The setup around the science cell

After having discussed the experimental sequence followed at the Fermix experiment in order to create a cold sample of potassium 40, I will now introduce the setup around the science cell. The science cell at Fermix consists of an uncoated vycor cell[10] in a cuboid shape, with outer dimensions of $23\,\mathrm{mm} \times 23\,\mathrm{mm} \times 10\,\mathrm{mm}$ and a wall thickness of 4 mm. This rectangular shape allows for a relatively large angle of access in the horizontal plane, with a small range of angles being blocked by the coil mounts for the end section of the magnetic transport and for the magnetic coils around the science cell itself. Around the science cell, there are several sets of coils in order to create the magnetic fields needed in the experimental steps and to offset eventual DC fields in the vicinity of the science cell, two RF/MW-Antennae to control the populations of the spin states of the atoms and several optical setups to manipulate and image the atoms. These parts are described in the following paragraphs. In order to avoid confusion, I will denote the vertical direction as the z-axis, the transport axis as the y-axis and the remaining horizontal axis as x.

The magnetic setup

The magnetic setup around the science cell is shown in Figure 3.6. Above and below the glass cell, there are two sets of magnetic coils, slightly offset from the center of the glass cell on the transport axis, with a circular hole giving optical access along the vertical direction. The inner coils produce a strong magnetic bias field of $8.00\,\mathrm{G\,A^{-1}}$ with a curvature of $0.31\,\mathrm{G\,cm^{-2}A^{-1}}$ when operated in Helmholtz configuration, or a magnetic gradient of $2.50\,\mathrm{G\,cm^{-1}A^{-1}}$ when operated in anti-Helmholtz configuration. The curvature of the inner coils' field can be compensated by operating the inner coils in conjunction with the outer coils, whose geometry is closer to an ideal Helmholtz configuration and which

[8] PCO Pixelfly QE 270XD

[9] Andor iKon-M 934

[10] Hellma GmbH

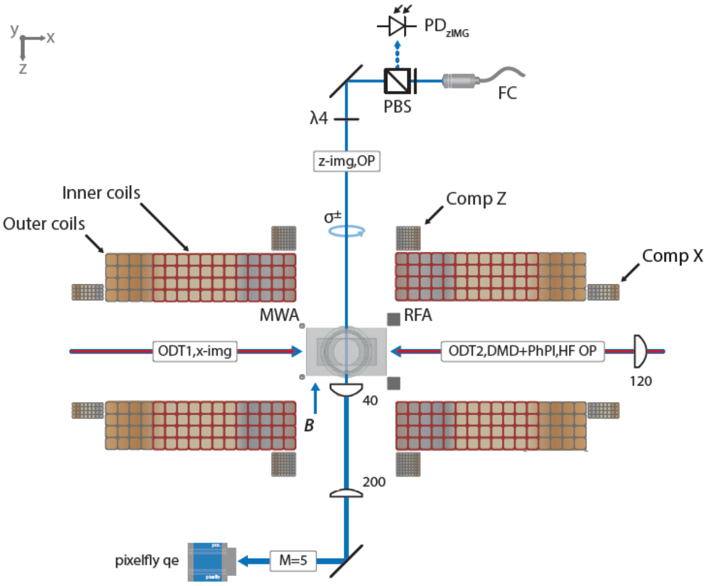

Figure 3.6. – Cut through the setup around the science cell perpendicular to the transport axis. Figure adapted from [104]. Two pairs of large coils (inner/outer) are located above and below the science cell, producing high bias fields with variable curvature or strong magnetic gradients. Additional pairs of compensation coils (Comp X,Z) are located horizontally and vertically around the science cell. Microwave and Radio-frequency antennas (MWA, RFA) are installed on either side of the science cell. A vertical imaging beam can also be used to pump the atoms into the stretched state of the Zeeman manifold. In the horizontal plane, several optical beams are used to address the atoms (compare fig. 3.7). These are the two ODTs, two imaging beams (y-imaging not shown) as well as additional beams (DMD+PhPl, HF OP) which have been installed for a future project. Not shown are the compensation coil on the transport axis and the optics needed for the lattice project.

provide an opposite curvature of $-0.026\,\mathrm{G\,cm^{-2}A^{-1}}$ at a bias field of $0.24\,\mathrm{G\,A^{-1}}$.

During the experiment, the inner coils can be supplied by two different power supplies. After the magnetic transport steps, the coils are operated in anti-Helmholtz configuration, providing the magnetic quadrupole field for the microwave evaporation. This configuration is also used for Stern-Gerlach imaging of the atomic cloud. For these two purposes, the coils are supplied by a power supply[11] which can deliver currents up to 140 A, but whose large output range leads to a coarse resolution that is insufficient to do high-precision experiments at low magnetic fields or to precisely address the relatively narrow Feshbach resonance of potassium at 202 G[12]. After the sample is transferred to optical dipole traps, IGBT switches therefore allow a second, highly-stable power supply[13] to be connected to the inner coils, delivering up to 30 A at a specified stability of $\sim 10^{-5}$.

In order to compensate stray magnetic offset fields at the position of the atoms, a set of small coils is located close around the science cell, which were designed in the course of this thesis. Two circular coils with 65 windings are placed on top and below the cooling plate of the magnetic transport, centered around the circular cutouts of the coils. Two

[11] Delta Electronica SM45-140

[12] The specified stability is 10^{-4} in CC operation, which yields 0.2 G. This corresponds already to 2.5% of the width of the Feshbach resonance.

[13] High Finesse UC 30/15

rectangular coils with 23 windings are located next to the coil holders in order to take care of fields along the x-direction. Finally in the y-direction, a single rectangular coil with 60 windings is used at the end of the coil holders. Here, a single coil had to be used, since the magnetic transport setup occupies most of the space opposite of this coil. For all of these coils, sets of aluminium supports have been designed such that the coils fit closely to the already existing coil supports and no additional optical access is lost. The supports are cut open and have been fixed to the breadboards and to the metallic cooling plate of the transport under avoidance of metallic contact in order to prevent perturbing eddy currents.

RF-Antennae

Around the science cell, there are two antennae used to manipulate the spin state of the atoms, covering two distinct frequency ranges. One antenna consists of a single large loop located on top of the science cell. It is used to address transitions at energies corresponding to the hyperfine splitting of ^{40}K around 1.285 MHz. The second antenna has a smaller radius and multiple windings and is approached to the science cell from the side under a diagonal angle. It is used to radiate radio-frequencies up to a few tens of MHz, in order to address transitions within a given hyperfine manifold. This antenna is for instance used for the Landau-Zener sweep to the negative hyperfine states or for balancing of spin populations. Additional information on the MW/RF system can be found in [104].

The optical setup

The final components to the setup around the Fermix science cell are the optical traps and the imaging optics. A top view of the setup is shown in Fig. 3.7. In order to cool the potassium sample down to degeneracy, two 1064 nm dipole traps are available, entering the science cell from both sides at an angle of 20 ° with respect to the x-axis and intersecting at the magnetic center. Both beams are provided by high-power photonic crystal fibers supplied by a high power Nd:YAG laser[14]. The first beam ('ODT1') has a maximum power of up to 7 W and is focused down to a $1/e^2$-waist of 39 µm, which yields a trap depth of maximum 290 µK. The crossed trap ('ODT2') is significantly weaker than the first ODT, featuring a waist of 110 µm, which yields a maximum trap depth of 16 µK[15].

In order to image the density distribution of the atoms in the science cell, three different imaging directions are available. The different imaging axes have different magnifications and serve different functions in the experiment. Along two axes, the cloud is imaged by the Pixelfly CCD cameras, operated in double-shutter mode, with low magnifications: Along gravity (z-axis) the crossed dipole trap can be imaged with a magnification of $M = 4$. A second (auxiliary) imaging direction runs along the optical path of the ODT1. It has a magnification of $M = 1$

[14] Innolight Mephisto MOPA 16 W

[15] For future projects, a second high power laser (IPG Photonics YLR-300-LP-WC) has been installed next to the science cell, which can replace the ODT2 arm at high powers of up to 150 W at the position of the atoms. In addition, a two-dimensional optical lattice has recently also been constructed which creates a lattice geometry consisting of vertical tubes and is projected to be used for studies of the 1D-3D dimensional crossover with potassium atoms. Both setups have not been used in the course of this thesis. They are described in greater detail in [104, 105].

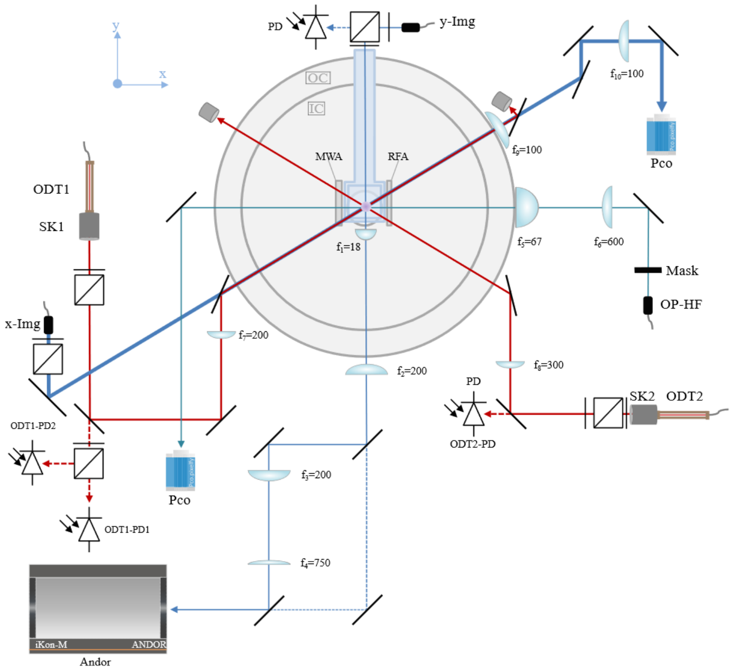

Figure 3.7. – Top view schematic of the optical setup around the science cell at the Fermix experiment. Figure adapted from [105] The science cell sits slightly off-center with respect to the inner and outer coils. Red: Two optical dipole traps intersect at the magnetic center under an angle of 20 °. Blue: Two imaging paths are available in the transport plane. The so-called x-imaging follows the same path as the ODT1, whereas the y-imaging is collinear to the transport axis. The x-imaging has a magnification of $M = 1$. For the y-imaging, two different paths allow for a magnification of $M = 4$ or $M \approx 19$. Finally, an optical pumping beam (OP-HF, Mask) is shown, which is used for a future project [104, 105]. Not shown is the z-imaging beam which passes vertically through the chamber. SK1/SK2: Schäffter-Kirchhoff outcouplers. MWA/RWA: Microwave and radio-frequency antennas.

and can be used to measure the trapping frequencies of the optical dipole traps. The sensitivity of the cameras used here is typically sufficient to image clouds with down to 10^5 atoms, which is typically reached at the end of the optical evaporation steps. A big advantage of this imaging setup is that the x-imaging beam is overlapped with the path of the ODT1 and thus integrates the atomic density along its axial direction, allowing for the detection of very dilute gases trapped in the optical dipole trap. In addition, it leaves room for additional optics perpendicular to the transport axis. On the other hand, one has to note that the second ODT is imaged under an angle when this imaging direction is used.

Finally there is another imaging beam along the transport axis. In order to detect the atoms at the small signal-to-noise ratios, a highly sensitive CMOS camera (Andor Ikon M) is used at a high magnification of $M = 19$. The imaging resolution reached in this path is $\sim 1.6\,\mu\text{m}$, which is smaller than the lattice constant of $\sim 2.5\,\mu\text{m}$. Mirrors mounted on magnetic stages allow however to use a different optical path with a smaller magnification of $M = 5$ for less critical applications. Both imaging paths along the y- and z-axis have been redesigned in the course of this thesis.

3.3. Further upgrades to the experimental setup

3.3.1. Experiment control

The experiment is controlled via TTL, analog (0-10V) as well as GPIB signals generated by a rack of National Instruments PXI-cards[16]. These signals are fed through optocouplers in order to isolate the sensitive PXI racks from ground loops or high voltages flowing back from the circuitry around the experimental table. The sequences are programmed and sent to the PXI-cards by a computer running Cicero Word Generator in combination with Atticus Server, a software kit developed at MIT[17]. The timing of the sequence is provided by an external FPGA clock, which allows each time step to run at a different time resolution, reducing the size of the buffers significantly, particularly in the long evaporative cooling steps or during lifetime measurements.

In the course of this thesis, the experiment control software was updated in order to provide the possibility to synchronize the experimental sequence with the 50 Hz-frequency of the main power network. The version of Cicero/Atticus which was in use before did not offer this functionality, and had additionally been modified in-house to allow for an integration of the Pixelfly cameras with the experiment control software. Unfortunately, these modifications were not compatible with newer version of Cicero/Atticus, which required the development of new imaging software based on python. In contrast to the prior implementation, this new program is independent of the experiment control software, performing the sole task of receiving and storing the images taken in the course of the experimental sequence. This limited scope has the advantage that the program is easier to maintain and update for use with different camera models (for instance the Andor Ikon) or future versions of Cicero/Atticus. A disadvantage on the other hand is that it there is no direct way to recover the sequence parameters from the images or to automatically group the images of a given sequence together. While this correspondence between sequences and images had always been done manually in the group (by recording the image IDs for each sequence in the lab book), these capabilities would be very useful additions for future versions of the imaging software.

3.3.2. Laser frequency generation

During the course of this thesis, the optical system for the D2-line has been expanded and upgraded in several points. Its full scheme is shown in figure 3.8[18].

A master laser is locked onto the crossover line of ^{39}K with a fixed offset created with the help of an AOM, using modulation transfer spectroscopy [124]. The use of ^{39}K for this purpose originates in the low natural abundance of ^{40}K at only 0.012%, which renders direct locking

[16] NI PXI-6533, NI PXI-6535, NI PXI-6713, NI PXI-GPIB

[17] More information available at `http://akeshet.github.io/Cicero-Word-Generator`

[18] The D1 setup is built after a similar scheme. Details to this setup can be found in [100, 102, 104].

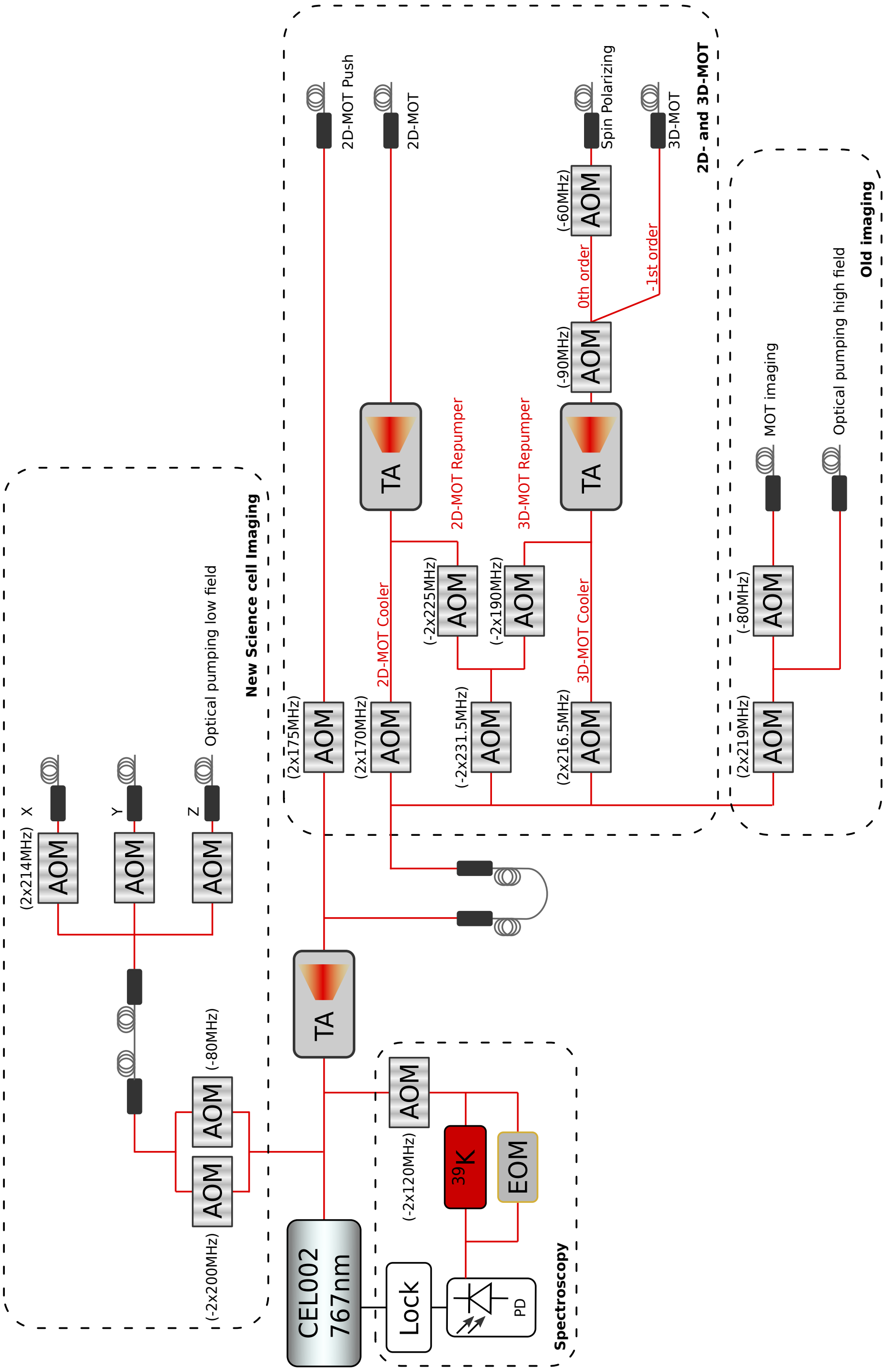

Figure 3.8. – The full laser setup for the generation of the frequencies on the potassium 2D-line. There are four functional parts: A spectroscopy section is used to stabilize the laser frequency using the D2-crossover line of ^{39}K. For the operation of the 2D- and 3D-MOT, the beam is split into multiple paths after amplification of the laser power in a TA and the frequencies are shifted in a series of AOMs. The principal and repumper paths of the 2D and 3D-MOTs are combined and seed a second stage of TAs before being transported to the optical table in polarization-maintaining single-mode optical fibers. In addition, there are two separate imaging systems for the science cell and the MOT chamber.

on this isotope experimentally unpractical. The crossover frequencies of ^{39}K fortunately lies close enough to the D2 frequencies of ^{40}K to enable locking on the other isotope. The light originating from the laser is then fed into a homebuilt tapered amplifier system [97]. After mode cleaning with the help of a single-mode optical fiber, the light is split into the different paths and the frequencies are generated with the help of successive AOMs. The cooler and repumper beams of the 2D and 3D MOTs are superimposed, yielding two bichromatic pairs and amplified again in a second TA stage before finally being transported onto the main table with polarization-maintaining single-mode fibers. AOMs in front of the fibers allow to switch the different beams on and off on µs-timescales. Slower mechanical shutters further reduce stray light when the light is not needed for a longer period of time.

On this setup, I carried out the addition of a small optical system that enables optical pumping and fast subsequent imaging of the atoms from different directions. As mentioned before, it is important to avoid open transitions during the imaging process, which could cause the atoms to fall into states that are not addressed by the imaging light, in order to measure the populations of the different hyperfine states of potassium accurately (or at least in order to calibrate the detection probability for the different states). Hence, prior to the imaging pulse, the atoms are transferred into the stretched state $|m_F = 9/2\rangle$, which features a closed transition tot he $|F' = 11/2\rangle$ state. This transfer is done with circularly polarized resonant light along the direction of the magnetic field. In the past, the imaging axes of the setup could unfortunately not be independently addressed. Shutters and waveplates had to be adjusted manually in order to feed light into the different paths, which prevented us from imaging along a horizontal direction directly after optical pumping. In order to allow for optical pumping both at low magnetic fields and at fields close to the Feshbach resonance at 202 G and fast subsequent imaging from different axis, a new imaging setup was built, featuring fast electronic control over the intensities in all three imaging axes with the help of dedicated AOMs. The old imaging setup has been kept in a modified way for imaging inside the MOT chamber.

4. Characterization of a D-Wave Feshbach Resonance

In this chapter, I report on the characterization of a d-wave Feshbach resonance in a cold gas of ^{40}K *and on measurements of the dynamics of the hyperfine spin-state populations in its vicinity. The results of this project are published in the thesis of Thomas Reimann*

> Thomas Reimann. *Resonant spin dynamics and 3D-1D dimensional crossovers in ultracold Fermi gases.* PhD thesis, École Normale Supérieure Paris, Université PSL - PSL Research University, 2018.

This project was carried out in the beginning of my time as a PhD student, and the results were obtained mainly through the efforts of the senior PhD students Thomas Reimann and Cédric Enesa.

As we have already discussed in earlier parts of this manuscript, Feshbach resonances are a very important tool in the field of cold atoms, providing the possibility of adjusting the interactions between the particles. Large interaction strengths are important on one hand to increase the efficiency of evaporative cooling, enabling the gas to reach quantum degeneracy. On the other hand, Feshbach resonances give the experimenter a tool to create bound molecules from free atomic particles. In the case of a Fermi gas, they even allow to change the character of the sample from a gas of weakly bound Cooper pairs to a gas of tightly bound dimers in the so-called BEC-BCS crossover.

In our previous discussion, we have introduced s-wave Feshbach resonances which enhance scattering between particles in the s-wave channel with zero angular momentum. Feshbach resonances can however enhance scattering in higher angular momentum channels as well. This effect is particularly intriguing since high-T_c superconductivity seems to rely on unconventional pairing between electrons, most notably pairing in the d-wave channel [6–9]. Studying Feshbach resonances involving higher angular momenta might uncover some details of this mechanism, or could provide an access to simulate such interactions in a targeted manner. The Feshbach resonance which we will discuss in this chapter involves such states with d-wave symmetry.

Although extensive research on Feshbach resonances in potassium 40 had been carried out [125–128], the resonance that will be discussed in this chapter was previously unreported. It has been found by M. Rabinovic during the characterization of the evaporation efficiency of a mixture of the positive hyperfine states of potassium for different magnetic fields [103]. Hereby, an imbalanced mixture of atoms in the states

$|F=9/2, m_F=9/2\rangle$ and $|F=9/2, m_F=7/2\rangle$ was evaporated in an optical dipole trap during a fixed time at varying magnetic field. The final atom number in the trap showed two clear dips around 8 G and around 160 G (see [103] p. 106). A second more precise measurement of the field-dependence of the remaining atom number at low magnetic field confirmed the enhanced losses and showed three distinct peaks between 8 G and 12 G [104] (compare fig. 4.1).

We can qualitatively understand the origin of these enhanced losses by considering the energy balance during a collision event. There are three main cases to distinguish at this point. Firstly, the collisions between the particles can be elastic, which is the case if there are only two scattering partners and the incoming and outgoing particles remain in the same spin states. In this case, no energy is transferred from the particle motion into other degrees of freedom, and the enhanced collision rate leads mostly to a fast thermalization rate and to efficient evaporation of particles from the trap. Secondly, there is the possibility of inelastic two-particle collisions. Inelastic losses can occur if one of the scattering partners changes its internal state, for instance its spin. In the case of this thesis, the potassium atoms start out in a mixture of the positive hyperfine states $|m_F=9/2\rangle$ and $|m_F=7/2\rangle$ of the $F=9/2$ manifold and can flip towards states with lower m_F. In the presence of a magnetic field, this spin flip frees energy of the order of the Zeeman splitting, which needs to be accounted for by the motion of the two scattering partners in the outgoing channel. In this case, the kinetic energy of the outgoing scattering partners is higher than the energy of the incoming partners, leading to a loss of particles from the trap or for small energies to an effective heating of the cloud. Angular momentum conservation requires in addition that the difference in spin must be compensated by the angular momentum of the outgoing partial wave.

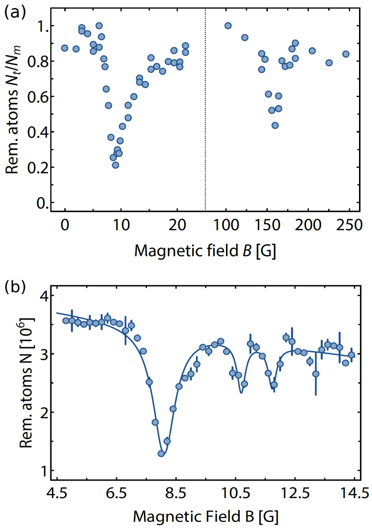

Figure 4.1. – (a) First observation of the Feshbach resonances at 8 G and 160 G via enhanced losses during evaporation. (b) A more precise scan of the lower resonance reveals three separate peaks. The continuous line is a Lorentzian fit to the data, serving as a guide to the eye. Figure adapted from [104].

Finally there is the possibility that more than two scattering partners are involved during an interaction. This happens mostly in the case of dense samples and large interaction strengths. In this case, the formation of deeply bound molecular states is possible, since the additional particles can carry away the energy difference. These n-body collisions lead to high losses due to the large energies being freed in the scattering process.

In this thesis, we will focus on the lowest of the three resonances shown in fig. 4.1. For any new resonance, it is of interest to fully characterize it in order to be able to use it for manipulating the properties of atomic ensembles or even to avoid its unwanted influence in other applications. Formula 2.24 which we have introduced before, describes only the behavior of the s-wave scattering length. If higher angular momenta are involved, the full characterization of a Feshbach resonance requires obtaining knowledge about its position B_0 and about the shape of its resonance peak. The involved spin states in the incoming, bound and outgoing channels have to be known as well as the partial wave in which the collision occurs. Two measurements have been carried out to characterize the resonance and to obtain additional information on the dynamics at magnetic fields around the peak of the atom losses. The first of these measurements extracts the two-body loss rate from the particle losses occurring in a shallow optical dipole trap for relatively long hold times. The second measurement looks at the spin composition and the heating of the gas in a deep optical dipole trap at short hold times.

4.1. Measurement of the two-body loss rate

The telling sign of the Feshbach resonance in our experiment are enhanced atom losses leading to lower particle lifetimes. These losses are due to the change of the internal state of the scattering partners during the collisions. This state change can be associated with the liberation of energy of the scale of the Zeeman or hyperfine splittings. Enhanced losses could also occur due to the liberation of the binding energy of a bound molecular state in the case of three-body collisions.

In order to characterize the Feshbach resonance, we have thus performed a series of measurements of the particle loss rate at various magnetic fields around the resonance. For this, an imbalanced sample of different spin states of potassium has been prepared in the crossed dipole trap at a small magnetic background field away from the Feshbach resonance. The spin composition of typically $\sim 60\%$ $|m_F = 9/2\rangle$, 28% $|m_F = 7/2\rangle$ and 12% $|m_F = 5/2\rangle$ corresponds to the natural spin population after the evaporative steps. The temperature of the sample is set to four different values by adjusting the end point of the final optical evaporation step and recompressing the trap to a constant value of $U_0/k_{\mathrm{B}}T \approx 8.4$, leading to initial cloud temperatures between $2\,\mu\mathrm{K}$ and $30\,\mu\mathrm{K}$. Here, U_0 is the height of the optical dipole trap.

U_0 : Trapping potential height

The magnetic field is then jumped to the target value and the atoms are held in the trap for variable times. The particle numbers are then measured using absorption imaging and the temperatures of the cloud after a given hold time are extracted from the expansion velocity of the cloud during time of flight. These measurements had been taken before the spin-selective imaging sequences were set up. We therefore only have access to the total atom number after a given hold time as well as to the typical initial spin composition after evaporation, which was calibrated during later measurements. The particle numbers are subject to a quite high systematic uncertainty which we will assume here to amount to ±50%.

In order to continue to the extraction of the two-body loss coefficient $L^{(2)}$ from this data, let us first set up the theoretical framework to describe the dynamics in this situation.

$L^{(2)}$: Two-body loss rate

4.1.1. Derivation of the rate equation for particle losses

We start out with the description of i-body losses in a single component gas. According to [61], these losses can be described by terms of the form

$$\dot{N}^{(i)}(t) = -\int d^3r\, L^{(i)} n^i(\mathbf{r}, t), \tag{4.1}$$

$L^{(i)}$: i-body loss rate
N : Particle number
n : Density

where $L^{(i)}$ is the i-body loss coefficient, $N(t)$ the total particle number and $n(\mathbf{r},t)$ the atomic density. For one-body losses, i.e., collisions with background particles, there is a simple expression for the loss coefficient $L^{(1)} = 1/\tau$, leading to the usual exponential decay of the atom number over time: $\dot{N}(t) = -N(t)/\tau$. We can now write down similar expressions for a multi-component gas, consisting for instance of atoms in the three different spin states $|m_F = 9/2\rangle$, $|m_F = 7/2\rangle$ and $|m_F = 5/2\rangle$. The atom losses in the spin state $|m_F = 9/2\rangle$ can for instance be written as:

$$\begin{aligned}\dot{N}_9(t) = &- L_9^{(1)} N_9(t) \\ &- \int d^3r\, [L_{99}^{(2)} n_9(\mathbf{r},t)^2 + L_{97}^{(2)} n_9(\mathbf{r},t) n_7(\mathbf{r},t) \\ &\qquad\qquad + L_{95}^{(2)} n_9(\mathbf{r},t) n_5(\mathbf{r},t)] \\ &- \int d^3r\, [L_{999}^{(3)} n_9(\mathbf{r},t)^3 + \ldots] - \ldots \end{aligned} \tag{4.2}$$

Here, the subscripts 9,7 and 5 denote the three spin states $|m_F = 9/2\rangle$, $|m_F = 7/2\rangle$ and $|m_F = 5/2\rangle$. L_{ij} are the coefficients associated with collisions between two atoms in $m_F = i/2$ and $m_F = j/2$, and similarly for L_{ijk} in the case of three-body collisions. The first line thus describes one-body losses, the second line the two-body terms, and the third line contains three-body terms and higher processes. We have also assumed that the trap is shallow enough that all involved particles are lost after a collision event. Similar expressions hold for the populations of $|m_F = 7/2\rangle$ and $|m_F = 5/2\rangle$. These expressions are coupled rate equations for the different spin channels. In the next paragraphs, we try to simplify and decouple these equations as much as possible.

To do so, we first note that the one-body losses have the same loss constant for all species, since the background collisions do not depend on the spin state. We therefore set $L_9^{(1)} = L_7^{(1)} = L_5^{(1)} = L^{(1)}$.

Second, we can use theoretical input by E. Tiesinga[1], who kindly provided us with numerical simulations of the expected two-body loss rate in different entrance channels at various magnetic fields around the resonance. From his input, we know that the resonance enhances the scattering between the spin states $|m_F = 9/2\rangle$ and $|m_F = 7/2\rangle$ only, and that it is d-wave in nature, i.e. the molecular state has an angular momentum of $l_b = 2$. The interaction between the incoming particles is to first order due to the magnetic dipole interaction (cf. eq. 2.26) between the two spins, which was given as [62]

$$\hat{V}^{dd} \propto -\frac{1}{r^3}[3(\hat{\mathbf{r}}\cdot\hat{\sigma}_1)(\hat{\mathbf{r}}\cdot\hat{\sigma}_2) - \hat{\sigma}_1\cdot\hat{\sigma}_2], \tag{4.3}$$

This interaction couples states with different angular momenta l and l'. The selection rules for these transitions are $\Delta l = 0, 2$ and $l = 0 \to l' = 0$ forbidden. In addition, the projection of the total angular momentum m_t is conserved. We can therefore use the fact that at sufficiently low temperatures, the Pauli principle suppresses collisions between atoms of the same spin state, since the spatial wave function is even. We obtain $L_{99}^{(2)} = L_{77}^{(2)} = L_{55}^{(2)} = 0$.

[1] Communication with T. Reimann, compare [104]

Third, the atoms in $|m_F = 5/2\rangle$ do not undergo enhanced inelastic losses and the corresponding two-body terms can be neglected, leaving only $L_{97}^{(2)}$ and $L_{79}^{(2)}$. These two numbers must be the same since they describe identical scattering events. We abbreviate them as $L_{97}^{(2)} = L_{79}^{(2)} = L^{(2)}$.

Finally, we neglect three-body losses, since we are working in the dilute limit, where two-body losses should occur at significantly higher rates than three-body losses, provided, there is no additional enhancement of such processes. As an a-posteriori justification, it turns out that the evolution of the particle numbers and temperatures in the shallow trap can already be well described by two-body losses. In total, the particle losses in the three spin states can then be written in the form

$$\begin{aligned}
\dot{N}_9(t) &= -L^{(1)} N_9(t) - L^{(2)} \int d^3r\, n_9(\mathbf{r},t) n_7(\mathbf{r},t) \\
\dot{N}_7(t) &= -L^{(1)} N_7(t) - L^{(2)} \int d^3r\, n_9(\mathbf{r},t) n_7(\mathbf{r},t) \\
\dot{N}_5(t) &= -L^{(1)} N_5(t).
\end{aligned} \tag{4.4}$$

Already at this point, we have gained a bit of overview. Since the losses of atoms in $|m_\mathrm{F} = 5/2\rangle$ are entirely due to single body losses and since collisions between atoms in the other spin states lead to direct losses, the evolution of the population in $|m_F = 5/2\rangle$ will simply decay exponentially:

$$N_5(t) = N_5(0) \exp(-L^{(1)} t). \tag{4.5}$$

For the next step, we remind ourselves that the atoms are held in an optical dipole trap, which provides a harmonic confinement along all directions $U(x_i) = m\omega_i^2 x_i^2/2$. Introducing the effective trap volume

$$V_e = \int d^3r\, e^{-U(\mathbf{r})/k_\mathrm{B}T} = \sqrt{\frac{2\pi k_\mathrm{B} T}{m\overline{\omega}^2}}^{\,3}, \tag{4.6}$$

$U(\mathbf{r})$: Trapping potential
ω_i : Trapping frequencies
m : Particle mass
n_0 : Central density
V_e : Effective trap volume
$\overline{\omega}$: Effective trap frequency

where $\overline{\omega} = (\omega_x \omega_y \omega_z)^{1/3}$ is the geometric mean of the trapping frequencies along the different directions, the density distribution of a trapped gas can then be written as $n(\mathbf{r}) = n_0 \exp(-U(\mathbf{r})/k_\mathrm{B}T)$, where $n_0 = N/V_e$. We thus find the expression

$$\int d^3r\, n_9(\mathbf{r},t) n_7(\mathbf{r},t) = \frac{N_9 N_7}{2\sqrt{2} V_e},$$

which yields

$$\begin{aligned}
\dot{N}_9(t) &= -L^{(1)} N_9(t) - L^{(2)} \frac{N_9(t) N_7(t)}{2\sqrt{2} V_e(t)} \\
\dot{N}_7(t) &= -L^{(1)} N_7(t) - L^{(2)} \frac{N_9(t) N_7(t)}{2\sqrt{2} V_e(t)}
\end{aligned}$$

for the 9/2 and 7/2 states.

N_m : Majority atom number $N_9 + N_7$

ΔN : Imbalance $N_9 - N_7$

To reduce notational ballast, we will leave out the explicit time dependence of the atom numbers from now on. We would now like to remove the product $N_9 N_7$ from these equations. To do so, we change the variables to the majority atom number $N_m = N_9 + N_7$ and the imbalance $\Delta N = N_9 - N_7$ between the populations of $|m_F = 9/2\rangle$ and $|m_F = 7/2\rangle$. The population imbalance is not affected by two-body losses, since both atoms are lost equally. Hence, the contributions of the two-body losses cancel and we find $\dot{\Delta N} = \dot{N}_9 - \dot{N}_7 = -L^{(1)}(N_9 - N_7) = -L^{(1)}\Delta N$, from which we obtain another exponential decay governed again by the single-body loss rate.

$$\Delta N(t) = \Delta N(0)\exp(-L^{(1)}t). \tag{4.7}$$

N_t : Total atom number

To obtain the rate equation for the majority population, we start from the rate equation for the total atom number $N_t = N_9 + N_7 + N_5$. It reads

$$\dot{N}_t = \dot{N}_9 + \dot{N}_7 + \dot{N}_5 = -L^{(1)}N_t - L^{(2)}\frac{N_9 N_7}{\sqrt{2}V_e}.$$

In this equation, we now replace $N_9 = \frac{1}{2}(N_t - N_5 + \Delta N)$ and $N_7 = \frac{1}{2}(N_t - N_5 - \Delta N)$ to obtain

$$\dot{N}_t = -L^{(1)}N_t - \frac{L^{(2)}}{4\sqrt{2}V_e}((N_t - N_5)^2 - \Delta N^2).$$

We subtract $\dot{N}_5 = -L^{(1)}N_5$ from both sides and obtain the rate equation for the losses in the majority populations:

$$\dot{N}_m(t) = -L^{(1)}N_m(t) - \frac{L^{(2)}}{4\sqrt{2}V_e(t)}(N_m(t)^2 - \Delta N(t)^2). \tag{4.8}$$

4.1.2. Extracting the two-body loss rate

τ : single particle lifetime

To extract the two-body loss rate $L^{(2)}$ from our data, we first reduce the number of unknown quantities in equation 4.8. The one-body loss rate $L^{(1)}$ can for instance be measured via lifetime measurements off-resonance and has been determined to $L^{(1)} = 1/\tau = 1/(47\,\mathrm{s})$ at a background field of 18 G. The population of $|m_F = 5/2\rangle$ decays exponentially with the a decay rate set by $L^{(1)}$. We therefore extract $N_m(t) = N_t(t) - N_5(t)$ from the imaged total atom number under the assumption that the initial fractional population in $|m_F = 5/2\rangle$ is 12% of the total population, which corresponds to the natural population after the final evaporation. Thus, we have $N_5(t) = 0.12\,N_t(0)\exp(-t/47\,s)$. In addition, we use the fact that the imbalance ΔN between the majority spin components also decays exponentially and write $\Delta N(t)^2 = \delta N^2 N_t(0)^2 \exp(-2t/\tau)$, with $\delta N = \Delta N(0)/N_t(0)$.

δN : fractional initial imbalance $\Delta N(0)/N_t(0)$

Finally, the effective trapping volume V_e also follows from the experimental parameters but contains a dependence on temperature (compare eq. 4.6). Since the temperature of the gas increases in the course of the collision events, however, the trapping volume cannot be assumed to be constant. The reason for this effect is anti-evaporation heating. Since two-body losses are dependent on the density, these processes happen most likely where the density of the sample is largest, i.e. in the trap center. Here, the typical energy of the particles is lower than the typical energy of the particles in the wings of the cloud. After a loss of two atoms from this trap region, the remaining atoms have on average more energy than before, which leads to a temperature increase after thermalization. To deal with this temperature change, two options have been found.

Following [129], the temperature and particle variation in thermal equilibrium owing to i-body losses are related by

$$\frac{\dot{T}}{T} = -\frac{i-1}{2i} L^{(i)} \frac{\dot{N}}{N}.$$

Assuming that the one-body processes occur on a much slower time scale than the two-body losses, one obtains

$$\frac{\dot{N}_m}{N_m} \approx -4\frac{\dot{T}}{T}. \tag{4.9}$$

Equations 4.8 and 4.9 can be parametrically fitted to the atom number and temperature data, with the initial imbalance δN and the two-body loss rate as parameters, an approach taken in [104]. Unfortunately the fit to the data remains quite sensitive to the initial conditions and constraints. In this thesis, we therefore use a slightly different approach to cross-check the results of [104].

For this, we do not use the temperature equation 4.9, but instead use a simple linear interpolation of the temperature data to directly insert the temperature into the effective volume V_e in eq. 4.8. We end up with the following fitting expression:

$$\dot{N}_m = -\frac{N_m}{47\,\mathrm{s}} - \frac{a}{T^{3/2}}\left[N_m^2 - \delta N^2 N_t(0)^2 \exp\left(-\frac{t}{\tau}\right)\right], \tag{4.10}$$

with δN and a as fitting parameters. The two-body loss rate then results from a as

$$L^{(2)} = 4\sqrt{2}a\left(\frac{2\pi k_\mathrm{B}}{m\bar{\omega}^2}\right)^{\frac{3}{2}}.$$

Even though we are left with only two fitting parameters, the robustness of the fit is still suboptimal. Especially on resonance, the initial imbalance has a relatively large influence on the fit result. To mitigate this, we have first performed the fit with a free initial imbalance and then used the median of the resulting values for a second fitting step.

Figure 4.2 shows the results of this measurement. We measure a peak of the two-body loss rate at a magnetic field of $B_0 = 7.3\,\mathrm{G}$. The peak value of the loss rate is measured to be $L^{(2)}_\mathrm{max} = 1.95(11) \cdot 10^{-12}\,\mathrm{cm}^3\,\mathrm{s}^{-1}$ and is reached for the coldest dataset at $T(0) = 2.8\,\mathrm{\mu K}$. This value is about a factor 1.7 lower than the value of $3.25(10) \cdot 10^{-12}\,\mathrm{cm}^3\,\mathrm{s}^{-1}$ given in [104], which is probably due to the different fitting algorithm and a factor

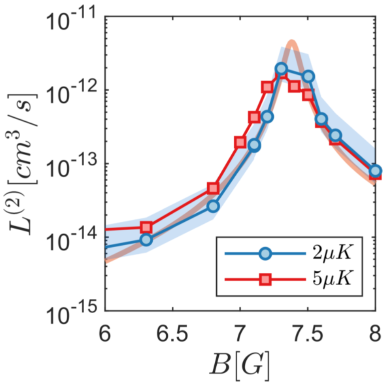

Figure 4.3. – Resonance peak of the 2-body loss rate for the two coldest datasets. The orange line is the theoretical prediction shifted to the left by 0.42 G. This offset has been obtained by minimizing the quadratic deviation between the data at $T = 2\,\mu\text{K}$ and the theoretical values. The overall shape of the resonance peak and the loss coefficients corresponds very well. The shaded area corresponds to the systematic uncertainty of ±50% in the particle numbers.

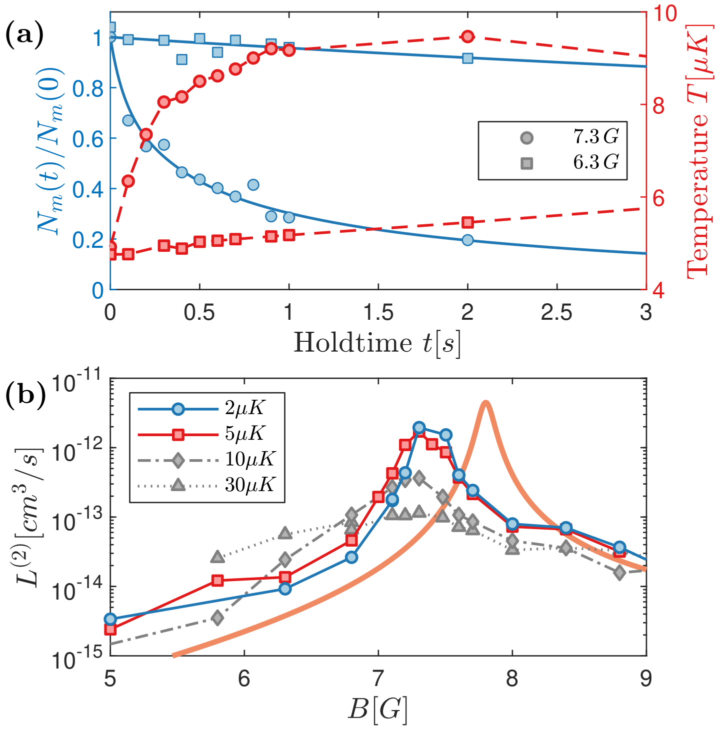

Figure 4.2. – Measurement of the two-body loss rate. (a) Measurement of the majority atom number $N_m(t)$ and the temperature over time for two different magnetic fields. Off resonance (6.3 G, square symbols), the atom number decays on a timescale of tens of seconds and the temperature increases correspondingly slowly. On resonance (6.3 G, circles), the dynamics are much faster, on the time scale of a second. The lines correspond to the fit according to equation 4.10 and to the linear interpolation of the temperature data. (b) Extracted two-body loss rates for different initial temperatures between 2 µK and 30 µK. The orange line is a theoretical prediction from E. Tiesinga for a collision energy of $E = k_\mathrm{B} \cdot 60\,\mathrm{nK}$. The peak height decreases at larger initial temperatures, which originates in recapture at stronger recompression of the ODT. The shifted resonance position is within the uncertainty of the theoretical prediction (compare [104]).

2.3 lower than the theoretical prediction of $4.48 \cdot 10^{-12}\,\mathrm{cm^3\,s^{-1}}$. This discrepancy could be due to the spacing of the data points around the resonance and due to the different fitting algorithm. It should be noted that the given error is only the statistical error given by solving the fitting model. The assumed systematic errors of ±50% in the particle numbers allow for values of $1.30 \cdot 10^{-12}\,\mathrm{cm^3\,s^{-1}} \leq L^{(2)}_{\mathrm{max}} \leq 3.89 \cdot 10^{-12}\,\mathrm{cm^3\,s^{-1}}$, which is a range compatible with the previous analysis. The data also displays a shift of with respect to the theoretical prediction towards lower magnetic fields. This shift is also present in the previous data evaluation and is within the uncertainty of the theoretical prediction [104]. The overall shape of the two coldest resonance curves corresponds very well to the theoretical prediction (compare Fig. 4.3). For higher temperatures, the height of the loss peak decreases, which we can explain by increasing recapture of atoms as we will see in the following subsection, and its width seems to increase.

Two vs three-body losses

Let us now return to the question whether we observe two- or three-body losses. A first argument for two-body losses is given by the fact that the extracted two-body loss rate coefficients at low temperatures reproduce the theoretical prediction quite well. The temperature dependence of the loss rate provides a second argument for two-body losses. For the datasets at higher temperatures, the constant recompression factor of $U_0/k_\mathrm{B}T \sim 8$ leads to an increase of the trap depth to up to 222 µK for the hottest samples. The energy which is released during the collision events however is constant. In the case of two-body collisions, the energy comes from a change in the spin state of the scattering particles. Here, energy of the order of the Zeeman splitting E_Z can be released or, if one particle occupies the $F = 7/2$ manifold, energy of the order of the hyperfine splitting E_hf can be freed. Hyperfine changing collisions can be excluded, since the atomic population is already in the lowest hyperfine manifold. The Zeeman splitting amounts to $E_\mathrm{Z}/2k_\mathrm{B} \sim 55\,\mu\mathrm{K}$ per atom at 7.3 G, the position of the loss curve peak. Due to the small energy release, we expect increased recapture rates when the trap depth becomes comparable to the released Zeeman energy at higher initial temperatures.

E_Z : Zeeman splitting
E_hf : Hyperfine splitting

In the case of eventual three-body losses, the released energy is typically given by the binding energy of a deeply bound dimer, which is usually much higher than the maximum trap depth and thus does not lead to increased recapture. While there are several weakly bound states available which would release significantly less energy, the effective influences of these states on the measured two-body loss rate are of the order of low $10^{-14}\,\mathrm{cm}^3\mathrm{s}^{-1}$, which lies about two orders of magnitude lower than the observed peaks (see [104] for details).

Entrance and bound channels

Theoretical insight into the loss spectrum around the resonance at 7.3 G has been kindly provided by Eite Tiesinga. Apart from the loss rate prediction shown in Fig. 4.2, his calculations also yield information on the entrance channel and the bound state taking part in the enhanced collision processes.

According to E. Tiesinga, the bound state has an angular momentum of $l_b = 2$ and a spin of $s_b = 6$, which yields possible total angular momenta of $m_b = s_b + l_b = 6, 7, 8$. Due to the selection rules, $\Delta l = 0, 2$ and $l = 0 \to l' = 0$ forbidden for dipole-dipole interactions, the incoming particles can thus have an angular momentum of either $l_i = 0$ or $l_i = 2$. In addition, the projection of the total angular momentum m_t is conserved. Since the atoms entering the collision process have a spin projection of $s_i = 9/2 + 7/2 = 8$ and the total angular momentum projection is conserved, bound states with angular momentum projection $m_b = 6$ or $m_b = 7$ can only be populated if the angular momentum of the incident particles is $l_i = 2$, i.e., if the entrance channel is d-wave. For an s-wave entrance channel, only $l_b = 8$ can be populated. The

l_b : Angular momentum and
s_B : Spin of the bound state
m_b : total angular momentum projection, bound state
l_i : Initial angular momentum
s_i : Spin projection, initial state.

corresponding inelastic collision rates for the d-wave entrance channel would exhibit three peaks, one for each possible collision channel, which we do not observe[2]. Theoretical calculations by E. Tiesinga yield loss rate peaks of $\approx 3 \times 10^{-18}\,\mathrm{cm}^3\,\mathrm{s}^{-1}$[104], which is several orders of magnitude smaller than our observed loss rates. We thus conclude that the particle losses are mainly due to particles colliding in an s-wave entrance channel.

A consequence of this fact is that there is no centrifugal barrier to overcome for particles to collide. A centrifugal barrier would introduce a temperature dependence for the loss rate. It is expected for instance that the width and height of the loss curve would increase with temperature for a d-wave entrance channel [132], which is clearly not visible in our data. We can therefore confirm that the particles indeed enter the collision with an angular momentum of $l_i = 0$.

4.2. Spin dynamics close to a d-wave Feshbach resonance

In this final section, we investigate the outgoing channel of the collision. According to the selection rules of the interaction between the particles, the projection of the total angular momentum has to be conserved. The outgoing channel must therefore have an angular momentum projection of $m_{\mathrm{out}} = m_{\mathrm{in}} = 8$. In addition, we know from theoretical simulations that the bound state has an angular momentum of $l_b = 2$, which must come from the change in spin of the particles. Depending on the angular momentum projection, the spin of the colliding particles can therefore change by at most $\Delta m_F = 2$.

Let us quickly discuss the possible cases. For $\Delta m_F = 0$, no energy is released. The collision is elastic and does not lead to any particle losses. For $\Delta m_F = 1$, the spin of the particles evolves like $|9/2, 7/2\rangle \rightarrow |9/2, 5/2\rangle$ and an energy of $\Delta E = 1E_{\mathrm{Z}} \approx k_{\mathrm{B}} \cdot 55\,\mu\mathrm{K}$ is released during the collision. Here, the molecular state however has a spin of $s_b = 7$, which would contradict E. Tiesinga's input. For $\Delta m_F = 2$, we have the process $|9/2, 7/2\rangle \rightarrow |7/2, 5/2\rangle$, which occurs under the release of an energy $\Delta E = 2E_{\mathrm{Z}}$[3].

To summarize, the two possible inelastic processes are

$$|i\rangle = |L = 0, m_L = 0\rangle \otimes \frac{1}{\sqrt{2}}(|9/2, 7/2\rangle - |7/2, 9/2\rangle)$$
$$\rightarrow \begin{cases} |f_1\rangle = |2, 1\rangle \otimes \frac{1}{\sqrt{2}}(|9/2, 5/2\rangle - |5/2, 9/2\rangle), \Delta E_1 = E_{\mathrm{Z}} \\ |f_2\rangle = |2, 2\rangle \otimes \frac{1}{\sqrt{2}}(|7/2, 5/2\rangle - |5/2, 7/2\rangle), \Delta E_2 = 2E_{\mathrm{Z}}, \end{cases}$$

where $|i\rangle$ denotes the initial and $|f_i\rangle$ the final states. At this point, we already have a strong suspicion that the first channel is not allowed. To experimentally verify which process is occurring at the Feshbach resonance, we perform the following measurement. Similarly as for the loss rate measurements, we prepare a spin-imbalanced gas of atoms at a magnetic field off resonance. We recompress the optical dipole trap strongly

[2] Such multiplet structures have been observed in various experimental settings. For example for a p-wave resonance in potassium [130], or a d-wave resonance between two isotopes of rubidium [131].

[3] One might in principle think about another channel that could participate in the dynamics, given by $|9/2, 7/2\rangle \rightarrow |7/2, 7/2\rangle$. This process is forbidden for symmetry reasons: The spatial wave function of the bound state is symmetric, since it has an angular momentum of $l = 2$. Therefore, the spin wave function has to be antisymmetric, which is only possible with different spins for the two atoms.

to its maximum potential height of $U_0/k_\mathrm{B}T \approx 220\,\mu\mathrm{K}$ to suppress losses and recapture the colliding atoms. The magnetic field is then jumped to its target value and the atomic populations and cloud temperatures are measured after various short hold times.

4.2.1. Spin population in the compressed trap limit

To describe the evolution of the spin populations, we set up a set of rate equations for the atom numbers in the different states. For this we first note that the total collision rate between atoms in $|m_F = 9/2\rangle$ and $|m_F = 7/2\rangle$ is again given by $L^{(2)}$. However, in the strongly compressed trap, we now recapture all atoms after their collision and will moreover neglect one-body losses, so that the total atom number stays constant during the duration of the experiment. From the expressions of the final states given above, we see that the number of atoms in $|m_F = 9/2\rangle$ only decreases through collisions in the channel $|i\rangle \to |f_2\rangle$, whereas the number of atoms in $|m_F = 7/2\rangle$ is only affected by the collision channel $|i\rangle \to |f_1\rangle$. The atom number in $|m_F = 5/2\rangle$ increases equally for both collision channels. We may therefore introduce the branching ratio ρ and write

$$\dot{N}_7 = -\Gamma_1^{(2)} = -\rho L^{(2)} \frac{N_7 N_9}{\sqrt{2} V_e} \tag{4.11}$$

$$\dot{N}_9 = -\Gamma_2^{(2)} = -(1-\rho) L^{(2)} \frac{N_7 N_9}{\sqrt{2} V_e} \tag{4.12}$$

$$\dot{N}_5 = \Gamma_1^{(2)} + \Gamma_2^{(2)} = L^{(2)} \frac{N_7 N_9}{\sqrt{2} V_e}, \tag{4.13}$$

where $\Gamma_i^{(2)}$ is the loss rate in the i-th channel. Since the total atom number is constant, the change in energy of the gas can be expressed as

$\Gamma_i^{(2)}$ Loss rate in the i-th channel.
ρ : Branching ratio

$$\dot{E} = 3Nk_\mathrm{B}\dot{T} = E_\mathrm{Z}\Gamma_1^{(2)} + 2E_\mathrm{Z}\Gamma_2^{(2)}. \tag{4.14}$$

These equations can be cast in a dimensionless form. Using the fractional spin population x_k, the dimensionless temperature τ and the dimensionless time u, defined by

x_k : Fractional spin populations
u : Dimensionless time
τ : Dimensionless temperature

$$x_k = \frac{N_k}{N_t} \quad , \quad \tau = \frac{k_\mathrm{B}T}{E_\mathrm{Z}} \quad , \text{ and } \quad u = \frac{L^{(2)} N_t}{\sqrt{2} V_e(E_\mathrm{Z}/k_\mathrm{B})} t,$$

where $V_e(E_\mathrm{Z}/k_\mathrm{B}) = \sqrt{2\pi E_\mathrm{Z}/m\bar{\omega}^2}^3$, one obtains the following system of equations

$$\frac{dx_7}{du} = -\rho \frac{x_7 x_9}{\tau^{3/2}}, \tag{4.15}$$

$$\frac{dx_9}{du} = -(1-\rho) \frac{x_7 x_9}{\tau^{3/2}}, \tag{4.16}$$

$$\frac{dx_5}{du} = -\frac{dx_7}{du} - \frac{dx_9}{du}, \tag{4.17}$$

$$\frac{d\tau}{du} = (2-\rho) \frac{x_7 x_9}{3\tau^{3/2}}. \tag{4.18}$$

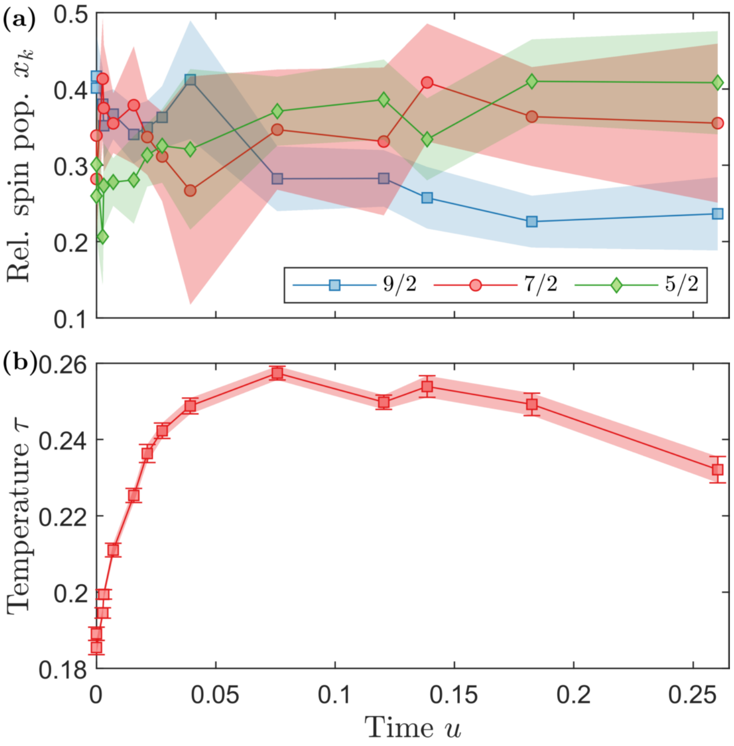

Figure 4.4. – Spin dynamics close to the Feshbach resonance at $B = 7.8\,\mathrm{G}$. Here $L^{(2)} = 1.073\cdot 10^{-13}\,\mathrm{cm^3 s^{-1}}$. (a) Evolutions of the relative spin populations measured with microwave spectroscopy. We observe a decay of the population of $|9/2\rangle$ and a rise of the atom number of the $|5/2\rangle$ state. The shaded areas correspond to the measurement uncertainties (linearly extrapolated in between the points). Within the accuracy of the measurement, the population in $|7/2\rangle$ stays constant indicating a value of ρ compatible with 0. (b) Strong heating during is observed, originating in the freeing of energy E_Z during the collisions and the subsequent recapture of atoms in the recompressed trap. For $u > 0.0.5$, the onset of evaporative losses stops the temperature increase. Even with improved statistics, the rate equations 4.15 - 4.18 will thus not be able to capture the dynamics beyond this time.

The evolution of the atomic populations and the temperature is strongly dependent on the value of the branching ratio. For $\rho = 0$ and $\rho = 1$, only one collision channel exists. In these cases, N_7 or N_9 are unaffected by the collision events and the respective population stays constant. The other collision partner is converted into $|m_F = 5/2\rangle$ until the original population is depleted and no more collision events can take place. The temperature rises during the collision events due to the released Zeeman energy. The timescale for the temperature increase is faster for the collision channel 2, since more energy is liberated per collision event. A clear signature of the presence of both collision channels ($0 < \rho < 1$) would be given by the depletion of both the populations of $|m_F = 9/2\rangle$ and $|m_F = 7/2\rangle$ at the same time.

Figure 4.4 shows exemplarily a result of a spin dynamics measurement close to the Feshbach resonance. Overall, we observe a depletion of the population of $|m_F = 9/2\rangle$ and a corresponding increase of $|m_F = 5/2\rangle$. The maximum hold time shown here corresponds to 20 s. During this time, the population of $|m_F = 7/2\rangle$ stays constant within the accuracy of our measurement, which would be consistent with a branching ratio of $\rho = 0$. However, there are some caveats to be addressed. As can be seen in Fig. 4.4 (b), the temperature of the gas increases strongly during the first 2 s ($u < 0.05$), then levels off and starts to slowly decrease. The temperature decrease on long time scales is probably due to evaporation and spilling losses occurring at higher temperatures. The rate equations we derived earlier do not account for these effects, but can only describe our system for short times up to $u \approx 0.05$. At these short times, Fig. 4.4 (a) gives the impression as if the main losses occurred in the $|m_F = 7/2\rangle$ state. However, this impression might be caused by the data point at $u = 0.039$, which is the only point showing a relative population in $|m_F = 7/2\rangle$ that lies below the initial population. In addition, it is subject to a rather large uncertainty.

We thus conclude that our measurements are compatible with a branching ratio of $\rho = 0$. This implies that the outgoing channel of the Feshbach resonance is given by

$$|f_2\rangle = |L = 2, m_L = 2\rangle \otimes \frac{1}{\sqrt{2}}(|7/2, 5/2\rangle - |5/2, 7/2\rangle).$$

Within the accuracy of our measurement, however, a contribution of the first loss channel cannot be ruled out. The measurement accuracy is mostly limited by shot to shot fluctuations of $\sim 20\%$ of the atom number. Since the analysis relies on the detection of small changes in particle number differences, these fluctuations introduce relatively large scatter on the data and prevented us from performing a precision measurement of the spin populations. Much more statistics and a higher trap depth could help to alleviate this issue.

4.3. Conclusion

In this chapter we have characterized a new Feshbach resonance in ^{40}K in multiple aspects: Using measurements of particle losses in a shallow trap, we have characterized the overall shape and height of the resonance peak. The particle losses are well described by a two-body process involving the initial states $|m_F = 9/2\rangle$ and $|m_F = 7/2\rangle$. The peak value of the loss rate deviates from previous analysis by a factor 1.7 [104], however, the loss rates at lower initial temperatures are in very good agreement with the theoretical prediction and the deviation is most likely due to the data spacing and a slightly different analysis method. Accounting for systematic errors, the new value is in good agreement with the previous analysis. From the evolution of the peak shape with temperature, we could confirm the s-wave nature of the entrance channel.

During the collisions, the atoms undergo a spin flip to an outgoing state $|7/2, 5/2\rangle$, which is consistent with the measured evolution of the spin populations in a strongly recompressed optical dipole trap. This outgoing state is a d-wave state with an angular momentum of $L = 2$, which is the same angular momentum as exhibited by the bound state.

Within the accuracy of our measurement, we could however not rule out a small contribution of a collision channel involving the outgoing state $|9/2, 5/2\rangle \otimes |L = 2, m_L = 1\rangle$.

For the future, the accuracy of our measurements could be improved with a higher intensity dipole trap, allowing the system to heat to higher temperatures before evaporative losses become dominating. Thus, loss rates at higher initial temperatures could be extracted and the spin dynamics could be observed over longer time scales, obtaining a closer grip on the value of the branching ratio ρ. Furthermore, it would be interesting to repeat the loss rate measurements with a spin-resolved imaging method. Although the extracted loss rates already show good agreement to the theory prediction, we only estimated the decay of the population in $|5/2\rangle$ during the hold time from the typical population after the evaporative cooling steps. In addition, the initial imbalance $\delta f = f_9 - f_7$ has been fitted to the data. Having gained access to this information with the newly implemented spin-selective imaging methods, these measurements could in the future be reconfirmed with higher accuracy.

Part II.

Ultracold Two-Dimensional Fermi Gases

5. Creating Two-Dimensional Fermi Gases

This chapter shall familiarize the reader with the 2D lithium experiment of the Moritz group at the university of Hamburg. I joined the experiment at a time when the main building and optimizing phase was already finished and was mainly a user of the setup built by Wolf Weimer, Kai Morgener and Klaus Hueck and further optimized by Jonas Siegl, Niclas Luick and Lennart Sobirey. My work on the experimental setup focused on the preparation of a new optical setup for the generation of tailored optical potentials necessary for the creation of 2D gases, which I will discuss in the end of this chapter. Before that, an overview over the main functional parts of the machine is given and the typical experimental sequence is discussed. The entire experimental setup is described in great detail in the theses of Wolf Weimer [133] and Kai Morgener [134]. For further information about the setup around the science cell, in particular in relation to the creation of 2D gases, I would like to refer the reader to the thesis of Klaus Hueck [116]. A detailed discussion of the in-vacuo resonator setup can be found in the theses of Klaus Hueck [116] and Niclas Luick [135].

After having discussed the characterization of a d-wave Feshbach resonance in potassium 40, let us now transition towards two-dimensional Fermi gases of lithium. In this chapter, I will present the lithium experiment of the Moritz group in Hamburg. The main ideas followed for the realization of ultracold lithium gases are very similar to the steps presented in the previous part. The vacuum system in which the experiment is performed is shown in Figure 5.1. A macroscopic block of lithium is heated to roughly 450 °C in the oven chamber, creating a vapor which escapes through an aperture, forming a divergent atomic beam. The atoms are slowed down with the help of a Zeeman slower [17] and then trapped in a magneto-optical trap (MOT) [19] in the main chamber of the apparatus.

To cool down below the Doppler limit, the gas is loaded into optical dipole traps (ODTs) [92] created with infrared lasers and evaporative cooling steps [114] are carried out. In a succession of ODTs of different geometries, the gas is cooled down towards quantum degeneracy using evaporative cooling stages.

To improve lifetimes and optical access, the gas is transported to a separate science cell. Here, the atoms are transferred into a highly elliptical infrared dipole trap (the so-called 'squeeze' trap) which pre-flattens the atoms, and then loaded into a single node of a repulsive optical lattice,

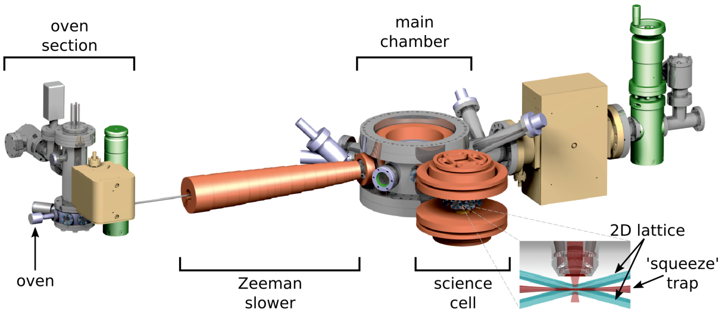

Figure 5.1. – CAD drawing of the vacuum system of the Hamburg experiment including the magnetic coil setup (copper colored) around the experiment (adapted from [134]). An atomic jet of lithium is created in the oven, which is slowed down in the Zeeman slower and captured in a MOT in the center of the main chamber. To reach sub-Doppler temperatures, the gas is then transferred to a sequence of optical dipole traps and cooled down to degeneracy using successive evaporative cooling steps. Before performing experiments, the atoms are moved into the science cell, which is offset from the main apparatus by a few tens of cm. Here, a highly oblate infrared trap ('squeeze') and a blue-detuned optical lattice are used to convert the geometry of the system from 3D to quasi-2D. Green: Valves separate the vacuum system into multiple chambers for easier maintenance. Beige: Ion pumps. Not labeled are Titanium sublimation pumps, vacuum feedthroughs and vacuum gauges.

bringing the sample from the 3D into the quasi-2D regime [60]. Additional repulsive potentials are used to confine the atoms horizontally in flat-bottom potentials of different shapes.

After these preparatory steps, the experiment-specific steps of the sequence are carried out. Finally, the atoms are imaged using high-intensity absorption imaging [115, 136] either in situ or after a short time of flight in a weak underlying harmonic trap. These two imaging procedures give access to the spatial density distribution when imaged in situ or to the momentum distribution when imaged after free evolution for a quarter period in the underlying harmonic trap using Matter-Wave-Imaging [137, 138].

5.1. The experimental setup

As for the Fermix experiment, I would now like to give a more detailed description of some key parts of the experimental setup. Note however, that this section is not intended to provide a full description of every aspect of the machine, since this would be beyond the scope of this thesis. A detailed description of the vacuum system can be found in [133]. The magnetic field configuration is detailed in [134]. Extensive information on the cooling resonator setup has been provided by [116, 135].

5.1.1. Vacuum system and magnetic setup

Similar to the Fermix experiment, the vacuum system of the lithium machine in Hamburg consists of multiple functional parts which are separated from each other by differential pumping stages, which allow maintaining different pressure levels in different parts of the machine.

Oven section and Zeeman slower

The first of these regions is the oven section. A cut through this section is shown in Figure 5.2. The lithium reservoir is located on one end of the section. A series of beam apertures is used to limit the divergence of the escaping atomic jet. When the MOT is fully loaded, the beam can be blocked using a mechanical shutter. Two sublimation and getter pumps are used to maintain a high vacuum of $\sim 10^{-9}$ mbar in the heated oven chamber. A valve can be used to separate the oven chamber from the main vacuum part, such that the lithium reservoir can be refilled without destroying the vacuum in the entire machine. The oven section is connected to the Zeeman slower section via a flexible bellows and a long and thin ($l = 280\,\text{mm}$, $d = 4\,\text{mm}$) vacuum tube, acting as a differential pumping stage.

The Zeeman slower [134], built in decreasing field configuration, consists of a long and thin steel tube, which is surrounded by magnetic coils over a length of 52 cm, creating a spatially varying magnetic field. In addition, a red-detuned laser of circular polarization is shone into the slower tube in opposite direction of the atomic jet. At the beginning of the slower, the magnetic field shifts the atomic D2-transition of the atoms of one given velocity class into resonance with the laser frequency. The field is designed to keep these atoms in resonance during their travel through the tube by compensating for the changing Doppler effect during the deceleration. Over a series of many absorption and reemission cycles the atoms are effectively slowed down, since the net transfer of momentum is opposite their direction of motion. Atoms entering the slower at a lower velocity are off-resonant at first and thus are decelerated at a lower rate, until the faster atoms catch up to them. The Zeeman slower employed at the experiment allows the majority of the atoms with an initial velocity inferior to $v_{\max} \approx 1000\,\text{ms}^{-1}$ to be slowed down to a final velocity of approximately $50\,\text{ms}^{-1}$ [134].

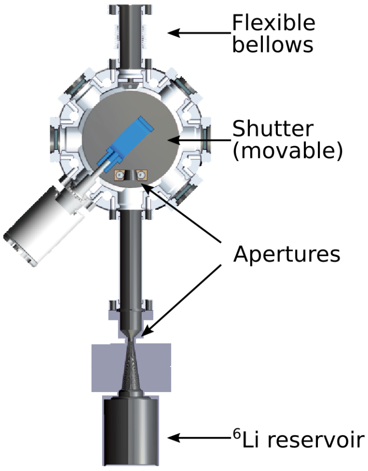

Figure 5.2. – Top view into the oven chamber (adapted from [134]).

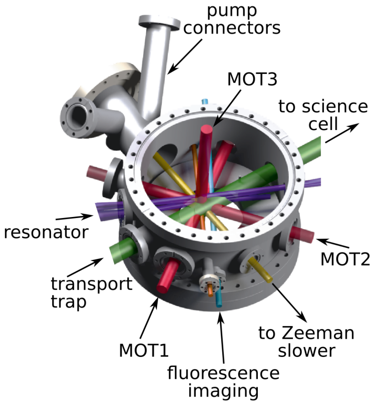

Figure 5.3. – CAD drawing of the laser configuration in the main chamber of the experiment (adapted from [134]). After leaving the Zeeman slower (yellow), the atoms are captured in the MOT (red) and cooled to the Doppler limit. The cloud is loaded into an infrared resonator-enhanced optical dipole trap (purple) and first evaporation steps are carried out. Finally, the atoms are transferred into a running wave ODT (green), which transports the cloud towards the science cell. There are additional viewports for imaging (light blue) and for connecting an optional 2D MOT for future projects at the experiment (orange, not labeled).

Main chamber

The main vacuum chamber is connected to the other end of the Zeeman slower. As can be seen in Fig. 5.3, the main chamber provides viewports for various purposes:

Three pairs of counter-propagating laser beams are shot in from orthogonal directions to form the magneto-optical trap in which the atoms are trapped after exiting the Zeeman slower (compare [134]). After the MOT phase, the temperature of the gas corresponds to the Doppler temperature ($T_{\text{D}} \approx 140\,\mu\text{K}$ for lithium). Before evaporative cooling stages can be efficient, the density of the gas has to be strongly increased or its temperature has to be strongly reduced. To achieve this, as mentioned previously (compare section 3.1.2), one could use narrower cooling transitions, reducing the Doppler temperature, or employ sub-Doppler techniques, as is done in Paris at the Fermix experiment using the D1-gray molasses technique [113]. In the Hamburg experiment, an in-vacuo bowtie resonator [116, 133, 135] has been implemented instead, seeded by two infrared beams at 1064 nm, which are shone into the main chamber through two other windows.

In addition, a second infrared ODT is projected onto the resonator under an angle of 90° with respect to the Zeeman slower. This trap is used to transport the atoms from the main chamber into into the science cell which is attached to the other side of the main chamber. The transport itself is performed by shifting the focus of the transport dipole trap over a distance of 326 mm. To achieve this, the focusing lens of the transport trap is located on an air bearing linear translation stage[1], which moves the lens with a high precision over the required distance in about 1 s. The pointing of the transport trap is controlled by measuring the position of the beam on a quadrant photodiode for the two positions of the focusing lens and can be adjusted with piezo-actuated mirrors.

On the opposite side of the Zeeman slower, another section of the vacuum system is attached, holding one more ion getter pump and another Titanium sublimation pump. This section ends with a sapphire viewport through which the Zeeman laser is shone into the system. A valve separates this viewport from the main vacuum chamber in order to allow for cleaning or replacement. Finally, some additional windows on the main chamber allow the fluorescence of the MOT to be imaged or serve as backups for eventual expansions of the system.

Several magnetic coils are placed around the main chamber [134]. The coils for the MOT are located above and below the main chamber, in recesses within the outer frame of the main chamber, minimizing the distance between the atoms and the coils. Three more coils, one at the end of the Zeeman slower, one around the entry window of the transport trap and one wound directly onto the upper MOT coil, can be used to shift the magnetic center of the MOT in order to optimize the overlap between the MOT and the resonator. This capability is necessary for two reasons: On the one hand, the resonator mirrors are placed inside the vacuum and cannot easily be adjusted. On the other hand, this setup provides a smoother transition from the Zeeman slower field into the field needed for the MOT.

Figure 5.4. – The science cell during installation (Figure adapted from [135]). Its octagonal shape gives optical access from eight directions. The windows are coated and slightly tilted with respect to each other to minimize reflections. The top and bottom windows are recessed to allow the imaging optics to come as close as possible to the atomic sample. Here, a paper sheet has been put on top of the cell to align a pilot beam for the microscope alignment.

Science cell

The final part of the vacuum system is the science cell. In the science cell, the final evaporation steps are carried out and the cloud is brought into the quasi-2D regime by a series of successively tighter optical trapping potentials [60, 116] (see section 5.2).

The high number of optical potentials and imaging beams that can be projected onto the atoms requires high optical access from all sides. In addition, two large microscope objectives[2] [133, 140] (diameter $d = 44\,\mathrm{mm}$) with a high numerical aperture of $\mathrm{NA} = 0.62$ are used to project the optical potentials needed for the horizontal confinement and for the experimental steps from the top of the cell and to finally image the

[1] Heason AirGlide, Ultra Precise Air Bearing System, 350 mm; Controller: Aerotech, Ensemble ML10-40 digital controller and linear amplifier.
More recently, optical transports have also been realized using focus-tunable lenses [139].

[2] Special Optics, New Jersey, USA

atoms from below. The working distance of the microscopes of 10.5 mm to the atoms imposes limits on the vertical dimensions of the chamber. To meet these conditions, a custom glass cell has been produced in the shape of a flat octagon[3]. The windows have an anti-reflection coating for the important wavelengths used at the experiment (532 nm, 671 nm, 780 nm, 1064 nm) and opposite windows are tilted with respect to each other by 2° to avoid unwanted reflections which could create standing wave potentials. The total distance between the outer faces of the top and bottom windows is only 16 mm. A front view of the science cell during installation is shown in Figure 5.4.

To access the Feshbach resonance, which allows us to tune the interactions of the ultracold sample, and to enable different magnetic field configurations, a sizable collection of coils is placed above and below the science cell. This setup is shown in Figure 5.5. The 'Feshbach' coil pair (red) is used to generate strong magnetic fields which can be tuned over several 100 G around the Feshbach resonance, however the field produced by these coils exhibits a weak curvature which results in a weak harmonic confinement of ≈ 27.6 Hz. A second coil pair, the 'Helmholtz' coils (blue) are used to produce a highly homogeneous field at the position of the atoms. Additional 'cloverleaf' coil pairs allow to produce magnetic gradients. The 'jump' coils feature a small inductance and help to quickly switch the magnetic fields. Finally, the 'levitation' coils are used to generate a small vertical gradient to compensate for gravitation.

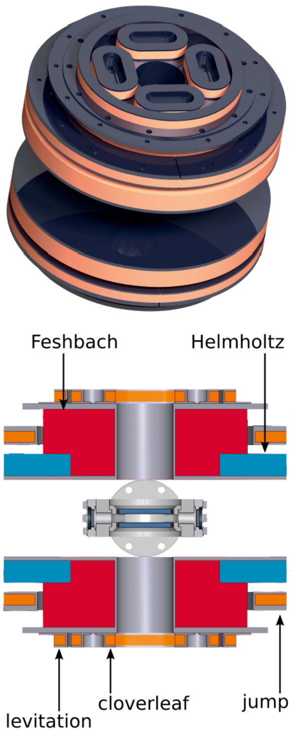

Figure 5.5. – Isometric view and cut of the coil setup around the science cell (figure adapted from [134]).

5.1.2. The laser setup

The laser setup follows a different scheme than the laser setup used at Fermix. It is shown in Fig. 5.6. Instead of one master laser whose light is split and amplified, several commercial lasers are available which produce light for one or two tasks each, at four main frequencies. Using separate laser sources for the different beams has the advantage that eventual degradations in the lasers or the beam paths are less likely to affect the performance of multiple experimental stages at the same time. In addition, the frequencies of the lasers can be adjusted using their separate locking electronics, which incurs less intensity loss and better beam profiles with respect to a chained AOM setup. On the other hand, such a setup is more costly.

Near-resonant frequencies

For the operation of the MOT and the Zeeman slower as well as for absorption imaging step in the end of the experimental sequence, (near-)resonant light at 671 nm is used. The transition chosen for these purposes is the D2-transition, which connects the ${}^2S_{1/2}$ ground state to the ${}^2P_{3/2}$ excited state and which is shown in Fig. 5.7. More precisely, the Zeeman slower and MOT operate on the transition $F = 3/2 \rightarrow^2 P_{3/2}$, labeled here as 'cooler'. To prevent atoms from populating the $F = 1/2$ state, the MOT features a 'repumper' beam operating on the transition

---

[3] Until 2018, a metal cell had been installed on the machine. Unfortunately, the pumping rate out of this cell turned out to be insufficient to maintain the ultrahigh vacuum necessary for long lifetimes and led to increased heating of the gas [135, 141]. It was therefore replaced by a glass cell, increasing the resulting lifetimes by almost a factor 20 up to ≈ 120 s [135].

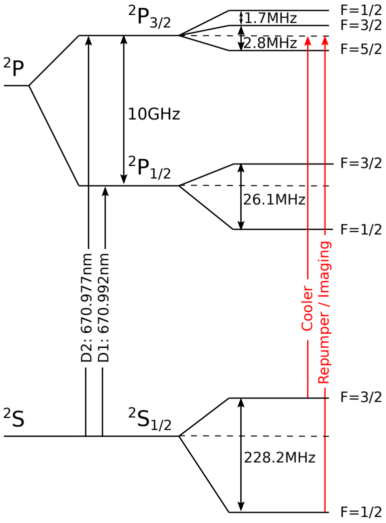

Figure 5.7. – Level scheme of ^{6}Li. The energy splittings are not to scale. The lithium experiment operates on the D2-Line between the $^2S_{1/2}$ ground states and the $^2P_{3/2}$ states. Since the hyperfine splitting of this state is smaller than the natural linewidth of $\Gamma \approx 6\,\text{MHz}$, the excited states cannot be addressed individually using optical transition. They therefore decay in both hyperfine ground states, making a repumping laser necessary.

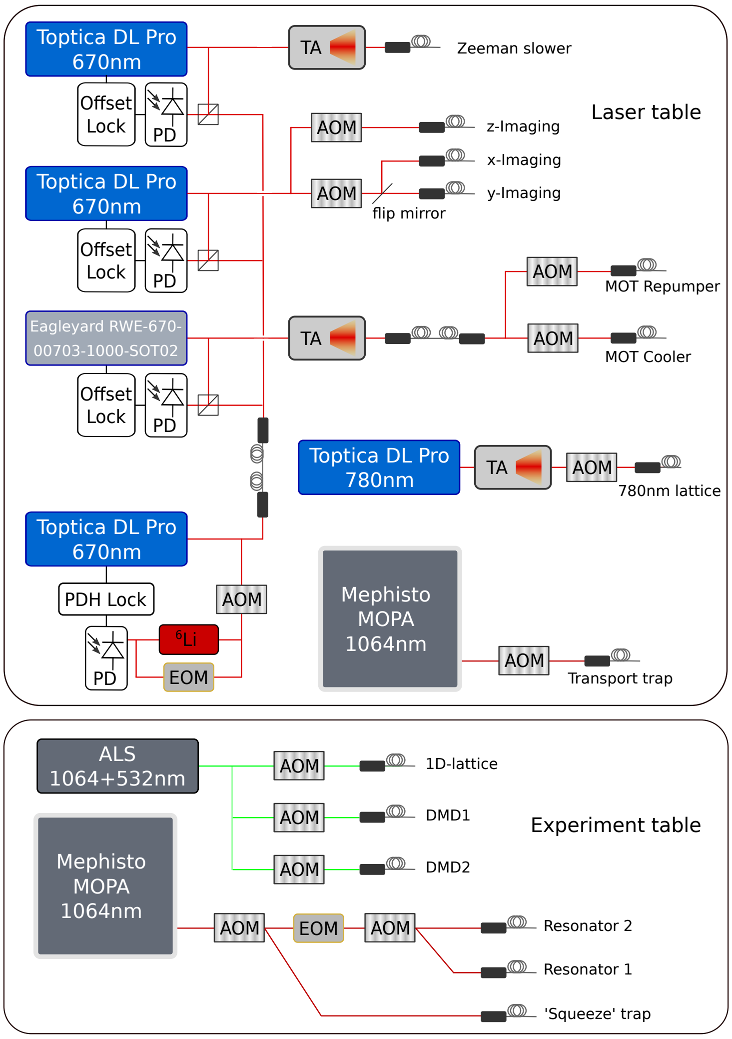

Figure 5.6. – Diagram of the laser setup on the lithium experiment. Beam shaping and routing optics as well as shutters are not shown. Most lasers are located on a separate laser table and their light is transferred to the main experiment table via single-mode polarization maintaining optical fibers in order to limit stray light on the experiment table. Due to limited space availability, some lasers are placed on the main table.

$F = 1/2 \rightarrow ^2 P_{3/2}$. The 'repumper' transition is also used for absorption imaging at the end of the sequence.

To create these frequencies, a total of four lasers is used. A reference laser[4] is locked onto the crossover line of the D2 transition of lithium 6 using the Pound-Drever-Hall locking scheme [142, 143]. The other three lasers, two Toptica DL Pro 670 nm for Zeeman slower and imaging light and one homebuilt model utilizing an Eagleyard RWE-670-00703 diode for the MOT, are frequency-locked onto this laser using an offset-locking technique [144]. The use of offset locks has the main advantage that the frequency of the light can easily and independently be shifted over large ranges without affecting the laser intensity. The capability to tune the laser frequency over a large range is especially important for the imaging laser, which has to operate at large detuning differences due to the fact

[4] Toptica DL Pro 670 nm

that the imaging can take place at different magnetic field values around the Feshbach resonance.

In the case of the MOT and Zeeman lasers, the light is first amplified with tapered amplifiers (TA) and then split into the different beam paths. For imaging purposes, low powers are sufficient. The beam of the imaging laser is therefore directly split into the three paths for the different imaging directions. The light transported from the laser table to the main table using polarization maintaining single-mode fibers.

In order to control the intensity of the beams and prevent stray light on the main table, combinations of AOMs and shutters are used before the light is coupled into the optical fibers and transported to the experiment table. The intensities are measured behind the fibers with photodiodes and stabilized with PI controllers. For the imaging light, the photon counts of the cameras during the imaging shot are used as an intensity measurement.

Far-detuned lasers

The setup also features two lasers[5] at 1064 nm, one of which is used to create light for the transport ODT, the other producing the light for the resonator and the 'squeeze' trap. The light is split into the different paths and transported to the experiment using photonic crystal fibers. For the transport trap and the squeeze, the exact frequency of the light is unimportant and the lasers are operated without frequency stabilization. To operate the cooling resonator however, the wavelength of the laser has to be locked to match the resonator mode. Moreover, the intensity of the resonator light needs to be ramped down over several orders of magnitude during the first evaporative cooling step, without influencing the frequency stability. To precisely control both intensity and frequency of the two resonator beams, an involved stabilization scheme has been developed, which requires a large number of additional optical and electronic components. The details of this setup can be found in [116] and [135].

In addition to the infrared beams, a frequency-doubled 1064 nm laser[6] produces 10 W of green light at 532 nm, which are used to provide the vertical and horizontal confinement to bring the atoms into the desired geometry and to produce excitation pulses. The light of this laser is split into three paths, which are each independently fed through AOMs and coupled into a high-power optical fiber. One of these paths is used to produce the repulsive optical lattice which is used to confine the atoms into a 2D plane. Two of the other paths illuminate two separate digital micromirror devices (DMDs), which are then imaged onto the atomic plane through the upper microscope objective. With this setup, it is possible to create two different repulsive potentials of arbitrary shape in the 2D plane. Finally, an optical setup creating a repulsive ring potential in an axicon cascade is also available and can be used instead of one of the DMDs (see supplementary materials to [60]).

---

[5] Mephisto MOPA 25

[6] AzurLight Systems 1064/532 dual output

5.1.3. High intensity imaging

After the experimental steps have been performed, the atom distribution is imaged using absorption imaging, either in situ or after a short time of flight to obtain information about the phase of the gas. There are several options available for this process. The main imaging system, which is used for most measurements taken on the experiment, projects the atomic plane in the vertical direction through the lower microscope objective and a telephoto lens onto the chip of a sensitive EMCCD camera[7], at a high magnification of $M = 40$. For alignment and diagnostic purposes, two auxiliary low-magnification imaging setups can be used to image the atoms in the horizontal plane, which use standard CCD cameras[8]. Of particular use hereby is the 'BEC-X' imaging, which is used to verify that the atoms are loaded in only a single plane of the repulsive lattice. The 'BEC-Y' imaging monitors the experiment along the transport axis and permits us to image the optical resonator in the main chamber.

As mentioned previously, the microscope of the main imaging system has a numerical aperture of 0.62 and a field of view of about 150 µm. The high NA allows for a diffraction limited resolution of 700 nm at a wavelength of 671 nm, which is slightly lower than the typical interparticle spacing in the two-dimensional gas, however it also incurs a limited depth of field of only 2 µm. To reduce the motion of the atoms during the imaging, short (5 µs) imaging pulses at intensities comparable to the saturation intensity of the imaging transition are used. Although the imaging pulse is kept short, the low mass of the lithium atoms causes them to acquire a substantial velocity during the imaging pulse, which results in a Doppler shift comparable to the natural linewidth. To compensate for this effect, the imaging pulse is chirped at a rate of typically 1.5 MHz/µs with the help of the final AOM on the laser table, which is positioned in double-pass configuration.

At high imaging intensities, the optical density of the atomic sample is given by [115, 136]

$$od(x,y) = n_{2\mathrm{D}}(x,y)\sigma_{\mathrm{eff}} = -\ln\left(\frac{I_{\mathrm{out}}(x,y)}{I_{\mathrm{in}}(x,y)}\right) + \frac{I_{\mathrm{in}}(x,y) - I_{\mathrm{out}}(x,y)}{I_{\mathrm{sat}}^{\mathrm{eff}}}, \tag{5.1}$$

where I_{in} and I_{out} is the intensity of the light before and after passing the atomic sample, $\sigma_{\mathrm{eff}} = \alpha 3\lambda^2/2\pi$ is the absorption cross section (corrected for imperfect polarization or magnetic field orientation by the factor $\alpha > 1$) and $I_{\mathrm{sat}}^{\mathrm{eff}} = \alpha\pi hc\Gamma/3\lambda^3$ is the saturation intensity.

od :	Optical density
σ_{eff} :	effective absorption cross section
λ	Imaging wavelength
α	Correction factor
I_{eff} :	Effective saturation intensity
c:	Speed of light
C:	Photoelectron counts

The light intensity and the number of photo-electrons counted by the camera are linearly related [115]. Therefore, the atomic density can directly be calculated from the photon counts on the camera according to

$$\sigma_{\mathrm{eff}} n_{2\mathrm{D}}(i,j) = -\ln\left(\frac{C_{\mathrm{out}}(i,j)}{C_{\mathrm{in}}(i,j)}\right) + \frac{C_{\mathrm{in}}(i,j) - C_{\mathrm{out}}(i,j)}{C_{\mathrm{sat}}^{\mathrm{eff}}}, \tag{5.2}$$

where i, j denote the pixel coordinate of the camera sensor, C_{in} and C_{out} are the number of photo-electrons counted during the imaging pulse in

---

[7] Andor Ixon3

[8] PointGrey Chameleon 13S2M

the absence or presence of atoms, respectively and C_{eff} is the number of photo-electrons counted for $I = I_{\mathrm{eff}}$. To obtain the atomic density, it is thus in principle sufficient to take only two images, provided σ, α and C_{sat} are known. However, in addition to the absorption and reference images, two additional images are taken without imaging light in order to correct the photon counts by the number of dark counts of the camera. Additional information on the imaging system and the calibration procedure can be found in [115, 116, 135].

5.1.4. Experiment and camera control

The experimental hardware itself is controlled via a system of digital and analog output cards provided by National Instruments[9] and Jäger Messtechnik[10]. The correct timing of the experimental sequence is insured by an external clock, which provides a continuous clock rate of 10 MHz. The 'Experiment Wizard'[11] software controlling the experiment consists of three main functional parts that communicate with each other during the sequence:

For each output channel, the outputs during each time step are programmed prior to the sequence in a spreadsheet-like graphical user interface called 'experiment control'. The channel outputs can depend on user defined variables, which can be scanned systematically over lists of values in a randomized or non-randomized way.

The 'experiment runner' creates buffers of output values from the values defined in 'experiment control' and sends these buffers to the NI cards. It also features a queue to manage the succession of sequences to be run. In a recent update, it has become possible to schedule an entire block of different sequences, while systematically changing parameters over the different repetitions of the entire sets. This capability has proven very useful during longer measurements, since it provides us with the capability to run diagnostic sequences interspersed with the measurement sequences at regular time intervals to verify the functional state of the machine.

Finally a third part, 'camera control', manages the image acquisition during the sequences. The cameras are implemented as objects in experiment control, which allows the parameters of the sequence and the camera to be stored together with the images. The user defines a list of images which are to be taken with given cameras during the sequence, together with a list of preprocessing commands. Camera control collects the images taken by the cameras and applies the preprocessing commands, thus automatically generating atomic density images together with a set of derived quantities. These quantities can be used to do quick on-the-fly analysis. The main data analysis is done in Matlab at a later time using the unprocessed images from the cameras.

5.2. Creating a homogeneous 2D Fermi gas

During my time in the group, the experimental setup has been highly robust. It was generally possible to run the machine for several weeks

[9] National Instruments PCI-6723 / PCI-6733

[10] ADwin-Pro II AOUT8/16 / DIO32 TiCo

[11] The 'Experiment Wizard' software is developed and maintained by groups in Zurich (T. Esslinger), Hamburg (H. Moritz) and Barcelona (L. Tarruell).

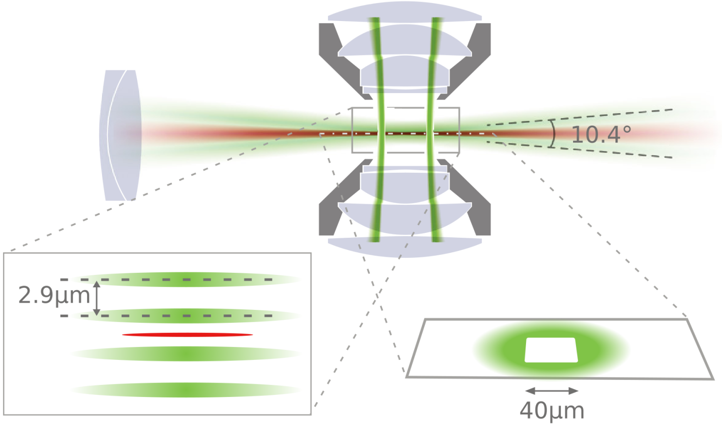

Figure 5.8. – The optical setup for the creation of two-dimensional single layer gases (view into the transport axis, figure adapted from [141]). The highly oblate squeeze trap (red) precompresses the atoms. Then, the sample is loaded into a single node of a repulsive optical lattice (green), which is formed via interference of two beams intersecting under a shallow angle of 10.4 °. The horizontal confinement is created by projecting repulsive potentials through the upper microscope. This can be done using two DMDs to create potentials of arbitrary shape or with the help of an axicon setup to create a circular trap with high and sharp walls. The science cell is not shown here for better visibility.

without having to reoptimize fiber couplings or alignments between different optical traps. Part of the reasons for this high stability are the presence of multiple interlock systems [134], the remote accessibility of the experiment control and of course its queuing function, which allowed us to keep the the machine running over night and over the weekends, avoiding dethermalization of the setup. Up to the arrival of the atoms in the science cell, the experimental sequence was tried and tested and thus the part of the system at which most optimizations and adjustments took place is the part around the science cell. Here, the atoms are converted from 3D to 2D in a process that is quite sensitive to power deficits or misalignments between the optical and magnetic potentials which are involved. In the following, I present the existing setup and procedure to create and influence the 2D gas as well as the steps which are planned to improve the setup in an update in the close future.

5.2.1. Preparing a single layer gas

The concept of the setup is shown in Figure 5.8. Once the atoms arrive in the science cell, they are trapped in the transport trap, which is a standard running wave 1064 nm optical dipole trap with an elongated three-dimensional shape. In order to reduce the dimensionality of the sample towards 2D, the cloud is transferred into two successively tighter traps until finally all relevant energy scales are smaller than the level spacing in the tightly confined direction [84]. To achieve this, the cloud is first transferred into the 'squeeze' trap [116], a highly oblate dipole trap with waists of $\omega_x \approx \omega_y \approx 350\,\mu\text{m}$ and $\omega_z \approx 10\,\mu\text{m}$. In this trap, a final evaporation is carried out, which reduces the temperature and leaves us with a small enough atom number to ensure a low enough chemical potential in the later steps. By increasing the power of the squeeze beam, the cloud is adiabatically compressed and flattened to a vertical size of only about 1 µm in preparation for the transfer to the optical lattice, which has a lattice constant of $d_{\mathrm{lat}} = 2.9\,\mu\mathrm{m}$. Afterwards, the blue-detuned lattice is ramped up and the squeeze is ramped down and switched off. The typical trap frequencies used during the experiments are on the order of $\omega_z \approx 8-9\,\mathrm{kHz}$, which exceeds the chemical potential, the Fermi energy and the thermal energy of the atoms across most of the BEC-BCS crossover at the typical 2D-densities of $1\,\mu\mathrm{m}^{-2}$.

Verification of single-layer loading

To obtain valid results on our 2D gas, it is crucial that the loading of the optical lattice occurs in such a way that only a single layer in the lattice is occupied. The dynamics in neighboring occupied layers might differ, for instance due to different densities, slightly different potentials and the camera cannot discern between the atoms located in the different potential wells. Finally, weak coupling between the pancakes might influence the atoms in neighboring layers, destroying the two-dimensional character of the system. In order to successfully load the atoms from the squeeze trap into the optical lattice, the alignment between the two potentials has to be precise on the micrometer level.

To verify that only a single layer of the optical lattice is populated, a simple scheme has been developed [60, 116] that removes the need of a high-resolution imaging or a precise RF spectroscopy setup. It relies instead on spatially separating the atoms in neighboring sites to resolve the lattice wells from the side using the standard auxiliary imaging. The confining lattice is switched off suddenly and the atoms are allowed to expand for a short time (≈ 50 µs), which creates an atomic pancake in each occupied well. Then, the squeeze trap is shortly flashed on, which results in different attractive potentials for the neighboring sites, thus accelerating the atomic pancakes towards each other. After a short time of free flight, the atoms are imaged and we can see double occupancy in the presence of two distinct clouds (compare fig. 5.9).

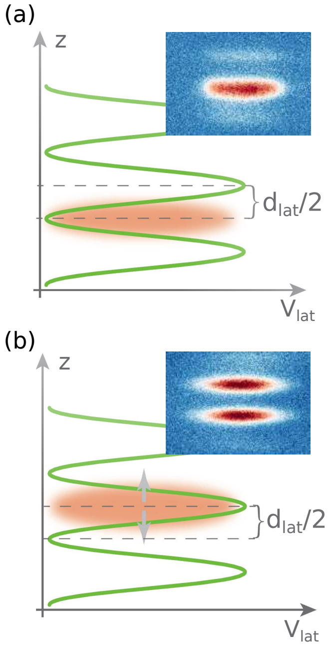

Figure 5.9. – The single-layer loading scheme (adapted from [116]). (a) The squeeze trap and the lattice are aligned correctly and the cloud loads into a single minimum of the lattice potential. After the squeeze is flashed on, the cloud remains together. (b) The squeeze is misaligned with respect to the lattice such that its center coincides with a maximum of the lattice potential. Once the atoms are released from the squeeze, they fill both adjacent layers. After the flash of the squeeze, the two clouds are accelerated towards each other, forming two distinct clouds after time of flight.

An active feedback mechanism has been implemented to automatically minimize the number of atoms in the side maxima by moving the vertical position of the squeeze trap using small increments on a piezo mirror located in the beam path of the squeeze trap. During normal operation of the machine, the verification of single-layer loading was typically performed every few hours in between the measurement sequences. Manual alignment have to be done only on the timescale of a few days, which permitted us to run the measurements presented in chapters 6.3, 7.1 and 7.4 continuously on the timescale of a week.

5.2.2. Horizontal confinement

Past experiments with two-dimensional Fermi gases have always been realized with harmonic trapping potentials. While these potentials are

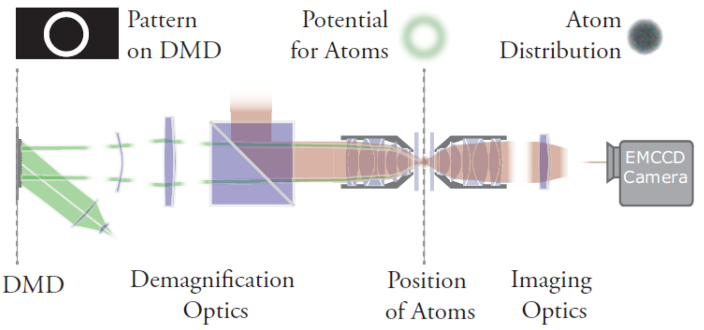

Figure 5.10. – Schematic view of a DMD setup (adapted from [116]). The DMD is illuminated and displays an image of the desired trapping geometry. Its mirror plane is imaged onto the atoms via the upper microscope objective. The DMD and the imaging beams are overlapped in polarizing beam splitter cubes ahead of the microscope. The second microscope is used to image the atomic plane onto the EMCCD camera.

well understood, they result in an inhomogeneous gas, which means that nonlocal quantities can only be extracted as trap averages [60] and which "hinders the observation of critical phenomena with a diverging correlation length and exotic phases such as the Fulde-Ferell-Larkin-Ovchinnikov (FFLO) state" [60]. In our experiment, we trap the atoms in homogeneous potentials created by blue-detuned light, which results in a constant density over the entire extent of the sample. Thus, the chemical potential and many resulting thermodynamic properties do not vary throughout the gas. The potential walls trapping the atoms horizontally inside the 2D plane are projected onto the atoms from the top through the upper high-resolution microscope objective. There are three light sources available on the experiment, which are all illuminated by the 532 nm ALS laser.

During the experiments presented in section 6.3 and 7.1, two digital micromirror devices (DMDs) have been used[12]. DMDs contain an array of micrometer-sized mirrors that can be switched individually between an 'off' and an 'on' position. They provide the unique ability to project arbitrary two-dimensional potentials onto the atoms. To do so, the mirror plane is imaged onto the plane of the atoms while displaying an image of the desired intensity distribution. The scheme of such a setup is shown in Figure 5.10. In our experiment, the setup is designed such that the image of a mirror of the DMD is smaller than the resolution of the imaging system. Flipping only a part of the mirrors thus results in grayscale values of the imprinted potential, allowing to create potential gradients. Potentials featuring small structures can be used as an easy way to adjust the focus of the upper and lower microscope objectives on the atomic plane.

While DMDs provide the advantage of arbitrary potential shapes[13], they have two main disadvantages. Firstly, the entire area of the DMD chip has to be illuminated, even if most of the light is not reflected onto the atomic plane but into unused reflection orders. Since the entire mirror plane is imaged onto the atomic plane, the walls of the system

[12] Texas Instruments DLP LightCrafter 6500

[13] ...and ease of use for that matter, one can for instance create potential shapes in Microsoft Paint...

also correspond to only a few of the illuminated DMD pixels. These two reasons limit the efficiency of a DMD, such that relatively high powers are necessary to confine quite dilute gases of atoms, especially in the fermionic regime, where the chemical potential of the gas is high. Secondly, dynamic potentials are difficult to realize using a DMD. The repetition rate of our DMDs is 105 µs, a timescale that corresponds to the timescale set by the Fermi energy of the gas. In addition, updating an image on the DMD leads to a short flicker of the entire image of the order of a µs, which can lead to heating of the cloud. Due to these two reasons, the DMDs can only be used in a static way.

The third source of horizontal potentials remedies one of these two disadvantages. An optical cascade setup [60, 135] of three conical lenses (axicons) can be used instead of one of the DMDs to split a laser beam along its axis, creating a circular ring of light with steep inner walls and variable diameter. For this setup, the entire laser power remains in the potential walls confining the atoms, which enables the creation of much higher walls with relative ease. The axicon setup was used for the measurements of section 7.4.

5.3. Total performance

To conclude the presentation of the existing experimental setup, let us look at the experimental sequence in closer detail and the typical performance of the experiment. The typical cycle is depicted once more in Figure 5.11.

The machine creates an ultracold two-dimensional gas about every 15 s. Starting from a hot block of lithium in the oven, the atoms are first decelerated in the Zeeman slower and are trapped in the magneto-optical trap. The MOT is loaded in 5 s and holds a typical number of approximately 6×10^7 atoms at a temperature of $\sim 140\,\mu$K, limited by photon absorption and reemission processes. Once the MOT is loaded, the Zeeman slower is switched off, in order not to disturb the ensuing optical cooling process. In order to load the atoms from the MOT into the resonator, the MOT is compressed by reducing the detunings of the MOT cooler and repumper as well as their intensities. At the same time, the magnetic gradient is increased and the offset fields are changed such that the MOT is moved towards the loading position of the resonator, a few cm off-waist of the bowtie cavity to optimize overlap between the MOT and the resonator. This process takes about 250 ms.

At the new position, the MOT beams are switched off, while the power of the beams seeding the resonator are stabilized to 1 W. The atoms are now trapped in a resonator-enhanced infrared standing wave, entering the evaporative cooling stages of the experiment. The particles are transferred to the waist of the resonator by detuning one resonator arm with respect to the other, creating a moving standing wave. The MOT coils are switched from anti-Helmholtz to Helmholtz configuration and a magnetic bias field of 300 G is applied to increase the collision rate of the atoms and to increase the thermalization efficiency during

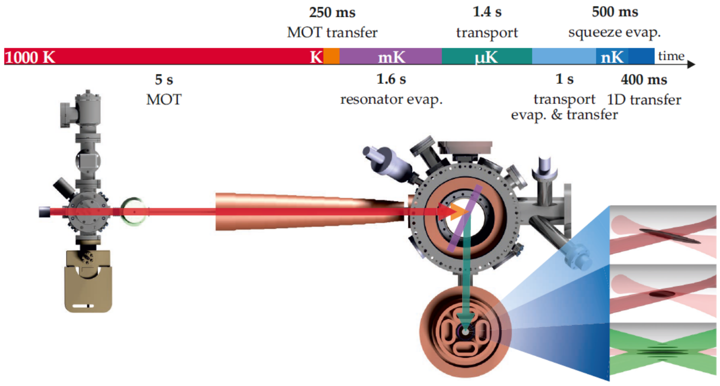

Figure 5.11. – Summary of the experimental procedure for the preparation of a 2D Fermi gas (adapted from [134]). (Red arrow) The atomic beam exits the oven and is decelerated in the Zeeman slower. The atoms are trapped in a MOT which is loaded in about 5s. After saturation of the atom number, the MOT is shifted to the resonator loading position and the atoms are transfered into a deep standing wave potential inside an in-vacuo resonator (purple). A first evaporative cooling step takes place and the atoms are subsequently loaded into a running wave optical dipole trap. Over 1.4 s, the focus of this trap is moved forward (green arrow) and the atoms are transported into the science cell. Here, the gas is loaded into the highly elliptic squeeze trap (inset pic. 1,2), which flattens the cloud to a vertical size of $\sim 1\,\mu\text{m}$. Finally the gas is loaded into the repulsive optical lattice (inset pic. 3), which confines the gas to the quasi-2D regime.

evaporation. The power of the resonator is ramped down to a final value of about 10 mW in a first evaporation step. The entire resonator evaporation takes additional 1.6 s, after which the evaporated resonator holds a typical $\sim 10^6$ atoms.

At the end stage of the resonator evaporation, one of the two resonator arms is entirely switched off, which changes the trap from a standing wave to a running wave dipole trap. Simultaneously, the transport trap is ramped up. To prepare the atoms for the transport into the science cell, a second evaporative cooling step is carried out followed by a recompression of the transport trap. In 1.4 s, the translation stage moves the trap's focusing lens over a distance of 350 mm, thereby transporting about $3 \cdot 10^5$ atoms into the science cell.

Upon arrival in the science cell, the Feshbach coils are switched on to produce a magnetic field close to the Feshbach resonance between the two lowest lying hyperfine states $|F, m_F = 1/2, \pm 1/2\rangle$ at 832 G. A series of RF-sweeps balances the population of these two states in order to maximize thermalization efficiency. The transport trap is then ramped down to 100 mW in 500 ms and the squeeze trap is ramped on to a power of ~ 300 mW before the transport trap is finally switched off. In the squeeze, a final evaporation takes place determining the number and the temperature of the atoms at the beginning of the experimental steps. At this point, the gas is typically deeply degenerate with temperature of $T/T_\text{F} \sim 0.03$.

Now, the squeeze trap is adiabatically ramped back up to powers of the order of 1 W to flatten the gas and to prepare it for loading into the optical lattice. The horizontally confining potentials are switched on and atoms remaining trapped outside of the potential walls can be removed if necessary by a pulse of repulsive light by one of the DMDs. Then the lattice is switched on, transferring the gas into the quasi-2D regime in another 400 ms. Finally the squeeze trap is switched off adiabatically and the preparation of the sample is finished. Typical atom numbers are on the order of low 1000 for the experiments presented in this thesis. Then, the experimental steps are performed and the gas is finally imaged in another few milliseconds.

As previously mentioned, the machine is very robust up to the arrival in the science cell. Even after power cuts, it has often been sufficient to restart the continuously running sequence and let the room thermalize in order to recover good performance up to the loading of the squeeze. Most adjustments had to be made in the setup around the science cell, most notably refocusing the imaging setup and properly overlapping the transport trap, squeeze and lattice potentials. Even then, thanks to the automatic feedback on single layer loading, at top performance, manual corrections were only necessary on the order of once per week.

5.4. An updated optical setup for the generation of 2D potentials

After having introduced the experimental setup and the sequence followed to produce a quasi-two-dimensional Fermi gas in the lab, I would like to give a short description of an upgrade to the optical setup around the science cell, which was initially supposed to be installed in late spring 2020. This upgrade is primarily aimed at improving the day-to-day usability of the optical setup while still maintaining a good utilization of the limited space around the science cell. This section is mostly meant as a documentation of the setup and is not relevant to the results discussed in the remainder of this thesis. A reader primarily interested in the experiments performed on the setup described above may therefore skip this section and continue with chapter 6.

In the current setup around the science cell, the optical elements needed for the horizontal trapping potentials and for the high-resolution imaging are located above and below the atomic plane. However, a large number of optical elements have to be arranged in-plane around the science cell. These are the optics and cameras for the auxiliary imaging setups, the optics for the squeeze trap and the 2D-lattice and the quadrant photodiode for the transport trap. The main constraint to this part of the setup is given by the limited amount of available space around the science cell. In order to approach optical elements close to the cell, a special setup had been realized on a thin non-magnetic breadboard, which could be pushed in between the coil ensembles above and below the cell. Due to the proximity and large size of the coils, the use of standard-sized optical components was rendered impossible and many of the mechanical mounts had to be custom-built. An impression of the

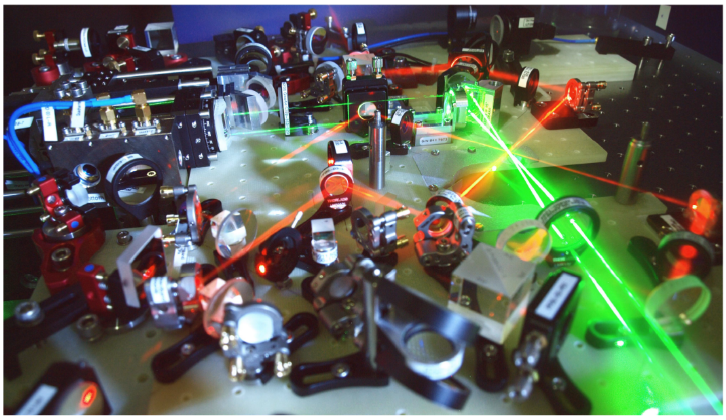

Figure 5.12. – Impression of the existing 2D breadboard before insertion into the experiment (image from [134]). The atoms are located at the intersection point of the laser beams, which have been made visible using dry ice. In the foreground, one can very well see the high density and small size of the optical elements used for this setup.

currently installed 2D-breadboard is shown in Figure 5.12. To improve the stability of the setup, a minimum of movable parts has been used. While this setup uses the available space to its maximum capacity it also comes with some limitations: The thinness of the breadboard limits the rigidity of the entire setup and the omission of some not strictly necessary adjustment possibilities makes day-to-day adjustments rather cumbersome and time-consuming. Over the course of time, some of the piezo mechanics on the breadboard have irreversibly broken, which makes a number of necessary degrees of freedom inaccessible. Therefore, an update to the experiment has become desirable.

For the new setup around the science cell, a new coil setup and new breadboards have been planned and manufactured by Lennart Sobirey and Bernd Lienau. The key idea was to design smaller coil assemblies (with a diameter $d < 170\,\mathrm{mm}$) that allow us to place a breadboard close to the science cell at a level of 60 mm below the atomic plane and thus use standard optics up to a distance of 100 mm from the atoms. If it should become necessary to place optics even closer to the cell, the distance of $> 50\,\mathrm{mm}$ between the coil assemblies permits the use of standard 1" optics in lens tubes. This eliminates the need to slide a thin breadboard in between the coil assemblies. My part in this new setup consisted in planning and testing the optical setup for the generation of 2D potentials, i.e. for the new squeeze trap and lattice potentials, as well as a new auxiliary imaging setup, which I will now discuss in more detail.

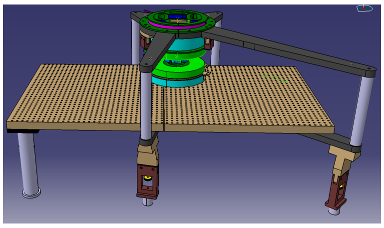

Figure 5.13. – CAD drawing of the new 2D breadboard and the coil setup. The breadboard is placed around the lower coil ensemble, at a level of 60 mm below the atomic plane, allowing to place optics on standard mounts close to the science cell up to a distance of 100 mm to the atoms. The breadboard is produced in two halves of approximately 400mm by 400 mm by 20 mm and can be slid out of the ensemble easily.

5.4.1. Constraints and requirements

Figure 5.13 shows the design of the new coils and the new breadboards. The breadboards have an area of roughly 400 mm by 400 mm each and a thickness of 20 mm, with a circular cutout of radius $r = 87\,\mathrm{mm}$. The breadboards are placed around the lower coil ensemble and are designed in two halves to enable sliding them out around the coil holders in order to easily modify the setup in later stages. The projected beam height above the breadboard is 60 mm. The requirements for the new setup are:

- The trapping frequencies of the squeeze trap and the horizontal frequencies of the lattice should come as close as possible to the values of the previous setup, since the performance was very good in the past. The vertical lattice frequency can be increased to allow for higher chemical potentials in the BCS-regime without populating higher motional states. For the squeeze trap, the trapping frequencies are determined by the beam waists, which were $w_y \approx 380\,\mu\text{m}$ and $w_z \approx 8\,\mu\text{m}$. In case of the lattice potential, they are also given by the beam waists $w_y \approx 370\,\mu\text{m}$ and $w_z \approx 35\,\mu\text{m}$, however the trapping frequency in the vertical direction is mostly determined by the intersection angle which was $10.4\,^\circ$ (full angle between the beams).

- In order to keep the interference pattern of the lattice beams as stable as possible, the separation of the lattice beam into two paths should be done as late as possible in the setup. After the separation, the beams must follow a symmetric path and cross as few different optical elements as possible such that the optical path difference between the two beams is weakly affected by mechanical or thermal fluctuations in the system.

- As few parts as possible should be movable, however the new setup should decouple the degrees of freedom of the traps to allow for independent adjusting.

- The setup should be as small as reasonably possible to save place on the breadboard for future additions. For the same reason, the beams for the squeeze, the lattice and auxiliary imaging should enter the science cell through the same viewport, at 90° with respect to the transport axis. The transport featuring the power and position stabilization for the transport trap as well as another auxiliary imaging, this leaves the four diagonal viewports free for future upgrades.

- The magnification for the x-imaging should be at least a factor of 5 in order to resolve the vertical extent of the squeeze trap. The imaging beam should be roughly collimated at the location of the atoms at a waist of about 1 mm, however this requirement is not crucial since this imaging has an auxiliary role.

- Catalog optics should be used for now. The final lens may be replaced later by a specially designed achromatic multiplet working at the three most important wavelengths (532 nm, 671 nm and 1064 nm).

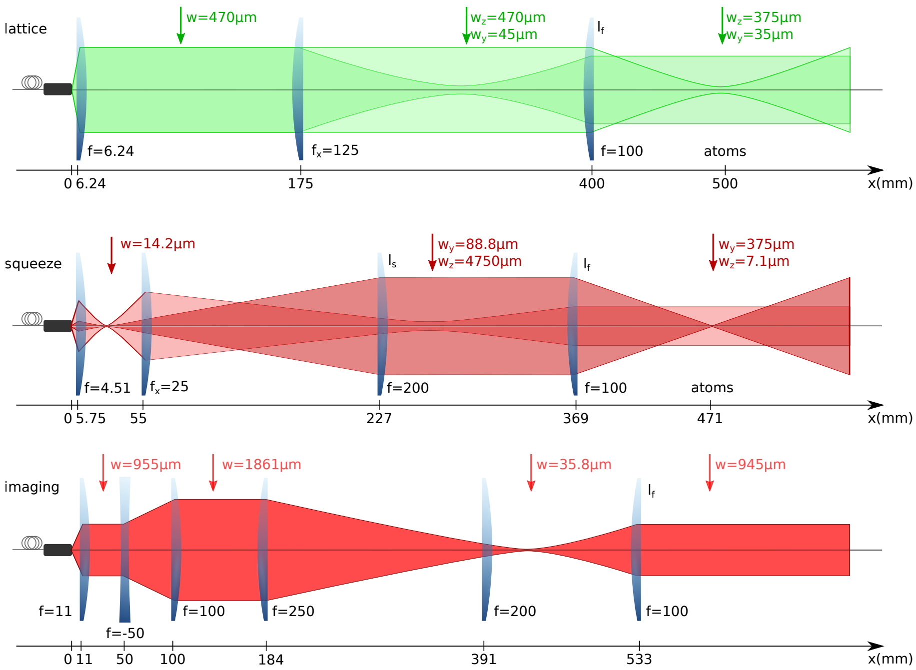

Figure 5.14. – Parameters of the optical setups on the new breadboard. The lattice beam is split into the two paths after the first collimating lens, which is not shown here. The second lens in the lattice and squeeze setups are cylindrical lenses, creating the elliptic beam profiles. The imaging and squeeze are overlapped on a back-polished mirror and share the two final lenses. The two beams are then overlapped with the lattice beams on a dichroic mirror. All beams share the same final high precision doublet lens f_l (Melles Griot LAI-100.0-30.0). The beam waists and distances of the three diagrams are not drawn to the same scale. For the squeeze schematics, the scale vertical beam axis is reduced by a factor 5 with respect to the horizontal axis to draw them in the same diagram.

5.4.2. Realization

The final optical setups and the resulting beam parameters are depicted in Fig. 5.14. Since the three beams are supposed to enter the cell through the same viewport, they have to pass the same final lens. We chose a high-precision doublet lens (LAI-100.0-30.0) with a focal length of $f = 100\,\mathrm{mm}$ and a diameter of 30 mm. This lens is optimized to compensate spherical aberration but uncorrected for chromatic aberration, which requires a slight compensation of the focal shift between the squeeze and lattice beams. It is placed on top of a non-magnetic titanium translation stage with a travel range of 3 mm.

Lattice

To create the lattice beams we start from a beam that is collimated by a standard aspheric lens[14] after the fiber outcoupler. The different beam waists of the lattice beams are created by a cylindrical lens[15] which focuses the beams along the horizontal direction, while keeping the vertical direction collimated. The cylindrical lens is placed in telescope configuration with the final lens, creating beams that are horizontally collimated but which exhibit a focus in the vertical axis at the location

---

[14] Thorlabs C110TMD-A

[15] Thorlabs LJ1640L1-A

of the atoms.

In order to split the lattice beam into the two paths, a lens-free beam splitter setup (see fig. 5.15 for an impression) can be used anywhere in the collimated part of the beam in front of the cylindrical lens. The optics for splitting the lattice beam into the two paths consist of four mirrors and a polarizing beam splitter which are mounted vertically inside a metal enclosure of dimensions 90 mm × 90 mm × 120 mm that can be clamped onto the breadboard. The top and bottom plates of the enclosure can be exchanged, such that the beam splitter can be used in a right-handed or left-handed configuration (i.e. exiting beams to the right/left with respect to the incoming beam). The mounting plate of the enclosure has been dimensioned with a thickness of 20 mm as to reduce mechanical motion and thermal drifts. The first two mirror mounts are immovable, whereas small holes behind the final mirror mounts give access to their adjustment screws, enabling control of each of the lattice beams independently. After the beam splitting setup, the two beams pass the same optical elements up to a $\lambda/2$-waveplate which aligns the two polarizations for interference. After exiting the beam splitter, the two beams have a distance to each other of 21.9 mm, which results in an angle of incidence of 12.5 ° between the two beams and yields a lattice constant of $\approx 2.4\,\mu$m. The measured waists are $w_y = 375\,\mu\text{m}$ and $w_z = 37\,\mu\text{m}$.

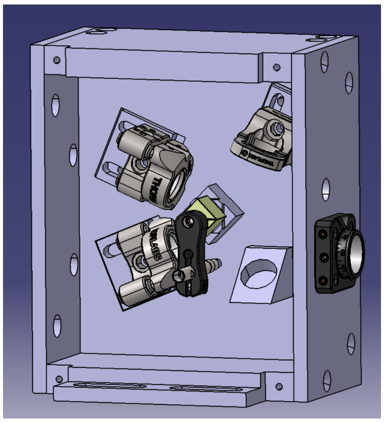

Figure 5.15. – Open view of the beam splitter optics. The beam enters the box through the front wall (not shown) and is reflected up and then downward using two fixed mirrors into the polarizing beam splitter (yellow). The two resulting beams are reflected out of the right hand side of the box via two mirrors, which can be adjusted via holes in the back plate of the box. The lower beam passes a wave plate which rotates its polarization to match the polarization of the other beam. After the wave plate the remaining optical path length is the same for both beams.

For day-to-day use, the focus position is adjusted using the translation stage of the final focusing lens (lattice focus along the beam axis) and a non-magnetic piezo-driven mirror mount in front of the dichroic mirror (focus correction in vertical/transport axis). Since the beam is collimated in the horizontal direction, it is not crucial to have adjustability on the micrometer level for the cylindrical lens, which is therefore fixed on the breadboard. The vertical size of the waist can be corrected using the collimation lens behind the fiber, which is placed in a one-axis translation mount. If the two beams misalign with respect to each other, the mirror mounts inside the beam splitter can be adjusted.

Squeeze

In the case of the squeeze trap, the strong ellipticity of the desired beam profile ($8\,\mu\text{m} : 350\,\mu\text{m}$) did not allow us to create a design starting with a collimated beam while maintaining a short optical path. Instead, we moved the collimation lens[16] out of focus to create a strongly converging beam in which the cylindrical lens[17] is placed. This creates two different divergence rates for the different axis. The placement of the cylindrical lens is such that the beam is horizontally collimated after the final lens. Vertically, the squeeze beam is collimated by an $f = 200$ mm achromatic doublet[18] at a beam waist of 4.75 mm before being focused by the final lens. The horizontal convergence of the beam is only weakly affected by this $f = 200$ mm lens. The squeeze beam is superimposed with the lattice beams on a dichroic mirror[19], placed in front of the focusing lens. This dichroic mirror transmits the infrared squeeze beam but reflects the lattice beams. This configuration reduces the number of boundary

[16] Thorlabs C230TME-1064

[17] Thorlabs LJ1810L1-B

[18] Thorlabs AC254-200-B

[19] Laser Components 1.5”, Coating: HR532HT1064/45/AR

layers that could incur unwanted phase errors between the two lattice beams.

With this setup, waists of $\omega_y = 370\,\mu\text{m}$ and $\omega_z = 7.1\,\mu\text{m}$ have been achieved. While it ensures a short optical path of only 471 mm, it has the disadvantage that the lenses are not decoupled from each other. Since the horizontal axis is never collimated in front of the final lens, the positions of the lenses are fixed with respect to each other. Adjusting this setup is therefore still an iterative process. The fact that the lattice and squeeze setup share the movable focusing lens also couples the adjustment process of the two setups. By placing the second-to-last lens of the squeeze onto a translation stage, however we are now able to compensate for changes in the position of the focusing lens.

In day-to-day work, the second-to-last lens can be used to shift the focus point along the beam axis (also after the lattice focus is moved). The vertical and horizontal focus point can be adjusted using a non-magnetic piezo mirror in front of the dichroic mirror and the outcoupling lens can be used to correct the waist sizes.

Imaging

The third beam which is supposed to be part of this setup is the imaging beam at 671 nm, in plane with the atoms and perpendicular to the transport axis. This imaging is planned to be a diagnostic imaging, for which it is not necessary to follow standards as high as for the other two setups. The basic requirements for the imaging beam have been that it should be roughly collimated at the location of the atoms, with a waist of about 1 mm.

The imaging is overlapped with the squeeze beam on a back-polished mirror mirror that is transparent at visible wavelengths but reflects infrared light. The two beams then pass the same two final lenses. In order to meet the required waist, the beam is first collimated and widened with a telescope. A suitable focusing lens has then been inserted at a position such that it approximately produces a telescope with the final lens. The second-to-last lens has little effect on the divergence of the beam.

A final waist of 945 µm has been achieved. Behind the science cell, a telescope of two lenses with focal lengths of 80 mm and 400 mm images the atomic cloud or the optical lattice under a magnification of about 5.

A picture drawing of the complete setup is shown in Figure 5.16.

Outlook

In conclusion, the optical potentials created on the new 2D breadboard setup reproduce the geometrical parameters of the old setup and should in principle allow us to generate two-dimensional Fermi gases with a similar performance, but improved stability and more adjustment possibilities. The upgrade of the machine was originally planned for late spring 2020, however, due to COVID-19 restrictions, the integration of the new coil assembly and the new breadboard into the experiment has been postponed for the moment.

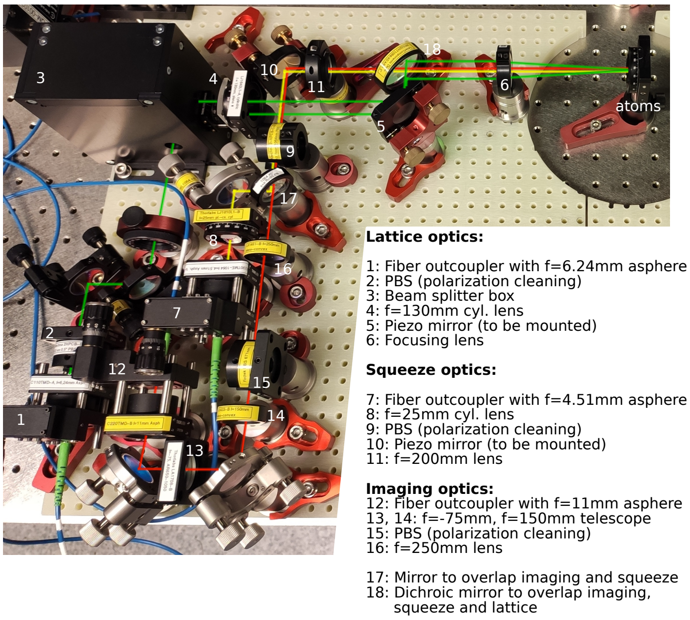

Figure 5.16. – Photograph of the new 2D breadboard during the building process, including the beam shaping optics. The three setups have been placed on the far left corner of the breadboard to leave as much space as possible for eventual upgrades. The beams are inserted into the picture using Inkscape: Green: Lattice, Red: Imaging, Yellow: Squeeze.

In addition to the parts that have already been built on the new breadboard, our group is pursuing two projects for the future. We are currently setting up a new way of producing two-dimensional gases using an optical accordeon. Shooting a beam into a 50/50-beamsplitter cube parallel to its symmetry axis, we can split the beam into two parallel beams that can then be overlapped to build an optical lattice. By changing the distance between the symmetry plane and the incoming beam, the distance between the outgoing beams can be tuned continuously, which allows to change the angle between the interfering lattice beams and thus the lattice constant. This may offer a new and more flexible way to load the atoms from the squeeze into a true 2D geometry.

6. Sound Propagation and Attenuation in 2D Fermi Gases

In this chapter I first give an introduction to hydrodynamic theory and sound waves both in a normal fluid and within Landau's two-fluid model.
I then present measurements of sound propagation in a homogeneous quasi-two-dimensional Fermi gas. We measure the sound velocity and show that it smoothly transitions from the velocity of a weakly interacting Bose gas in the BEC regime to the velocity of the Bogoliubov-Anderson mode in the BCS regime. We extract the compressibility equation of state of the material and compare it to an independent static measurement as well as to quantum Monte-Carlo predictions, finding good agreement between the three.
Finally, we measure the damping of the sound mode. This allows us to extract the sound diffusivity of the ultracold gas across the entire crossover. We show that it approaches a lower bound of order $D \sim \hbar/m$ in the strongly correlated regime, a value compatible with quantum-limited transport. The strongly correlated 2D Fermi gas is therefore a nearly perfect fluid.
These results are published in

> Markus Bohlen, Lennart Sobirey, Niclas Luick, Hauke Biss, Tilman Enss, Thomas Lompe and Henning Moritz. Sound Propagation and Quantum-Limited Damping in a Two-Dimensional Fermi Gas. *Phys. Rev. Lett.* **124**, 240403 (2020).

and parts of this chapter are reproduced from this publication with modifications.
The findings presented in this chapter represent the main result of this thesis.

We have seen that the character of an ultracold Fermi gas can be tuned to access drastically different regimes, ranging from a weakly interacting bosonic gas of dimers across a strongly correlated gas to a weakly interacting fermionic ensemble. While the BEC and BCS regimes are theoretically well understood, the description of the strongly correlated gas remains challenging. Nevertheless, this regime is of particular interest, since strongly correlated systems appear in many different areas of physics, covering radically different objects such as neutron stars, atomic nuclei, high-temperature superconductors and ultracold atomic gases. A powerful experimental method to gain access to the thermodynamic and transport properties of these systems is to study their collective excitations, such as sound modes.

In this chapter, I present measurements of sound propagation and attenuation in an ultracold 2D Fermi gas across the BEC-BCS crossover. The sound velocity of the gas transitions smoothly from the sound velocity obtained for a weakly interacting Bose fluid in the BEC regime to the velocity of the Bogoliubov-Anderson mode in the BCS regime. The attenuation of the sound mode, however, exhibits a clear minimum in the strongly correlated regime, where the particles are most strongly interacting. At first glance, the minimum of attenuation in the strongly correlated regime seems counter-intuitive. For strong interactions and high collision rates between the particles, one would naïvely expect increased sound damping with respect to the weakly interacting limit. However, this is not the case for sound waves, as we shall motivate with the following arguments.

6.1. Collisionless and hydrodynamic regimes

The character of the excitations depends on the strength of interactions between the particles in the gas. There are two limits to be distinguished, the collisionless regime for weak interactions and the hydrodynamic regime in the case of strong interactions. In the collisionless regime, the particles of the gas can be assumed to interact instantaneously and move ballistically in between the collisions. Even in strongly interacting systems, it is often possible to describe the system in terms of weakly interacting quasiparticles or elementary excitations. The typical example for this is the Landau Fermi liquid [145], which provides a good description of most normal metals at low temperatures as well as liquid Helium 3 [146]. The Landau Fermi liquid is obtained from a non-interacting Fermi gas by switching on the interactions between the particles adiabatically slowly. In this case, the ground state of the non-interacting system smoothly evolves into the new ground state of the interacting system. There also exists a one-to-one correspondence between the elementary excitations of the non-interacting Fermi gas (adding/removing a particle) and the interacting gas (adding/removing a 'quasiparticle'), although the true nature of the excitations might be very different from adding or removing a particle. The dynamics of the gas in the collisionless regime is described by kinetic theory, in particular by the Boltzmann equation, which is a continuity equation for the so-called quasiparticle distribution function, describing the likelihood for the occupation of quasiparticle states.

For strongly correlated systems, the quasiparticle description can break down. In this case, a hydrodynamic description of the system is appropriate[1]. Hydrodynamics is based on the assumption that the interactions between the particles happen on very short time scales, such that the particles are in local equilibrium with the surrounding gas at all times. For several conserved quantities, such as density, momentum and energy, one can set up continuity equations, which govern the dynamics

[1] We note that the hydrodynamic equations can also be derived from the moments of the Boltzmann equation. See for instance [147]

of the gas. These equations have the form $\dot{Q} = -\boldsymbol{\nabla} \cdot \mathbf{j}_Q$, where Q is the thermodynamic quantity and $\mathbf{j}_Q$ the current density related to this quantity. Since the system is supposed to be in local equilibrium, excitations appear in the form of large-range variations in the thermodynamic variables. These variations lead to diffusive currents, to first order described by $\mathbf{j}_Q = -D_Q \boldsymbol{\nabla} Q$, which tend to smoothen out the initial variations. One can see this by inserting $\mathbf{j}_Q$ into the continuity equation, which yields $\dot{Q} = D_Q \Delta Q$, which is a diffusion equation for the quantity Q. The coefficient D_Q is called the diffusion coefficient.

Q :	Thermodynamic quantity
$\mathbf{j}_Q$:	Current density related to Q
D_Q :	Diffusion coefficient for diffusion of quantity Q.

As we will derive in the following sections, the damping of collective modes such as sound waves depends on the transport coefficients of the gas, notably on its viscosity and heat conductivity. These coefficients describe how well a certain quantity (momentum and temperature in this case) can be transported through the material, and can be shown to be proportional to the diffusivity in the respective attenuation channel. We can now motivate the minimum in sound damping in the strongly correlated regime.

According to kinetic theory, the transport coefficients and thus the damping of collective modes are proportional to the quasiparticle lifetimes[2]. In other words, the diffusion coefficient is related to the mean free path of the (quasi-)particles and their mean velocity according to $D \sim \langle v \rangle \, l_{\mathrm{mfp}}$. Strong interactions between the (quasi-)particles lead to short quasiparticle lifetimes or short mean free paths, and the energy contained in an excitation cannot be transported away effectively. Thus, we obtain weak sound damping for stronger interactions. Since the mean free path cannot be smaller than the interparticle spacing, this sets a lower limit to the diffusivity of the strongly correlated gas.

$\langle v \rangle$:	Mean particle velocity
l_{mfp} :	Mean free path

Applicability of Hydrodynamics

Classically, hydrodynamics apply, when the system shows fast local equilibration times τ and short mean free paths l_{mfp} compared to the frequency ω and wavenumber k of the excitation: $\omega\tau \ll 1, k l_{\mathrm{mfp}} \ll 1$. However, as we will see in the next section, the concept of mean free path is in fact not needed to derive the equations of hydrodynamics. If we assume the particles to be in constant contact and equilibrium with their surroundings, the mean free path is in fact always zero. In this case, hydrodynamics is derived purely as a macroscopic theory describing long-range dynamics and low-energy excitations of the gas. The transport and diffusion coefficients appear in the hydrodynamic equations only in the form of proportionality factors whose values cannot be derived from within using hydrodynamic principles, but must be obtained using other theories. In linear response theory for instance, the transport coefficients are connected to correlation functions via the Kubo formulas. These correlation functions can in turn be calculated from field theoretical methods, which can become very cumbersome in the case of strong interactions. Often, an easier way to obtain the values of the transport coefficients in specific materials is to extract them experimentally.

[2] See for instance the respective calculations for gases or electron gases in [148].

Around the Feshbach resonance, the enhanced collision rates ensure in our case that the gas can be described using hydrodynamics[3]. The condition of short collision times is however not the only condition which ensures hydrodynamic conditions. A degenerate Bose gas for instance is only weakly interacting, however hydrodynamic equations can be derived from the Gross-Pitaevskii equation (see for instance chapter 7 in [85]). Similarly to the classical case, hydrodynamics apply when the wavelength of the excitations is large compared to the length scale on which the gas equilibrates with its surroundings. In a degenerate Bose gas, this scale is given by the healing length ξ.

6.2. Hydrodynamics and the theory of sound waves

In the following sections, I will review the theory of sound waves in the hydrodynamic framework. I will start out by establishing the equations of motion following Landau and Lifshitz [149]. In a second step, I will follow the approach of Smith and Jensen [148] to solve these equations for a classical gas and for a superfluid and obtain the low-energy excitations of the gas. As we will see, these excitations have a dispersion relation of the form $\omega^2 = c^2 q^2 + i\omega D_s q^2$, where q and ω are the wave number and frequency of the excitation, c is the adiabatic sound velocity and D_s the sound diffusivity. The real part is linear in momentum and describes sound waves, whose velocity c is related to the compressibility of the medium. Hence a measurement of the sound velocity gives us access to its equation of state. The imaginary part corresponds to diffusive damping, which occurs due to viscous flow and thermal conduction.

ω : Excitation frequency
q : Excitation momentum
c : (Adiabatic) sound velocity
D_s : Sound diffusivity

6.2.1. The hydrodynamic equations

Sound waves in a gas consist of simultaneous spatial variations in several thermodynamic quantities, namely the pressure p, temperature T, mass density ϱ, entropy density s and the local particle velocity $\mathbf{v}$. As mentioned earlier, the equations of hydrodynamics follow from the conservation of particle density, momentum and energy, providing us with three equations relating the five unknown quantities.

p : Pressure
T : Temperature
ϱ : Mass density
$\mathbf{v}$: Particle velocity
s : Entropy density per unit mass: $s = S/Nm$

The continuity equation describes the conservation of particles.

$$\frac{\partial \varrho}{\partial t} + \boldsymbol{\nabla} \cdot (\varrho \mathbf{v}) = 0, \tag{6.1}$$

The momentum balance equation describes the change in momentum of a mass particle of the gas. It is given in component notation by

$$\frac{\partial (\varrho v_i)}{\partial t} + \frac{\partial \Pi_{ik}}{\partial x_k} = 0, \tag{6.2}$$

where Π_{ik} is the momentum current tensor, which will be explained in more detail later on. In this chapter, we will use Einstein's sum convention: Any index $i, j, k \ldots$ runs from 1 to 3 enumerating the x, y, z-directions and repeated indices are to be summed over.

Π_{ik} : Momentum current tensor

[3] We will give a quantitative estimation of the mean free path later.

The third equation we will derive in this part of the text is the heat or entropy equation, which follows from the conservation of energy. It is

$$\varrho T \frac{ds}{dt} = \sigma'_{ik} \frac{\partial v_i}{\partial x_k} + \boldsymbol{\nabla} \cdot (\varkappa \boldsymbol{\nabla} T) \,. \tag{6.3}$$

Here, σ'_{ik} the viscous part of the stress tensor and $\varkappa$ the thermal conductivity. The viscous stress tensor σ'_{ik} and the thermal conductivity $\varkappa$ describe dissipative processes as terms in which velocity or temperature gradients are transformed irreversibly into thermal energy due to friction or heat conduction. If we neglect these processes, we see that the entropy in the system is conserved and we recover adiabatic conditions.

σ'_{ik} : Viscous stress tensor
$\varkappa$: Thermal conductivity

For the derivations of all three equations, we follow the steps detailed in [149]. We will start by reviewing the quite short derivation of the first of the continuity equation.

The continuity equation

The change in mass inside a given volume is given by the density current that flows through the boundaries of this volume:

$$\frac{\partial M}{\partial t} = -\frac{\partial}{\partial t} \int \varrho \, dV = \oint \varrho \mathbf{v} \cdot d\mathbf{a}, \tag{6.4}$$

where M is the total mass inside the volume and $d\mathbf{a}$ the oriented area element of the boundary of the volume. Using the divergence theorem, this equation can be transformed into

V : Volume
M : Total mass inside V
$d\mathbf{a}$: Surface element bounding V

$$\int \left[\frac{\partial \varrho}{\partial t} + \boldsymbol{\nabla} \cdot (\varrho \mathbf{v}) \right] dV = 0. \tag{6.5}$$

Since mass conservation has to hold true for any arbitrary volume of the fluid, the integrand itself must be zero, which leaves us with the continuity equation 6.1. This reasoning is valid not only for mass but for any quantity that is conserved in the system. In particular, we will later make use of the conservation of entropy, which yields

$$\frac{\partial s}{\partial t} + \boldsymbol{\nabla} \cdot (\mathbf{v} s) = 0. \tag{6.6}$$

Euler's equation

In order to derive the momentum balance equation, we first have to introduce Euler's equation, which is the hydrodynamic analogue of Newton's second law. Neglecting gravity, the force acting on the fluid is given by the gradient of the pressure p:

$$\varrho \frac{d\mathbf{v}}{dt} = -\boldsymbol{\nabla} p. \tag{6.7}$$

The total or substantial derivative

$$\frac{d\mathbf{v}}{dt} = \frac{\partial \mathbf{v}}{\partial t} + \frac{\partial x_i}{\partial t} \frac{\partial \mathbf{v}}{\partial x_i} = \frac{\partial \mathbf{v}}{\partial t} + (\mathbf{v} \cdot \boldsymbol{\nabla}) \mathbf{v}, \tag{6.8}$$

expresses the fact that the velocity of a particle can change over time in one given point ($\partial\mathbf{v}/\partial t$), but also due to the movement of the particle with the flow of the fluid, which carries it into regions with higher or lower velocity, expressed by the term $(\mathbf{v}\cdot\boldsymbol{\nabla})\mathbf{v}$. Euler's equation is thus

$$\frac{\partial\mathbf{v}}{\partial t}+(\mathbf{v}\cdot\boldsymbol{\nabla})\,\mathbf{v}=-\frac{1}{\varrho}\boldsymbol{\nabla}p. \tag{6.9}$$

The momentum balance equation

We now want to derive an expression for the change of momentum in a small volume dV. The momentum change in a given time interval is given by $\partial(\varrho\mathbf{v})/\partial t$. For the i-th component, this yields

$$\frac{\partial}{\partial t}(\varrho v_i)=\frac{\partial\varrho}{\partial t}v_i+\varrho\frac{\partial v_i}{\partial t}, \tag{6.10}$$

which is transformed using the continuity and Euler equations:

$$6.1\rightarrow\frac{\partial\varrho}{\partial t}=-\frac{\partial(\varrho v_k)}{\partial x_k}, \tag{6.11}$$

$$6.9\rightarrow\frac{\partial v_i}{\partial t}=-v_k\frac{\partial v_i}{\partial x_k}-\frac{1}{\varrho}\frac{\partial p}{\partial x_i}. \tag{6.12}$$

And thus

$$\begin{aligned}\frac{\partial}{\partial t}(\varrho v_i)&=-v_i\frac{\partial}{\partial x_k}(\varrho v_k)-\varrho v_k\frac{\partial v_i}{\partial x_k}-\frac{\partial p}{\partial x_i}\\&=-\frac{\partial}{\partial x_k}(\varrho v_i v_k)-\frac{\partial p}{\partial x_i}=-\frac{\partial\Pi_{ik}}{\partial x_k},\end{aligned} \tag{6.13}$$

where the momentum current tensor Π_{ik} is defined as $\Pi_{ik}:=p\delta_{ik}+\varrho v_i v_k$.

This equation has the form of a continuity equation. On the left side, we see the i-th component of the momentum. Its change in time is determined by the sum of the derivatives of three components of Π_{ik}. Π_{ik} can therefore be interpreted as the flow of the i-th component of the momentum through a surface perpendicular to the x_k-axis per unit time. A vector quantity is changing in time, and since all three components of the vector can flow away in all three directions, its current density is a tensor of rank two.

To understand the momentum current tensor more deeply, we write the momentum balance equation in its integral form by integrating and using the divergence theorem. Since Π_{ik} is the momentum flowing through a surface perpendicular to the x_k-axis, we obtain

$$\frac{\partial}{\partial t}\int\varrho v_i\,dV=-\oint\Pi_{ik}\,da_k=-\oint\Pi_{ik}n_k\,da, \tag{6.14}$$

where $d\mathbf{a}=\mathbf{n}da$ is the oriented surface element of the boundary of the volume, and $\mathbf{n}$ the unit normal to the surface element. The quantity $\Pi_{ik}n_k=pn_i+\varrho v_i v_k n_k$ can be written in vector form as

$$p\mathbf{n}+\varrho\mathbf{v}(\mathbf{v}\cdot\mathbf{n}). \tag{6.15}$$

This vector is the current of momentum flowing out of the volume in the direction of the unit vector $\mathbf{n}$. In the direction perpendicular to the flow of the fluid ($\mathbf{n} \perp \mathbf{v}$), the momentum current density is given by the pressure. A net pressure difference between two regions will result in a transfer of momentum to the particles of the fluid. In the direction parallel to the flow of the fluid ($\mathbf{n} || \mathbf{v}$), the fluid transfers the additional momentum ϱv^2, given by the kinetic energy density.

$\mathbf{n}$: Unit vector, normal on surface element da

Momentum current density of a viscous fluid

Up until this point, the momentum balance equation incorporates forces and mechanical movement of the particles, thus reversible changes in momentum. In a viscous medium however, energy and momentum are lost irreversibly due to friction. These processes are added manually into Π_{ik} by adding a term $-\sigma'_{ik}$, which incorporates all friction effects. We write

$$\Pi_{ik} = p\delta_{ik} + \varrho v_i v_k - \sigma'_{ik} = -\sigma_{ik} + \varrho v_i v_k. \tag{6.16}$$

The form of the unknown tensor σ'_{ik} is subject to a few constraints. Viscous effects depend only on the relative velocities of different parts of the fluids, therefore σ'_{ik} must depend on the derivatives $\partial v_i / \partial x_k$ of the velocities with respect to the coordinates. Moreover, there also should be no viscous effects when the system performs a uniform rotation $\mathbf{v} = \boldsymbol{\Omega} \times \mathbf{r}$. These two conditions are fulfilled for the symmetric combinations of the partial derivatives

$\boldsymbol{\Omega}$: Angular velocity

$$\frac{\partial v_i}{\partial x_k} + \frac{\partial v_k}{\partial x_i}. \tag{6.17}$$

We assume that the velocities vary slowly in space, such that we can neglect all higher order derivatives as well as quadratic terms in the derivatives. This yields a tensor of the form

$$\sigma'_{ik} = a\left(\frac{\partial v_i}{\partial x_k} + \frac{\partial v_k}{\partial x_i}\right) + b\frac{\partial v_l}{\partial x_l}\delta_{ik}, \tag{6.18}$$

with two constants a and b. Conventionally, this tensor is written in a slightly different form which separates the symmetric tensor σ'_{ik} into a trace free part and a diagonal part:

$$\sigma'_{ik} = \eta\left(\frac{\partial v_i}{\partial x_k} + \frac{\partial v_k}{\partial x_i} - \frac{2}{d}\delta_{ik}\frac{\partial v_l}{\partial x_l}\right) + \zeta\delta_{ik}\frac{\partial v_l}{\partial x_l}, \tag{6.19}$$

where d is the number of spatial dimensions. The diagonal part describes friction effects that occur in the dilation or compression of the fluid, whereas the trace-free part describes shear friction. At this point we see the first occurrence of the transport coefficients ζ and η, which are called the bulk and shear viscosities. They appear as coefficients whose value needs to be determined through measurement or other theoretical methods.

d : Number of dimensions

η : Shear viscosity
ζ : Bulk viscosity

The Navier-Stokes equation

Incorporating the effects of the viscous stress tensor into Euler's equation (eq. 6.9), one obtains the Navier-Stokes equation, which is the equation of motion of a viscous incompressible fluid. One starts out by extending Euler's equation with σ'_{ik}.

$$\varrho\left(\frac{\partial \mathbf{v}}{\partial t} + (\mathbf{v}\cdot\boldsymbol{\nabla})\mathbf{v}\right) = -\boldsymbol{\nabla}p + \frac{\partial \sigma'_{ik}}{\partial x_k}, \tag{6.20}$$

or in component notation and full length:

$$\begin{aligned}\varrho\left(\frac{\partial v_i}{\partial t} + v_k\frac{\partial v_i}{\partial x_k}\right) = -\frac{\partial p}{\partial x_i} &+ \frac{\partial}{\partial x_k}\left[\eta\left(\frac{\partial v_i}{\partial x_k} + \frac{\partial v_k}{\partial x_i} - \frac{2}{d}\delta_{ik}\frac{\partial v_l}{\partial x_l}\right)\right]\\ &+ \frac{\partial}{\partial x_i}\left(\zeta\frac{\partial v_l}{\partial x_l}\right).\end{aligned} \tag{6.21}$$

Taking the viscosities to be constant throughout the system, they can be moved in front of the derivatives. The equation transforms to

$$\varrho\left(\frac{\partial v_i}{\partial t} + v_k\frac{\partial v_i}{\partial x_k}\right) = -\frac{\partial p}{\partial x_i} + \eta\frac{\partial^2 v_i}{\partial x_k^2} + \zeta\frac{\partial}{\partial x_i}\frac{\partial v_l}{\partial x_l} \tag{6.22}$$

in two dimensions ($d = 2$). In an incompressible liquid, $\boldsymbol{\nabla}\cdot\mathbf{v} = 0$, such that the last term vanishes. We are then left with the Navier-Stokes equation, which takes the following form in vector notation:

$$\frac{\partial \mathbf{v}}{\partial t} + (\mathbf{v}\cdot\boldsymbol{\nabla})\mathbf{v} = -\frac{1}{\varrho}\boldsymbol{\nabla}p + \frac{\eta}{\varrho}\Delta\mathbf{v}. \tag{6.23}$$

We see that the bulk viscosity ζ drops out in an incompressible liquid. This is of course to be expected, since the bulk viscosity describes friction when the fluid is compressed or dilated, processes which cannot occur in an incompressible fluid. Interpreting this equation as the continuum form of Newton's second law, we find that the forces acting on a fluid particle in an incompressible viscous fluid are given by the pressure and by a viscous force which tends to equalize the velocities of neighboring particles. The ultracold gases considered in this thesis however are compressible and thus the bulk viscosity stays relevant.

The heat equation

We now tackle the derivation of the heat equation. For this, we need to work a bit more than for the first two equations. First, an expression for the change of energy in a small volume dV can be derived under adiabatic conditions. In a second step, dissipative processes are allowed. This leads to two different equations for the energy change in the system. By comparing the two expressions, we will then see that the heat equation has to hold true. I will not reproduce the entire calculation here, since I find this a rather technical point that does not aid in understanding the physical mechanisms at hand. If the reader is interested, the calculation can be found in Appendix B.

ε : Energy density
w : Enthalpy density (both per unit mass)

The energy density in a small volume is given by the sum of the contributions of kinetic energy $\varrho v^2/2$ and internal energy $\varrho\varepsilon$, where ε is the internal energy per unit mass. Under adiabatic conditions, the change of energy can be written as (see appendix B for the details of the calculation):

$$\frac{\partial}{\partial t}\left(\frac{\varrho v^2}{2}+\varrho\varepsilon\right)=-\boldsymbol{\nabla}\cdot\left[\varrho\mathbf{v}\left(\frac{v^2}{2}+w\right)\right]. \tag{6.24}$$

Here, $w=\varepsilon+p/\varrho$ is the enthalpy density in the system. The energy balance equation has the form of yet another continuity equation. The change in energy in a given volume over time is given by the amount of energy density that flows through the boundaries of this volume. We can identify the quantity $\varrho\mathbf{v}(v^2/2+w)$ with the energy current density. This energy is carried in and out of the volume by a displacement of the fluid.

In a viscous fluid, this is however not the only process which can transport energy. As we have seen, the viscosity of the fluid allows momentum to flow from one location to another if there are momentum gradients in the fluid. This momentum transfer carries an energy $\mathbf{v}\cdot\sigma'=v_i\sigma'_{ik}$. Similarly, gradients of temperature $\boldsymbol{\nabla}T$ allow for heat currents $\mathbf{q}=-\varkappa\boldsymbol{\nabla}T$ to flow through the material, transporting energy in the process. These heat currents are proportional to the thermal conductivity $\varkappa$. Both processes have to be incorporated into the energy balance equation. In analogy to the introduction of the viscous stress tensor into the momentum balance equation, we therefore modify equation 6.24 by hand to read

$$\frac{\partial}{\partial t}\left(\frac{\varrho v^2}{2}+\varrho\varepsilon\right)=-\boldsymbol{\nabla}\cdot\left[\varrho\mathbf{v}\left(\frac{v^2}{2}+w\right)-(\mathbf{v}\cdot\sigma')-\varkappa\boldsymbol{\nabla}T\right]. \tag{6.25}$$

This is the first equation we need for the derivation of the heat equation.

Performing several more steps detailed in appendix B, one can also derive the following equation:

$$\begin{aligned}\frac{\partial}{\partial t}\left(\frac{\varrho v^2}{2}+\varrho\varepsilon\right)=&-\boldsymbol{\nabla}\cdot\left[\varrho\mathbf{v}\left(\frac{v^2}{2}+w\right)-(\mathbf{v}\cdot\sigma')-\varkappa\boldsymbol{\nabla}T\right]\\&+\varrho T\left(\frac{\partial s}{\partial t}+\mathbf{v}\cdot\boldsymbol{\nabla}s\right)-\sigma'_{ik}\frac{\partial v_i}{\partial x_k}-\boldsymbol{\nabla}\cdot(\varkappa\boldsymbol{\nabla}T).\end{aligned} \tag{6.26}$$

By comparing these two equations, it becomes clear that the sum of the last three terms have to equal zero. We are left with the heat equation:

$$\varrho T\left(\frac{\partial s}{\partial t}+\mathbf{v}\cdot\boldsymbol{\nabla}s\right)=\sigma'_{ik}\frac{\partial v_i}{\partial x_k}+\boldsymbol{\nabla}\cdot(\varkappa\boldsymbol{\nabla}T). \tag{6.27}$$

The left hand side of this equation is the total time derivative of the heat density.

$$\varrho T\frac{ds}{dt}=\sigma'_{ik}\frac{\partial v_i}{\partial x_k}+\boldsymbol{\nabla}\cdot(\varkappa\boldsymbol{\nabla}T). \tag{6.28}$$

Under adiabatic conditions, it is equal to zero. Entropy and heat are then conserved in the system, but may flow between different parts of the system. Under the effects of friction and heat conduction, there are additional source terms on the right hand side of the equation, which represent the amount of heat that a unit mass acquires per unit time. Due to friction, kinetic energy can be transformed to heat. Additionally, heat conduction will dissipate temperature differences across the material, thereby increasing entropy.

6.2.2. The dispersion relation of sound waves in a normal fluid

The next step in our discussion of sound waves is to derive the dispersion relation of sound waves, i.e. derive expressions for the speed and the attenuation of sound. I will derive these first in the case of a normal fluid and then show the results that one obtains for a superfluid as well. For this discussion, I follow the approach of Smith and Jensen [148], since I find it to be more concise than the approach detailed by Landau and Lifshitz [149].

ω : Oscillation frequency
$\mathbf{q}$: Oscillation wave vector

We assume that the particles of the fluid are oscillating harmonically with a frequency ω along a certain direction given by a wave vector $\mathbf{q}$, i.e. the velocity is given by $\mathbf{v}(\mathbf{r},t) = \mathbf{v}\exp[i(\mathbf{q}\cdot\mathbf{r}-\omega t)]$. This movement causes small fluctuations of the form $x(\mathbf{r},t) = x_0 + x'\exp(i(\mathbf{q}\cdot\mathbf{r}-\omega t))$ in the thermodynamic variables ϱ, p, T and s.

For small oscillations, the hydrodynamic equations 6.1 - 6.3 can be linearized in the small oscillating quantities $\mathbf{v}, \varrho', p', T'$ and s', yielding

$$6.1 \to \omega\varrho' - \varrho\mathbf{q}\cdot\mathbf{v} = 0, \tag{6.29}$$

$$6.2 \to \omega\varrho\mathbf{v} - \mathbf{q}p' + i\eta q^2\mathbf{v} + i\left(\frac{d-2}{d}\eta + \zeta\right)\mathbf{q}(\mathbf{q}\cdot\mathbf{v}) = 0, \text{ and} \tag{6.30}$$

$$6.3 \to \varrho\omega T s' + i\varkappa q^2 T' = 0. \tag{6.31}$$

The linearized momentum balance equation can only be fulfilled if $\mathbf{q}$ and $\mathbf{v}$ are collinear, i.e. if the movement of the particles occurs in the same direction as the wave is propagating. Therefore, sound waves must be longitudinal waves. To proceed, one makes use of the fact that the thermodynamic variables are not independent, but are related by the equation of state of the material, such that the variations in density and entropy can be expressed by the variations in pressure and temperature.

$$\varrho' = \left(\frac{\partial\varrho}{\partial p}\right)_T p' + \left(\frac{\partial\varrho}{\partial T}\right)_p T' \qquad \text{and} \qquad s' = \left(\frac{\partial s}{\partial p}\right)_T p' + \left(\frac{\partial s}{\partial T}\right)_p T'. \tag{6.32}$$

Eliminating ϱ' and s' in this way leaves one with a set of three equations linear in the unknown quantities $p', T', \mathbf{v}$:

$$\begin{pmatrix} \omega\left(\frac{\partial\varrho}{\partial T}\right)_p & -\varrho\mathbf{q} & \omega\left(\frac{\partial\varrho}{\partial p}\right)_T \\ 0 & \omega\varrho + i\left(\frac{2d-2}{d}\eta + \zeta\right)q^2 & -\mathbf{q} \\ \omega\varrho T\left(\frac{\partial s}{\partial T}\right)_p + i\varkappa q^2 & 0 & \omega\varrho T\left(\frac{\partial s}{\partial p}\right)_T \end{pmatrix} \cdot \begin{pmatrix} T' \\ \mathbf{v} \\ p' \end{pmatrix} = \begin{pmatrix} 0 \\ 0 \\ 0 \end{pmatrix}.$$

(6.33)

The solutions to this system can be found by setting the determinant of the coefficient matrix to zero. Using thermodynamic relations, the resulting equation can be cast into the form

$$\omega^3 + i\frac{\omega^2 q^2}{\varrho}\left(\eta + \zeta + \varkappa\varrho\frac{C_p - C_v}{C_p C_v}\right) - \omega q^2 c^2 - \frac{\omega q^4 \varkappa}{\varrho C_v}(\eta + \zeta) = 0 \tag{6.34}$$

in two dimensions. The interested reader can find the calculation in Appendix B. Here, c is the adiabatic sound velocity and C_p and C_v are the heat capacities at constant pressure and volume, given by

c : Adiabatic sound velocity
C_p : Heat capacity at constant pressure
C_v : Heat capacity at constant volume

$$c^2 = \left(\frac{\partial p}{\partial \varrho}\right)_s = \frac{C_p}{C_v}\left(\frac{\partial p}{\partial \varrho}\right)_T \qquad \text{and} \qquad C_{p,v} = \varrho T\left(\frac{\partial s}{\partial T}\right)_{p,v}. \tag{6.35}$$

The final term is dropped, since we are interested in long-wavelength and low frequency excitations, for which the other terms will dominate. Then, one obtains

$$\omega^2 = c^2 q^2 - i\omega q^2\left(\frac{\eta}{\varrho} + \frac{\zeta}{\varrho} + \frac{C_p - C_v}{C_p C_v}\varkappa\right). \tag{6.36}$$

For a dissipationless system, $\eta = \zeta = \varkappa = 0$, and this equation reduces to $\omega = cq$. In this case, sound is recovered as plane waves, oscillating with a frequency $\omega_0 = cq$, and propagating with the adiabatic sound velocity $c = \sqrt{(\partial p/\partial \varrho)_s}$.

ω_0 : Bare (undamped) sound frequency

In the case of a dissipative system, solving the quadratic equation is still straightforward and yields the dispersion relation

$$\omega = -i\frac{\Gamma}{2} + \sqrt{c^2 q^2 - \frac{\Gamma^2}{4}}, \qquad \text{with} \qquad \Gamma = q^2\left(\frac{\eta}{\varrho} + \frac{\zeta}{\varrho} + \frac{C_p - C_v}{C_p C_v}\varkappa\right). \tag{6.37}$$

This relation is the dispersion relation of a damped harmonic oscillator. For $\Gamma/(2\omega_0) < 1$, the sound waves are weakly damped and decay exponentially in time with a rate of $\Gamma/2$. The frequency of the oscillations is reduced with respect to the undamped situation and given by the real part of ω as

Γ : Sound damping rate

$$\omega = cq\sqrt{1 - \left(\frac{\Gamma}{2cq}\right)^2} \overset{\Gamma \ll 2\omega_0}{\approx} \omega_0\left(1 - \frac{\Gamma^2}{8\omega_0}\right). \tag{6.38}$$

For $\Gamma > 2\omega_0$, the oscillator is overdamped and there are no oscillating solutions.

The propagation speed of the sound waves is obtained from the real part as

$$c_s = \frac{\omega}{q} = \left(\frac{\partial p}{\partial \varrho}\right)_s \sqrt{1 - \left(\frac{\Gamma}{2\omega_0}\right)^2}. \tag{6.39}$$

6.2.3. Two-fluid hydrodynamics

After having derived the equations for sound excitations in normal fluids, we now turn to the hydrodynamic description of sound in superfluids in the two-fluid model. In a superfluid, the presence of both a normal and a superfluid component allows more than just one sound mode to propagate. The two modes propagate at different speeds and are commonly denoted as first and second sound. The speed of the two modes will be determined by the sound velocity c, which we have introduced already and by a second quantity c_2, which involves the ratio between the superfluid density and the normal density, and which can be interpreted as the velocity of temperature waves (compare chapter 10 in [85]). In the derivation of the sound velocities, we will follow the derivations presented in [148] and [85] and we will only consider the dissipationless case. Similar to the procedure we followed before, we will now first derive two wave equations for the entropy and the density. We will linearize the system and eliminate a few thermodynamic variables using the equation of state. Finally, we will solve the linearized system via the determinant of the coefficient matrix.

ϱ_s :	Superfluid density
ϱ_n :	Normal density
$\mathbf{v}_{s/n}$:	Velocity of the superfluid normal components
$\mathbf{j}$:	Current density

In the two-fluid model, the density of the fluid is given by $\varrho = \varrho_n + \varrho_s$, where the subscripts denote the superfluid and normal components. Correspondingly, the current density is $\mathbf{j} = \varrho_n \mathbf{v}_n + \varrho_s \mathbf{v}_s$. The acceleration of the superfluid component $\dot{\mathbf{v}}_s$ can be related to the gradient of the chemical potential $\boldsymbol{\nabla}\mu$: In 1941, Kapitza found that the pressure difference across a superleak is related to the temperature according to $\Delta p = \varrho s \Delta T$ in the steady state [150]. These variables are also related by the Gibbs-Duhem relation $N d\mu = V dp - S dT$, which we can write as $\varrho d\mu/m = dp - \varrho s dT$. Using both relations, we obtain $d\mu = 0$ across a superleak in the steady state, which suggests that the acceleration of the superfluid component depends only on the gradient of the chemical potential, $m\dot{\mathbf{v}}_s = -\boldsymbol{\nabla}\mu$ [148]. One then obtains

$$\frac{\partial \mathbf{v}_s}{\partial t} = -\frac{1}{m}\boldsymbol{\nabla}\mu = -\frac{1}{\varrho}\boldsymbol{\nabla}p + s\boldsymbol{\nabla}T. \tag{6.40}$$

Inserting this relation into $\partial\mathbf{j}/\partial t = \varrho_n \partial\mathbf{v}_n/\partial t + \varrho_s \partial\mathbf{v}_s/\partial t$ and solving for $\partial\mathbf{v}_n/\partial t$ yields

$$\frac{\partial}{\partial t}\mathbf{v}_n = \frac{1}{\varrho_n}\left(\frac{\partial}{\partial t}\mathbf{j} - \varrho_s \frac{\partial}{\partial t}\mathbf{v}_s\right). \tag{6.41}$$

Subtracting eqs. 6.40 and 6.41, we obtain a relation between the accelerations of the normal and superfluid parts of the system:

$$\frac{\partial}{\partial t}(\mathbf{v}_n - \mathbf{v}_s) = -\frac{\varrho}{\varrho_n} s\boldsymbol{\nabla}T. \tag{6.42}$$

In a superfluid, entropy is conserved, but carried only by the normal density. In the entropy continuity equation 6.6, we thus have to replace $\mathbf{v}$ by $\mathbf{v}_n$, which gives

$$\frac{\partial}{\partial t}(\varrho s) + \boldsymbol{\nabla}\cdot(\varrho s \mathbf{v}_n) = 0. \tag{6.43}$$

This equation can be linearized in the varying quantities, which gives

$$s\frac{\partial \varrho}{\partial t} + \varrho\frac{\partial s}{\partial t} + s\varrho\boldsymbol{\nabla}\cdot\mathbf{v}_n = 0. \tag{6.44}$$

Using the continuity equation $\partial\varrho/\partial t = -\boldsymbol{\nabla}\cdot\mathbf{j}$, one can rewrite this equation as

$$\frac{\partial s}{\partial t} = s\frac{\varrho_s}{\varrho}\boldsymbol{\nabla}\cdot(\mathbf{v}_s - \mathbf{v}_n), \tag{6.45}$$

and with eq. 6.42, we obtain

$$\frac{\partial^2 s}{\partial t^2} = s^2\frac{\varrho_s}{\varrho_n}\Delta T. \tag{6.46}$$

This is the first of the two differential equations we will need.

The second equation follows from the continuity and Euler equations. Combining $\partial\varrho/\partial t = -\boldsymbol{\nabla}\cdot\mathbf{j}$ with $\partial\mathbf{j}/\partial t = -\boldsymbol{\nabla}p$, we obtain

$$\frac{\partial^2 \varrho}{\partial t^2} - \Delta p = 0. \tag{6.47}$$

We now choose the density and temperature as independent variables. Allowing for small fluctuations of the form $\sim \exp(i\mathbf{q}\cdot\mathbf{r} - i\omega t)$, we linearize 6.47 and 6.46 to yield

$$6.47 \rightarrow \omega^2\varrho' - q^2\left[\left(\frac{\partial p}{\partial \varrho}\right)_T \varrho' + \left(\frac{\partial p}{\partial T}\right)_\varrho T'\right] = 0 \tag{6.48}$$

$$6.46 \rightarrow \omega^2\left[\left(\frac{\partial s}{\partial \varrho}\right)_T \varrho' + \left(\frac{\partial s}{\partial T}\right)_\varrho T'\right] - q^2\frac{\varrho_s}{\varrho_n}s^2 T' = 0. \tag{6.49}$$

After introducing the adiabatic and isothermal sound velocities c, c_T, the heat capacity C_v, as well as the additional quantity

$$c_2^2 = \frac{\varrho_s}{\varrho_n}s^2\frac{\varrho T}{C_v}, \tag{6.50}$$

one can use thermodynamic relations to rewrite these equations as

$$(u^2 - c_T^2)\varrho' - \left(\frac{\partial p}{\partial T}\right)_\varrho T' = 0 \tag{6.51}$$

$$u^2(c_T^2 - c^2)\left(\frac{\partial p}{\partial T}\right)_\varrho^{-1}\varrho' + (u^2 - c_2^2)T' = 0, \tag{6.52}$$

where $u = \omega/q$. This calculation is lengthy and can be found in appendix B. This system of equations has solutions for

$$(u^2 - c_T^2)(u^2 - c_2^2) + u^2(c_T^2 - c^2) = 0$$

This is a quadratic equation in u^2, which can easily be solved to yield the sound velocities of first and second sound:

$$u_{1/2}^2 = \frac{c_s^2 + c_2^2}{2} \pm \sqrt{\left(\frac{c_s^2 + c_2^2}{2}\right)^2 - c_T^2 c_2^2}. \tag{6.53}$$

$u_{1/2}$: Velocities of first and second sound

In a superfluid, there are two sound modes propagating at different speeds. At the critical temperature, the superfluid density vanishes, $\varrho_s = 0$, such that $c_2 = 0$. In this case, only the normal sound mode remains, which propagates at the adiabatic speed of sound c_s. The presence of two sound modes has been predicted by L. Tisza [151] and fully derived by L. Landau [152][4]. Second sound was first observed by V. Peshkov in superfluid ^{4}He [154]. In ultracold Fermi gases, second sound was first measured by L. A. Sidorenkov et al. in the group of R. Grimm[155].

The damping rate of second sound is also modified by the presence of both a normal and a superfluid component. The heat equation obtains additional source terms involving not only the velocity of the normal component, but also terms involving the superfluid component as well as terms mixing both component. According to [148], the result is

$$\begin{aligned}\varrho T\left(\frac{\partial s}{\partial t}+\frac{\partial}{\partial x_i}(v_{ni}s)\right) &= \sigma'_{ik}\frac{\partial v_{ni}}{\partial x_k}+\zeta_3(\boldsymbol{\nabla}(\mathbf{j}-\varrho\mathbf{v}_n))^2\\ &\quad+\zeta_4\boldsymbol{\nabla}\mathbf{v}_n\boldsymbol{\nabla}(\mathbf{j}-\varrho\mathbf{v}_n)+\boldsymbol{\nabla}(\varkappa\boldsymbol{\nabla}T),\end{aligned}\tag{6.54}$$

with

$$\sigma'_{ik}=\eta\left(\frac{\partial v_{ni}}{\partial x_k}+\frac{\partial v_{nk}}{\partial x_i}-\frac{2}{d}\delta_{ik}\frac{\partial v_{nj}}{\partial x_j}\right)+\delta_{ik}\zeta\frac{\partial v_{nj}}{\partial x_j}+\delta_{ik}\zeta_1\frac{\partial(j-\varrho v_n)_j}{\partial x_j}.\tag{6.55}$$

$\zeta_{1/3/4}$: Viscosity coefficients involving superfluid component

Γ_2 : Attenuation rate of second sound

ζ_1, ζ_3 and ζ_4 are additional viscosity coefficients. Under the condition $(C_p - C_v)/C_v \ll 1$, one finds the following expression for the attenuation rate of second sound[5].

$$\Gamma_2 = q^2\left(\frac{\eta}{\varrho}+\frac{\zeta}{\varrho}+\varrho\zeta_3-2\zeta_1+\frac{\varrho_n\varkappa}{\varrho_s C}\right),\tag{6.56}$$

where $C=\varrho T\frac{ds}{dT}$ is the general heat capacity of the material.

6.2.4. Diffusion coefficients and quantum limited transport

Diffusion coefficients

The damping rate $\Gamma \propto q^2$ of the sound waves is not universal, but is dependent on the wave vector. This dependency is the typical sign of a diffusive process. In the beginning of this chapter, we have already motivated that the damping of sound modes occurs via diffusive transport. After having derived the damping rate of the sound waves and its connection to the transport coefficients η, ζ and $\varkappa$, let us now make the link between these and the diffusion coefficients D_η, D_ζ and $D_\varkappa$.

One fundamental assumption underlying hydrodynamics is that the dynamics on a microscopic level happen on a time scale that ensures local thermal equilibrium at any point in time. Gradients in the thermodynamic variables lead to diffusive currents, which tend to equilibrate the imbalance over time. A temperature gradient across the thermodynamic

---

[4] The two-fluid model is often fully credited to Landau. For a more in-depth analysis about the discovery of superfluidity and its theoretical description, see for instance [153].

[5] This condition ensures that the contribution of the thermal conductivity to the attenuation is small. This is the case for instance for liquid ^{4}He and other degenerate gases [148], however it is not the case in non-degenerate gases.

volume for instance leads to a heat current according to $\mathbf{q} = -\varkappa\boldsymbol{\nabla}T$. Assuming the fluid at rest, the heat that is transferred through a given volume by this current changes the temperature in the volume according to

$$\frac{dT}{dt} = -\frac{1}{C_p}\boldsymbol{\nabla}\cdot\mathbf{q} = \frac{\varkappa}{C_p}\Delta T = D_\varkappa \Delta T. \tag{6.57}$$

This equation is the diffusion equation with the heat diffusion constant $D_\varkappa$.

$D_\varkappa$: Heat diffusion coefficient
D_η : Shear diffusion coefficient
D_ζ : Bulk diffusivity
D_s : Sound diffusion constant

In this chapter, we have also seen another occurrence of a diffusion equation in the form of the Navier-Stokes equation 6.23. For vanishing density variations, it states the diffusion of velocity gradients in an incompressible fluid:

$$\frac{d\mathbf{v}}{dt} = \frac{\eta}{\varrho}\Delta\mathbf{v} = D_\eta \Delta\mathbf{v}. \tag{6.58}$$

We thus identify $D_\eta = \eta/\varrho$ as the shear diffusivity. Identifying $D_\zeta = \zeta/\varrho$ as the bulk diffusivity in an analogous way, the sound diffusion constant can be defined by

$$D_s = \frac{\Gamma}{q^2} = \frac{\eta}{\varrho} + \frac{\zeta}{\varrho} + \varkappa\frac{C_p - C_v}{C_p C_v} = D_\eta + D_\zeta + D_\varkappa \frac{C_p - C_v}{C_v}. \tag{6.59}$$

Quantum limited transport

The shear viscosity can be used to quantify whether a material is a 'good' or 'bad' fluid. In materials with a small shear viscosity, particles at rest in the vicinity of moving particles remain relatively unaffected, whereas a high shear viscosity couples the motion of neighboring parts of the liquid and transforms the kinetic energy of the shear motion into heat. This raises the question which materials make for 'good' fluids and under which conditions one can expect 'good' or 'bad' fluidity.

A very simple argument can be found by going back to weakly interacting systems. In kinetic theory, the diffusion constant is related to the mean velocity and the mean free path of the particles via the relation $D \sim \langle v \rangle l_{\mathrm{mfp}}$. At weak interactions, long-lived quasiparticles can transport heat or momentum over long distances and therefore smooth out density and pressure variations very efficiently, leading to high diffusivities and strong attenuation of sound waves. In this case, the fluid has a relatively high viscosity. For stronger interactions, the mean free path shortens and the diffusivity is reduced. Increasing the interactions further into the strongly correlated regime, well-defined quasiparticles cease to exist and the concept of mean free path loses its validity. Extending the line of reasoning even further nevertheless, one finds particles scattering with a mean free path comparable to the average interparticle spacing. Hence, diffusive processes transporting away heat or momentum should become strongly suppressed. Since the interparticle spacing imposes a lower bound on the mean free path, this raises the question whether there are lower bounds on the diffusivity and on the viscosity.

In other words, we can ask the question whether there are 'perfect' fluids in the sense that they approach a fundamental lower bound on the viscosity. In such a fluid, hydrodynamics could provide a valid description of the dynamics even on distances comparable to the interparticle spacing [65].

A lower bound for the ratio of shear viscosity and entropy density of $\eta/\varrho s \geq \hbar/(4\pi k_{\mathrm{B}})$ was first conjectured to exist by P. Kovtun, D. Son and A. O. Starinets (KSS) in the context of quantum field theories with holographic duals "for all relativistic quantum field theories at finite temperature and zero chemical potential" [156][6]. Since then, almost ideal hydrodynamic flow has been measured in various systems. Although it is in principle possible to construct counter-examples, the KSS conjecture turns out to hold for all real fluids [157]. Lower bounds for the viscosity of order $\eta/\varrho s \sim \hbar/k_{\mathrm{B}}$ and $\eta/n \sim \hbar$ have for instance been observed for a wide range of fluids [65], ranging from water over liquid Helium to ultracold quantum gases and even quark gluon plasmas. For a review of these results, I would like to refer the reader to [65].

In the context of ultracold Fermi gases, lower bounds for the diffusivities $D \gtrsim \hbar/m$ and thus quantum limited transport have been predicted and observed in several transport channels. For ultracold 2D geometries, a minimum in shear viscosity in dependence on temperature has been reported by E. Vogt et al. [57] and described theoretically by G. M. Bruun, T. Schäfer and T. Enss et al. [158–160] using a kinetic theory picture. In three dimensions, the shear viscosity has been calculated to exhibit a minimum by P. Massignan et al. [161] in the context of kinetic theory and by T. Enss et al. using a diagrammatic approach to the stress tensor in the Kubo formula [157]. C. Cao et al. [162] observed experimentally that the viscosity to entropy ratio of the 3D Fermi gas indeed obeys the string theory limit. Similar results were obtained by various groups for the spin diffusion coefficient in 2D [58, 59, 158, 160] and 3D Fermi gases [163–167]. The sound propagation of three-dimensional unitary Fermi gases was also observed to approach a lower limit by P. Patel et al. in the group of M. Zwierlein [168].

Several hypotheses have been brought forward to provide an explanation for quantum limited transport [169]: One, motivated by holographic duality [156], is that it occurs near scale invariant points in the phase diagram. The unitary 3D Fermi gas is an example that seems to support this hypothesis since it is strongly interacting as well as scale invariant and exhibits quantum limited shear and spin diffusion. In contrast, 2D Fermi gases exhibit a quantum scale anomaly that breaks scale invariance [170–173].

In our experiment, we investigate the propagation and damping of sound in a strongly interacting 2D Fermi gas and thereby probe a crucial test case for this hypothesis. We observe that the damping approaches the quantum limit $D \approx \hbar/m$ in the strongly interacting regime, where scale invariance is most dramatically violated, showing that scale invariance or quantum criticality is in fact not required for quantum limited transport. Similar observations were made for transverse spin diffusion in [59]. Our results confirm a scenario of incoherent transport that has

[6] Note that the KSS bound is usually written in the form $\eta/s \geq \hbar/(4\pi k_{\mathrm{B}})$. The difference originates in the definition of entropy density s per units of mass instead of volume in this text.

emerged in recent years from the study of anomalous transport in high-temperature superconductors and other ’bad metals’ [174–176] and links quantum limited transport to strong correlations.

6.3. Measuring sound in ultracold 2D Fermi gases

We perform our studies of sound propagation with an ultracold gas of ^{6}Li atoms in a spin-balanced mixture of the lowest two hyperfine states, trapped in a two-dimensional box potential [60, 177] as detailed in section 5.2. The gas is vertically confined in a single node of the repulsive optical lattice with a trap frequency of $\omega_z/2\pi = 8.4(3)\,\mathrm{kHz}$. At our densities of about $n_{\uparrow/\downarrow} \equiv n \approx 1\,\mathrm{\mu m}^{-2}$ per spin state, the chemical potential μ is smaller than the vertical level spacing $\hbar\omega_z$, which ensures that our gas is in the kinematic 2D regime. Using a DMD illuminated with blue detuned light ($\lambda_{\mathrm{DMD}} = 532\,\mathrm{nm}$), we trap the gas in the horizontal plane in a two-dimensional box with a typical size of $l_x \times l_y = 30\,\mathrm{\mu m} \times 40\,\mathrm{\mu m}$.

ω_z : Vertical trapping frequency
n : Density per spin state
μ : Chemical potential
$l_{x/y}$: Horizontal box dimensions

Temperature determination

Usually, the temperature in cold atom systems is determined from the occupation of high-energy states by the thermal part of the cloud. Since our gas is confined in a box potential, there is no region of low density or high potential, where such a measurement could be performed easily. While we currently do not have a quantitative temperature determination in our homogeneous trap (compare [177]), previous measurements in a similar system [177] (see section 7.3) show clear evidence of phase coherence and thus suggest that the temperature in our system is below the critical temperature for superfluidity T_c for a large parameter range from the BEC limit up to the strongly correlated regime.

T_c : Critical temperature for superfluidity

Calculating a theoretical value for the critical temperature in the strongly correlated regime is not straightforward. Classical-field Monte-Carlo calculations of a weakly interacting 2D Bose gas yield a BKT transition temperature of [94, 178]:

$$\frac{T_c}{T_{\mathrm{F}}} = \frac{1}{2}\frac{1}{n\lambda_{\mathrm{dB}}^2} = \frac{1}{2}\left[\ln\left(\frac{380}{4\pi}\ln\left(\frac{4\pi}{(k_{\mathrm{F}}a_{\mathrm{2D}})^2}\right)\right)\right]^{-1}. \tag{6.60}$$

In the Fermi limit, the critical temperature can be obtained by determining the point at which the superfluid gap Δ vanishes. Linearizing the gap equation yields [94]:

$$\frac{T_c}{T_{\mathrm{F}}} = \frac{2e^{\gamma}}{\pi k_{\mathrm{F}} a_{\mathrm{2D}}}. \tag{6.61}$$

Here, $\gamma \approx 0.577$ is the Euler constant. These two equations yield critical temperatures $T_c \geq 0.08\,T_{\mathrm{F}}$ in the bosonic regime and $T_c \geq 0.06\,T_{\mathrm{F}}$ in the fermionic regime.

γ : Euler constant

For our previous measurements, we estimated the temperature of the gas in two ways (see supplementary materials of [177]). As mentioned in section 5.3, a pulse of repulsive light is normally used to remove the thermal atoms that are trapped on the outside of our repulsive potentials, in the weak harmonic confinement produced by the Feshbach coils. Leaving these atoms in place, we can perform time-of-flight measurements and extract a temperature under the assumption that these atoms are in thermal equilibrium with the atoms inside the box, which however is not necessarily obvious. This measurement yielded a temperature of $T/T_\mathrm{F} \approx 0.03$ [177].

The temperature can also be extracted by measuring the equation of state of the gas. To do this, we imprint a potential step ΔV_s and measure the density response $\Delta n(\Delta V_s)$ of the gas. Following [56], we can extract the chemical potential from the slope of $\Delta n(\Delta V_s)$ in a bosonic gas, and compare it to simulated curves for different temperatures (see supplementary material to [177]). The best fit between simulation and data is again obtained for $T/T_\mathrm{F} \approx 0.03$. Both estimates coincide and put our sample in the superfluid regime.

While this temperature determination was done in a slightly different system than the one used for the sound measurements (the box potential used in [177] was split in the middle by a thin barrier), we assume that the absence of the barrier does not strongly affect the temperature of the gas. For the sound measurements presented here, we thus assume that the gas is in the low-temperature regime with $T/T_\mathrm{F} < 0.1$. For most of our data, we also expect to have $T < T_c$, with the possible exception of the extreme BCS regime.

6.3.1. Experimental procedure

V_pulse : Excitation potential

ϕ_0 : (Initial) phase difference between the box halves

For our experiments, we build on the experimental procedure developed in [180], where sound propagation was studied in weakly interacting 2D Bose gases. To excite a sound mode in the box we follow the approach of [177] and illuminate one side of the box with a spatially homogeneous optical potential V_pulse for a short duration $\tau < \tau_\mathrm{F} = h/E_\mathrm{F}$. This time scale is short enough that the particles do not have time to adapt to the additional potential. The density in the box therefore stays constant, but a relative phase of $\phi_0 = \exp(-iV_\mathrm{pulse}\tau/\hbar)$ is imprinted between two halves of the system, which imprints a velocity on the particles in the boundary region and induces density oscillations in the box. We then observe these oscillations by imaging the density distribution after different hold times using in-situ absorption imaging. An example of such an oscillation is shown in Fig. 6.1. A sound wave traveling back and forth between the two sides of the box is clearly visible in the density profile. A second, weaker wave propagating in the opposite direction can be seen as well. This second oscillation is phase shifted with respect to the first oscillation, but since it has the same oscillation period as the first wave, it can be attributed to an imperfect excitation.

To extract the oscillation frequency $f = \omega/2\pi$ and the damping rate Γ of the sound wave, we calculate the relative particle imbalance $\Delta n/n = 2(n_\mathrm{t} - n_\mathrm{b})/(n_\mathrm{t} + n_\mathrm{b})$ from the densities n_t and n_b in the top and bottom halves of the box and fit it with a damped sinusoidal of the form $A(t) =$

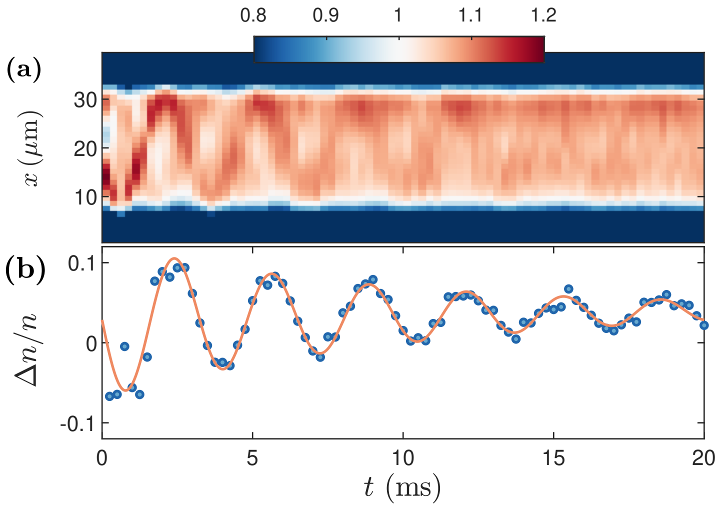

Figure 6.1. – Propagation of a sound wave in a box potential: (a) Density profiles $n(x,t)/n(t)$ averaged along the direction perpendicular to the sound propagation and normalized to the average density $n(t)$ within the box. A density wave propagating through the box is visible. Each profile $n(x,t)/n(t)$ is the average of 120 individual realizations. Note that the color scale has been chosen to enhance the visibility of the sound wave. (b) Relative density imbalance between the two sides of the box for the same data set. The solid line shows a damped sinusoidal fit to the data. The statistical errors are typically smaller than the marker size. Figure reproduced from [179].

$A_0 \cos(\omega t + \phi) \exp(-\Gamma t/2) + b$ (see Fig. 6.1 (b)). The factor 1/2 in the exponential of the fit function takes into account that Γ is the damping rate of the oscillation energy, which is proportional to the square of the oscillation amplitude.

As a first check that this approach is valid, we measure the oscillation frequency for different boxes with lengths between $l_x = 15\,\mu$m and $l_x = 40\,\mu$m and find that it is in good approximation proportional to the inverse of the box length (see Fig. 6.2). This confirms that we observe a sound wave traveling at a constant velocity $c = 2l_x f$. While we cannot rule out edge effects from our data, the conclusions we draw from our measurements should not be altered significantly.

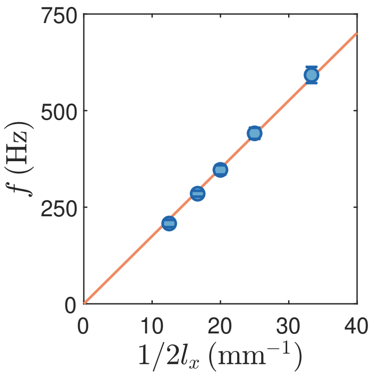

Figure 6.2. – Frequency of the density oscillations as a function of the inverse box length. The slope of the linear fit (solid line) corresponds to the speed of sound. Each data point is the average of 23 realizations.

$n_{\mathrm{t,b}}$: Densities in the top/bottom half of the box

To probe sound as a function of interaction strength, we perform measurements in a box with $l_x = 30\,\mu$m at magnetic fields around the Feshbach resonance. Examples of the resulting oscillations as well as the evolution of the oscillation frequency as a function of magnetic field are shown in Figure 6.3. As the field is varied from the BEC side to the BCS side of the crossover, the oscillation frequency increases, which is expected since the compressibility of a Fermi gas is much lower than that of a weakly repulsive Bose gas. On the Fermi side, the gas is thus stiffer with respect to density fluctuations and sound waves propagate faster than on the Bose side.

The damping of the oscillations normalized to their frequency shows a broad minimum around the Feshbach resonance at 832 G and a strong increase of damping towards the BEC and BCS regimes, i.e., towards more weakly interacting systems. As can be seen in Fig. 6.3 (a), the

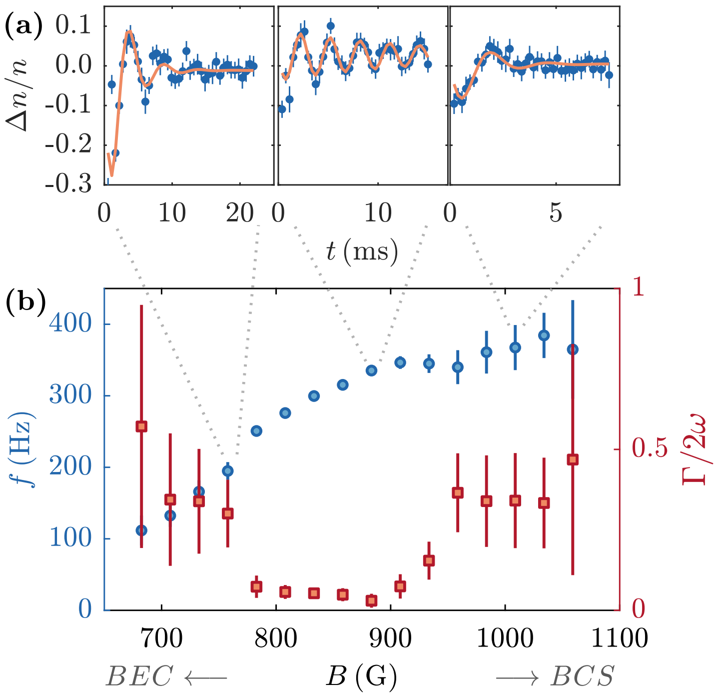

Figure 6.3. – Results of the sound measurements across the BEC-BCS crossover. (a): Oscillations in the density imbalance at $B = 758\,\mathrm{G}$, $B = 883\,\mathrm{G}$ and $B = 1009\,\mathrm{G}$. Solid lines represent damped sinusoidal fits. (b): Frequency (blue circles) and damping (red squares) of sound oscillations as a function of magnetic field. The frequency increases smoothly from the BEC to the BCS side and starts to saturate at high magnetic fields. The damping shows a clear minimum in the strongly interacting regime and increases strongly towards either side. Each data point is the average of 39 realizations. The difference between the sizes of the error bars on the BEC and BCS regimes may seem striking at first. The relative errors on both sides however are of same order of magnitude (19% for the leftmost point, the rest below 15%). Around the resonance, the relative errors are below 5%. The main contribution to the uncertainty is the uncertainty in the frequency determination. This trend can also be seen in the following figures.

oscillations are quite strongly damped, increasing the fitting uncertainty of our data in these regimes.

At this point, we should stop to further motivate the description of our oscillations in the hydrodynamic framework. We will give two arguments here, which are both valid in the framework of kinetic theory and are not strictly applicable in a purely hydrodynamic picture, since both employ the concept of a mean free path. Nevertheless, these arguments tell us that kinetic theory is not valid for our system and therefore provide us with a rough guideline when hydrodynamics should be the more appropriate framework to use.

As mentioned earlier, hydrodynamics assumes fast local equilibration of the thermodynamic quantities, which leads to diffusive attenuation of variations in these variables. The typical length scale for these variations therefore must be much larger than the typical mean free path between particles: $kl_{\mathrm{mfp}} \ll 1$. In a kinetic picture, the mean free path is related to the total scattering cross section σ and the density according to $l_{\mathrm{mfp}} = 1/(n\sigma)$. For a typical scattering momentum given by the Fermi momentum, the total cross section is given by [94]

$$\sigma = 2\pi \frac{d\sigma}{d\theta} = \frac{4\pi^2}{k_{\mathrm{F}}} \frac{1}{4\ln^2(k_{\mathrm{F}}a_{\mathrm{2D}}) + \pi^2}, \tag{6.62}$$

yielding

$$l_{\mathrm{mfp}} = \frac{1}{n\sigma} \simeq \frac{1}{2}\sqrt{\frac{\pi}{n}} \left(1 + \frac{4\ln^2(k_{\mathrm{F}}a_{\mathrm{2D}})}{\pi^2}\right). \tag{6.63}$$

Evaluating this at our densities of typically $n \sim 1\,/\mu\mathrm{m}^2$, the mean free path remains smaller than the wavevector of the oscillations $1/k = l_x/\pi$ for most of our experimental range, except for the data points in the far BEC regime[7].

The second argument follows from the relations of the diffusivity coefficient with the damping and the mean free path. In hydrodynamics the damping is related to the diffusivity as $\Gamma \sim Dk^2$. On the other hand kinetic theory links the diffusivity to the mean free path and the typical velocity as $D \sim l_{\mathrm{mfp}}\langle v\rangle$. Together, this implies $kl_{\mathrm{mfp}} \sim kD/\langle v\rangle \sim k^2D/ck \sim \Gamma/\omega \ll 1$. Hydrodynamic conditions thus are valid as long as the sound oscillations are weakly damped, which is certainly the case in the strongly correlated regime around the Feshbach resonance.

In conclusion, these two points suggest that the hydrodynamic description is better suited for our data than a description in terms of weakly interacting particles for our data range. Away from the strongly correlated regime, the mean free path becomes longer, but the low damping rate and the small mean free path provide a strong argument for the use of a hydrodynamic description.

6.3.2. Speed of sound and compressibility across the BEC-BCS crossover

Speed of sound

Next, we use the measurement of the oscillation frequency in the box to extract the speed of sound and the compressibility equation of state of the gas across the BEC-BCS crossover. The speed of sound is calculated using $c = 2l_x f$ and plotted as a function of the 2D interaction parameter $\ln(k_{\mathrm{F}}a_{\mathrm{2D}})$ in Figure 6.4.

As we have derived earlier, in a superfluid, two-fluid hydrodynamics predict the occurrence of two sound modes which propagate at different velocities, as observed in [155]. These modes generally mix density and entropy degrees of freedom. For strongly interacting 2D-superfluids, however, and Fermi gases in particular, density and entropy excitations have been predicted to be well decoupled [181–183], and hence the sound mode we observe should correspond to an almost pure density wave. In this case, the velocity of a sound wave is in first order given by

$$c = \sqrt{\frac{n}{m}\frac{\partial\mu}{\partial n}\bigg|_s} \tag{6.64}$$

---

[7] While this estimation neglects effects arising from Pauli blocking, which might reduce the scattering cross section and therefore increase the mean free path in a degenerate Fermi gas, we note that below T_c, superfluid hydrodynamics should apply nevertheless.

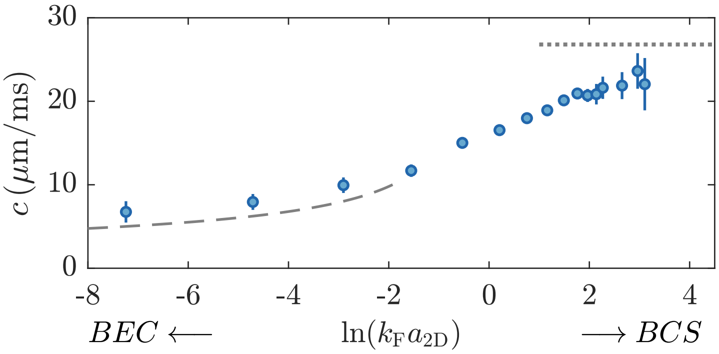

Figure 6.4. – Speed of sound across the BEC-BCS crossover. Gray lines represent the two theoretical limits: In the BEC regime, Bogoliubov theory predicts $\mu = gn$ and hence $c_\mathrm{B} = (gn/2m)^{1/2}$, where g is the interaction parameter between bound dimers defined as in [96, 177]. On the BCS side, $\mu \to E_\mathrm{F}$ yields a constant sound velocity $c_\mathrm{F} = v_\mathrm{F}/\sqrt{2}$ where $v_\mathrm{F} = \hbar k_\mathrm{F}/m$ is the Fermi velocity.

κ : Isentropic compressibility

and is directly related to the isentropic compressibility $\kappa = \frac{1}{n^2}\left(\frac{\partial n}{\partial \mu}\right)_s$. Here we assumed adiabatic conditions since the oscillation frequency is large compared to the damping ($\omega \geq \Gamma$).

Very recent simulations of the sound velocity in a 2D Bose gas [184] indicate however, that the density and entropy modes remain coupled even for relatively strongly interacting Bose gases, leading to sound velocities which differ from the Bogoliubov prediction. This should be observable as a difference between the static and dynamic measurements of the compressibility. If such a difference exists in our system, it is smaller than the uncertainty of our measurement, as seen below in fig. 6.6, in which we compare the compressibilities extracted from the dynamic and static measurements. We therefore proceed with the assumption that we can use formula 6.64 to describe the speed of sound in our system to a good accuracy.

This relation then gives us simple zero-temperature expressions for the speed of sound in the BEC and BCS limits of the crossover. In a weakly interacting bosonic gas, the Bogoliubov quasiparticles at low momentum have a linear dispersion relation $E(k) \approx \hbar c k$, with $c = \sqrt{gn/m}$. In the BEC limit, the sound velocity is therefore given by

c_B : Sound velocity of the Bogoliubov quasiparticles in the BEC limit

c_F : Sound velocity in an ideal Fermi gas

$$c_\mathrm{B} = \sqrt{\frac{\hbar^2 n}{m_\mathrm{d}^2}\sqrt{8\pi}\frac{a_\mathrm{dd}}{l_z}}, \tag{6.65}$$

where $m_\mathrm{d} = 2m$ is the mass of a dimer, $a_\mathrm{dd} = 0.6\,a_\mathrm{3D}$ the scattering length between dimers [93, 185], and $\frac{\hbar^2}{m_\mathrm{d}}\sqrt{8\pi}\frac{a_\mathrm{dd}}{l_z} = \frac{\hbar^2}{m_\mathrm{d}}\tilde{g} = g$ the interaction strength between the dimers [83]. For an ideal Fermi gas at $T = 0$, the chemical potential coincides with the Fermi energy. From equation 6.64, one obtains $c_\mathrm{F} = v_\mathrm{F}/\sqrt{2}$, which coincides with the velocity of the Bogoliubov-Anderson mode in two dimensions [186]. Our data approaches these limits in the BEC and BCS regimes and interpolates smoothly across the BEC-BCS crossover, as shown in Figure 6.4.

Compressibility scaling function

For a more general analysis we use eq. 6.64 to extract the inverse compressibility scaling function $f_\kappa = 1/nE_\mathrm{F}\kappa$ of a two-dimensional Fermi gas. This dimensionless function is proportional to the inverse of the compressibility and increases smoothly from 0 to 1 across the BEC-BCS crossover, which follows directly from the expressions for the chemical potential in the BEC and BCS regimes. Since the compressibility relates different thermodynamic variables, the measurement of the speed of sound thus gives access to the equation of state (EOS) of the gas from dynamic properties of the system. In addition to this dynamic measurement of the equation of state, we also perform a static measurement of the compressibility EOS by determining the density response of our system to a static repulsive potential, similar to the work performed in [54–56, 60]. We imprint a weak homogeneous potential ΔV_s onto one half of the cloud and wait for the system to equilibrate. This results in a density difference Δn between the two halves of the system as seen in Figure 6.5.

f_κ : Inverse compressibility scaling function

ΔV_s : Height of the imprinted potential step

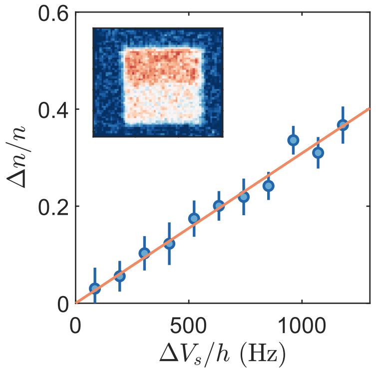

Figure 6.5. – Static measurement of the compressibility. A repulsive potential V is imprinted onto one half of the box resulting in a density imbalance $\Delta n/n$ (blue points). We extract the compressibility from the initial slope of the data points according to $1/n^2\kappa = \lim_{\Delta n\to 0}\Delta V_s/\Delta n$ in a local density approximation. Each data point and the inset are averages of 20 realizations.

According to the local density approximation, this density difference corresponds to a difference in chemical potentials between the two sides, which is in turn equal to the height of the imprinted potential $\Delta V_s = \Delta\mu = \mu(n+\Delta n/2) - \mu(n-\Delta n/2)$. The compressibility can then be extracted from the slope of the density difference with respect to potential height according to

$$\frac{1}{n^2\kappa} = \frac{\partial\mu}{\partial n} = \lim_{\Delta n\to 0}\frac{\mu(n+\Delta n/2)-\mu(n-\Delta n/2)}{\Delta n} = \lim_{\Delta V_s\to 0}\frac{\Delta V_s}{\Delta n}. \tag{6.66}$$

For large potential steps, care must be taken in order to avoid nonlinear effects in the density response. Since this measurement of the compressibility is performed with a static system, dynamic effects during the reflection of the sound wave do not come into play here.

The two independent measurements of f_κ show good agreement with each other (see Fig. 6.6). In the BCS regime, the two curves coincide within the margin of error. In the BEC limit, the dynamic measurement results lie slightly above the static data points. Interpolating between the data points yield relative deviations below 30% in the range $B \geq -6\,\mathrm{G}$.

Finally we compare our data to theory for a true two-dimensional gas by extracting f_κ from Quantum Monte Carlo (QMC) calculations of the ground state energy E_0 of a homogeneous 2D Fermi gas [187]. We define an energy scaling function $f(\xi)$ by

$$f(\xi) = \frac{E_0}{E_\mathrm{FG}} + 2e^{-2\xi}, \tag{6.67}$$

where $\xi = \ln(k_\mathrm{F}a_\mathrm{2D})$. Remembering that the 2D-binding energy is given by $E_\mathrm{B}^{(2D)} = \hbar^2/ma_\mathrm{2D}^2$ and the total energy of a Fermi gas $E_\mathrm{FG} = NE_\mathrm{F}/2$, we find that

$$f(\xi) = \frac{1}{E_\mathrm{FG}}\left(E_0 + \frac{N}{2}E_\mathrm{B}\right). \tag{6.68}$$

E_0 : Ground state energy [187] of a zero-temperature Fermi gas
$f(\xi)$: Energy scaling function
ξ : Interaction parameter $\xi = \ln(k_\mathrm{F}a_\mathrm{2D})$

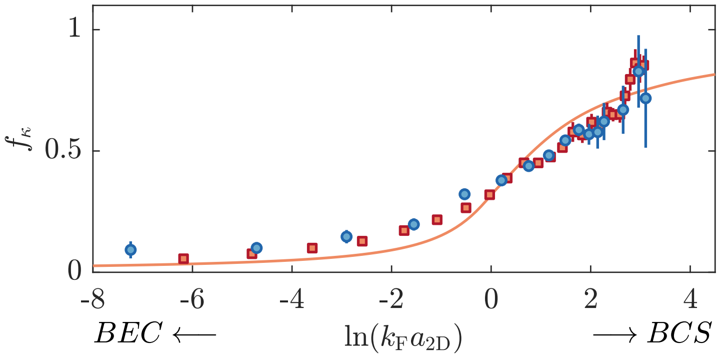

Figure 6.6. – Comparison between the compressibility scaling functions f_κ obtained from the speed of sound (blue circles), the density response to an imprinted static potential (red squares) and QMC calculations [187].

This function therefore describes the total energy of a Fermi gas across the BEC-BCS crossover as the ground state energy E_0, from which we subtract the binding energy of $N/2$ dimers $NE_\mathrm{B}^{(2D)}/2$. It is normalized to the total energy $E_\mathrm{FG} = E_\mathrm{F}/2$ of an ideal Fermi gas and thus should vary between $f(\xi \to -\infty) = 0$ in the BEC regime to $f(\xi \to \infty) = 1$ in the BCS regime. Via differentiation, one can then calculate the chemical potential. We note that

$$\frac{\partial E_\mathrm{FG}}{\partial N} = \frac{1}{2} E_\mathrm{F} + \frac{N}{2} \frac{\partial E_\mathrm{F}}{\partial N} = E_\mathrm{F}, \text{ and} \tag{6.69}$$

$$\frac{\partial \xi}{\partial N} = \frac{\partial}{\partial N} \ln(k_\mathrm{F} a_\mathrm{2D}) = \frac{1}{k_\mathrm{F} a_\mathrm{2D}} \frac{k_\mathrm{F} a_\mathrm{2D}}{2N} = \frac{1}{2N}, \tag{6.70}$$

and obtain

$$\begin{aligned}\mu &= \frac{\partial E}{\partial N} = \frac{\partial}{\partial N}(E_\mathrm{FG} f(\xi)) \\ &= \frac{\partial E_\mathrm{FG}}{\partial N} f(\xi) + E_\mathrm{FG} \frac{\partial f(\xi)}{\partial \xi} \frac{\partial \xi}{\partial N} = E_\mathrm{F} f(\xi) + \frac{E_\mathrm{FG}}{2N} f'(\xi) \\ &= E_\mathrm{F} \left[f(\xi) + \frac{1}{4} f'(\xi) \right].\end{aligned} \tag{6.71}$$

The compressibility scaling function follows similarly via the relation

$$\begin{aligned}f_\kappa &= \frac{1}{n E_\mathrm{F} \kappa} = \frac{n}{E_\mathrm{F}} \frac{\partial \mu}{\partial n} \\ &= \frac{\partial E_\mathrm{FG}}{\partial N} \left[f(\xi) + \frac{1}{4} f'(\xi) \right] + E_\mathrm{FG} \frac{\partial}{\partial \xi} \left[f(\xi) + \frac{1}{4} f'(\xi) \right] \cdot \frac{\partial \xi}{\partial n} \\ &= f(\xi) + \frac{3}{4} f'(\xi) + \frac{1}{8} f''(\xi).\end{aligned} \tag{6.72}$$

On the BCS side, the experimental results agree well with the theoretical prediction (see Fig. 6.6). On the BEC side, both the static and the dynamic measurements lie above the zero-temperature prediction. This difference is consistent with the predicted increase of the sound velocity at finite temperature [188] and with a corresponding decrease of the compressibility at finite temperature observed in [56], which increases the value of f_κ. In addition, we should not be too surprised by deviations between the experimental and theoretical results in the BEC regime, since the theoretical compressibility scaling function f_κ is derived using the formula for the binding energy in a true 2D system, whereas the experimental results are obtained in a quasi-2D system. It would therefore be interesting to see whether quasi-2D theories (for instance recently developed theories incorporating effective range corrections to the scattering length [189]) are able to reproduce and explain these deviations.

6.3.3. Quantum limited damping

We now turn our attention to the damping of the sound waves. As we have argued above, in our strongly correlated system, the mean free path l_{mfp} of the particles is much smaller than the oscillation wavelength and their collision rate is high with respect to the oscillation frequency ω. Hence the system is in the hydrodynamic regime and the damping occurs via diffusive transport of longitudinal momentum, transverse momentum and heat, whose magnitudes are proportional to the bulk and shear viscosities ζ and η and to the heat conductivity $\varkappa$ [148, 149]. This diffusive damping can be described with the sound diffusion constant

$$D_s = \frac{\eta}{\rho} + \frac{\zeta}{\rho} + \varkappa \frac{C_p - C_v}{C_p C_v} = \Gamma / k_0^2, \tag{6.73}$$

where $k_0 = \pi / l_x$ is the wave vector of the sound wave and C_p and C_v are the heat capacities at constant pressure and volume. The evolution of D_s across the BEC-BCS crossover is shown in Figure 6.7. It exhibits a broad minimum in the crossover regime $-1 < \ln(k_{\mathrm{F}} a_{2\mathrm{D}}) < 2$ and increases steeply towards the BEC and BCS limits.

k_0 : Wave vector of the sound wave

Before comparing our data to theory, we note that making quantitative predictions for transport coefficients of strongly interacting 2D Fermi gases in the low-temperature regime is still a major theoretical challenge. Approaches such as Fermi liquid theory and BCS theory [148] are only accurate at weak coupling. In the superfluid regime, the interplay between the normal and superfluid fractions of the gas lead to additional complexity. Results obtained for the high-temperature regime ($T \geq T_{\mathrm{F}}$) indicate that the shear viscosity and heat conductivity have a minimum in the strongly correlated regime [158–160] whereas the bulk viscosity is maximal near resonance yet contributes much less to the damping [190–192]. In total, high-temperature theory predicts a minimum of the sound diffusion in the crossover regime. Although our measurements are performed in the low-temperature regime, the observed behavior is in qualitative agreement with an extrapolation of the high-temperature results to the low-temperature regime, performed by Tilman Enss.

A prediction for a lower bound of D_s in the strongly interacting regime can be obtained via a simple scaling argument: The diffusion coefficient is given by the mean free path and the velocity via $D_s \sim \langle v \rangle \, l_{\mathrm{mfp}}$. For

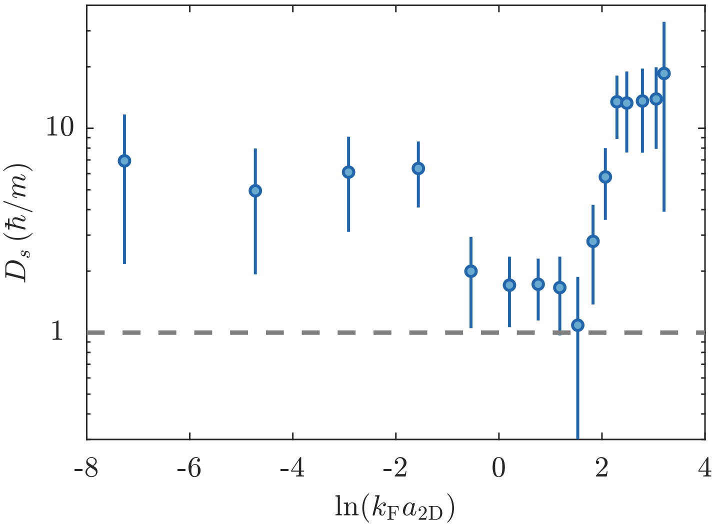

Figure 6.7. – Sound diffusion coefficient across the BEC-BCS crossover. In the strongly correlated regime, the diffusion coefficient reaches a minimum which agrees well with the universal quantum bound for diffusion at $\hbar/m$ (dashed line). The strong increases of the diffusivity at $\ln(k_{\mathrm{F}}a_{2\mathrm{D}}) \approx -1$ and $\ln(k_{\mathrm{F}}a_{2\mathrm{D}}) \approx 2$ are striking. The step towards the fermionic side might be due to a transition from the superfluid towards the normal regime, however our temperature should still be lower than the critical temperature $T_c \approx 0.15T_{\mathrm{F}}$ at this point.

a strongly interacting degenerate gas the mean free path l_{mfp} is on the order of the interparticle separation $n^{-1/2}$ and the velocity on the order of the Fermi velocity $\langle v \rangle \sim v_{\mathrm{F}} \sim \hbar n^{1/2}/m$, resulting in a diffusion coefficient $D_s \sim \hbar/m$. Since the interparticle separation is a lower limit for the mean free path, this yields a generic lower bound for the damping, which is in agreement with our measured diffusion coefficient of $D_s \approx 1.8(2)\hbar/m$ in the strongly correlated regime. The sound diffusion is given by the sum of three contributions, therefore this value at the same time gives an upper bound for the diffusivities due to shear and bulk viscosity and for heat diffusion. Thus our strongly interacting 2D Fermi gas is a nearly perfect fluid despite the fact that scale invariance is broken and that the system is not at a quantum critical point.

6.4. Conclusion

In this chapter we have presented measurements of sound propagation and attenuation in a strongly interacting homogeneous 2D Fermi gas across the BEC-BCS crossover. Since the gas is strongly interacting, a hydrodynamic description has been used to relate the speed of sound to the equation of state of the gas and to relate the damping of the sound waves to diffusion constants. The sound velocity was found to extrapolate well between the limiting cases of weakly interacting Bose gases for $\ln(k_{\mathrm{F}}a_{2\mathrm{D}}) \ll -1$ and ideal Fermi gases for $\ln(k_{\mathrm{F}}a_{2\mathrm{D}}) \gg 1$. These limits are given by the phonon part of the Bogoliubov dispersion relation with $\mu = gn$ and by the speed of sound of the Bogoliubov-Anderson mode, respectively. Although we expect the gas to be in the superfluid regime for a large range of interaction strengths, we could not discriminate between first and second sound in our experiment. This can be explained by the fact that both sound modes are only weakly coupled in strongly interacting Fermi gases. Our measurement of a density wave therefore corresponded to a measurement of almost pure first sound.

The damping of sound shows a clear minimum in the strongly correlated regime. This minimum is compatible with quantum limited damping of order $D \sim \hbar/m$, originally predicted in the context of field theories with gravity duals and motivated here by lower limits on the mean free path in a kinetic picture. Simultaneously, we demonstrated that the diffusivities of each individual channel cannot be much larger than this lower value, indicating that the strongly interacting 2D Fermi gas is a nearly perfect fluid. Since the 2D Fermi gas is a system with broken scale invariance, this particular property is not needed for perfect fluidity. Instead we confirm that perfect fluidity is due to strong correlations.

Our results are in line with a range of theoretical predictions [157–161, 164, 165] as well as several experimental results performed in the groups of Michael Köhl [57, 58], John Thomas [162], Martin Zwierlein [163], Joseph Thywissen [59, 166] and Giacomo Roati [167], which found quantum limited shear viscosity and spin diffusion in ultracold 3D and 2D Fermi gases.

Finally, our results may provide a benchmark for the development of theories for the strongly interacting gas. Very recently, calculations using a Gaussian pair fluctuations approach have been able to reproduce the first sound velocity in the strongly correlated gas across the BEC-BCS crossover [193].

Outlook

There are a few open questions which can be addressed in future measurements. A first interesting measurement could be the study of sound attenuation in dependence of the wave vector of the wave and the transition from diffusive to Landau-type attenuation as seen in [168] in unitary 3D Fermi gases. Another interesting extension of our measurements would be to study the temperature dependence of D_s as done in [168]. In the fermionic regime, this would allow us to observe whether there is a maximum of D_s at the critical temperature of superfluidity, similar to measurements in ^{3}He [194]. In the deep BEC regime, control over the temperature of the gas would enable studies of second sound in a strongly interacting Bose gas [183, 184].

7. Phase Coherence and Superfluidity in 2D Fermi Gases

The reduced dimensionality of a two-dimensional gas has strong effects on its physical properties. We have seen in the last chapter that the strong confinement influences the collisional properties of the interacting gas. Another striking difference to the three-dimensional case is the fact that in reduced dimensions, thermal fluctuations are enhanced, destroying long-range order for any nonzero temperature in the thermodynamic limit. As first observed by Peierls ([195], cited by [196]), one- and two-dimensional systems cannot exhibit crystal structures, since thermal fluctuations grow linearly with system size in 1D and logarithmically in 2D. The argument has been formalized by N. Mermin and H. Wagner [1] and by P. Hohenberg [2] and is known today as the Mermin-Wagner-Hohenberg theorem. It states that in a system with short-range interactions and dimensionality less then three, there can be no spontaneously broken continuous symmetry at nonzero temperature. This forbids for instance an ordered phase of the wave function and therefore, phenomena such as Bose-Einstein condensation or superfluidity should not be possible in 2D. The two-dimensional case is in fact special: The decay of coherence in space is logarithmically slow. While this technically prohibits long-range order for large systems, typical experimental systems are small enough that a significant level of coherence can survive over the scale of the sample. Still, thermal fluctuations are enhanced with respect to the 3D case and one would naively expect phenomena relying on phase coherence to play a minor role in reduced dimensions.

The physical reality however paints a very different picture: While the exact mechanism at play are still unclear, two-dimensional structures seem to play a critical role in almost all materials exhibiting superconductivity at high temperatures (i.e. reachable with liquid Nitrogen). This is well visible when one plots the critical temperature for of a superconductor over its Fermi temperature in a so-called Uemura-Plot (after Yasutomo Uemura [197, 198]). In Figure 7.1 an Uemura plot is shown that was recently created by N. Luick [135] with data from [8] and [49]. It is striking to see that the strongly correlated 2D materials, i.e. the cuprates, iron-pnictides, the magic angle bilayer graphene and the two-dimensional atomic Fermi gas, are consistently very close to $T_c/T_\mathrm{F} = 0.1$, which is expected to be an upper limit in the 2D BEC-BCS crossover [199].

In order to shed light on this complex topic, some experiments to test phase coherence and measure superfluidity in a two-dimensional Fermi gas have been carried out in the course of this thesis. The results have been obtained mainly by my colleagues Niclas Luick and Lennart So-

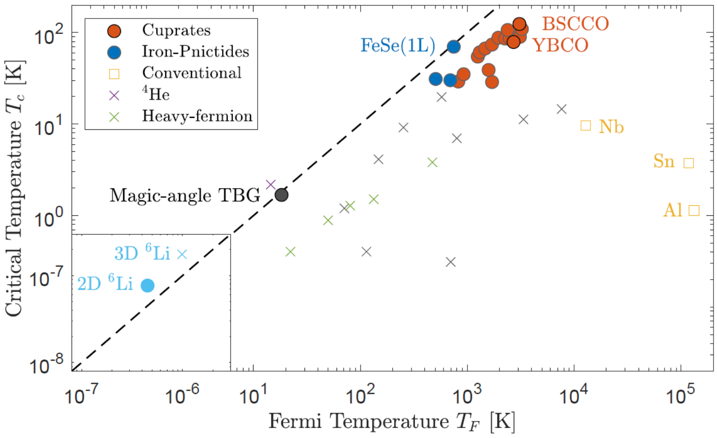

Figure 7.1. – Critical temperature T_c of several supercondcutors as a function of their Fermi temperature T_F. The plot is reproduced from [135] with data from [8] and [49]. The highest values of T_c/T_F are reached in materials featuring two-dimensional structures. Conventional materials conversely appear on the bottom right hand side of the graph, at low T_c/T_F. Atomic 2D-Fermi gases are found at $T_c \sim 0.1\,T_\mathrm{F}$ with Fermi temperatures of the order of µK.

birey and are presented in greater detail in their respective theses [135][1]. I will here present some of the results, since they relate closely to the measurements of sound propagation shown in the previous chapter. The next few sections will deal with the realization of a Josephson junction in a 2D Fermi gas. Josephson junctions and their applications are prime examples of technologies relying on quantum mechanics and in particular on the phase coherence between two superconductors or superfluids in our case. Both the experimental system and the methods utilized are very similar to the methods shown earlier. In fact, our sound measurements can be seen as a limiting case of the measurements with a Josephson junction geometry without barrier. In later sections, I will show measurements of the critical velocity in a 2D gas. Here, sound waves present one of the fundamental excitations limiting superfluidity in a two-dimensional gas.

---

[1] The thesis of L. Sobirey is to be published in the coming months.

7.1. The Josephson effect

In the following sections, I report on the experimental realization of a Josephson junction in an ultracold 2D Fermi gas, which has been achieved during the first year of my participation in the Moritz group. These results have mainly been obtained by Niclas Luick and are presented in great detail in his thesis [135]

> Niclas Luick. *An ideal Josephson junction in an ultracold two-dimensional Fermi gas*, PhD thesis, Universität Hamburg, 2020.

as well as in the following publication [177]:

> Niclas Luick, Lennart Sobirey, Markus Bohlen, Vijay Pal Singh, Ludwig Mathey, Thomas Lompe and Henning Moritz. An ideal Josephson junction in an ultracold two-dimensional Fermi gas. *Science* **369**(6499), 89-91 (2020).

Parts of this chapter are reproduced from this publication. My contribution to this project consisted mainly in machine maintenance as well as in the verification of data analysis and mathematical models.

One of the reasons quantum mechanics is counter-intuitive in many ways is the fact that its phenomena are only manifest at small scales. Our everyday world is unaffected by quantum mechanical effects due to decoherence in large systems or at long time scales and we are simply not exposed to it. The Josephson effect is one of the hallmark examples of a quantum effect that affects macroscopic structures. First predicted by Brian Josephson in 1962 [200] and later observed by Anderson and Rowell [201], this effect allows an electric current to flow between two superconductors that are separated by a small insulating barrier, a so-called Josephson junction, even without an externally applied voltage. Instead the current is driven by the quantum-mechanical phase difference between the wave functions of the two superconductors. Since the discovery of the Josephson effect, it has been put to use in a variety of different applications, providing for instance the basis for SQUIDs (superconducting quantum interference devices), for a new voltage standard or for the realization of qubits. The primary advantage of Josephson junctions is their high sensitivity to quantum mechanical effects while offering the possibility to incorporate them in classical electrical circuits. These devices therefore bridge the gap between quantum mechanics and classical physics, which strongly suggests their use in high sensitivity metrology applications, in the field of quantum information, or as probes for quantum mechanical states of matter.

7.1.1. Principle of the Josephson effect

The mechanism behind the Josephson effect is the tunneling of Cooper pairs through the tunneling junction between the two superconductors. In contrast to the classical case, this tunneling is not driven by a voltage drop across the junction, but rather by a difference between the phases of the so-called order parameters of the two sides. The main relation defining a Josephson junction is the sinusoidal current-phase relation

$$I(\varphi) = I_c \sin\varphi, \tag{7.1}$$

which relates the current I to the phase difference $\varphi = \varphi_B - \varphi_A$. I_c is called the critical current of the junction and depends both on the coupling strength between the two superconductors and on the superconducting densities. When a voltage V is applied across the junction, the phase difference between the two sides will evolve in time according to

$$\frac{\partial}{\partial t}\varphi = \frac{2eV}{\hbar}. \tag{7.2}$$

I : Current through the junction
$\varphi_{A/B}$: Phase of the wavefunction of superconductor A/B
φ : Phase difference $\varphi = \varphi_B - \varphi_A$
I_c : Critical current
V : Voltage applied across the junction
e : Electron charge

Derivation of the main relations of a Josephson junction

Let us give a quick derivation of the main relations governing the physics of Josephson junctions. In Ginzburg-Landau theory, the superconducting state of a metal close to the phase transition to the superconducting state can be characterized by a complex number ψ, the order parameter. It can be interpreted as the wave function of the superconducting component, i.e. the Cooper pairs. Then the order parameter is given by $\psi(\mathbf{r}, t) = \sqrt{n_s(\mathbf{r}, t)}e^{i\varphi_s(\mathbf{r},t)}$, where $\varphi_s(\mathbf{r}, t)$ is the phase of the wave function. We assume that two supercondcutors A and B are brought close to each other so that there is a small coupling of strength K between the two wave functions. A voltage V is applied between the two sides, leading to an energy shift of $\Delta E = \pm 2eV$ for a Cooper pair tunneling between the sides. This results in a Schrödinger equation of the form

$$i\hbar\frac{\partial}{\partial t}\begin{pmatrix}\psi_A \\ \psi_B\end{pmatrix} = \begin{pmatrix} eV & K \\ K & -eV\end{pmatrix}\begin{pmatrix}\psi_A \\ \psi_B\end{pmatrix}.$$

$\psi(\mathbf{r}, t)$: Order parameter of the superconductor (SC)
$n_s(\mathbf{r}, t)$: Density of the order parameter
$\varphi_s(\mathbf{r}, t)$: Phase of the order parameter
K : Coupling strength between SC A and B
ΔE : Energy shift SC A and B

With $\frac{\partial}{\partial t}\psi_{A/B} = \left(\frac{\dot{n}_{A/B}}{2\sqrt{n_{A/B}}} + i\dot{\varphi}_{A/B}\sqrt{n_{A/B}}\right)e^{i\varphi_{A/B}}$, this yields the following two equations:

$$\frac{\dot{n}_A}{2\sqrt{n_A}} + i\dot{\varphi}_A\sqrt{n_A} = \frac{1}{i\hbar}\left(eV\sqrt{n_A} + K\sqrt{n_B}e^{i\varphi}\right)$$
$$\frac{\dot{n}_B}{2\sqrt{n_B}} + i\dot{\varphi}_B\sqrt{n_B} = \frac{1}{i\hbar}\left(-eV\sqrt{n_B} + K\sqrt{n_A}e^{-i\varphi}\right),$$

where $\varphi = \varphi_B - \varphi_A$ is the phase difference between the two order parameters. The equations for $\dot{n}_{A/B}$ and $\dot{\varphi}_{A/B}$ are given by the real and imaginary parts of the two equations:

$$\dot{n}_A = \frac{2K}{\hbar}\sqrt{n_A n_B}\sin\varphi, \qquad \dot{\varphi}_A = -\frac{1}{\hbar}\left(eV + K\sqrt{\frac{n_B}{n_A}}\cos\varphi\right)$$
$$\dot{n}_B = -\dot{n}_A, \qquad \dot{\varphi}_B = \frac{1}{\hbar}\left(eV - K\sqrt{\frac{n_A}{n_B}}\cos\varphi\right)$$

The current flowing across the junction is given by $I = e\dot{n}_A$. Assuming in addition that the superfluid density is roughly equal on both sides of the junction, $n_A \approx n_B$, we then obtain the two fundamental equations of a Josephson junction:

$$\begin{aligned} I(\varphi) &= I_c \sin\varphi \\ \frac{\partial}{\partial t}\varphi &= \frac{2eV}{\hbar}. \end{aligned}$$

The critical current I_c is given by $I_c = \frac{2eK}{\hbar}\sqrt{n_A n_B}$

7.1.2. The AC - and DC - Josephson effects

There are three effects that are typically distinguished which can occur in a simple Josephson junction which have found important technical and scientific applications.

The DC - Josephson effect

This is the effect described above, in which a continuous (DC) tunneling current occurs without an external applied voltage. It is the key principle behind SQUIDs (superconducting quantum interference device), devices which allow to measure magnetic fields to very high precision[2]. The basic idea behind a SQUID is to translate changes in magnetic field to changes of the resistive behavior of the device.

Consider a superconducting loop in a magnetic field that incorporates two Josephson junctions, each supporting a voltage-free current of I_c, as shown in Figure 7.2. Without external magnetic field, the flux enclosed by the loop is zero and the device supports a bias current of $2I_c$ without voltage drop. Since the phase of the order parameter must be unique at each point of the superconductor, the change in phase along the loop must add up to a multiple of 2π and the magnetic flux enclosed by the superconducting loop must therefore be a multiple of the magnetic flux quantum $\Phi = h/2e$. If a small magnetic field is switched on, a screening current I_s will start flow through the superconducting loop, such as to cancel the additional flux through the loop. This screening current flows in addition to the externally applied current I, increasing the current in one of the two arms, thus reducing the maximum possible bias current which can be applied without voltage drop across the device. Once the flux enclosed by the loop reaches $\Phi/2$, it becomes energetically favorable to enclose one more flux quantum and the current inside the loop reverses. From this point onwards, the maximum current supported by the SQUID increases again until it reaches the original value of $2I_c$ at an external flux of Φ. When driving the SQUID with a constant bias current close to the maximum value $2I_c$, there is a voltage drop across the device, because the critical current is exceeded along one arm. However, this voltage drop oscillates periodically with the strength of the applied magnetic field and the corresponding screening current. This oscillation can can be used to determine the strength of unknown magnetic fields.

Φ: Magnetic flux quantum
I : Applied DC current
I_s : Screening current

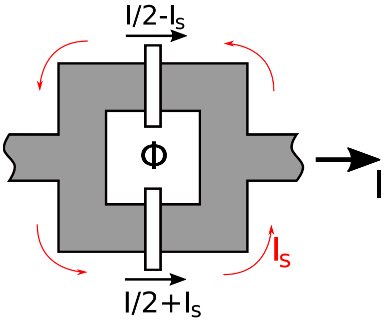

Figure 7.2. – Scheme of a DC-SQUID magnetometer. A superconducting loop is split into two halves by two Josephson junctions. When the device is supplied with a bias current I, a current of $I/2$ flows through each arm. A magnetic flux Φ induces a screening current I_s. If the current in one of the two arms increases above I_c, a voltage drop across the device occurs. This principle is used to measure small changes in magnetic field.

[2] Typical SQUIDS have a sensitivity which is sufficient to measure the stray field of a single atomic layer with a lateral size of a few mm^2 of magnetic material [202]

The AC - Josephson effects

The two AC - Josephson effects relate continuous voltages to frequencies. This correspondence allows for a very precise determination of voltages and is the basis for the usage of Josephson junctions as a voltage standard. The standard AC - Josephson effect occurs when applying a fixed voltage V_{DC} across the junction. In this case, the phase difference between the sides evolves linearly in time, leading to an alternating current with a frequency $f = eV_{\text{DC}}/\pi\hbar$.

The inverse AC - Josephson effect occurs when the junction is driven with a voltage of the form $V(t) = V_{\text{DC}} + V_{\text{AC}} \cos(\omega t)$, which can be realized for instance by irradiating the Josephson junction with a radio-frequency signal. The resulting current is typically an alternating current, however for $V_{\text{DC}} = n\hbar\omega/2e$, i.e., when the energy drop across the junction matches multiples of the energy of the AC frequency, the current becomes a DC current (for a derivation, see Appendix B.3). While this formula suggests that this happens only at very specific values of the voltage, the Josephson junction in reality tends to phase-lock with respect to the oscillation frequency and the voltage-current curve of a Josephson junction exhibits a series of plateaus (compare fig. 7.3). This effect has been first observed by Shapiro in 1963 [203] and the steps in the voltage-current curve are often called Shapiro-steps.

The inverse AC - Josephson effect can be used to define a reference voltage standard. The high precision of frequency generation and measurement techniques allowed already in 1997 to generate these voltage steps with a high accuracy better than 3 parts in 10^{19} [204]. With the redefinition of the SI units in 2019, the numerical values of the elementary charge and Planck's constant have been set as fundamental constants used for the definitions of the SI units. Josephson junctions therefore provide a robust standard of the Volt as well as a relatively accessible way to create a reference Volt in the lab[3].

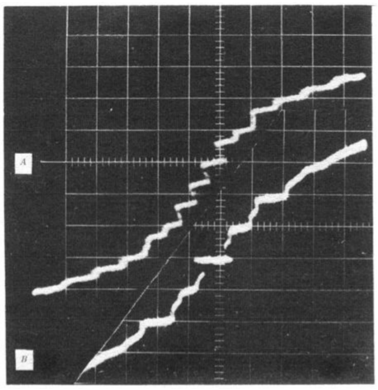

Figure 7.3. – Shapiro's observation of steps of constant voltage in the V(I) curve of a superconducting tunneling junction for two different microwave frequencies V_{AC}. (Figure adapted from [203]). The upper curve is obtained for a microwave frequency of $\nu_A = 9300\,\text{MHz}$. The steps occur at multiples of $h\nu_A/2e = 19.2\,\mu\text{V}$. The lower curve is obtained for a higher frequency of $\nu_B = 24850\,\text{MHz}$, corresponding to $h\nu_B/2e = 51.4\,\mu\text{V}$. For A, the vertical scale is 58.8 µV/cm and the horizontal scale is 67 nA/cm, for B, the scales are 50 µV/cm and 50 µA/cm.

The nonlinear current phase relation

The characteristic feature of a Josephson junction is the nonlinear (sinusoidal) relation between current and phase difference across the junction. It lies at the heart of the three effects described above and enables the use of Josephson junctions in SQUIDs or to define voltage standards. It is also the fundamental property which enables the use of Josephson junctions as one of the most promising candidates for qubits, the building block for quantum computing circuits.

The prototypical realization of a Josephson qubit is the charge qubit (also called the Cooper pair box). Here, a small superconducting island is coupled to a superconducting reservoir via a Josephson junction[4] (compare fig. 7.4). The quantum states $|n\rangle$ of the qubit is given by the number n of excess Cooper pairs on the superconducting island. In principle, such a circuit implements an LC-circuit and can thus be described by a harmonic oscillator with equidistant energy levels. As discussed in [208], the sinusoidal current phase relation of the Josephson junction

---

[3] The proportionality constant of $h/2e = 2.068\,\text{mV/THz}$ being rather small, a single Josephson junction only allows to create voltage steps of the order of $\sim 0.2\,\text{mV}$ with typical RF frequencies. Since the late 1980 however, arrays of Josephson junctions allowed for the creation of highly accurate voltages up to $\sim 10\,\text{V}$ [205].

[4] In order to reduce noise and decoherence, other Josephson qubit designs have been developed, most notably the transmon [206], which was recently used in [207] for a proof of concept algorithm reaching quantum supremacy. These devices increase the relaxation times into the ms range and increase the dephasing times by a factor ~ 400 over the simple charge qubit [206]. Their description can be reduced to the description of a single charge qubit.

however introduces an anharmonicity L_J in the inductance, which shifts the energy levels. Due to this shift, a specific transition can be individually addressed, generating the effective two-level system of a qubit (compare fig. 7.5).

L_J : Nonlinear Josephson inductance

To see the origin of this nonlinearity, it is helpful to remember that an inductance L relates the voltage across the inductor to the variation of the current. For the Josephson junction, this yields $V = L_J \dot{I}$. From the current-phase relation 7.1 of a Josephson junction, we obtain $\dot{I} = I_c \dot{\varphi} \cos(\varphi)$ via differentiation. We can now replace $\dot{\varphi}$ in equation 7.2 and obtain the relation $V = \frac{\hbar}{2e} \frac{\dot{I}}{I_c \cos\varphi}$. Thus the quantity $\frac{\hbar}{2e} \frac{\dot{I}}{I_c \cos\varphi}$ can be interpreted as a nonlinear inductance.

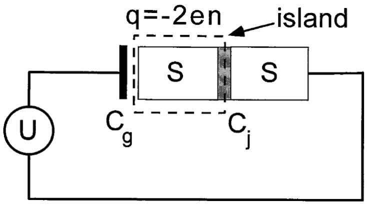

Figure 7.4. – Schematics of a charge qubit. A superconducting island is in contact with a superconductor via a weak link, forming a Josephson junction. Excess Cooper pairs can flow onto the island when the chemical potential of the island is modified using a gate voltage U. The capacitance of the gate electrode controlling the occupation of the states $|n\rangle$, and of the Josephson junction are denoted by C_g and C_J, respectively. (Figure adapted from [209]).

7.2. The Josephson effect in ultracold atomic systems

The wide interest for Josephson junctions and their different applications have been a strong incentive to build Josephson junctions in ultracold atom systems and to make use of their high sensitivity in the toolkit of quantum simulation. The idea of using Bose-Einstein condensates in optical traps to create Josephson junctions has been proposed in 1986 [210], even before the creation of the first atomic BEC in 1995 [20, 21]. The first ultracold atom Josephson junctions were realized with BECs of ^{87}Rb, as an array of junctions created via an optical lattice potential [211], and soon after as isolated junctions in a double well potential [212, 213]. More recently, ultracold atomic Josephson junctions have also been created in reduced dimensions [214] or with variable interactions in bosonic and fermionic gases [215, 216]. They have been used to create an atomic SQUID [217]. Furthermore, dissipation of Josephson dynamics has been examined [218, 219] and it has been shown that atomic Josephson junctions can be used to probe the order parameter of the superfluids themselves [177, 220].

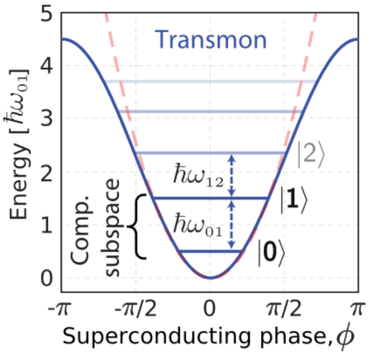

Figure 7.5. – Energy levels of a transmon qubit. A transmon (or a Cooper-pair-box) can be seen as an LC-circuit with a nonlinear inductance, which introduces an anharmonicity into the system. The energy eigenstates are not equidistant anymore, $\omega_{12} < \omega_{01}$, and can be addressed individually. The computational subspace is reduced to two levels of this anharmonic oscillator. (Figure adapted from [208].)

7.2.1. Josephson oscillations and self-trapping

The main difference between Josephson junctions realized in ultracold atom systems and in solid state systems lies in the fact that different variables are held constant. In an electronic system, applied voltages hold the chemical potential of the electrodes at a constant level. In ultracold atom experiments however, the total particle number is conserved and upon tunneling of particles, the relative particle number and hence the chemical potential difference will vary. After creating a density or phase difference between the wells, this will lead to periodic oscillations of the particles between the two sides of the junction. In order to truly recreate the DC - Josephson effect, a more complicated setup with a moving barrier is needed, as it has been utilized in [220].

The occurrence of oscillations can be understood in a simple 1D case: Consider a BEC trapped in a symmetric double well potential, with a small particle $z = (N_1 - N_2)/(N_1 + N_2)$ imbalance between the wells

z : Relative particle imbalance

1 and 2. Due to the particle imbalance, the chemical potential on one side of the barrier will be higher than on the other side, which advances the phase of the wave function of one condensate with respect to the other condensate. This in turn induces a tunneling current between the two condensates according to $\dot{z} \approx -\sin(\varphi)$, which reduces the particle imbalance. Since there is still a phase difference between the two sides, the current 'overshoots' and the particle imbalance is reversed, leading to a periodic back and forth between the two wells. For small initial imbalances, the phase difference evolves slow enough that the current has time to invert the entire imbalance. Yet for high enough imbalances however, the phase difference advances so quickly that the particles do not have enough time to tunnel into the other potential well, trapping the system in a state of imbalance which shows only small and fast oscillations, the so-called self-trapping regime. Both regimes have been observed for the first time in [212].

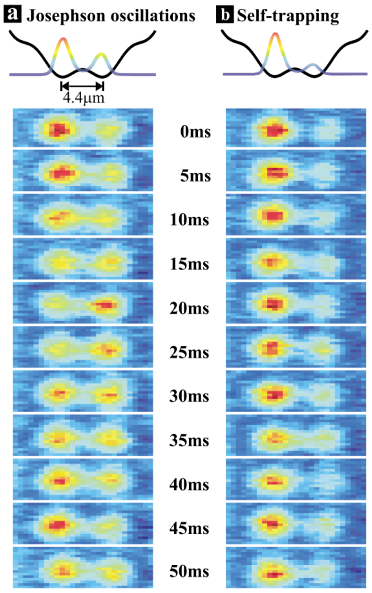

Figure 7.6. – Observation of the two regimes of cold atom Josephson junction. Figure from [212]. a) Josephson regime: The initial imbalance is small enough that the phase difference rotates only slowly. The condensate has time to tunnel through the barrier. b) Self-trapping regime: The imbalance is higher and the phase rotates so quickly that the condensate does not have enough time to tunnel. The imbalance is frozen.

The two-mode model

The two regimes can be understood more quantitatively in the so-called two-mode model, developed in [221]: The behavior of a weakly interacting BEC is described by the Gross-Pitaevskii equation

$$i\hbar\frac{\partial\Psi}{\partial t} = -\frac{\hbar^2}{2m}\Delta\Psi + (V_{\text{ext}}(\mathbf{r}) + g|\Psi|^2)\Psi,$$

where g is the interaction parameter of the gas. By making the Ansatz $\Psi(\mathbf{r},t) = \psi_1(t)\Phi_1(\mathbf{r}) + \psi_2(t)\Phi_2(\mathbf{r})$ for the wave function of the condensate in the two wells, this leads to two coupled equations for the amplitudes ψ_i in each well:

$$\begin{aligned} i\hbar\frac{\partial\psi_1}{\partial t} &= (E_1 + U_1N_1)\psi_1 - K\psi_2 \\ i\hbar\frac{\partial\psi_2}{\partial t} &= (E_2 + U_2N_2)\psi_2 - K\psi_1 \end{aligned}$$

N_1 and N_2 are the particle numbers in each well and the parameters E_i, U_i and K are given by

$\Psi(\mathbf{r},t)$: Condensate wave function
E_i : Energy eigenstate of the i-th potential well
U_i : Interaction energy
K : Coupling strength between the wells

$$\begin{aligned} E_i &= \int \left[\frac{\hbar^2}{2m}|\boldsymbol{\nabla}\Phi_i|^2 + |\Phi_i|^2 V_{\text{ext}}\right] d\mathbf{r} \\ U_i &= g\int |\Phi_i|^4\, d\mathbf{r} \\ K &\approx -\int \left[\frac{\hbar^2}{2m}(\boldsymbol{\nabla}\Phi_1\cdot\boldsymbol{\nabla}\Phi_2) + \Phi_1 V_{\text{ext}}\Phi_2\right] d\mathbf{r}. \end{aligned}$$

These coupled equations are similar to the equations introduced in the derivation of the main equations of Josephson junctions. The E_i are the energies of the occupied state in each well and K is again the coupling strength between the wells. The interaction terms U_iN_i are new however, which leads to a nonlinearity in the following steps. The equations can be brought into the form

$$\dot{z} = -\sqrt{1-z^2}\sin(\varphi) \tag{7.3}$$

$$\dot{\varphi} = \Lambda z + \frac{z}{\sqrt{1-z^2}}\cos(\varphi) + \Delta E, \tag{7.4}$$

in terms of the phase difference φ and the population imbalance between the two sides, where $\Delta E = (E_1 - E_2 + N(U_1 - U_2))/4K$ and $\Lambda = N(U_1 + U_2)/(4K)$ with $N = N_1 + N_2$ are interaction-dependent parameters.

For a symmetric system, the energies of the condensates in both wells are the same and $\Delta E = 0$. Linearizing the equations in z, one obtains

$$\dot{z} \approx -\sin(\varphi) \tag{7.5}$$

$$\dot{\varphi} \approx (\Lambda + \cos(\varphi))z, \tag{7.6}$$

which leads to a sinusoidal relation between current and phase: $I = \dot{z}N/2 = I_0 \sin(\varphi)$. Linearizing the equations in φ as well and setting $U_1 \approx U_2 \approx U$, we recover harmonic oscillations with a frequency $\omega = \sqrt{2UNK + 4K^2}$. For a review of the different regimes described by the two-mode model, I would like to refer the reader to [222].

Limitations of the two-mode model

For our purposes, the two-mode model cannot easily be used. The two-mode model implicitly assumes that the wave function of the condensates can be described by a single wave function in each well. The parameters E_i, U_i and K determining the dynamics of the system are determined microscopically by the overlaps between the wave functions in the different wells. In our experiment, Josephson junctions are created by imprinting a thin barrier in the middle of the box potential we have already introduced in the previous chapters. This results in a system which allows for additional dynamics (i.e. sound modes) due to its relatively large extent. These dynamics involve wave functions that are superpositions of different basis wave functions, which makes the calculations of the parameters rather involved. The description in terms of a condensate occupying only two modes is therefore not apt to describe our system.

In addition, the system is subject to dissipation, which is not included in the two-mode description. In addition to the diffusive attenuation mechanism we have studied before, the coherent dynamics can decay via the creation of vortices at the barrier (compare [135, 177, 219, 223]). In the following, we will ignore the effects of damping and describe the multi-mode system with an LC-circuit model.

7.3. A Josephson junction in an ultracold 2D Fermi gas

Some examples of Josephson junctions in systems of different sizes are shown in Fig. 7.7. As mentioned before, the experimental setup is very similar to the one used for the sound measurements. A spin-balanced

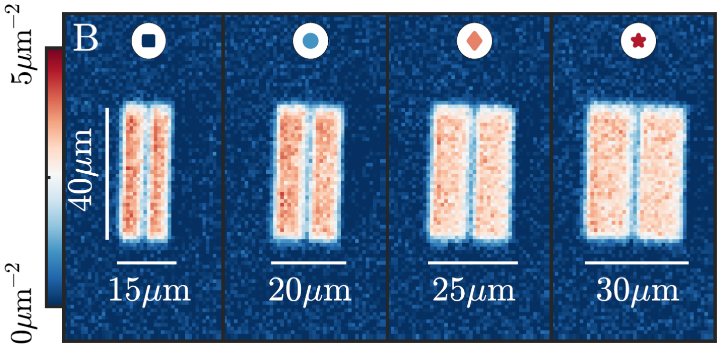

Figure 7.7. – Examples of Josephson junctions in 2D gases with different geometries. As before, we denote with l_x the direction of the oscillations, and with l_y the direction perpendicular to l_x, determining the length of the barrier.

mixture of ^{6}Li atoms in the lowest two hyperfine states is trapped in a box potential as described previously. Again, the densities are chosen such that the sample is in the quasi-2D regime, with a temperature of $T \approx 0.03T_\mathrm{F}$. The horizontal confinement is created with a DMD. In addition to the box itself, the DMD also projects a thin barrier in the middle of the box, separating the gas into two parts, which form the two sides of the Josephson junction. The barrier can be described by a Gaussian profile of waist $w = (0.81 \pm 0.06)\,\mu\mathrm{m}$, which is limited by the optical resolution of the imaging system ($\sim 700\,\mathrm{nm}$). In the imaging plane, each DMD pixel has a width of roughly $0.1\,\mu\mathrm{m}$. The height of a narrow potential barrier can therefore be adjusted by changing the width of the barrier on the DMD.

φ_0 : Imprinted initial phase difference

ΔN : Particle imbalance

The experimental procedure is essentially the same as before: One half of the system is illuminated for a short time ($\leq 20\,\mu\mathrm{s}$) using the second DMD. This advances the phase on this side by an amount φ_0 with respect to the other side and induces dynamics. Then, the system evolves freely for a time t and is finally imaged either in-situ or after a short time of flight in a weak underlying magnetic trap after all optical trapping potentials have been switched off. The in-situ imaging gives us access to the density distribution in the system. As with the sound measurements, we take the mean of the densities in the left and right box halves to extract the particle imbalance $\Delta N = N_\mathrm{L} - N_R$, and hence average out the dynamics inside the boxes. By releasing the 2D confinement and letting the cloud evolve for a quarter period in the underlying harmonic potential due to the remaining magnetic field curvature before imaging, we perform matter wave focusing [138] and gain access to the momentum distribution of the gas [60]. The condensate shows a characteristic peak at zero momentum. When the phase difference between the two sides is nonzero, the position of the peak shifts slightly, which gives us access to the phase difference $\varphi(t)$ between the sides of the box. The phase measurement is calibrated from the repeating displacement pattern for different phase excitation times (compare Fig. 7.8).

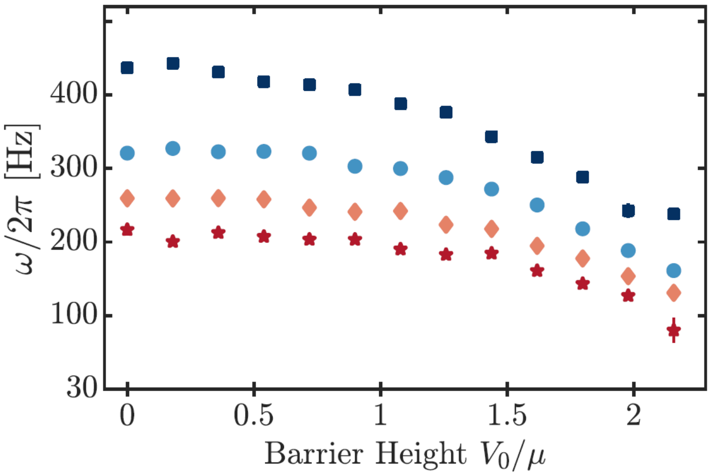

Figure 7.9. – Frequencies of the Josephson oscillations at different barrier heights for box sizes of 15 µm (blue squares), l_x = 20 µm (blue circles), 25 µm (orange diamonds) and 30 µm (red stars). At vanishing barrier height, the frequencies are determined by the speed of sound and are proportional to $1/l_x$. The frequencies decrease for increasing barrier height. Oscillations are visible up to barrier heights of $V_0 > 2\mu$.

7.3.1. From sound waves to Josephson oscillations

In our geometry, the Josephson oscillations are visible both in particle imbalance $\Delta N(t)$ and in phase difference $\varphi(t)$. They feature a characteristic phase shift of $\pi/2$ between imbalance and phase and are weakly damped due to phononic excitations and the nucleation of vortex-antivortex pairs in the junction (see supplementary material of [177] and [223]). The frequencies of the phase and particle oscillations are shown in Figure 7.9 for different barrier heights, using the four different reservoir geometries shown in Fig. 7.7.

At zero barrier height, the dynamics consist of the sound waves we have seen before. The oscillation frequency is thus determined by the speed of sound and inversely proportional to the box length l_x. For increasing barrier height, we see a decrease in the oscillation frequency, but oscillations remain visible until the barrier potential is significantly higher than the chemical potential $V_0 > 2\mu$. Since the amplitude of the density oscillations is only a few percent ($\Delta N/N < 0.05$), the chemical potential remains lower than the barrier during the oscillations and the dynamics we see can only be due to tunneling through the barrier. With increasing barrier height, the dynamics smoothly cross over from the sound-dominated to the Josephson-dominated regimes.

The LC-model

To understand these Josephson oscillations, we use a circuit model commonly used to describe superconducting Josephson junctions [218, 224, 225]. The system without barrier is described as a simple LC-circuit, which oscillates at a frequency determined the speed of sound $\omega_s = 2\pi c/(l_x/2) = \pi c/l_x$. The current in this circuit is the particle current

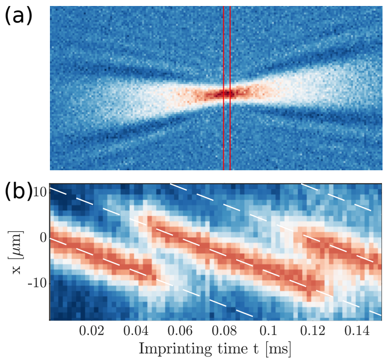

Figure 7.8. – Imaging the phase difference of the 2D gas in the box: The momentum distribution is accessed by letting the atoms evolve freely for a quarter period in an underlying weak harmonic potential, which in equilibrium yields a peak at $k = 0$. (a) During this evolution, the atoms quickly expand along the vertical direction, forming a cigar-shaped cloud whose upper and lower parts are out of focus of our microscope objectives. By tilting the imaging beam slightly with respect to the vertical, the unfocused upper and lower parts of the column are shifted to the left or right on the image, whereas the focused central part is now visible in the center of the image. We use the central slice (red box) to fit the position of the central peak. (b) Calibrating the phase measurement: By imprinting the repulsive potential for different times, we imprint different phase differences onto the two sides of the box. The image shows the central slices of the momentum distribution measured as described above for the different phase imprints $\Delta V_{\text{pulse}}t$. For increasing imprinting time, the position of the pair condensation peak shifts in space linearly, showing a periodic pattern with a period of $\varphi_0 = 2\pi \approx 7$ ms. This displacement pattern is used to calibrate the initial phase imprint for the experimental sequence. The displacement of the peak is also used to measure the phase difference during the Josephson oscillations.

$I = \frac{1}{2}\frac{\partial \Delta N}{\partial t}$ between the two sides of the junction. The capacitance $C = \frac{1}{4}\frac{\Delta N}{\Delta \mu} = \frac{V}{8}\frac{\Delta n}{\Delta \mu}$ is closely related to the compressibility of the system. It relates the energy gained by 'charging' the system with $\Delta N/2$ particles to a difference in 'voltage' $2\Delta\mu$[5]. Here, V is the total volume of the box.

The equation of motion of the LC-circuit is therefore given by

$$U_\mathrm{C} + U_\mathrm{B} = U_\mathrm{C} + L_\mathrm{B}\frac{\partial I}{\partial t} = \frac{\Delta N}{2C} + \frac{L_\mathrm{B}}{2}\frac{\partial^2(\Delta N)}{\partial t^2} = 0, \tag{7.7}$$

where U_C and U_B are the voltages across the capacitance and bulk inductance, respectively. This yields an oscillation frequency $\omega_s = \pi c/l_x = 1/\sqrt{L_\mathrm{B}C}$. With the speed of sound given by $c^2 = \frac{n}{m}\frac{\partial \mu}{\partial n}$ (cf. eq. 6.64), we find the bulk inductance to be $L_\mathrm{B} = 8ml_x^2/\pi^2 N = 8ml_x/\pi^2 n l_y$, which is proportional to the mass of the particles and to the size of the system l_x perpendicular to the junction, and inversely proportional to the length of the junction l_y. It can be interpreted as a measure of the inertia of the gas, opposing a change in current.

ω_s :	Bare oscillation frequency (without barrier)
I :	Particle current
C :	Capacitance of the system
L_B :	Bulk inductance
L_J :	Josephson inductance

As we have already motivated above, the effects of the barrier are described by an additional inductance L_J, which is connected in series to these two elements. This can be understood in the frame of our model in the following way: The phase difference between the two reservoirs of a Josephson junction develops in time as $\partial\varphi/\partial t = \Delta\mu_\mathrm{pair}/\hbar = 2\Delta\mu/\hbar$. A Josephson junction follows a current phase relation $I(\varphi)$. We can differentiate this relation with respect to time and replace $\partial\varphi/\partial t$ in the equation above to find $2\Delta\mu = \hbar/(\partial I/\partial\varphi)\cdot(dI/dt)$. Since the chemical potential difference plays the role of the voltage in our model, we see that the Josephson junction relates the voltage to the time derivative of the current, as does an inductance. We may thus identify

$$L_\mathrm{J} = \frac{\hbar}{\partial I(\varphi)/\partial\varphi} \tag{7.8}$$

as the Josephson inductance and the resulting equation of motion now reads

$$\frac{\Delta N}{2C} + (L_\mathrm{B} + L_\mathrm{J})\frac{\partial^2(\Delta N)}{2\partial t^2} = 0. \tag{7.9}$$

The additional inductance reduces the oscillation frequency of the system to $\omega = 1/\sqrt{(L_\mathrm{B} + L_\mathrm{J})C}$. Since the bulk inductance only depends on known parameters, the Josephson inductance can be easily extracted from the ratio of the oscillation frequencies with and without barrier according to

$$L_\mathrm{J} = L_\mathrm{B}\left(\frac{\omega_s^2}{\omega^2} - 1\right). \tag{7.10}$$

While the oscillation frequency is dependent on the size of the box owing to the change in bulk inductance and capacitance, the Josephson inductance should only depend on the properties of the barrier itself. Indeed, as shown in Figure 7.10, all measurements of L_J versus barrier height

[5] The factor 2 here is due to the fact that the tunneling particles are Fermion pairs whose chemical potential is twice as high as the chemical potential μ of a single atom. The additional factor 1/2 comes from the fact that we consider the particle numbers in the different halves of the system: $\Delta n_{R/L} = \Delta N_{R/L}/(V/2)$.

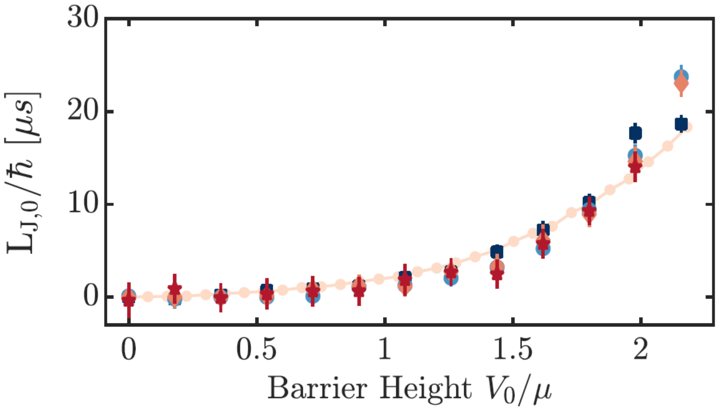

Figure 7.10. – Extraction of the Josephson inductance versus barrier height for the different box sizes of figure 7.7. While the oscillation frequencies are dependent on the system size, the Josephson inductances collapse onto one line and depend only on the barrier height. We obtain the calibration of the barrier height V_0 by matching the data to a numerical simulation (light red line) [177].

collapse onto one curve, independent of box size, which shows that the inductance of the junction depends only on the barrier height. We can therefore use this model to separate the physical effects originating in the barrier from the dynamics due to the bulk of the material, without knowledge of the microscopic quantities such as wave function overlaps for instance.

7.3.2. Extracting the nonlinear current-phase relation

Let us finish this part by discussing the nonlinearity of the current-phase relation. As we have motivated, this is the origin of the nonlinearity of the inductance and thus fundamental for some applications of Josephson junctions, in particular for their use as qubits. In contrast to the solid state case, it is not possible in a cold atom system to apply a fixed phase difference to the junction and measure the current. While it is possible in principle to measure the instantaneous particle current $I(\varphi)$ during the oscillations to obtain the current-phase relation, it is experimentally challenging to do so. The small oscillation amplitude of about 30 particles implies large relative errors, and the noise in the particle numbers will be increased substantially during differentiation. This route would therefore require an exceedingly large amount of data.

In order to probe the current-phase relation of our Josephson junction, we use the fact that a nonlinearity changes the period of an oscillation for large excursions. Similar to the increase of the oscillation period of a rigid pendulum for large initial excursions, the anharmonicity of a Josephson junction leads to a decrease of the oscillation frequency for large initially imprinted phase differences. This behavior is also predicted by the two-mode model [222] and has been observed in cold atom Josephson junctions for instance in [216]. We use the information contained in this frequency shift to probe the nonlinear current phase relation.

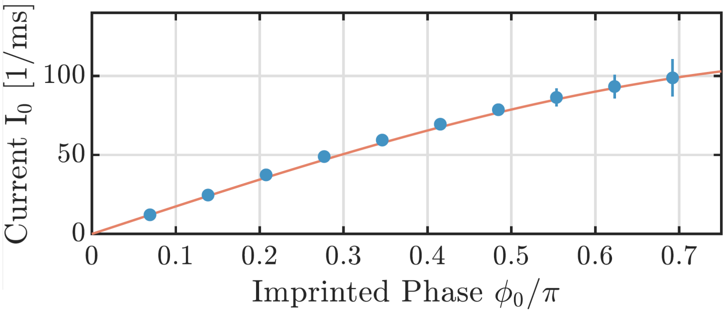

Figure 7.11. – Effective current I_0 through the junction. The data points are obtained by integrating the values of $L_{J,0}$ obtained from the reduced oscillation frequencies according to $\partial I/\partial\varphi = \hbar/L_J$. Our data is in excellent agreement with the theoretical prediction $I_0(\varphi_0) = 2I_c\sin(\varphi_0/2)$ for an ideal Josephson junction (red line), where the initial slope is determined from the first three data points.

$L_{J,0}(\varphi_0)$:	effective Josephson inductance
$I_0(\varphi_0)$:	effective current

To do this, we determine an effective inductance $L_{J,0}(\varphi_0)$ according to equation 7.10 for various initial phase imprints φ_0. Rearranging relation 7.8, we then calculate an effective current

$$I_0(\varphi_0) = \int_0^{\varphi_0} \frac{\hbar}{L_{J,0}(\varphi_0^{'})} d\varphi_0^{'} \tag{7.11}$$

by performing a Riemann sum over all experimentally determined values of $\hbar/L_{J,0}(\varphi_0^{'})$ with $\varphi_0^{'} < \varphi_0$. Note that both $L_{J,0}$ and I_0 are different from the instantaneous inductance and current during the oscillations, and rather represent effective quantities which relate the initial phase imprint φ_0 to quantities of dimensions of an inductance or a current. Nevertheless, we can still connect this effective current phase relation $I_0(\varphi_0)$ back to the instantaneous current phase relation $I(\varphi)$. For a system that follows the ideal current phase relation $I(\varphi) = I_c\sin(\varphi)$, we find that the resulting effective relation should read [177]

$$I_0(\varphi_0) \approx 2I_c \sin\frac{\varphi_0}{2}. \tag{7.12}$$

The derivation of this relation can be found in appendix B.4.

The comparison between the data and the expected effective current-phase relation is shown in Fig. 7.11. Our data is in excellent agreement with this theoretical prediction, indicating that our junction is an ideal Josephson junction. This strongly implies that the current across the junction is indeed a supercurrent, driven by the phase difference between the two superfluids.

This junction provides a useful tool to investigate superfluid properties of the gas in the strongly correlated regime, owing to its sensitivity with respect to the phase of the superfluid. In further measurements [177], which are not discussed in this thesis, we have ramped the gas to various points in the BEC-BCS crossover and imprinted a phase difference between the two sides. We could observe Josephson oscillations in the entire experimentally accessible interaction range, indicating that the gas is phase coherent and providing strong evidence for superfluidity in the two-dimensional geometry. For a detailed description of the experiments shown above and of the further measurements carried out in the system, I would like to refer the reader again to the PhD thesis of Niclas Luick [135].

7.4. Superfluidity in an ultracold 2D Fermi gas

In the following section, I report on the measurement of the critical velocity in an ultracold 2D Fermi gas across the BEC-BCS crossover. These results have mainly been obtained by Lennart Sobirey and are published in [226]:

> Lennart Sobirey, Niclas Luick, Markus Bohlen, Hauke Biss, Henning Moritz and Thomas Lompe. Observation of superfluidity in a strongly correlated two-dimensional Fermi gas. Preprint: arXiv:2005.07607v1 (2020), under review in Science.

The results will also be presented in greater detail in the thesis of Lennart Sobirey which will be published in the close future.
My contribution to this project consisted in building parts of the experimental setup, notably the adjustable optical lattice with is moved through the gas to create excitations.

Our experiments performed on a Josephson junction provide clear evidence for phase coherence in our two-dimensional quantum gas. While these results also strongly suggest that the system is superfluid, they do not provide irrefutable proof for the superfluid state of the low-dimensional system. We have recently performed measurements that show unambiguously that the system is superfluid below a critical temperature T_c. When dragging a lattice through the system we observe no heating and hence frictionless flow below a critical velocity v_c. The system hence fulfills Landau's criterion of superfluidity across nearly the entire accessible BEC-BCS crossover from tightly bound molecules to weakly bound Cooper pairs.

T_c : Critical temperature
v_c : Critical velocity for superfluidity

7.4.1. Landau's criterion of superfluidity

According to Landau's criterion of superfluidity, a system is superfluid if a perturbation moving through the system cannot dissipate energy at velocities smaller than a finite critical velocity v_c.

To see this, imagine a perturbation moving through a fluid with a velocity $\mathbf{v}$. It will be useful to describe this situation in the comoving frame of the perturbation. Generally, a state with momentum $\mathbf{p}$ and energy $E(p) = p^2/2M$ in the rest frame will have an energy $E' = (\mathbf{p} - M\mathbf{v})^2/2M = E(p) - \mathbf{p}\cdot\mathbf{v} + \frac{1}{2}Mv^2$ in the comoving frame, where M is the total mass of the system. For the ground state without excitations, the energy in the comoving frame is simply the sum of the ground state energy E_0 and the kinetic energy: $E' = E_0 + \frac{1}{2}Mv^2$. If an excitation of momentum $\mathbf{p}$ and energy $E(p)$ is created by the perturbation, we therefore have a total energy of $E' = E_0 + E(p) - \mathbf{p}\cdot\mathbf{v} + \frac{1}{2}Mv^2$ in the comoving frame. An excitation therefore changes the energy of the system by an amount $\Delta E = E(p) - \mathbf{p}\cdot\mathbf{v}$. An excitation can only be stable if the energy of the system is reduced in the comoving frame, i.e. if $E(p) < \mathbf{p}\cdot\mathbf{v}$. Conversely, they are unstable if $E(p) > \mathbf{p}\cdot\mathbf{v}$, which is certainly the case if $E(p) > |p||v| \geq \mathbf{p}\cdot\mathbf{v}$. This reasoning holds for any momentum p. The critical velocity is thus determined by the minimum velocity for which all possible excitations at lower velocities are unstable. We therefore see that a perturbation moving at a velocity v is unable to dissipate energy into the fluid as long as

$$v < v_c = \min \frac{E(p)}{|p|}, \tag{7.13}$$

which is Landau's criterion for superfluidity.

The critical velocity can be read from the dispersion relation of the system in a plot of excitation energy versus momentum (compare fig. 7.12). The quantity $E(p)/|p|$ corresponds to the slope of the straight line that goes through a given point of the excitation spectrum $E(p)$ and the origin. The critical velocity is the minimal possible slope of these lines for all possible excitations. From this, one can easily conclude that a non-interacting gas cannot be superfluid, since at $p = 0$, the slope of the line vanishes. The weakly interacting Bose gas and the BCS-gas are superfluid however, since the minimum slopes in these systems are nonzero.

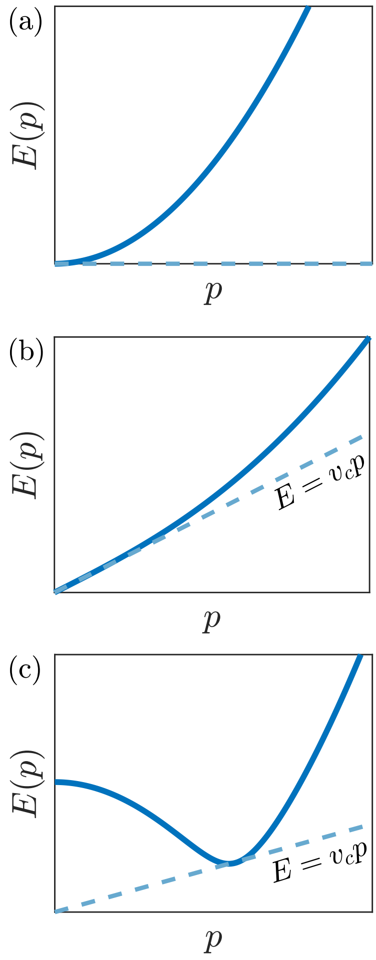

Figure 7.12. – Illustration of Landau's criterion for superfluidity: The critical velocity is set by the minimum slope of the line connecting the origin to any point of the dispersion relation $E(p)$. In a non-interacting gas (a), the minimum slope is zero and the gas is a normal fluid. In the case of weakly interacting Bose-Einstein condensates and BCS-type gases, the minimum slope is nonzero and the gas is superfluid. In the BEC regime (b), the minimal slope of the Bogoliubov dispersion relation occurs at small momenta. For the BCS gas (c), the minimal slope occurs at a wave vector of k_F, where the excitation spectrum is minimally gapped.

Superfluidity in cold atom gases

In the past, critical velocities have been measured in cold atomic systems. In Bose gases, critical velocities have been observed by various groups in 3D [227–230] as well as in 2D [231]. In the case of 3D Fermi gases, frictionless flow below a critical velocity has been observed using different excitation schemes, by dragging a lattice through the gas [232] or stirring it with a repulsive laser beam [233]. Additionally, the experiments of Kwon et al. [220] reproduce the DC-Josephson effect in a 3D Fermi gas and can thus be seen as strong evidence of superfluidity. While our observation of Josephson oscillations provides such evidence in the two-dimensional case, a clear observation of the critical velocity in 2D Fermi gases were yet outstanding. These measurements have been performed in our group [226] and I will present some of our results in the following.

7.4.2. Measuring the critical velocity

The system used in these experiments consists of a Fermi gas in a cylindrical homogeneous 2D box potential, containing a balanced mixture of about $N \approx 6000$ atoms in the lowest two hyperfine states. The vertical confinement in a single layer is provided by the repulsive lattice, whereas the horizontal confinement is realized by a ring-shaped potential created with the axicon setup (cf. supplementary materials in

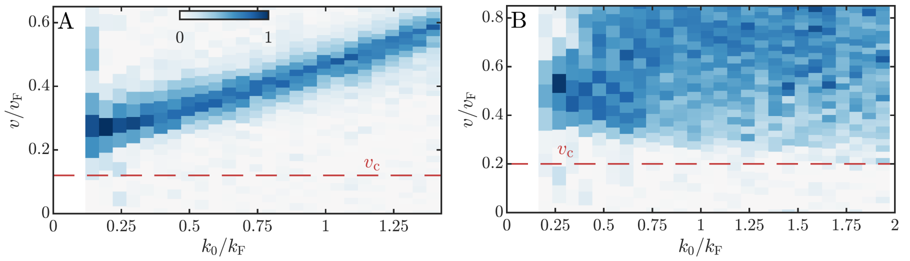

Figure 7.14. – Response function $r(k_0, v)$ of the gas in the BEC (A) and BCS(B) regimes. In the bosonic gas, the Bogoliubov dispersion relation is visible: The moving lattice excites phononic modes at small wavevectors, traveling at a constant velocity v_s. At higher wavevectors, the peak of the heating rate moves linearly to higher velocities, indicating a quadratic dispersion. The response shows a clear peak for all wavevectors and decays back to zero for high velocities. In the fermionic gas, the minimal velocity at which the gas can be excited occurs at a wavevector of $k_0 = 2k_{\mathrm{F}}$. For higher excitation velocities, there is a continuum of possible excitations. This spectrum corresponds to pair-breaking excitations. For both regimes, the excitation rate is minimal below a critical velocity v_c. Figure taken from [226]

[60]). Compared to the horizontal confinement generated with a DMD as used in the experiments described previously, this approach allows for a higher confinement potential, enabling the trapping of hotter samples without evaporation even in the BCS regime, where the chemical potential increases. In order to measure the critical velocity in the system, we project an impurity in the form of a periodic lattice potential onto the gas through the top microscope and move it through the gas at varying velocities. A schematic picture of this setup is shown in Figure 7.13. The impurity is created by interfering two red-detuned laser beams ($\lambda = 780\,\mathrm{nm}$) in the center of the trap. The crossing angle of the two beams is adjustable, resulting in a sinusoidal potential whose wavelength can be tuned. By detuning the frequencies of the two beams with respect to each other by a few MHz, the lattice can be moved through the gas at a velocity $v = L\Delta\nu$, where L is the spacing between two maxima of the optical potential.

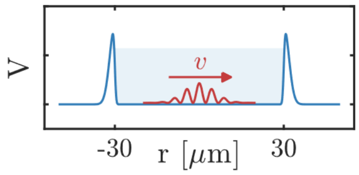

Figure 7.13. – Sketch of the perturbation scheme of the 2D gas. A lattice potential (red) is imprinted from the top into the homogeneous gas. By detuning the two lattice beams, the lattice moves at an adjustable velocity v. The lattice constant can be tuned by adjusting the crossing angle of the two incident beams. Figure adapted from [226]

The periodic potential is moved through the system at different velocities v. During this movement, the lattice spacing determines the momentum $\hbar k_0 = 2\pi\hbar/L$ at which the gas can be excited, and the velocity the energy that is transferred to an excitation. The response of the system can be measured by performing matter-wave focusing as introduced in section 7.3 and monitoring the pair condensation peak of the momentum distribution after adiabatically ramping the magnetic field to the BEC-side of the Feshbach resonance. We define the quantity $r(v) = (n(k=0, v=0)/n(k=0, v)) - 1$, i.e., the relative suppression of the condensate peak, as a measure of the response of the gas. If excitations are possible at a given combination of momentum and energy, the gas will heat up. The occupation of the lowest momentum modes decreases when the temperature of the gas is increased, which reduces the height of the peak at zero momentum and the response $r(v)$.

$\Delta\nu$:	Detuning of the lattice beams
L :	Lattice spacing
v :	Lattice velocity
k_0 :	Lattice wavevector
$r(v)$:	Response function

Since the lattice imposes a fixed momentum k_0 at which the response

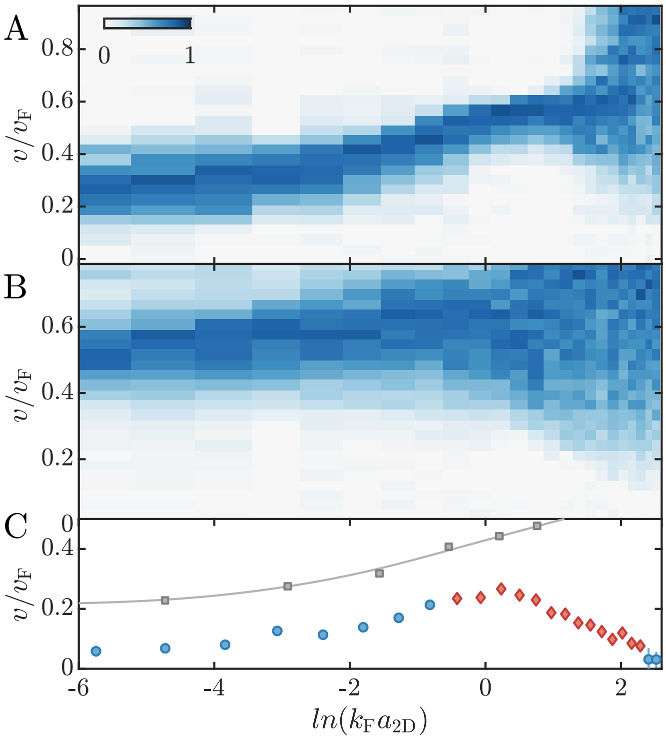

Figure 7.15. – Critical velocities across the BEC-BCS crossover. (A) Response of the gas to an excitation at $k_0 \approx 0.3k_\mathrm{F}$. (B) Response of the gas to an excitation at $k_0 \approx 2k_\mathrm{F}$. (C) Critical velocities extracted from the spectra of (A) and (B). In the BEC-regime the critical velocity is determined by the Bogoliubov sound mode (blue data points), whereas pair breaking excitations. On the BCS-side, the spectrum broadens to a continuum as pair-breaking excitations become the dominant excitation type, which determine the critical velocity (red data points). The sound velocity (gray data points) measured in [179] (see chapter 6.3) is shown for comparison. Figure from [226].

of the gas is probed, measurements were taken at different spacings L of the periodic potential and at different lattice velocities. The excitation spectra on the BEC- and BCS sides of the resonance are shown in fig. 7.14. The two spectra show striking differences. In the bosonic regime, the response of the gas shows a clear peak for any given lattice momentum, indicating a well-defined excitation mode. The excitations for low momenta occur at a constant velocity. For higher momenta, the peak in the excitation spectrum moves linearly toward higher velocities, indicating a quadratic dispersion, since $E(v) \propto k_0 v$. The excited mode therefore corresponds to the Bogoliubov sound mode. In the fermionic regime, there is no clear mode apart from at very low momenta, but instead a continuum of excitations with a minimum velocity around $k_0 = 2k_F$. These excitations correspond to pair-breaking excitations of Cooper pairs. In both cases there is a minimal velocity below which the excitation rate is negligible. Therefore, the gas clearly obeys Landau's criterion for superfluidity in the two limits of a BEC- and BCS-type gas.

In order to measure the critical velocity over the entire BEC-BCS crossover, we have measured the response of the gas at the two wavevectors corresponding to the minima in the BEC- and BCS regimes, i.e. at $k_0 \approx 0.3k_\mathrm{F}$ and $k_0 \approx 2k_\mathrm{F}$, obtaining two onset velocities for dissipation at each magnetic field. The critical velocity has then be defined as the lower of these two velocities. Figure 7.15 shows the resulting critical velocities together with the excitation responses of the gas at low (A) and high (B) momenta as well as the sound velocity in the gas obtained in the measurements presented in section 6.3 [179]. On the bosonic side, we see a clearly defined sound mode which determines the critical velocity. The behavior of the critical velocity follows the behavior of the speed of sound, rising toward the strongly correlated regime. Further toward the BCS-side, the sound mode broadens smoothly and turns into the fermionic pair-breaking continuum. Here, the critical velocity is determined by single-particle excitations around $k_0 \approx 2k_\mathrm{F}$ and decreases again toward the weakly interacting Fermi gas. The system is clearly superfluid across the entire BEC-BCS crossover, since it obeys Landau's criterion for a superfluid for all interaction strengths around the resonance. These measurements thus represent the first definitive evidence for superfluidity in a strongly correlated 2D Fermi gas. The maximum of the critical velocity around $\ln(k_\mathrm{F}a_\mathrm{2D}) \approx 0$ indicates that the superfluid is most stable in the strongly correlated regime.

7.4.3. Conclusion

In this chapter, I have presented the first realization of a Josephson junction in an ultracold two-dimensional Fermi gas. After creating a phase difference between the two reservoirs, that are separated by a thin barrier, we could observe clear Josephson oscillations, even when the barrier is significantly higher than the chemical potential of the gas. The oscillations persist over a large range of interactions across the experimentally accessible BEC-BCS crossover. Using the frequency shift of the oscillations with increasing imprinted phase, we could show that our system follows the current phase relation of an ideal Josephson junction. Our measurements represent clear proof of phase coherence and establish Josephson junctions as a tool which could be used in the future for investigations of the order parameter in the two-dimensional gas.

In addition, I have presented the first measurements of the critical velocity in a two-dimensional Fermi gas. We have shown that the Fermi gas is superfluid across the entire crossover and that its superfluidity is most stable in the strongly correlated regime. In the Bose regime, superfluidity is limited by the excitation of sound waves in the gas. The critical velocity according to Landau's criterion is here given by the speed of sound. In the Fermi regime, pair breaking excitations are the limiting excitation mechanism.

Using the same excitation mechanism, we have also observed the superfluid phase transition of the gas by heating the system up above the critical temperature T_c. For further details on these additional measurements, I would like to refer the reader to [226]. The same experimental technique is now used in our group to measure the superfluid gap across the BEC-BCS crossover (a publication is in preparation). Performing similar experiments in a three-dimensional box potential in the near future (and eventually with an accordeon lattice after replacing the 2D-breadboard), we would like to obtain similar data for the three-dimensional Fermi gas and thus hope to shed light onto the role of dimensionality for the establishment and the stability of superfluidity.

8. Conclusion and Outlook

In this thesis we have presented experiments with ultracold two- and three-dimensional Fermi gases that advance both the understanding of strongly correlated two-dimensional Fermi gases as well as their capability for the simulation of analogous solid state systems.

As the main result of the thesis, we have performed the first measurements of the sound velocity and its attenuation in a two-dimensional Fermi gas at varying interaction strengths across the BEC-BCS crossover. We have qualitatively explained the behavior of the sound velocity from the bosonic to the fermionic regime and we have found a lower bound for the sound attenuation in the strongly correlated regime, which is linked to a fundamental lower bound for the transport coefficients. The viscosity of the gas was found to be of the order of $\sim \hbar/m$ in this regime, indicating that the strongly correlated Fermi gas is a nearly perfect fluid. Our results stands in line with previous findings of lower bounds for viscosity and spin diffusivity as well as sound diffusivity in a three-dimensional Fermi gas.

In the future our findings might serve as a benchmark for the development of theories for the strongly interacting gas. Very recently, calculations using a Gaussian pair fluctuations approach have been able to reproduce the first sound velocity across the crossover [193]. After the development of controlled heating methods in subsequent experiments, our experimental scheme could now also be used to investigate the dependence of the sound velocity and attenuation with temperature, which would be particularly intriguing around the critical temperature for superfluidity.

We have also presented exciting experimental results concerning phase coherence and superfluidity in the two-dimensional Fermi gas, which were obtained during the course of this thesis, with Niclas Luick and Lennart Sobirey as the lead PhD students. We realized the first Josephson junction in a two-dimensional Fermi gas and showed that it obeys the current-phase relation $I(\varphi) = I_c \sin(\varphi)$ of an ideal Josephson junction. The critical current has been measured over a wide range of interactions across the BEC-BCS crossover. As shown in [135, 177], the junction could be used to measure the condensate fraction of the two-dimensional gas and could therefore serve as a novel probe for the order parameter in the strongly correlated two-dimensional gas. Furthermore, we have performed the first measurement of the critical velocity in a two-dimensional Fermi gas across the BEC-BCS crossover, thereby obtaining the first proof of superfluidity in such a system. In the bosonic regime, the critical velocity scales with the sound velocity, since the Bogoliubov quasiparticles are the lowest-lying fundamental excitations in the system. Of particular interest is the observation that the critical velocity is highest in the strongly correlated regime, which indicates that 2D-superfluidity is most stable in this regime.

Finally, we have presented work concerning the characterization of a d-wave Feshbach resonance via loss rate spectroscopy and measurements of the spin dynamics close to the resonance. The extracted two-body loss rates are in good agreement with predictions by E. Tiesinga. The evolution of the spin populations in a strongly recompressed trap was consistent with the expected final state, however strong fluctuations prevented us from doing a quantitative analysis. Additional future measurements might fill this gap and allow this d-wave resonance to become a tool for the experimental realization of non-standard pairing, which is one of the important ingredients for superfluidity at high critical temperatures.

Outlook: The superfluid gap in strongly correlated Fermi gases

In order to measure the critical velocity in our 2D gas, we have observed the heating response of the gas to a moving lattice potential in order to determine the onset of dissipation in the gas. Changing the vocabulary slightly, this excitation scheme may also be understood as a two-photon Bragg scattering process, occurring under a given momentum and energy transfer $\hbar q$ and $\hbar\omega$, determined by the angle between the beams and their detuning. If the heating response of the gas for an excitation (q, ω) is proportional to the probability of creating such an excitation, this will give us access to the dynamic structure factor $S(q, \omega)$, a quantity which describes the excitation spectrum and which can be used to derive for instance the response functions of the material.

Whilst this thesis was written, we have extended our measurements to map out the dynamic structure factor of the two-dimensional Fermi gas for different interaction strength and observe how the bosonic excitation spectrum of the dimers transitions into the excitation spectrum of a fermionic gas. Of particular interest here is the onset of the continuum of pair-breaking excitations that can occur at energies larger than the pairing gap Δ. The magnitude of the pairing gap depends both on the binding energy of two isolated fermions (which we have discussed in this thesis) and on a part originating in the interaction of a particle with the rest of the strongly correlated system. We extract the many-body part of Δ from the measurements dynamic structure factor and compare it to theory and previous experimental data.

Appendix

A. Publications

The results obtained in the course of this thesis have been published in the following publications:

1. An ideal Josephson junction in an ultracold two-dimensional Fermi gas. N. Luick, L. Sobirey, M. Bohlen, V. P. Singh, L. Mathey, T. Lompe and H. Moritz. *Science* **369**(6499), 89-91 (2020)
2. Sound Propagation and Quantum-Limited Damping in a Two-Dimensional Fermi Gas. M. Bohlen, L. Sobirey, N. Luick, H. Biss, T. Enss, T. Lompe and H. Moritz. *Phys. Rev. Lett.* **124**, 240403 (2020)
3. Observation of superfluidity in a strongly correlated two-dimensional Fermi gas. L. Sobirey, N. Luick, M. Bohlen, H. Biss, H. Moritz and T. Lompe. Preprint: arXiv:2005.07607v1 (2020), under review in Science.

A.1. An ideal Josephson junction in an ultracold two-dimensional Fermi gas.

QUANTUM GASES

An ideal Josephson junction in an ultracold two-dimensional Fermi gas

Niclas Luick[1,2], Lennart Sobirey[1,2], Markus Bohlen[1,2,3], Vijay Pal Singh[4,2], Ludwig Mathey[4,2], Thomas Lompe[1,2]*, Henning Moritz[1,2]

The role of reduced dimensionality in high-temperature superconductors is still under debate. Recently, ultracold atoms have emerged as an ideal model system to study such strongly correlated two-dimensional (2D) systems. Here, we report on the realization of a Josephson junction in an ultracold 2D Fermi gas. We measure the frequency of Josephson oscillations as a function of the phase difference across the junction and find excellent agreement with the sinusoidal current phase relation of an ideal Josephson junction. Furthermore, we determine the critical current of our junction in the crossover from tightly bound molecules to weakly bound Cooper pairs. Our measurements clearly demonstrate phase coherence and provide strong evidence for superfluidity in a strongly interacting 2D Fermi gas.

One of the most notable macroscopic manifestations of quantum mechanics is the dc Josephson effect (*1*, *2*), where a phase difference ϕ between two superconductors separated by a weak link drives a current $I(\phi)$ without any applied voltage. For an ideal Josephson junction, this current phase relation takes a sinusoidal form $I(\phi) = I_C \sin(\phi)$ (*3*), where I_C is the maximum supercurrent that can flow through the junction. This direct connection between the superfluid current and the phase of the macroscopic wave function makes Josephson junctions a powerful tool for probing properties of superconductors, providing, for example, clear evidence for the d-wave symmetry of the order parameter in cuprate superconductors (*4*).

Recently, ultracold quantum gases have been established as ideal model systems to study such strongly correlated two-dimensional (2D) fermionic systems (*5*–*12*). However, although pair condensation of fermions has been reported (*13*), fermionic superfluidity in two dimensions has not been directly observed. Here, we use a Josephson junction to unambiguously show phase coherence and provide strong evidence for superfluidity in an ultracold 2D Fermi gas. Josephson junctions have already been extensively studied in ultracold quantum gases (*14*–*22*), but the ideal sinusoidal current phase relation that directly links the phase difference to the supercurrent across the junction (*23*–*25*) has not been observed (*26*). In this work, we first confirm that our junction follows an ideal current phase relation. This implies that the current across the junction is a supercurrent that is driven by the phase difference between two superfluids. We then proceed to measure the evolution of the critical current of the junction as a function of interaction strength and thereby realize a probe for 2D superfluidity in the crossover from tightly bound molecules to weakly bound Cooper pairs.

For our experiments, we use a homogeneous Fermi gas of ^{6}Li atoms in a spin-balanced mixture of the lowest two hyperfine states, trapped in a box potential (*27*, *28*). A strong vertical confinement with trap frequency $\omega_z/2\pi = 8.8(2)$ kHz ensures that the gas is kinematically 2D with the chemical potential μ and temperature T being smaller than the level spacing $\hbar\omega_z$, where $\hbar$ is the reduced Planck constant. We create a Josephson junction by using a narrow repulsive potential barrier with

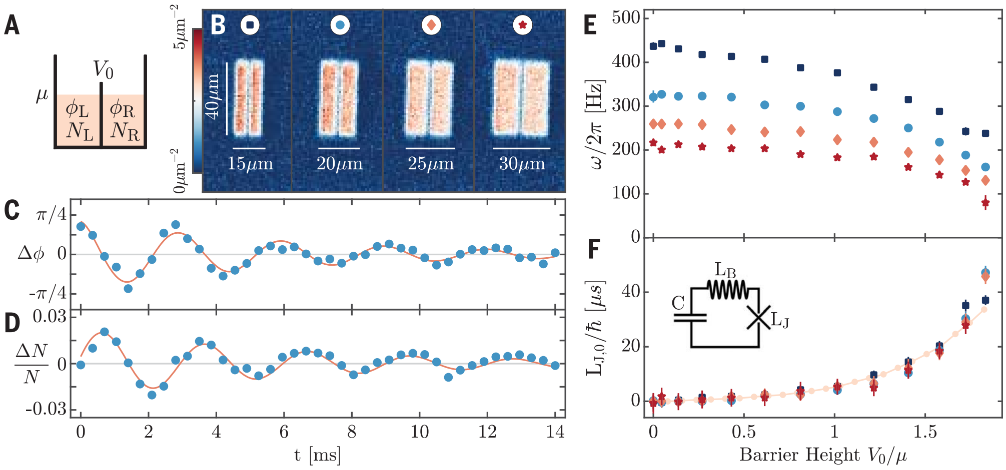

Fig. 1. Josephson oscillations in a homogeneous 2D Fermi gas. (**A**) Sketch of a Josephson junction consisting of two Fermi gases with chemical potential μ, particle numbers N_L and N_R, and phases ϕ_L and ϕ_R separated by a tunneling barrier with height V_0. (**B**) Absorption images of cold atom Josephson junctions. The width of the barrier is held fixed at a waist of $w = 0.81(6)\mu$m while the size $l_\perp$ of the system is increased. (**C** and **D**) Time evolution of the phase difference $\Delta\phi$ (C) and relative particle number difference $\Delta N/N$ (D) between the left and right side of the box after imprinting a relative phase difference of $\phi_0 \approx \pi/4$. The red lines represent a damped sinusoidal fit. (**E**) Oscillation frequency as a function of barrier height V_0 for different system sizes [symbols as in (B)], where the error bars denote the 1σ fit error. The inductance L_B and capacitance C of the bulk system are proportional to the length $l_\perp$ of the box, and therefore the oscillation frequency decreases with increasing system size for $V_0 = 0$. For nonzero values of V_0, the barrier adds a nonlinear Josephson inductance L_J to the system and the oscillation frequency decreases as a function of barrier height. (**F**) Josephson inductance $L_{J,0}(V_0)$ extracted from the frequency measurements using an LC circuit model. The Josephson inductances for all system sizes collapse onto a single curve, which shows that the inductance of the junction depends only on the height of the barrier and validates our LC circuit model. We obtain the calibration of the barrier height V_0 by matching the data to a full numerical simulation (light red line with circles) (*27*). The data are obtained by averaging 20 (B), 42 (C), 130 (D), and 7 [(E) and (F)] individual measurements.

---

[1]Institut für Laserphysik, Universität Hamburg, Luruper Chaussee 149, 22761 Hamburg, Germany. [2]The Hamburg Centre for Ultrafast Imaging, Universität Hamburg, Luruper Chaussee 149, 22761 Hamburg, Germany. [3]Laboratoire Kastler Brossel, ENS-Université PSL, CNRS, Sorbonne Université, Collège de France, 24 rue Lhomond, 75005 Paris, France. [4]Zentrum für Optische Quantentechnologien, Universität Hamburg, Luruper Chaussee 149, 22761 Hamburg, Germany.
***Corresponding author. Email: tlompe@physik.uni-hamburg.de**

a Gaussian beam waist of $w = 0.81(6)$ μm to split the system into two homogeneous 2D pair condensates connected by a weak link (Fig. 1, A and B). We imprint a relative phase ϕ_0 between the two sides of the junction by illuminating one-half of the system with a spatially homogeneous optical potential for a variable time between 0 and 20 μs (*27*). We then let the system evolve for a time t and extract the population imbalance $\Delta N = (N_L - N_R)$ and the phase difference ϕ between the two sides using either in situ or time-of-flight imaging. A typical Josephson oscillation of a molecular condensate at a magnetic field of $B = 731$ G (*29*) and a barrier height of $V_0/\mu = 1.08(5)$ featuring the characteristic $\pi/2$ phase shift between imbalance and phase is shown in Fig. 1, C and D. The oscillations are weakly damped with a relative damping of $\Gamma/\omega = 0.07$, which, according to a full numerical simulation of our system, can be explained by phononic excitations in the bulk and the nucleation of vortex-antivortex pairs in the junction (fig. S3) (*30*).

To understand these Josephson oscillations, we use a simple circuit model commonly used to describe superconducting Josephson junctions (*21*, *31*, *32*). In this model, we describe our junction as a nonlinear Josephson inductance L_J, which is connected in series to a linear bulk inductance L_B and a capacitance C (Fig. 1F), where the bulk inductance L_B characterizes the inertia of the gas and the capacitance C its compressibility. For vanishing Josephson inductance, the model reduces to a linear resonator with frequency $\omega_s = 1/\sqrt{L_B C} = 2\pi v_s / 2l_\perp$, which corresponds to the frequency of a sound mode propagating with the speed of sound v_s across the length $l_\perp$ of the system. Introducing a barrier with height V_0 adds a nonlinear inductance L_J to the system and reduces the oscillation frequency ω. Owing to the nonlinearity of the current phase relation, this L_J depends on the phase difference $\phi(t)$ across the junction, but for small phase excitations, there is a linear regime where $L_J[\phi(t)]$ can be approximated by a time-independent Josephson inductance $L_{J,0}$ and the oscillation frequency is given by $\omega = 1/\sqrt{(L_B + L_{J,0})C}$.

To confirm that our physical system is described by this model, we prepare a gas of deeply bound dimers, perform measurements of the oscillation frequency in the linear regime as a function of the barrier height for different system sizes (Fig. 1E), and extract the Josephson inductance $L_{J,0}$ (Fig. 1F). Because our system has a uniform density, the bulk inductance is given by the simple expression $L_B = 8ml_\perp/\pi^2 n l_\parallel$, where n is the density per spin state, m is the mass of a ^{6}Li atom, and $l_\perp$ ($l_\parallel$) is the diameter of the box perpendicular (parallel) to the barrier (*27*). Consequently, the Josephson inductance $L_{J,0}(\omega) = L_B(\omega_s^2/\omega^2 - 1)$ can be extracted from the frequency difference between the Josephson oscillations and the sound mode. Whereas the oscillation frequency is strongly dependent on the size of the box owing to the change in the bulk inductance L_B and the capacitance C, the measured Josephson inductance $L_{J,0}$ should depend only on the coupling between the two reservoirs. As can be seen from Fig. 1 F, all measurements of $L_{J,0}$ versus barrier height collapse onto a single curve regardless of the system size, which confirms that our Josephson junction can be described by an inductor-capacitor (LC) circuit model. For the barrier heights used in our experiments, we also find very good agreement with a full numerical simulation of our system (*27*).

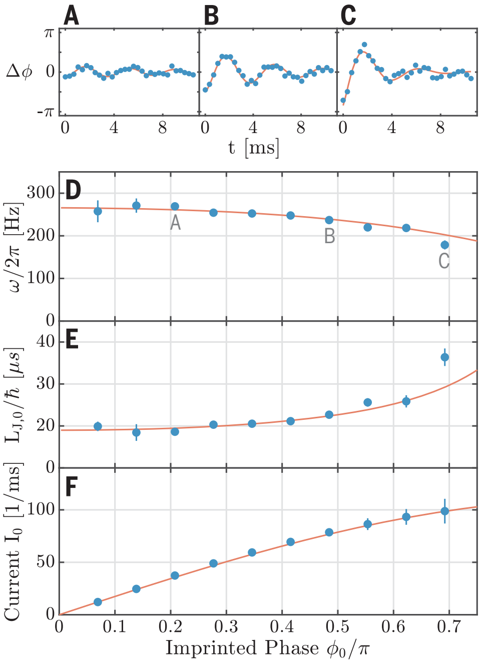

Fig. 2. Current phase relation. (**A** to **C**) Josephson oscillations through a tunneling barrier with height $V_0/\mu = 1.51(8)$ at initial phase imprints of $\phi_0 = 0.14\pi$ (A), 0.42π (B), and 0.62π (C). The amplitude of the oscillations increases for stronger phase imprints, whereas the frequency is reduced. (**D**) Oscillation frequency as a function of imprinted phase, where the error bars denote the 1σ fit error. The gray labels A, B, and C denote the frequencies obtained from the oscillations shown in (A) to (C). (**E**) Inductance of the junction calculated from the measured oscillation frequencies. (**F**) Effective current I_0 through the junction obtained by performing a Riemann sum over the measured values of $L_{J,0}$ shown in (E) according to $\partial I/\partial\phi = \hbar/L_J$ (*27*). Our data are in excellent agreement with the rescaled current phase relation $I_0 = 2I_C \sin(\phi_0/2)$ expected for an ideal Josephson junction (red lines), where the initial slope I_C is determined from the first three data points. Each data point in (A) to (C) is obtained by averaging 20 individual measurements.

Next, we probe the fundamental property of Josephson junctions: the nonlinearity of the current phase relation (*3*, *26*). For large phase excitations, the nonlinear current phase relation leads to anharmonic oscillations with an increased oscillation period. Our ability to imprint arbitrary phase differences ϕ_0 across the barrier enables us to measure this reduction of the fundamental frequency $\omega(\phi_0)$ as a probe of the nonlinearity (Fig. 2). To extract the nonlinear response of the current from our measurements of $\omega(\phi_0)$, we first calculate $L_{J,0}[\omega(\phi_0)]$ and then apply the relation $\partial I/\partial\phi = \hbar/L_J$ to $L_{J,0}(\phi_0)$ to obtain an effective current $I_0(\phi_0)$. For an ideal Josephson junction, I_0 follows a rescaled current phase relation $I_0(\phi_0) \approx 2I_C \sin(\phi_0/2)$ (*27*). We find that our measurement is in excellent agreement with this current phase relation, indicating that our junction is an ideal Josephson junction (*3*, *26*, *33*). This implies that the current across the junction is indeed a supercurrent, driven by the phase difference between two superfluids.

Following this result, we can now use our Josephson junction as a probe for 2D superfluidity in the strongly correlated regime. We observe Josephson oscillations over a wide range of interaction strengths, indicating the presence of superfluidity in the entire crossover from tightly bound molecules to weakly bound Cooper pairs (Fig. 3). To quantify the effect of interactions on our system, we extract the critical current I_C from the frequency of the Josephson oscillations. Because for a fixed barrier height V_0 the change in the critical current would be dominated by the interaction dependence of the chemical potential, we instead maintain a constant $V_0/\mu = 1.4(2)$ by adjusting the barrier height V_0 for each interaction strength according to a reference measurement of the equation of state (fig. S4). We observe that, within the uncertainty of our measurement, the critical current stays nearly constant, with a tendency toward smaller values of I_C when approaching the Bardeen-Cooper-Schrieffer (BCS) side of the resonance. Although there is currently no theory available that quantitatively describes a 2D Josephson junction in the whole Bose-Einstein condensate (BEC)–BCS crossover, in the bosonic limit we can calculate the critical current from the condensate density n_c and the overlap of the condensate wave functions (*27*, *34*). We use this theory to determine the condensate fraction from the measured critical current for interaction strengths $\ln(k_F a_{2D}) \leq -0.9$ and obtain $n_c/n = 0.72(8)_{\text{stat.}}(^{+0.1}_{-0.2})_{\text{sys.}}$, where stat. denotes the statistical error and the

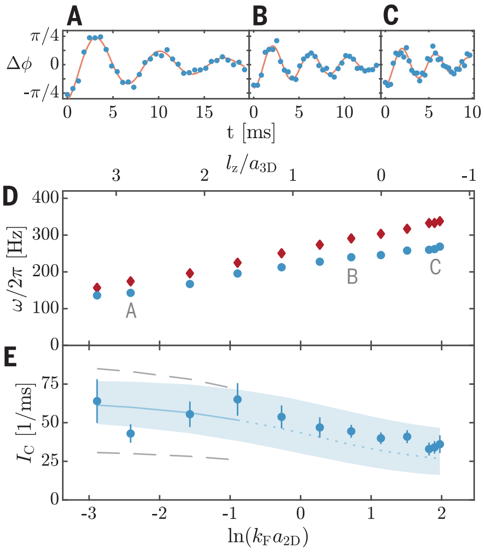

Fig. 3. Interaction dependence of the critical current. (**A** to **C**) Josephson oscillations for interaction strengths of $\ln(k_F a_{2D}) = -2.4$ (A), $\ln(k_F a_{2D}) = 0.7$ (B), and $\ln(k_F a_{2D}) = 1.9$ (C), where k_F is the Fermi wave vector and a_{2D} is the 2D scattering length as defined in (*13*, *27*). The measurements are performed in the linear regime with constant density $n = 1.21(9)\mu\text{m}^{-2}$ and relative barrier height $V_0/\mu = 1.4(2)$. (**D**) Oscillation frequency for sound (red diamonds) and Josephson (blue dots) oscillations as a function of the 2D interaction parameter $\ln(k_F a_{2D})$. The frequency increase of the bare sound mode when going from the molecular to the BCS regime reflects the interaction dependence of the chemical potential. The gray labels A, B, and C denote the frequencies obtained from the oscillations shown in (A) to (C). (**E**) Critical current of the junction extracted from the frequency difference between the sound mode and the Josephson oscillations. The error bars denote the 1σ fit error. The blue line is the critical current $I_C \propto n_c t_{k=0}$ calculated for a condensate fraction of $n_c/n = 0.72$ and a tunneling amplitude $t_{k=0}$ obtained from a mean field calculation of the transmission through the barrier (*27*). To calculate the tunneling amplitude, we approximate our junction with a rectangular barrier with a width $b = 0.81$ μm, which is a reasonable approximation for the Gaussian barrier used in the experiment. The shaded region denotes the systematic uncertainty resulting from the 15% uncertainty in V_0/μ. The dashed gray lines indicate the upper ($T = 0$) and lower ($T = T_c$) bound for the critical current obtained from our theory. Although it is unclear how far into the strongly correlated regime our bosonic theory is quantitatively accurate (*27*), it reproduces the qualitative behavior of our data across the entire BEC-BCS crossover. Each data point in (A) to (C) is obtained by averaging 42 individual measurements.

systematic error (sys.) arises from the 15% uncertainty in V_0/μ. For our homogeneous 2D system, Berezinskii-Kosterlitz-Thouless theory relates the condensate fraction $n_c/n \propto L^{-\eta}$ to the algebraic decay of phase coherence over the finite size L of the box, where $\eta \propto T/n_s$ is the algebraic scaling exponent (*35*, *36*). A measurement of the critical current as a function of system size can therefore be used to extract the algebraic scaling exponent and the superfluid density n_s, as recently suggested in (*37*).

Our homogeneous 2D Fermi gas provides an excellent starting point to study the influence of reduced dimensionality on strongly correlated superfluids in the crossover between two and three dimensions. The distinctive combination of reduced dimensionality, uniform density, low entropy, and high-resolution imaging makes our system a perfect platform to observe exotic phases such as the elusive Fulde-Ferrell-Larkin-Ovchinnikov state (*38*). Finally, our system is ideally suited to investigate whether periodic driving of Josephson junctions can strongly enhance coherent transport, as suggested by experiments with THz-driven cuprate superconductors (*39*, *40*).

REFERENCES AND NOTES

1. B. D. Josephson, *Phys. Lett.* **1**, 251–253 (1962).
2. P. W. Anderson, J. M. Rowell, *Phys. Rev. Lett.* **10**, 230–232 (1963).
3. A. A. Golubov, M. Y. Kupriyanov, E. Il'ichev, *Rev. Mod. Phys.* **76**, 411–469 (2004).
4. C. Tsuei, J. Kirtley, *Rev. Mod. Phys.* **72**, 969–1016 (2000).
5. B. Fröhlich *et al.*, *Phys. Rev. Lett.* **106**, 105301 (2011).
6. A. T. Sommer, L. W. Cheuk, M. J. H. Ku, W. S. Bakr, M. W. Zwierlein, *Phys. Rev. Lett.* **108**, 045302 (2012).
7. V. Makhalov, K. Martiyanov, A. Turlapov, *Phys. Rev. Lett.* **112**, 045301 (2014).
8. W. Ong, C. Cheng, I. Arakelyan, J. E. Thomas, *Phys. Rev. Lett.* **114**, 110403 (2015).
9. K. Fenech *et al.*, *Phys. Rev. Lett.* **116**, 045302 (2016).
10. D. Mitra, P. T. Brown, P. Schauß, S. S. Kondov, W. S. Bakr, *Phys. Rev. Lett.* **117**, 093601 (2016).
11. A. Mazurenko *et al.*, *Nature* **545**, 462–466 (2017).
12. J. Levinsen, M. M. Parish, in *Annual Review of Cold Atoms and Molecules*, K. W. Madison, K. Bongs, L. D. Carr, A. M. Rey, H. Zhai, Eds. (World Scientific, 2015), vol. 3, chap. 1, pp. 1–75.
13. M. G. Ries *et al.*, *Phys. Rev. Lett.* **114**, 230401 (2015).
14. F. S. Cataliotti *et al.*, *Science* **293**, 843–846 (2001).
15. M. Albiez *et al.*, *Phys. Rev. Lett.* **95**, 010402 (2005).
16. S. Levy, E. Lahoud, I. Shomroni, J. Steinhauer, *Nature* **449**, 579–583 (2007).
17. L. J. LeBlanc *et al.*, *Phys. Rev. Lett.* **106**, 025302 (2011).
18. T. Betz *et al.*, *Phys. Rev. Lett.* **106**, 020407 (2011).
19. G. Spagnolli *et al.*, *Phys. Rev. Lett.* **118**, 230403 (2017).
20. G. Valtolina *et al.*, *Science* **350**, 1505–1508 (2015).
21. A. Burchianti *et al.*, *Phys. Rev. Lett.* **120**, 025302 (2018).
22. C. Ryu, P. W. Blackburn, A. A. Blinova, M. G. Boshier, *Phys. Rev. Lett.* **111**, 205301 (2013).
23. G. Watanabe, F. Dalfovo, F. Piazza, L. Pitaevskii, S. Stringari, *Phys. Rev. A* **80**, 053602 (2009).
24. A. Spuntarelli, P. Pieri, G. C. Strinati, *Phys. Rev. Lett.* **99**, 040401 (2007).
25. F. Ancilotto, L. Salasnich, F. Toigo, *Phys. Rev. A* **79**, 033627 (2009).
26. S. Eckel, F. Jendrzejewski, A. Kumar, C. Lobb, G. Campbell, *Phys. Rev. X* **4**, 031052 (2014).
27. See supplementary materials.
28. K. Hueck *et al.*, *Phys. Rev. Lett.* **120**, 060402 (2018).
29. This corresponds to an interaction strength of $\ln(k_F a_{2D}) = -2.4$.
30. Notably, achieving this low damping requires a temperature of $T/T_F \lesssim 0.03$ (fig. S3), which is far below the predicted critical temperature $T_c/T_F \approx 0.1$ for 2D superfluidity at this interaction strength (*13*, *27*, *41*).
31. J. G. Lee, B. J. McIlvain, C. J. Lobb, W. T. Hill III, *Sci. Rep.* **3**, 1034 (2013).
32. S. Eckel *et al.*, *Phys. Rev. A* **93**, 063619 (2016).
33. We note that achieving a sinusoidal current phase relation requires a barrier deep in the tunneling regime, which is fulfilled for our barrier depth of $V_0/\mu \approx 1.5$.
34. M. Zaccanti, W. Zwerger, *Phys. Rev. A* **100**, 063601 (2019).
35. Z. Hadzibabic, J. Dalibard, *RIV Nuovo Cim.* **34**, 389 (2011).
36. N. V. Prokof'ev, B. V. Svistunov, *J. Exp. Theor. Phys.* **127**, 860–864 (2018).
37. V. P. Singh, N. Luick, L. Sobirey, L. Mathey, arXiv:2002.08375 [cond-mat.quant-gas] (19 February 2020).
38. J. J. Kinnunen, J. E. Baarsma, J.-P. Martikainen, P. Törmä, *Rep. Prog. Phys.* **81**, 046401 (2018).
39. W. Hu *et al.*, *Nat. Mater.* **13**, 705–711 (2014).
40. J.-i. Okamoto, W. Hu, A. Cavalleri, L. Mathey, *Phys. Rev. B* **96**, 144505 (2017).
41. D. Petrov, M. Baranov, G. Shlyapnikov, *Phys. Rev. A* **67**, 031601 (2003).
42. N. Luick *et al.*, Data for "An ideal Josephson junction in an ultracold two-dimensional Fermi gas." Zenodo (2020); https://doi.org/10.5281/zenodo.3744797.
43. N. Luick *et al.*, Simulation script and data for "An ideal Josephson junction in an ultracold two-dimensional Fermi gas." Zenodo (2020); https://doi.org/10.5281/zenodo.3786298.

ACKNOWLEDGMENTS

We thank K. Hueck and B. Lienau for their contributions during earlier stages of the experiment; T. Enss, A. Recati, and M. Zaccanti for stimulating discussions; and G. Roati and F. Scazza for careful reading of the manuscript and valuable suggestions regarding the interpretation of Fig. 3. **Funding:** This work was supported by the European Union's Seventh Framework Programme (FP7/2007-2013) under grant agreement no. 335431 and by the DFG in the framework of SFB 925 and the excellence clusters "The Hamburg Centre for Ultrafast Imaging" - EXC 1074 - project ID 194651731 and "Advanced Imaging of Matter" - EXC 2056 - project ID 390715994. M.B. acknowledges support by Labex ICFP of École Normale Supérieure Paris. **Author contributions:** N.L. and L.S. performed the experiments and data analysis with support from M.B. and T.L. V.P.S. and L.M. developed numerical and analytical models and contributed to the interpretation of our experimental data. N.L. and T.L. wrote the manuscript, and L.S. created the figures with input from all authors. T.L. and H.M. supervised the project. All authors contributed to the discussion and interpretation of our results. **Competing interests:** The authors declare no competing interests. **Data and materials availability:** All data presented in this paper and simulation scripts are deposited at Zenodo (*42*, *43*).

SUPPLEMENTARY MATERIALS

science.sciencemag.org/content/369/6499/89/suppl/DC1
Supplementary Text
Figs. S1 to S4
References (*44*–*49*)

23 August 2019; accepted 7 May 2020
10.1126/science.aaz2342

science.sciencemag.org/content/369/6499/89/suppl/DC1

Supplementary Materials for

An ideal Josephson junction in an ultracold two-dimensional Fermi gas

Niclas Luick, Lennart Sobirey, Markus Bohlen, Vijay Pal Singh, Ludwig Mathey,
Thomas Lompe*, Henning Moritz

*Corresponding author. Email: tlompe@physik.uni-hamburg.de

Published 3 July 2020, *Science* **369**, 89 (2020)
DOI: 10.1126/science.aaz2342

This PDF file includes:

- Supplementary Text
- Figs. S1 to S4
- References

Supplementary materials

Preparation of homogeneous 2D Fermi gases

We prepare our homogeneous 2D Fermi gas following the scheme described in (*28*). We start by evaporatively cooling a spin mixture of $^6\mathrm{Li}$ atoms in the $|F = 1/2, m_F = 1/2\rangle$ and $|F = 1/2, m_F = -1/2\rangle$ hyperfine states in a highly elliptical optical dipole trap at a magnetic field close to the 832 G Feshbach resonance of $^6\mathrm{Li}$. We then ramp to a magnetic field of 730 G and project our box potential onto the atoms using a digital micromirror device (DMD[1]) illuminated with blue-detuned ($\lambda = 532\,\mathrm{nm}$) light, which we refer to as DMD 1. Additionally, we briefly ramp up a second DMD (DMD 2), also illuminated with $532\,\mathrm{nm}$ light, that covers a larger area to push away residual atoms still trapped outside of the box. Finally, we load the atoms into a single node of an optical standing wave potential with a lattice spacing of approximately $3\,\mu\mathrm{m}$ and a trap frequency of $\omega_z = 2\pi \cdot 8.8(2)\,\mathrm{kHz}$ and thereby bring the atoms into the 2D-regime. For all measurements, the chemical potential is well below the trap frequency ($\mu < 0.7\,\hbar\omega_z$) and we can therefore parametrise the interaction strength by an effective 2D scattering length $a_{\mathrm{2D}} = l_{\mathrm{z}}\sqrt{\pi/0.905}\exp(-\sqrt{\pi/2} \cdot l_{\mathrm{z}}/a_{\mathrm{3D}})$ (*44*), where $l_{\mathrm{z}} = \sqrt{\hbar/m\omega_{\mathrm{z}}}$ is the harmonic oscillator length and a_{3D} is the 3D scattering length.

We note that performing thermometry of our homogeneous Fermi gas is challenging, since, in contrast to harmonic traps, there is no low density region where the gas is thermal. This makes it very difficult to observe and fit the thermal fraction of the cloud. We obtain an estimate of the temperature of the system by performing a time of flight measurement after DMD 1 has been ramped on and the atoms have been loaded into the lattice, but without pushing away the atoms outside the box with DMD 2. This measurement yields a temperature of $T/T_{\mathrm{F}} \approx 0.03$, where $T_{\mathrm{F}} = E_{\mathrm{F}}/k_{\mathrm{B}}$ is the Fermi temperature of a system with Fermi energy

---

[1] Texas Instruments DLP6500FYE

$E_\mathrm{F} = \hbar^2 k_\mathrm{F}^2/2m = \hbar^2 4\pi n/2m$ using the density n inside the box potential. However, it is *a priori* unclear whether the atoms inside and outside the box potential are fully thermalised, so a better method to perform thermometry is to measure the density equation of state $\mu(n, T)$ of a molecular condensate and compare it to a full numerical simulation (Fig. S4). This method yields the same temperature of $T/T_\mathrm{F} \approx 0.03$ as the time of flight measurement.

Generation of arbitrary potentials

To create the box potential and the tunnelling barrier, we image DMD 1 directly onto the atoms using a high resolution microscope. The DMD has a pixel size of $7.56\,\mu\mathrm{m}$ and is demagnified by a factor of 75 by the imaging system, so that each DMD pixel has a width of $0.1\,\mu\mathrm{m}$ in the image plane, which is much smaller than the resolution of the imaging system. For narrow barriers with a width $W \lesssim 10$ pixel, we can therefore adjust the height of the barrier by increasing the width of the barrier on the DMD image. We characterise the tunnelling barrier by using a second high resolution microscope to image the intensity distribution in the plane of the atoms (Fig. S 1) for all barrier widths W used in our experiments. From these images, we obtain a calibration of the relative change of the barrier height as a function of W as well as a determination of the barrier width $w = 0.81(6)\,\mu\mathrm{m}$, which is independent of W for $W \leq 11$ pixel (deviation $< 10\%$).

Phase control

To imprint a relative phase between the two sides of our Josephson junction, we briefly apply an optical potential ΔV_0 to the condensate in one of the reservoirs, which advances its phase by $\Delta V_0 t/\hbar$. The time t is much shorter than the Fermi time h/E_F, which ensures an almost pure phase excitation. The spatially homogeneous optical potential is created by DMD 2 and imaged onto the atom plane. We perform matter wave imaging (*28, 45*) and observe the relative

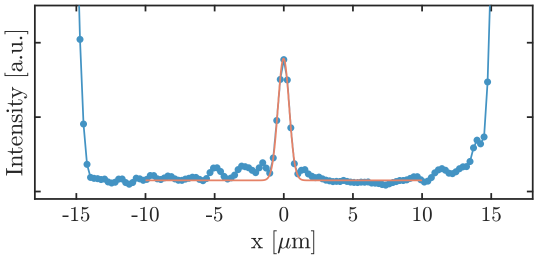

Fig. S 1: **Calibration of the barrier.** Line sum through an image of a box potential with a barrier in the center. The box has a width of 300 pixels on the DMD, which corresponds to a box size of 30 μm in the plane of the atoms. The barrier has a width of 4 pixels, which is broadened by the finite resolution of the imaging system used to project the image onto the atoms. From a Gaussian fit to the barrier (red line), we determine a $1/e^2$ waist of $w = 0.81(6)\mu$m.

phase difference between the reservoirs in the displacement of the pair condensation peak. We calibrate this procedure by measuring the periodic displacement of the momentum peak as a function of the time for which the imprinting potential is switched on. From the measurement shown in Fig. S 2, we obtain $\Delta V_0 = h \cdot 16.0(5)$ kHz for the potential height[2] and a displacement $\Delta x = 5.5(3)\mu\text{m}/\pi$.

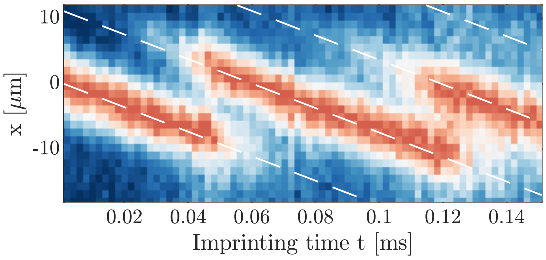

Fig. S 2: **Calibration of phase imprinting** We vary the time for which the imprinting potential is switched on and measure the shift in the position of the central momentum peak. From its periodic displacement, we obtain the height of the optical potential $\Delta V_0 = h \cdot 16.0(5)$ kHz. Each column represents a slice through the momentum distribution. The data shown is obtained by averaging over 38 realisations.

---

[2] We define ΔV_0 as the potential experienced by a pair of atoms, which has two times the polarisability and therefore experiences twice the optical dipole potential as a single atom.

LC Circuit Model

We use an electrical circuit model similar to the one used in (*21, 31, 32*) to model the dynamics of our Josephson junction. We describe our system as a capacitance C and a bulk inductance L_{B} connected in series to a Josephson junction, which is modelled as a nonlinear inductance $L_{\mathrm{J}}(\phi)$, see Fig. 1F. In this circuit, the current $I = \frac{1}{2}\frac{d(\Delta N)}{dt}$ is the instantaneous particle current across the junction determined by the change in the particle number imbalance $\Delta N = N_{\mathrm{L}} - N_{\mathrm{R}}$. The voltage over the capacitor is given by $U_{\mathrm{C}} = \Delta N/2C$, where $\Delta N/2$ corresponds to the charge of the capacitor. The voltage across the junction $U_{\mathrm{J}} = L_{\mathrm{J}}\frac{dI}{dt}$ is related to the phase difference ϕ via the Josephson-Anderson relation $U_{\mathrm{J}} = \hbar\frac{d\phi}{dt}$ and hence the junction has an inductance of $L_{\mathrm{J}}(\phi) = \hbar/\frac{dI(\phi)}{d\phi}$. According to Kirchhoff's law, the voltages across the capacitor, the bulk inductance and the junction add to zero and therefore the LC circuit is described by the differential equation

$$\frac{\Delta N}{C} + (L_{\mathrm{B}} + L_{\mathrm{J}}(\phi))\,\frac{\partial^2(\Delta N)}{\partial t^2} = 0. \tag{S1}$$

Linear Regime

For small phase excitations, $L_{\mathrm{J}}(\phi)$ can be approximated by a constant, phase independent inductance $L_{\mathrm{J},0}$ and Eq. S1 yields harmonic oscillations with frequency $\omega = \frac{1}{\sqrt{(L_{\mathrm{B}}+L_{\mathrm{J},0})C}}$. For a vanishing barrier, the oscillations correspond to a phononic excitation propagating between the boundaries of the box at the speed of sound v_{s}. In the circuit model, this corresponds to $L_{\mathrm{J}} = 0$ and the frequency is given by $\omega_s = \frac{1}{\sqrt{L_{\mathrm{B}}C}} = 2\pi\frac{v_{\mathrm{s}}}{2l_{\perp}}$. Hence, we can calculate $L_{\mathrm{J},0}$ from the ratio of the oscillation frequencies

$$L_{\mathrm{J},0} = L_{\mathrm{B}}\left(\frac{\omega_s^2}{\omega^2} - 1\right). \tag{S2}$$

For our homogeneous box system, the speed of sound $v_{\mathrm{s}} = \sqrt{\frac{n}{m}\frac{\partial\mu}{\partial n}}$ and the capacitance $C = \frac{1}{2}\frac{\partial N}{\partial\mu_B} = \frac{1}{4}\frac{\partial N}{\partial\mu} = \frac{1}{8}l_{\perp}l_{||}\frac{\partial n}{\partial\mu}$ are related to each other by the compressibility $\kappa = \frac{\partial\mu}{\partial n}$, where $\mu_{\mathrm{B}} = 2\mu$ is the chemical potential of a gas of bosonic dimers. Therefore, we can simply calculate the bulk inductance $L_{\mathrm{B}} = 1/\omega_s^2 C = 8m\, l_\perp / \pi^2 n\, l_{||}$ and thereby obtain the Josephson inductance $L_{\mathrm{J},0}$ without using the equation of state $\mu(n)$.

Current Phase Relation

For a phase excitation that is not small, the nonlinearity of the Josephson inductance leads to anharmonic oscillations. This nonlinear oscillation consists of a down-shifted fundamental frequency $\omega(\phi_0)$ and higher harmonics of this frequency. One possibility to extract the current phase relation from this anharmonic oscillation would be to obtain the instantaneous current $I(\phi(t))$ and relating it to the corresponding $\phi(t)$. However, this approach has the significant drawback that obtaining $I(\phi(t))$ requires numerical differentiation of $\Delta N(t)$, which is extremely sensitive to noise. Hence, we use the information contained in the shift of the fundamental frequency $\omega(\phi_0)$ to probe the current phase relation. We do this by extracting $L_{\mathrm{J},0}(\phi_0)$ from $\omega(\phi_0)$ according to Eq. S2 and then calculating an effective current $I_0(\phi_0) = \int_0^{\phi_0} \frac{\hbar}{L_{\mathrm{J},0}(\phi_0')}\, d\phi_0'$ by performing a Riemann sum over all experimentally determined values of $\frac{\hbar}{L_{\mathrm{J},0}(\phi_0')}$ for which $\phi_0' \leq \phi_0$. While this effective current is different from the instantaneous current, we can still relate the effective current phase relation $I_0(\phi_0)$ and the instantaneous current phase relation $I(\phi)$ by inserting the ideal current phase relation $I(\phi) = I_{\mathrm{C}} \sin(\phi)$ into Eq. S1. In principle, $I_0(\phi_0)$ can be found by solving Eq. S1 numerically, but it is instructive to consider a simplified case which can be solved analytically. If we assume that the dynamics of the system is dominated by the barrier ($L_{\mathrm{J}} \gg L_{\mathrm{B}}$), we can neglect the bulk inductance L_{B} in the LC circuit and write $\hbar\dot{\phi} + \frac{\Delta N}{2C} = 0$. Differentiating this equation, we get

$$\ddot{\phi} + \frac{I_{\mathrm{C}}}{\hbar C} \sin(\phi) = 0\,, \qquad \text{(S3)}$$

which is equivalent to the equation of motion of a mathematical pendulum. To first order, the oscillation frequency is given by $\omega(\phi_0)^2 \approx \frac{I_{\mathrm{C}}}{\hbar C}(1 - \phi_0^2/8) \approx \frac{I_{\mathrm{C}}}{\hbar C} \cos\frac{\phi_0}{2}$ and we can extract the corresponding inductance

$$L_{\mathrm{J},0}(\phi_0) \approx L_{\mathrm{J},0,\phi_0\to 0}\left(\frac{\omega_{\phi_0\to 0}}{\omega(\phi_0)}\right)^2 \approx \frac{\hbar}{I_\mathrm{C}\cos\left(\phi_0/2\right)}\,. \tag{S4}$$

After integration, we get a simple rescaled expression for the effective current

$$I_0(\phi_0) \approx 2I_\mathrm{C}\sin\frac{\phi_0}{2}\,. \tag{S5}$$

We compare this result with the current $I_0(\phi_0)$ extracted from the numerical solution of Eq. S1 for a system with $L_{\mathrm{J},0}/L_\mathrm{B} = 1.3$, which is the value of $L_{\mathrm{J},0}/L_\mathrm{B}$ for the system that was used for the measurements in Fig. 2. We find that for initial phase excitations $\phi_0 \lesssim 0.7\pi$, Eq. S5 and the numerical solution agree within 2%. Hence, we compare our data to Eq. S5.

Numerical simulations

We simulate the dynamics of a two-dimensional (2D) bosonic Josephson junction with the c-field simulation method that was used in Ref. (*46*). Our homogeneous 2D system is described by the Hamiltonian

$$\hat{H}_0 = \int \mathrm{d}\mathbf{r}\left[\frac{\hbar^2}{2M}\nabla\hat{\psi}^\dagger(\mathbf{r})\cdot\nabla\hat{\psi}(\mathbf{r}) + \frac{g}{2}\hat{\psi}^\dagger(\mathbf{r})\hat{\psi}^\dagger(\mathbf{r})\hat{\psi}(\mathbf{r})\hat{\psi}(\mathbf{r})\right], \tag{S6}$$

where $\hat{\psi}$ and $\hat{\psi}^\dagger$ are the bosonic annihilation and creation operators, respectively. The interaction g is given by $g = \tilde{g}\hbar^2/M$, where $\tilde{g}$ is the dimensionless interaction and M the mass of a $^6\mathrm{Li}_2$ molecule. Here, $\tilde{g}$ is determined by $\tilde{g} = \tilde{g}_0/\big(1 - \frac{\tilde{g}_0}{2\pi}\ln(2.09k_\mathrm{F}\ell_d)\big)$, with $\tilde{g}_0 = \sqrt{8\pi}a_s/\ell_d$ (*47*), where a_s is the molecular s-wave scattering length, $\ell_d = \sqrt{\hbar/(M\omega_z)}$ is the harmonic oscillator length in the transverse direction, and k_F is the Fermi wave vector. Analogous to the experiments, we consider 2D clouds of $^6\mathrm{Li}_2$ molecules confined in a box of dimensions $L_x \times L_y$. We discretise the space with a lattice of size $N_x \times N_y$ and a discretisation length $l = 0.5\,\mu\mathrm{m}$. Within our c-field representation, we describe the operators $\hat{\psi}$ in Eq. S6 and the equations of motion by complex numbers ψ. We sample the initial states in a grand canonical ensemble with chemical potential μ and temperature T via a classical Metropolis algorithm. The system parameters, such as the density n, $\tilde{g}$, and T are chosen in accordance with the experiments. To simulate the Josephson junction we add the term $\mathcal{H}_{ex} = \int \mathrm{d}\mathbf{r}\, V(\mathbf{r}) n(\mathbf{r})$, where $n(\mathbf{r})$ is the density at the location $\mathbf{r} = (x, y)$. The barrier potential $V(\mathbf{r})$ is given by

$$V(\mathbf{r}) = V_0 \exp\bigl(-2(x - x_0)^2 / w^2\bigr), \tag{S7}$$

where V_0 is the barrier height and w the width. The potential is centered at the location $x_0 = L_x/2$. We choose $w = 0.85\,\mu\mathrm{m}$ and V_0/μ in the range $0 - 2$, where we use $\mu = gn$. This splits the system in x-direction into two equal 2D clouds, which we refer to as the left and right reservoir. We then imprint a fixed value of the phase on one of the reservoirs, which creates a phase difference $\Delta\phi = \phi_{\mathrm{L}} - \phi_{\mathrm{R}}$, where ϕ_{L} (ϕ_{R}) is the mean value of the phase of the left (right) reservoir. The sudden imprint of phase results in oscillations of $\Delta\phi$ and the density imbalance $\Delta N = N_{\mathrm{L}} - N_{\mathrm{R}}$, where N_{L} (N_{R}) is the number of molecules in the left (right) reservoir. We analyse the time evolution of ΔN and $\Delta\phi$ for system parameters close to the ones used in the experiments. Fig. S 3 A-C shows simulations of $\Delta\phi(t)$ at three different temperatures of $T/T_{\mathrm{F}} \approx 0.01$, 0.03, and 0.06 for $n = 2.25\,\mu\mathrm{m}^{-2}$, $\tilde{g} = 1.8$ and a system size of $L_x \times L_y = 20 \times 40\,\mu\mathrm{m}^2$. The damping of the oscillations increases with temperature. To quantify this observation, we fit $\Delta\phi(t)$ with a damped sine function $f(t) = A_0 e^{-\Gamma t} \sin(\omega t + \theta)$, where A_0 is the amplitude, ω is the oscillation frequency, Γ is the damping, and θ is the phase shift. The determined ratio of Γ/ω is 0.05, 0.09, and 0.45 for $T/T_{\mathrm{F}} \approx 0.01$, 0.03, and 0.06, respectively. As the experimentally observed damping is on the order of $\Gamma/\omega \approx 0.07$, this suggests an experimental temperature on the order of $T/T_{\mathrm{F}} \lesssim 0.03$, which is consistent with the results from measurements of the momentum distribution and the equation of state shown in Fig. S 4. To obtain a calibration of the experimental barrier height, we simulate the system for a wide range of barrier heights V_0 and match the simulated and extracted Josephson inductances by fitting the calibration factor between the width W of the barrier on the DMD and the simulated barrier height V_0.

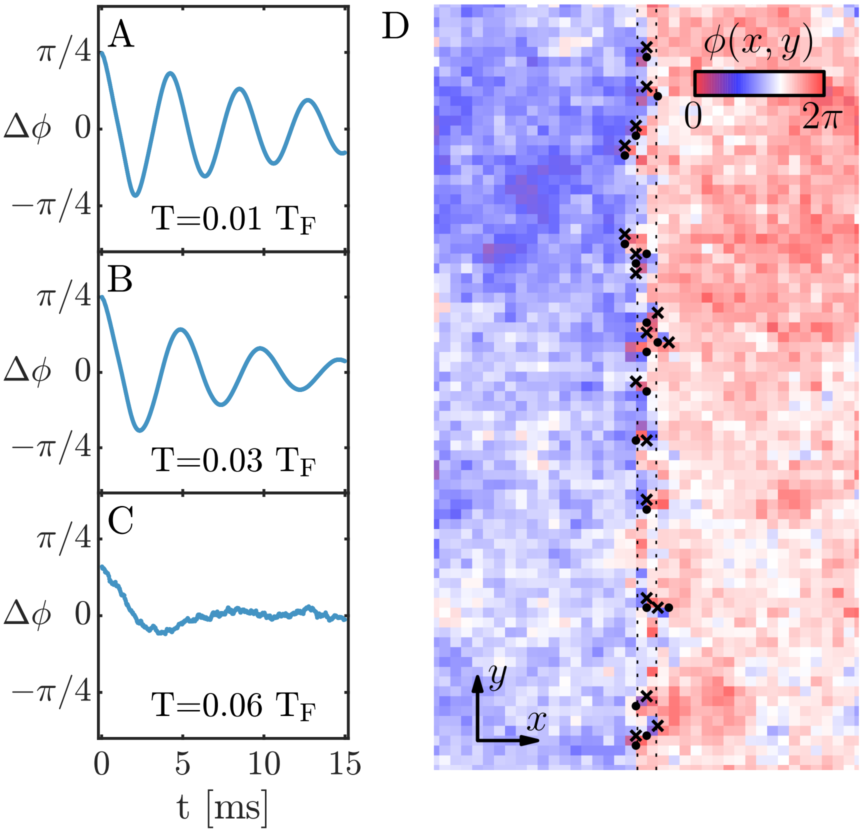

Fig. S 3: **Temperature dependence of Josephson oscillations.** **(A-C)** Time evolution of the simulated $\Delta\phi$ for $V_0/\mu \approx 1.0$ and a phase imprint of $\pi/4$ at three different temperatures. **(D)** Simulated phase evolution of one sample of the ensemble, 3.9 ms after a phase imprint of $\pi/4$, for $n = 2.25\,\mu\text{m}^{-2}$ and $T/T_\text{F} \approx 0.03$. The barrier height is $V_0/\mu \approx 2$ and its width of $0.85\,\mu$m is denoted by the two vertical dotted lines. The dots and the crosses represent vortices and antivortices, respectively. The box dimensions are $20 \times 40\,\mu\text{m}^2$.

To understand the mechanism for the thermal damping of the oscillations, we examine the phase evolution of a single sample of our ensemble. Figure S 3D shows the phase $\phi(x, y)$ at a point in time which is 3.9 ms after a phase imprint of $\pi/4$ for the same n, $\tilde{g}$ and box size as above, and $T/T_\text{F} \approx 0.03$. At this time the system exhibits distinct values of the mean phase for the left and right reservoir and a strong phase gradient across the barrier. As expected for a 2D system, the phase is weakly fluctuating within the reservoirs due to thermal phonons. In addition to the phonons, we identify the nucleation of vortex-antivortex pairs as an additional mechanism of dissipation. We calculate the phase winding around a lattice plaquette of size $l \times l$ using $\sum_{\Box} \delta\phi(x, y) = \delta_x\phi(x, y) + \delta_y\phi(x + l, y) + \delta_x\phi(x + l, y + l) + \delta_y\phi(x, y + l)$, where the phase differences between sites is taken to be $\delta_{x/y}\phi(x, y) \in (-\pi, \pi]$. We show the calculated phase winding in Fig. S 3D. A vortex and an antivortex are identified by a phase winding of 2π and -2π, respectively. The vortex pairs are nucleated mainly inside the barrier in the regions of low densities. Both the phonons and vortices lead to the damping of oscillations shown in Fig. S 3 A-C.

Equation of state

To keep our relative barrier height V_0/μ constant during measurements over the crossover, we need to measure the chemical potential μ as a function of interaction strength. We do this by following the approach established by Ref. (*48*). We therefore define our chemical potential as $\mu = \mu_0 + \epsilon_{\mathrm{B}}/2$, where μ is the chemical potential per atom and the contribution of the two-body binding energy ϵ_{B} is subtracted from the bare chemical potential μ_0. We use DMD 2 to introduce a potential offset ΔV between the two sides of the box and measure the resulting density difference Δn. For sufficiently small temperatures, the Thomas-Fermi approximation predicts $E_{\mathrm{F}} = c \cdot \mu$, and we can obtain $\mu/E_{\mathrm{F}} = 1/c$ from the linear slope of $\Delta n(\Delta V)$. The relative change in the measured chemical potential for different magnetic fields is shown in Fig. S 4 C.

To determine the temperature of our system we compare the measured $\Delta n(\Delta V)$ of the bosonic system with interaction strength $\ln(k_{\mathrm{F}} a_{\mathrm{2D}}) = -2.9$ with simulated curves for different temperatures obtained using the c-field method outlined above. The discrepancy between the measurement and the numerical simulations is minimised for a temperature of $T \approx 0.03\,T_{\mathrm{F}}$ (Fig. S 4A,B).

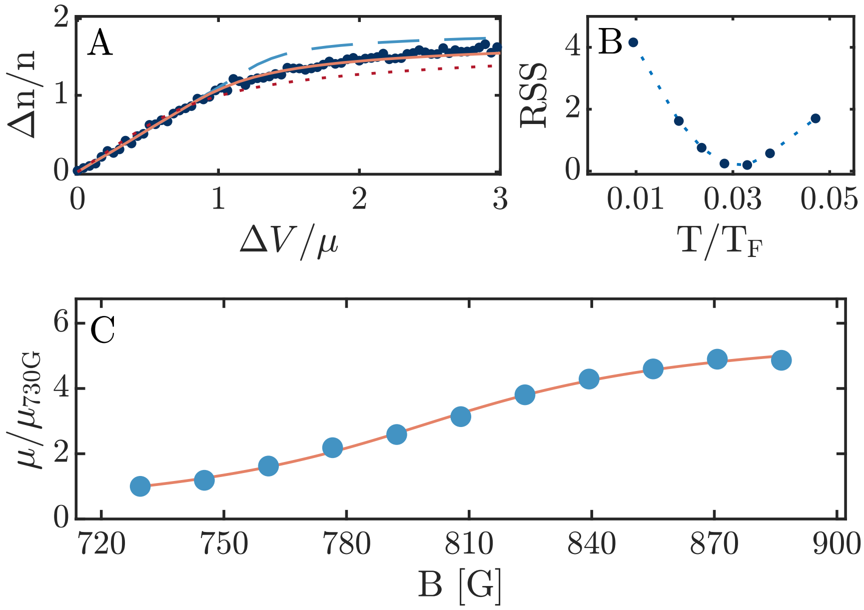

Fig. S 4: **Equation of state.** **(A)** Density difference Δn (dark blue dots) created by a potential step ΔV, compared to numerical simulations performed at $T/T_{\mathrm{F}} = 0.019$ (dashed blue line), $T/T_{\mathrm{F}} = 0.033$ (solid red line) and $T/T_{\mathrm{F}} = 0.047$ (dotted dark red line). **(B)** Residual sum of squares between the numerical simulations performed at different temperatures and the measured EOS. The dashed blue line is a guide to the eye. The best agreement between our measured equation of state and the simulation is achieved at a temperature of $T/T_{\mathrm{F}} = 0.03$. **(C)** Relative change of the chemical potential of our system for different magnetic fields, normalized to the chemical potential at a field of 730 G . The chemical potential is extracted from the initial slope of the EOS measurements shown in **(A)**. The red line is a heuristic fit we use to keep V_0/μ constant during our measurement across the crossover (Fig. 3). The data shown is obtained by averaging over 7 **(A)** and 3 **(C)** realisations.

Calculation of the critical current

In the following we derive an analytic expression for the critical current I_{C} of our 2D Josephson junction in the bosonic limit including phase fluctuations, motivated by recent work for 3D systems (*34*). Generally, we can express the current between the left and right reservoir

$$\mathbf{I} \;=\; -\frac{i}{\hbar}\Big(\sum_{\mathbf{k}} t_{\mathbf{k}}(a_l^\dagger(\mathbf{k})a_r(\mathbf{k}) - a_r^\dagger(\mathbf{k})a_l(\mathbf{k}))\Big) \tag{S8}$$

via the tunnelling amplitudes $t_{\mathbf{k}}$ and the bosonic creation and annihilation operators acting on the left and right reservoir. In the phase-density representation, neglecting density fluctuations, the annihilation operators are given by

$$a_{l/r}(\mathbf{k}) \;=\; \int \frac{d^2r}{\sqrt{A}} \exp(-i\mathbf{k}\mathbf{r})\sqrt{n_{l/r}}\exp(i\phi_{l/r} + i\delta\phi_{l/r}(\mathbf{r}))\,, \tag{S9}$$

where $A = L^2$ is the area of a box of size L, $n_l\,(n_r)$ is the density, $\phi_l\,(\phi_r)$ is the phase, and $\delta\phi_l\,(\delta\phi_r)$ is the fluctuation of the phase in the left (right) reservoir. To calculate the expectation value $\langle\mathbf{I}\rangle$, we insert Eq. S9 in Eq. S8 and assume independent Gaussian fluctuations of the phase in both reservoirs $\langle e^{i\delta\phi_{l/r}(\mathbf{r})}\rangle = e^{-\frac{1}{2}\langle\delta\phi^2_{l/r}(\mathbf{r})\rangle}$. For a 2D system, we can further approximate the phase fluctuations to lowest order as $\langle\delta\phi^2_{l/r}(\mathbf{r})\rangle = \eta\log(L/r_0)$, where $\eta = \frac{Mk_BT}{2\pi\hbar^2 n_s} = 2\frac{n}{n_s}\frac{T}{T_\mathrm{F}}$ is the algebraic scaling exponent and $r_0 \approx \xi$ is a short range cutoff on the order of the system's healing length ξ. To lowest order in k, we obtain

$$\langle\mathbf{I}\rangle \;=\; \frac{2nAt_{\mathbf{k}=0}}{\hbar}\left(\frac{L}{r_0}\right)^{-\eta}\sin\phi\,, \tag{S10}$$

where $\phi = \phi_r - \phi_l$ is the phase difference across the barrier. This result reproduces the ideal current phase relation $I(\phi) = I_\mathrm{C}\sin(\phi)$, where the critical current I_C is reduced by a factor of $\left(\frac{L}{r_0}\right)^{-\eta}$. Therefore, the critical current I_C is directly related to the algebraic decay of phase coherence in a 2D superfluid. Using the the condensate density

$$n_c \approx n(L/r_0)^{-\eta} \tag{S11}$$

of a finite size 2D gas as defined in ref. (*35*) we finally get the critical current

$$I_\mathrm{C} \approx \frac{2n_cAt_{\mathbf{k}=0}}{\hbar}\,. \tag{S12}$$

We calculate the tunnelling amplitude $t_{\mathbf{k}=0}$ for a rectangular potential barrier of width d and height V_B, centered around $x = 0$, with the following mean field ansatz

$$\psi(x) \;=\; \begin{cases} -\frac{1}{\sqrt{L}}\tanh((x+\delta)/(\sqrt{2}\xi)) & x < -d/2 \\ B\exp(-\kappa(x+d/2)) & x > -d/2\,, \end{cases} \tag{S13}$$

with

$$\delta \;=\; \frac{d}{2} - \frac{\xi}{\sqrt{2}}\mathrm{arcsinh}\Big(\frac{\sqrt{2}}{\kappa\xi}\Big) \tag{S14}$$

$$B \;=\; \frac{1}{\sqrt{L}}\tanh\Big(\frac{1}{2}\mathrm{arcsinh}\Big(\frac{\sqrt{2}}{\kappa\xi}\Big)\Big) \tag{S15}$$

where $\xi = \hbar/\sqrt{2M\mu_B}$ is the healing length for a gas of bosons with mass M and chemical potential μ_B. Outside the barrier $(x < -d/2)$, $\psi(x)$ is the exact solution to the Gross-Pitaevskii equation. Inside the barrier $(x > -d/2)$, we obtain the approximative solution by minimising the energy

$$E \;=\; \frac{B^2}{2\kappa}\Big(\frac{\hbar^2\kappa^2}{2M} + V_B - \mu_B\Big) + \frac{g}{2}\frac{B^4}{4\kappa} \tag{S16}$$

which yields the characteristic decay exponent $\kappa = \sqrt{k_0^2 + k_B^2}$ with $k_0^2 = 2M(V_B - \mu_B)/\hbar^2$ and $k_B^2 = MgB^2/2\hbar^2$. Using the continuity of the wave function and its derivative at $z = -d/2$ we further get

$$\kappa^2 \;=\; k_0^2 + \frac{MgB^2}{2\hbar^2} = \frac{n}{2\xi^2}\Big(1 - \frac{B^2}{n}\Big)^2\frac{1}{B^2} \tag{S17}$$

and obtain

$$B^2 \;=\; \frac{n}{1 + k_0^2\xi^2 + \sqrt{1/2 + 2k_0^2\xi^2 + (k_0^2\xi^2)^2}} \tag{S18}$$

$$\;=\; n\frac{\mu_B}{V + \sqrt{V_B^2 - \mu_B^2/2}}\,. \tag{S19}$$

Therefore, we finally obtain the tunnelling energy

$$t_{\mathbf{k}=0} \;=\; \frac{1}{L}\frac{\hbar^2\kappa}{m}\frac{\mu_B}{V_B + \sqrt{V_B^2 - \mu_B^2/2}}\exp(-\kappa d)\,, \tag{S20}$$

which we insert into Eq. S12 to obtain the critical current I_C.

We note that Eq. S12 which relates the critical current to the condensate density has previously been derived for a 3D system (*49*) and was found to quantitatively describe the behaviour across the 3D BEC-BCS crossover for high barriers $(V \gg \mu)$ (*34*). Our derivation of the critical current extends the validity of this relation in the bosonic limit to $V \gtrsim \mu$ by including the mean field contribution to the tunnelling amplitude inside the barrier. Following the same reasoning and assumptions given in (*34*), it seems plausible that Eq. S12 is quantitatively accurate beyond the bosonic case discussed above, but verifying this is beyond the scope of this paper. A more detailed discussion of Eq. S12 and its derivation is given in Ref. (*37*).

References and Notes

1. B. D. Josephson, Possible new effects in superconductive tunnelling. *Phys. Lett.* **1**, 251–253 (1962). doi:10.1016/0031-9163(62)91369-0

2. P. W. Anderson, J. M. Rowell, Probable observation of the Josephson superconducting tunneling effect. *Phys. Rev. Lett.* **10**, 230–232 (1963). doi:10.1103/PhysRevLett.10.230

3. A. A. Golubov, M. Y. Kupriyanov, E. Il'ichev, The current-phase relation in Josephson junctions. *Rev. Mod. Phys.* **76**, 411–469 (2004). doi:10.1103/RevModPhys.76.411

4. C. Tsuei, J. Kirtley, Pairing symmetry in cuprate superconductors. *Rev. Mod. Phys.* **72**, 969–1016 (2000). doi:10.1103/RevModPhys.72.969 Medline

5. B. Fröhlich, M. Feld, E. Vogt, M. Koschorreck, W. Zwerger, M. Köhl, Radio-frequency spectroscopy of a strongly interacting two-dimensional Fermi gas. *Phys. Rev. Lett.* **106**, 105301 (2011). doi:10.1103/PhysRevLett.106.105301 Medline

6. A. T. Sommer, L. W. Cheuk, M. J. H. Ku, W. S. Bakr, M. W. Zwierlein, Evolution of fermion pairing from three to two dimensions. *Phys. Rev. Lett.* **108**, 045302 (2012). doi:10.1103/PhysRevLett.108.045302 Medline

7. V. Makhalov, K. Martiyanov, A. Turlapov, Ground-state pressure of quasi-2D Fermi and Bose gases. *Phys. Rev. Lett.* **112**, 045301 (2014). doi:10.1103/PhysRevLett.112.045301 Medline

8. W. Ong, C. Cheng, I. Arakelyan, J. E. Thomas, Spin-imbalanced quasi-two-dimensional Fermi gases. *Phys. Rev. Lett.* **114**, 110403 (2015). doi:10.1103/PhysRevLett.114.110403 Medline

9. K. Fenech, P. Dyke, T. Peppler, M. G. Lingham, S. Hoinka, H. Hu, C. J. Vale, Thermodynamics of an attractive 2D Fermi gas. *Phys. Rev. Lett.* **116**, 045302 (2016). doi:10.1103/PhysRevLett.116.045302 Medline

10. D. Mitra, P. T. Brown, P. Schauß, S. S. Kondov, W. S. Bakr, Phase separation and pair condensation in a spin-imbalanced 2D Fermi gas. *Phys. Rev. Lett.* **117**, 093601 (2016). doi:10.1103/PhysRevLett.117.093601 Medline

11. A. Mazurenko, C. S. Chiu, G. Ji, M. F. Parsons, M. Kanász-Nagy, R. Schmidt, F. Grusdt, E. Demler, D. Greif, M. Greiner, A cold-atom Fermi-Hubbard antiferromagnet. *Nature* **545**, 462–466 (2017). doi:10.1038/nature22362 Medline

12. J. Levinsen, M. M. Parish, in *Annual Review of Cold Atoms and Molecules*, K. W. Madison, K. Bongs, L. D. Carr, A. M. Rey, H. Zhai, Eds. (World Scientific, 2015), vol. 3, chap. 1, pp. 1–75.

13. M. G. Ries, A. N. Wenz, G. Zürn, L. Bayha, I. Boettcher, D. Kedar, P. A. Murthy, M. Neidig, T. Lompe, S. Jochim, Observation of pair condensation in the quasi-2D BEC-BCS crossover. *Phys. Rev. Lett.* **114**, 230401 (2015). doi:10.1103/PhysRevLett.114.230401 Medline

14. F. S. Cataliotti, S. Burger, C. Fort, P. Maddaloni, F. Minardi, A. Trombettoni, A. Smerzi, M. Inguscio, Josephson junction arrays with Bose-Einstein condensates. *Science* **293**, 843–846 (2001). doi:10.1126/science.1062612 Medline

15. M. Albiez, R. Gati, J. Fölling, S. Hunsmann, M. Cristiani, M. K. Oberthaler, Direct observation of tunneling and nonlinear self-trapping in a single bosonic Josephson junction. *Phys. Rev. Lett.* **95**, 010402 (2005). doi:10.1103/PhysRevLett.95.010402 Medline

16. S. Levy, E. Lahoud, I. Shomroni, J. Steinhauer, The a.c. and d.c. Josephson effects in a Bose-Einstein condensate. *Nature* **449**, 579–583 (2007). doi:10.1038/nature06186 Medline

17. L. J. LeBlanc, A. B. Bardon, J. McKeever, M. H. T. Extavour, D. Jervis, J. H. Thywissen, F. Piazza, A. Smerzi, Dynamics of a tunable superfluid junction. *Phys. Rev. Lett.* **106**, 025302 (2011). doi:10.1103/PhysRevLett.106.025302 Medline

18. T. Betz, S. Manz, R. Bücker, T. Berrada, Ch. Koller, G. Kazakov, I. E. Mazets, H.-P. Stimming, A. Perrin, T. Schumm, J. Schmiedmayer, Two-point phase correlations of a one-dimensional bosonic Josephson junction. *Phys. Rev. Lett.* **106**, 020407 (2011). doi:10.1103/PhysRevLett.106.020407 Medline

19. G. Spagnolli, G. Semeghini, L. Masi, G. Ferioli, A. Trenkwalder, S. Coop, M. Landini, L. Pezzè, G. Modugno, M. Inguscio, A. Smerzi, M. Fattori, Crossing over from attractive to repulsive interactions in a tunneling bosonic Josephson junction. *Phys. Rev. Lett.* **118**, 230403 (2017). doi:10.1103/PhysRevLett.118.230403 Medline

20. G. Valtolina, A. Burchianti, A. Amico, E. Neri, K. Xhani, J. A. Seman, A. Trombettoni, A. Smerzi, M. Zaccanti, M. Inguscio, G. Roati, Josephson effect in fermionic superfluids across the BEC-BCS crossover. *Science* **350**, 1505–1508 (2015). doi:10.1126/science.aac9725 Medline

21. A. Burchianti, F. Scazza, A. Amico, G. Valtolina, J. A. Seman, C. Fort, M. Zaccanti, M. Inguscio, G. Roati, Connecting dissipation and phase slips in a Josephson junction between fermionic superfluids. *Phys. Rev. Lett.* **120**, 025302 (2018). doi:10.1103/PhysRevLett.120.025302 Medline

22. C. Ryu, P. W. Blackburn, A. A. Blinova, M. G. Boshier, Experimental realization of Josephson junctions for an atom SQUID. *Phys. Rev. Lett.* **111**, 205301 (2013). doi:10.1103/PhysRevLett.111.205301 Medline

23. G. Watanabe, F. Dalfovo, F. Piazza, L. Pitaevskii, S. Stringari, Critical velocity of superfluid flow through single-barrier and periodic potentials. *Phys. Rev. A* **80**, 053602 (2009). doi:10.1103/PhysRevA.80.053602

24. A. Spuntarelli, P. Pieri, G. C. Strinati, Josephson effect throughout the BCS-BEC crossover. *Phys. Rev. Lett.* **99**, 040401 (2007). doi:10.1103/PhysRevLett.99.040401 Medline

25. F. Ancilotto, L. Salasnich, F. Toigo, dc Josephson effect with Fermi gases in the Bose-Einstein regime. *Phys. Rev. A* **79**, 033627 (2009). doi:10.1103/PhysRevA.79.033627

26. S. Eckel, F. Jendrzejewski, A. Kumar, C. Lobb, G. Campbell, Interferometric measurement of the current-phase relationship of a superfluid weak link. *Phys. Rev. X* **4**, 031052 (2014). doi:10.1103/PhysRevX.4.031052

27. See supplementary materials.

28. K. Hueck, N. Luick, L. Sobirey, J. Siegl, T. Lompe, H. Moritz, Two-dimensional homogeneous Fermi gases. *Phys. Rev. Lett.* **120**, 060402 (2018). doi:10.1103/PhysRevLett.120.060402 Medline

29. This corresponds to an interaction strength of $\ln\left(k_\mathrm{F} a_\mathrm{2D}\right) = -2.4$.

30. Notably, achieving this low damping requires a temperature of $T / T_\mathrm{F} \lesssim 0.03$ (fig. S3), which is far below the predicted critical temperature $T_\mathrm{c} / T_\mathrm{F} \approx 0.1$ for 2D superfluidity at this interaction strength (*13*, *27*, *41*).

31. J. G. Lee, B. J. McIlvain, C. J. Lobb, W. T. Hill III, Analogs of basic electronic circuit elements in a free-space atom chip. *Sci. Rep.* **3**, 1034 (2013). doi:10.1038/srep01034 Medline

32. S. Eckel, J. G. Lee, F. Jendrzejewski, C. J. Lobb, G. K. Campbell, W. T. Hill, Contact resistance and phase slips in mesoscopic superfluid-atom transport. *Phys. Rev. A* **93**, 063619 (2016). doi:10.1103/PhysRevA.93.063619

33. We note that achieving a sinusoidal current phase relation requires a barrier deep in the tunneling regime, which is fulfilled for our barrier depth of $V_0 / \mu \approx 1.5$.

34. M. Zaccanti, W. Zwerger, Critical Josephson current in BCS-BEC–crossover superfluids. *Phys. Rev. A* **100**, 063601 (2019). doi:10.1103/PhysRevA.100.063601

35. Z. Hadzibabic, J. Dalibard, Two-dimensional Bose fluids: An atomic physics perspective. *RIV Nuovo Cim.* **34**, 389 (2011). doi:10.1393/ncr/i2011-10066-3

36. N. V. Prokof'ev, B. V. Svistunov, Algebraic time crystallization in a two-dimensional superfluid. *J. Exp. Theor. Phys.* **127**, 860–864 (2018). doi:10.1134/S1063776118110092

37. V. P. Singh, N. Luick, L. Sobirey, L. Mathey, Josephson junction dynamics in a two-dimensional ultracold Bose gas. arXiv:2002.08375 [cond-mat.quant-gas] (19 February 2020).

38. J. J. Kinnunen, J. E. Baarsma, J.-P. Martikainen, P. Törmä, The Fulde-Ferrell-Larkin-Ovchinnikov state for ultracold fermions in lattice and harmonic potentials: A review. *Rep. Prog. Phys.* **81**, 046401 (2018). doi:10.1088/1361-6633/aaa4ad Medline

39. W. Hu, S. Kaiser, D. Nicoletti, C. R. Hunt, I. Gierz, M. C. Hoffmann, M. Le Tacon, T. Loew, B. Keimer, A. Cavalleri, Optically enhanced coherent transport in $YBa_2Cu_3O_{6.5}$ by ultrafast redistribution of interlayer coupling. *Nat. Mater.* **13**, 705–711 (2014). doi:10.1038/nmat3963 Medline

40. J.-i. Okamoto, W. Hu, A. Cavalleri, L. Mathey, Transiently enhanced interlayer tunneling in optically driven high-T_c superconductors. *Phys. Rev. B* **96**, 144505 (2017). doi:10.1103/PhysRevB.96.144505

41. D. Petrov, M. Baranov, G. Shlyapnikov, Superfluid transition in quasi-two-dimensional Fermi gases. *Phys. Rev. A* **67**, 031601 (2003). doi:10.1103/PhysRevA.67.031601

42. N. Luick, L. Sobirey, M. Bohlen, V. P. Singh, L. Mathey, T. Lompe, H. Moritz, Data for "An ideal Josephson junction in an ultracold two-dimensional Fermi gas." Zenodo (2020); https://doi.org/10.5281/zenodo.3744797.

43. N. Luick, L. Sobirey, M. Bohlen, V. P. Singh, L. Mathey, T. Lompe, H. Moritz, Simulation script and data for "An ideal Josephson junction in an ultracold two-dimensional Fermi gas." Zenodo (2020); https://doi.org/10.5281/zenodo.3786298.

44. D. Petrov, G. Shlyapnikov, Interatomic collisions in a tightly confined Bose gas. *Phys. Rev. A* **64**, 012706 (2001). doi:10.1103/PhysRevA.64.012706

45. P. Murthy, D. Kedar, T. Lompe, M. Neidig, M. G. Ries, A. N. Wenz, G. Zürn, S. Jochim, Matter-wave Fourier optics with a strongly interacting two-dimensional Fermi gas. *Phys. Rev. A* **90**, 043611 (2014). doi:10.1103/PhysRevA.90.043611

46. V. P. Singh, C. Weitenberg, J. Dalibard, L. Mathey, Superfluidity and relaxation dynamics of a laser-stirred two-dimensional Bose gas. *Phys. Rev. A (Coll. Park)* **95**, 043631 (2017). doi:10.1103/PhysRevA.95.043631

47. A. V. Turlapov, M. Yu Kagan, Fermi-to-Bose crossover in a trapped quasi-2D gas of fermionic atoms. *J. Phys. Condens. Matter* **29**, 383004 (2017). doi:10.1088/1361-648X/aa7ad9 Medline

48. I. Boettcher, L. Bayha, D. Kedar, P. A. Murthy, M. Neidig, M. G. Ries, A. N. Wenz, G. Zürn, S. Jochim, T. Enss, Equation of state of ultracold fermions in the 2D BEC-BCS crossover region. *Phys. Rev. Lett.* **116**, 045303 (2016). doi:10.1103/PhysRevLett.116.045303 Medline

49. F. Meier, W. Zwerger, Josephson tunneling between weakly interacting Bose-Einstein condensates. *Phys. Rev. A* **64**, 033610 (2001). doi:10.1103/PhysRevA.64.033610

A.2. Sound Propagation and Quantum-Limited Damping in a Two-Dimensional Fermi Gas.

PHYSICAL REVIEW LETTERS **124,** 240403 (2020)

Editors' Suggestion

Sound Propagation and Quantum-Limited Damping in a Two-Dimensional Fermi Gas

Markus Bohlen,[1,2,3] Lennart Sobirey,[1] Niclas Luick,[1] Hauke Biss,[1,2] Tilman Enss,[4]
Thomas Lompe,[1,*] and Henning Moritz[1,2]
[1]*Institut für Laserphysik, Universität Hamburg, Luruper Chaussee 149, Hamburg 22761, Germany*
[2]*The Hamburg Centre for Ultrafast Imaging, Universität Hamburg, Luruper Chaussee 149, Hamburg 22761, Germany*
[3]*Laboratoire Kastler Brossel, ENS-Université PSL, CNRS, Sorbonne Université,*
Collège de France, 24 rue Lhomond, Paris 75005, France
[4]*Intitut für Theoretische Physik, Universität Heidelberg, Philosophenweg 19, Heidelberg 69120, Germany*

(Received 9 March 2020; revised manuscript received 26 April 2020; accepted 22 May 2020; published 16 June 2020)

Strongly interacting two-dimensional Fermi systems are one of the great remaining challenges in many-body physics due to the interplay of strong local correlations and enhanced long-range fluctuations. Here, we probe the thermodynamic and transport properties of a 2D Fermi gas across the BEC-BCS crossover by studying the propagation and damping of sound modes. We excite particle currents by imprinting a phase step onto homogeneous Fermi gases trapped in a box potential and extract the speed of sound from the frequency of the resulting density oscillations. We measure the speed of sound across the BEC-BCS crossover and compare the resulting dynamic measurement of the equation of state both to a static measurement based on recording density profiles and to quantum Monte Carlo calculations and find reasonable agreement between all three. We also measure the damping of the sound mode, which is determined by the shear and bulk viscosities as well as the thermal conductivity of the gas. We find that the damping is minimal in the strongly interacting regime and the diffusivity approaches the universal quantum bound $\hbar/m$ of a perfect fluid.

DOI: 10.1103/PhysRevLett.124.240403

Strongly interacting fermionic systems appear in many different areas of physics, yet understanding their behavior remains challenging. A powerful experimental method to gain access to their thermodynamic and transport properties is to study collective excitations such as sound modes. The speed of sound is determined by the compressibility of the medium, giving access to its equation of state. The damping of sound modes in the hydrodynamic regime is caused by the diffusion of heat as well as longitudinal and transverse momentum, and thus depends on the transport coefficients of the medium, i.e., thermal conductivity, bulk, and shear viscosity. In hydrodynamic systems which support well-defined quasiparticle excitations such as fermionic quasiparticles in a normal Fermi liquid or phonon excitations in a superfluid, kinetic theory predicts that the damping rate is proportional to the quasiparticle lifetimes. Long-lived quasiparticles can transport heat or momentum over long distances and therefore smooth out density and pressure variations very efficiently, leading to strong attenuation of sound waves. In contrast, no well-defined quasiparticles exist in the strongly correlated regime. Here, particles scatter with a mean free path comparable to the average interparticle spacing, leading to lower diffusivities and hence lower damping rates. A lower bound for the diffusivities $D \gtrsim \hbar/m$ and thus quantum-limited transport has been predicted and observed in several transport channels, including shear viscosity in ultracold 2D [1–4] and 3D [5–7] Fermi gases as well as spin diffusion in 2D [2,4,8,9] and 3D Fermi gases [10–14]. In measurements of sound propagation, this limit was observed in the sound diffusion of a unitary 3D Fermi gas [15].

Several hypotheses have been brought forward to provide an explanation for quantum-limited transport [16]: one, motivated by holographic duality [17], is that it occurs near scale invariant points in the phase diagram. The unitary 3D Fermi gas is an example that seems to support this hypothesis since it is strongly interacting as well as scale invariant and exhibits quantum-limited shear and spin diffusion. In contrast, 2D Fermi gases exhibit a quantum scale anomaly that breaks scale invariance [18–21]. Here, we investigate the propagation and damping of sound in a strongly interacting 2D Fermi gas and thereby probe a crucial test case for this hypothesis. We observe that the damping approaches the quantum limit $D \approx \hbar/m$ in the strongly interacting regime, where scale invariance is most dramatically violated, showing that scale invariance or quantum criticality is in fact not required for quantum-limited transport. Similar observations

---

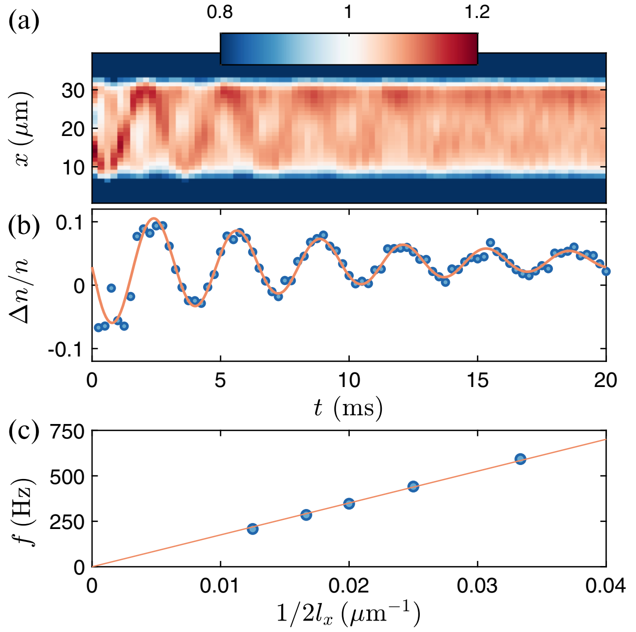

FIG. 1. Propagation of a sound wave in a box potential: (a) Density profiles $n(x,t)/n(t)$ averaged along the direction perpendicular to the sound propagation and normalized to the average density $n(t)$ within the box. A density wave propagating through the box is visible. Each profile $n(x,t)/n(t)$ is the average of 120 individual realizations. Note that the color scale has been chosen to enhance the visibility of the sound wave. (b) Relative density imbalance between the two sides of the box for the same data set. The solid line shows a damped sinusoidal fit to the data. (c) Frequency of the density oscillation as a function of the inverse box length. The slope of the linear fit (solid line) corresponds to the speed of sound. In (b) and (c), the statistical errors are smaller than the marker size. Each data point in (c) is the average of 23 realizations.

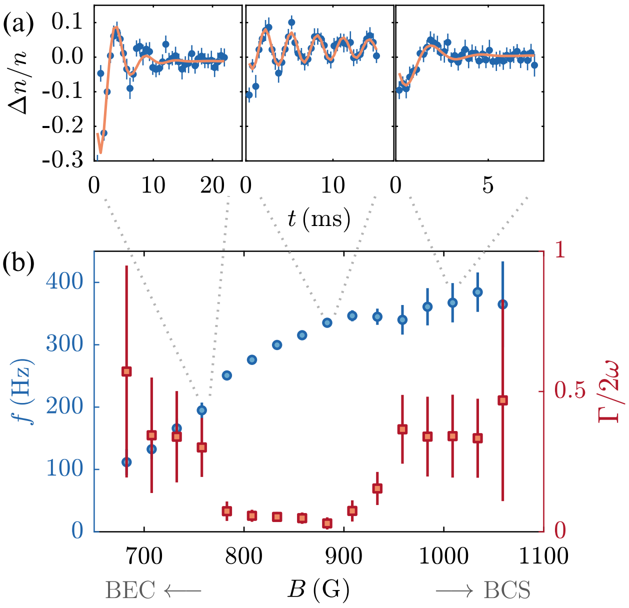

FIG. 2. (a) Oscillations in the density imbalance at $B = 758$ G, $B = 883$ G, and $B = 1009$ G. Solid lines represent damped sinusoidal fits. (b) Frequency (blue circles) and damping (red squares) of sound oscillations as a function of magnetic field. The frequency increases smoothly from the BEC to the BCS side and starts to saturate at high magnetic fields. The damping shows a clear minimum in the strongly interacting regime and increases strongly towards either side. Each data point is the average of 39 realizations.

were made for transverse spin diffusion in [9]. Our results confirm a scenario of incoherent transport that has emerged in recent years from the study of anomalous transport in high-temperature superconductors and other "bad metals" [22–24] and links quantum-limited transport to strong correlations.

We perform our studies of sound propagation with an ultracold gas of ^{6}Li atoms in a spin-balanced mixture of the lowest two hyperfine states, trapped in a two-dimensional box potential [25,26]. The gas is vertically confined in a single node of a repulsive optical lattice with trap frequency $\omega_z/2\pi = 8.4(3)$ kHz. At our densities of about $n_{\uparrow/\downarrow} \equiv n \approx 1\ \mu\text{m}^{-2}$ per spin state, the chemical potential μ is smaller than the vertical level spacing $\hbar\omega_z$, which ensures that our gas is in the quasi-2D regime. The confinement in the horizontal plane is created using a digital micromirror device illuminated with blue detuned light ($\lambda = 532$ nm), trapping the gas in a two-dimensional box with a typical size of $l_x \times l_y = 30 \times 40\ \mu\text{m}^2$. According to the temperature determination performed in [26], our system is in the low-temperature regime with $k_B T/E_F \leq 0.1$, where $E_F = \hbar^2 k_F^2/2m$ is the Fermi energy, $k_F = (4\pi n)^{1/2}$ the Fermi momentum and m the atomic mass of ^{6}Li.

For our experiments, we build on the experimental procedure developed in [27], where sound propagation was studied in weakly interacting 2D Bose gases. To excite a sound mode in the box we follow the approach of [26] and imprint a relative phase between two halves of the system by illuminating one side with a spatially homogeneous optical potential for a short duration $\tau < h/E_F$. We then observe the resulting density oscillations by imaging the density distribution after different hold times using *in situ* absorption imaging. An example of such an oscillation is shown in Fig. 1(a). A sound wave traveling back and forth between the two sides of the box is clearly visible in the density profile. To extract the oscillation frequency $f = \omega/2\pi$ and the damping rate Γ of this sound wave, we calculate the relative particle imbalance $\Delta n/n = 2(n_t - n_b)/(n_t + n_b)$ from the densities n_t and n_b in the top and bottom halves of the box and fit it with a damped sinusoidal of the form $A(t) = A_0 \cos(\omega t + \phi) \exp(-\Gamma t/2) + b$ [see Fig. 1(b)] [28]. We measure the oscillation frequency for different boxes with lengths between $l_x = 15\ \mu$m and $l_x = 40\ \mu$m and find that it is proportional to the inverse of the box length

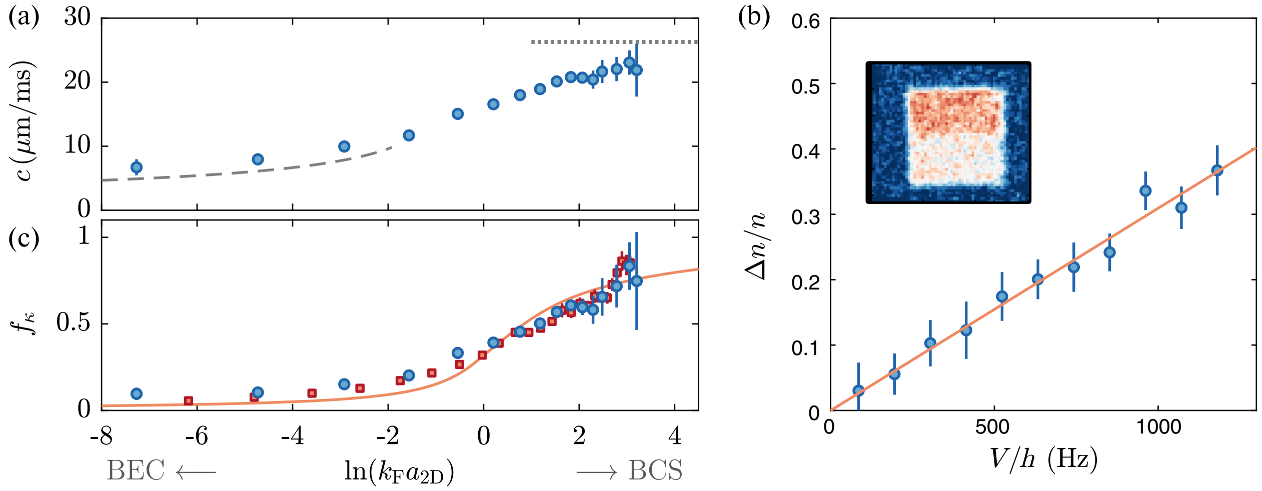

FIG. 3. (a) Speed of sound across the BEC-BCS crossover. Gray lines represent the two theoretical limits: in the BEC regime, Bogoliubov theory predicts $\mu = gn$ and hence $c_B = (gn/2m)^{1/2}$, where g is the interaction parameter between bound dimers defined as in [26,36]. On the BCS side, $\mu \to E_F$ yields a constant sound velocity $c_F = v_F/\sqrt{2}$ where $v_F = \hbar k_F/m$ is the Fermi velocity. (b) Static measurement of the compressibility. A repulsive potential V is imprinted onto one half of the box resulting in a density imbalance $\Delta n/n$ (blue points). We extract the compressibility from the initial slope of the data points according to $1/n^2\kappa = \lim_{\Delta n \to 0} V/\Delta n$ in a local density approximation. Each data point and the inset are averages of 20 realizations. (c) Comparison between the compressibility scaling functions f_κ obtained from the speed of sound (blue circles), the density response to an imprinted static potential (red squares) and QMC calculations [37,38].

[see Fig. 1(c)]. This confirms that we observe a sound wave traveling at a constant velocity $c = 2l_x f$ and that edge effects are negligible.

To probe the speed of sound as a function of interaction strength, we perform measurements in a box with $l_x = 30\ \mu$m at magnetic fields around the Feshbach resonance. Examples of the resulting oscillations as well as the evolution of the oscillation frequency as a function of magnetic field are shown in Fig. 2. As the field is varied from the BEC side to the BCS side of the crossover, the oscillation frequency increases, which is expected since the compressibility of a Fermi gas is much lower than that of a weakly repulsive Bose gas. On the Fermi side, the gas is thus stiffer with respect to density fluctuations and sound waves propagate faster than on the Bose side.

We plot the speed of sound extracted from the oscillation frequencies as a function of the 2D interaction parameter $\ln(k_F a_{2\mathrm{D}})$ [29] in Fig. 3(a). In a superfluid gas, two-fluid hydrodynamics predict the occurrence of two sound modes which propagate at different velocities, as observed in [32]. These modes generally mix density and entropy degrees of freedom. For strongly interacting 2D superfluids however, density and entropy excitations have been predicted to be well decoupled [33,34], and hence the sound mode we observe should correspond to an almost pure density wave. In this case, the velocity of a sound wave is given by

$$c = \sqrt{\frac{n}{m}\frac{\partial \mu}{\partial n}\bigg|_s} \qquad (1)$$

and is directly related to the isentropic compressibility $\kappa = (1/n^2)(\partial n/\partial \mu)|_s$ [35]. This relation gives us simple zero-temperature expressions for the speed of sound in the BEC and BCS limits of the crossover, which are in good agreement with our data [dashed and dotted lines in Fig. 3(a)].

For a quantitative analysis we use Eq. (1) to extract the compressibility of our gas from our measurement of the speed of sound. From this, we then determine the dimensionless inverse compressibility scaling function $f_\kappa = 1/nE_F\kappa$ of a two-dimensional Fermi gas.

In addition to this dynamic measurement of the equation of state (EOS), we also perform a static measurement of the compressibility EOS by determining the density response of our system to a static repulsive potential, similar to the work performed in [25,31,39,40] [see Fig. 3(b)]. This results in two independent measurements of f_κ, which show good agreement with each other [see Fig. 3(c)].

Finally we compare our data to theory by extracting f_κ from quantum Monte Carlo (QMC) calculations of the ground state energy E_0 of a homogeneous 2D Fermi gas [37,38]. On the BCS side, the experimental results agree well with the theoretical prediction. On the BEC side, both the static and the dynamic measurements lie above the zero-temperature prediction. This difference is consistent with the predicted increase of the sound velocity at finite temperature [41] and with a corresponding decrease of the compressibility at finite temperature observed in [31], which increases the value of f_κ.

Very recent simulations of the sound velocity in a 2D Bose gas [42] indicate that the density and entropy modes remain coupled even for relatively strongly interacting Bose gases, leading to sound velocities which differ from the Bogoliubov prediction. This should be observable as a difference between the static and dynamic measurements of the compressibility. However, if such a difference exists in our system, it is smaller than the uncertainty of our measurement.

We now turn our attention to the damping of the sound waves. In our strongly correlated system, the mean free path l_{mfp} of the particles is much smaller than the oscillation wavelength and their collision rate is high with respect to the oscillation frequency [43]. Hence the system is in the hydrodynamic regime. In this regime, the spatial variations in density and temperature that constitute a sound wave lead to diffusive currents of longitudinal momentum, transverse momentum and heat, whose magnitudes are proportional to the bulk and shear viscosities ζ and η and to the heat conductivity β [44,45]. These diffusive currents smooth out the density and temperature variations and thus damp the sound wave according to the sound diffusion constant

$$D_s = \frac{\eta}{\rho} + \frac{\zeta}{\rho} + \beta \frac{c_p - c_v}{c_p c_v} = \Gamma / k_0^2, \tag{2}$$

where $k_0 = \pi / l_x$ is the wave vector of the sound wave and c_p and c_v are the heat capacities at constant pressure and volume. The evolution of D_s across the BEC-BCS crossover is shown in Fig. 4. It exhibits a broad minimum in the crossover regime $-1 < \ln(k_F a_{2\mathrm{D}}) < 2$ and increases steeply towards the BEC and BCS limits.

Before comparing our data to theory, we note that making quantitative predictions for transport coefficients of strongly interacting 2D Fermi gases in the low-temperature regime is still a major theoretical challenge. Approaches such as Fermi liquid theory and BCS theory [45] are only accurate at weak coupling. Results obtained for the high-temperature regime ($T \geq T_F$) indicate that the shear viscosity and heat conductivity have a minimum in the strongly correlated regime [2–4] whereas the bulk viscosity is maximal near resonance yet contributes much less to the damping [46–48]. In total, high-temperature theory predicts a minimum of the sound diffusion in the crossover regime. Although our measurements are performed in the low-temperature regime, the observed behavior is in qualitative agreement with an extrapolation of the high-temperature result to the low-temperature regime.

A prediction for a lower bound of D_s in the strongly interacting regime can be obtained via a simple scaling argument: in kinetic theory, the diffusion coefficient is given by the mean free path and the velocity via $D_s \sim v l_{\mathrm{mfp}}$. For a strongly interacting degenerate gas the mean free path l_{mfp} is on the order of the interparticle separation $n^{-1/2}$ and the velocity on the order of the Fermi velocity $v \sim v_F \sim \hbar n^{1/2}/m$, resulting in a diffusion coefficient $D_s \sim \hbar/m$. Since the interparticle separation is a lower limit for the mean free path, this yields a generic lower bound for the damping. This lower limit is in agreement with our measured diffusion coefficient of $D_s \approx 1.8(2)\hbar/m$ in the strongly correlated regime. Thus our strongly interacting 2D Fermi gas is a nearly perfect fluid despite the fact that scale invariance is broken and that the system is not at a quantum critical point.

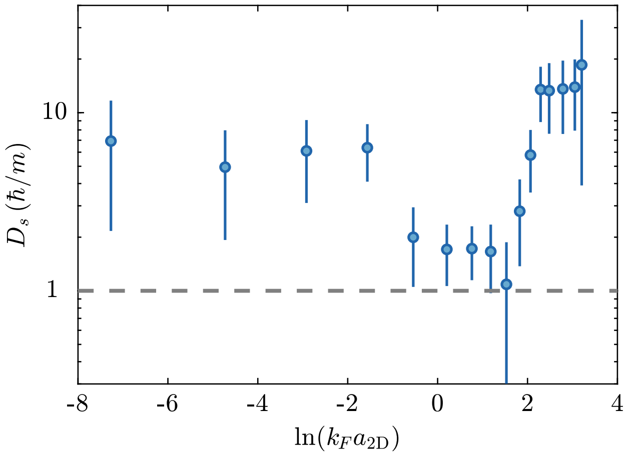

FIG. 4. Sound diffusion coefficient across the BEC-BCS crossover. In the strongly correlated regime, the diffusion coefficient reaches a minimum which agrees well with the universal quantum bound for diffusion at $\hbar/m$ (dashed line).

In this Letter, we have studied the propagation and damping of sound waves in a homogeneous 2D Fermi gas across the BEC-BCS crossover. We have extracted the compressibility EOS from a measurement of the speed of sound and find good agreement with $T = 0$ QMC calculations. We have measured the sound diffusion constant as a function of the interaction strength and find universal sound diffusion $D_s \sim \hbar/m$ and quantum-limited transport in the strongly interacting regime. This lower limit is reached at interactions where scale invariance is violated most severely [9,21], but where the mean free path is comparable to the particle spacing. Since sound diffusion is the sum of momentum and heat diffusion, we thus find upper bounds of order $\hbar/m$ on each diffusion channel individually in the crossover regime. This demonstrates that the 2D Fermi gas realizes a nearly perfect fluid [17,49] and provides a benchmark against which future theoretical predictions can be validated.

An interesting extension of our measurements would be to study the temperature dependence of D_s as done in unitary 3D Fermi gases [15]. In the fermionic regime, this would allow us to observe whether there is a maximum of D_s at the critical temperature of superfluidity, similar to measurements in ^{3}He [50]. In the deep BEC regime, control over the temperature of the gas would enable studies of second sound in a strongly interacting Bose gas [34,42].

We thank L. Mathey, V. Singh, A. Sinatra, Y. Castin, and N. Defenu for stimulating discussions. We also thank K. Morgener, K. Hueck, and W. Weimer for their work in the early stages of the experiment. This work is supported by the European Union's Seventh Framework Programme (Grant No. FP7/2007-2013) under Grant Agreement No. 335431 and by the Deutsche Forschungsgemeinschaft (DFG, German Research Foundation) in the framework of SFB 925 and "SFB 1225" (ISOQUANT), the excellence cluster "Advanced Imaging of Matter"—EXC 2056—Project No. 390715994 and under Germany's Excellence Strategy EXC-2181/1-390900948 (the Heidelberg STRUCTURES Excellence Cluster). M. B. acknowledges support by Labex ICFP of ENS Paris.

---

[*] tlompe@physik.uni-hamburg.de

[1] E. Vogt, M. Feld, B. Fröhlich, D. Pertot, M. Koschorreck, and M. Köhl, Phys. Rev. Lett. **108**, 070404 (2012).

[2] G. M. Bruun, Phys. Rev. A **85**, 013636 (2012).

[3] T. Schäfer, Phys. Rev. A **85**, 033623 (2012).

[4] T. Enss, C. Küppersbusch, and L. Fritz, Phys. Rev. A **86**, 013617 (2012).

[5] P. Massignan, G. M. Bruun, and H. Smith, Phys. Rev. A **71**, 033607 (2005).

[6] T. Enss, R. Haussmann, and W. Zwerger, Ann. Phys. (Amsterdam) **326**, 770 (2011).

[7] C. Cao, E. Elliott, J. Joseph, H. Wu, J. Petricka, T. Schäfer, and J. E. Thomas, Science **331**, 58 (2011).

[8] M. Koschorreck, D. Pertot, E. Vogt, and M. Köhl, Nat. Phys. **9**, 405 (2013).

[9] C. Luciuk, S. Smale, F. Böttcher, H. Sharum, B. A. Olsen, S. Trotzky, T. Enss, and J. H. Thywissen, Phys. Rev. Lett. **118**, 130405 (2017).

[10] A. Sommer, M. Ku, G. Roati, and M. W. Zwierlein, Nature (London) **472**, 201 (2011).

[11] G. M. Bruun, New J. Phys. **13**, 035005 (2011).

[12] T. Enss and R. Haussmann, Phys. Rev. Lett. **109**, 195303 (2012).

[13] A. B. Bardon, S. Beattie, C. Luciuk, W. Cairncross, D. Fine, N. S. Cheng, G. J. A. Edge, E. Taylor, S. Zhang, S. Trotzky, and J. H. Thywissen, Science **344**, 722 (2014).

[14] G. Valtolina, F. Scazza, A. Amico, A. Burchianti, A. Recati, T. Enss, M. Inguscio, M. Zaccanti, and G. Roati, Nat. Phys. **13**, 704 (2017).

[15] P. B. Patel, Z. Yan, B. Mukherjee, R. J. Fletcher, J. Struck, and M. W. Zwierlein, arXiv:1909.02555v2.

[16] T. Enss and J. H. Thywissen, Annu. Rev. Condens. Matter Phys. **10**, 85 (2019).

[17] P. K. Kovtun, D. T. Son, and A. O. Starinets, Phys. Rev. Lett. **94**, 111601 (2005).

[18] M. Olshanii, H. Perrin, and V. Lorent, Phys. Rev. Lett. **105**, 095302 (2010).

[19] M. Holten, L. Bayha, A. C. Klein, P. A. Murthy, P. M. Preiss, and S. Jochim, Phys. Rev. Lett. **121**, 120401 (2018).

[20] T. Peppler, P. Dyke, M. Zamorano, I. Herrera, S. Hoinka, and C. J. Vale, Phys. Rev. Lett. **121**, 120402 (2018).

[21] P. A. Murthy, N. Defenu, L. Bayha, M. Holten, P. M. Preiss, T. Enss, and S. Jochim, Science **365**, 268 (2019).

[22] J. A. N. Bruin, H. Sakai, R. S. Perry, and A. P. Mackenzie, Science **339**, 804 (2013).

[23] S. A. Hartnoll, Nat. Phys. **11**, 54 (2015).

[24] S. Hartnoll, A. Lucas, and S. Sachdev, *Holographic Quantum Matter* (The MIT Press, Cambridge, 2018).

[25] K. Hueck, N. Luick, L. Sobirey, J. Siegl, T. Lompe, and H. Moritz, Phys. Rev. Lett. **120**, 060402 (2018).

[26] N. Luick, L. Sobirey, M. Bohlen, V. P. Singh, L. Mathey, T. Lompe, and H. Moritz, arXiv:1908.09776v1.

[27] J. L. Ville, R. Saint-Jalm, E. Le Cerf, M. Aidelsburger, S. Nascimbène, J. Dalibard, and J. Beugnon, Phys. Rev. Lett. **121**, 145301 (2018).

[28] Note the factor 1/2 in the exponential of the fit function, which takes into account that Γ is the damping rate of the oscillation energy, which is proportional to the square of the oscillation amplitude.

[29] The 2D scattering length is defined as $a_{2D} = a_{2D}^{(0)}\exp[-0.5\Delta w(\mu/\hbar\omega_z)]$. Here, $a_{2D}^{(0)} = l_z\sqrt{\pi/0.905}\exp(-\sqrt{\pi/2}l_z/a_{3D})$ is the 2D scattering length for dilute gases, with the 3D-scattering length a_{3D}, the harmonic oscillator length in the strongly confined direction $l_z = \sqrt{\hbar/m\omega_z}$ and a positive scaling function $\Delta w(\mu/\hbar\omega_z) \lesssim 2.3$ which accounts for the energy dependence of 2D scattering [30,31].

[30] D. S. Petrov and G. V. Shlyapnikov, Phys. Rev. A **64**, 012706 (2001).

[31] I. Boettcher, L. Bayha, D. Kedar, P. A. Murthy, M. Neidig, M. G. Ries, A. N. Wenz, G. Zürn, S. Jochim, and T. Enss, Phys. Rev. Lett. **116**, 045303 (2016).

[32] L. A. Sidorenkov, M. K. Tey, R. Grimm, Y. H. Hou, L. Pitaevskii, and S. Stringari, Nature (London) **498**, 78 (2013).

[33] H. Hu, P. Dyke, C. J. Vale, and X.-J. Liu, New J. Phys. **16**, 083023 (2014).

[34] M. Ota and S. Stringari, Phys. Rev. A **97**, 033604 (2018).

[35] We use the adiabatic compressibility since the sound frequency is large compared to the damping ($\omega \geq \Gamma$).

[36] A. V. Turlapov and M. Y. Kagan, J. Phys. Condens. Matter **29**, 383004 (2017).

[37] H. Shi, S. Chiesa, and S. Zhang, Phys. Rev. A **92**, 033603 (2015).

[38] We obtain f_κ from QMC data for the ground state energy E_0 of the homogeneous 2D Fermi gas [37]. The dimensionless energy scaling function is given by $f(x) = (E_0 + NE_B/2)/(NE_F/2) = E_0/(NE_F/2) + 2e^{-2x}$, with $x = \ln(k_F a_{2D})$. It describes the ground state energy of the homogeneous gas relative to the binding energy $E_B = \hbar^2/ma_{2D}^2$ [31] of the Fermion pairs. From this function, we obtain $f_\kappa = (V^2/NE_F)(\partial^2 E/\partial V^2) = f(x) + 3/4f'(x) + 1/8f''(x)$ by differentiation.

[39] V. Makhalov, K. Martiyanov, and A. Turlapov, Phys. Rev. Lett. **112**, 045301 (2014).

[40] K. Fenech, P. Dyke, T. Peppler, M. G. Lingham, S. Hoinka, H. Hu, and C. J. Vale, Phys. Rev. Lett. **116**, 045302 (2016).

[41] G. Bighin and L. Salasnich, Phys. Rev. B **93**, 014519 (2016).

[42] V. P. Singh and L. Mathey, Phys. Rev. Research **2**, 023336 (2020).

[43] Within kinetic theory, the mean free path is estimated as $l_{\mathrm{mfp}} = 1/n\sigma \simeq 0.63 n^{-1/2}[1 + 4\ln^2(k_{\mathrm{F}} a_{2\mathrm{D}})/\pi^2]$. For our system, one obtains $l_{\mathrm{mfp}} \leq 16\ \mu\mathrm{m} < 2l_x$. Hydrodynamic estimates for the relaxation length $l = D_s/c$ and relaxation time $\tau = l/c$ yield $\Gamma/\omega \sim \omega\tau \ll 1$. Thus, both of these estimates suggest that hydrodynamic conditions are satisfied for our system.

[44] L. D. Landau and E. M. Lifshitz, *Course of Theoretical Physics—Vol. 6: Fluid Mechanics* (Pergamon Press, Oxford, 1987).

[45] H. Smith and H. Jensen, *Transport Phenomena* (Oxford Science Publications/Clarendon Press, Oxford, 1989).

[46] T. Enss, Phys. Rev. Lett. **123**, 205301 (2019).

[47] Y. Nishida, Ann. Phys. (Amsterdam) **410**, 167949 (2019).

[48] J. Hofmann, Phys. Rev. A **101**, 013620 (2020).

[49] T. Schäfer and D. Teaney, Rep. Prog. Phys. **72**, 126001 (2009).

[50] G. Eska, K. Neumaier, W. Schoepe, K. Uhlig, W. Wiedemann, and P. Wölfle, Phys. Rev. Lett. **44**, 1337 (1980).

A.3. Observation of superfluidity in a strongly correlated two-dimensional Fermi gas.

Observation of superfluidity in a strongly correlated two-dimensional Fermi gas

Lennart Sobirey,[1, *] Niclas Luick,[1, 2] Markus Bohlen,[1, 2, 3] Hauke Biss,[1, 2] Henning Moritz,[1, 2] and Thomas Lompe[1]
[1] *Institut für Laserphysik, Universität Hamburg*
[2] *The Hamburg Centre for Ultrafast Imaging, Universität Hamburg, Luruper Chaussee 149, 22761 Hamburg*
[3] *Laboratoire Kastler Brossel, ENS-Université PSL, CNRS, Sorbonne Université, Collège de France, 24 rue Lhomond, 75005 Paris, France*

Understanding how strongly correlated two-dimensional (2D) systems can give rise to unconventional superconductivity with high critical temperatures is one of the major unsolved problems in condensed matter physics. Ultracold 2D Fermi gases have emerged as clean and controllable model systems to study the interplay of strong correlations and reduced dimensionality, but direct evidence of superfluidity in these systems has been missing. Here, we demonstrate superfluidity in an ultracold 2D Fermi gas by moving a periodic potential through the system and observing no dissipation below a critical velocity $\mathrm{v_c}$. We measure $\mathrm{v_c}$ as a function of interaction strength and find a maximum in the crossover regime between bosonic and fermionic superfluidity. Our measurement establishes ultracold Fermi gases as a powerful tool for studying the influence of reduced dimensionality on strongly correlated superfluids.

Reducing the dimensionality of a quantum system from three to two dimensions significantly modifies its physical properties. One striking difference is the increased role of fluctuations in low-dimensional systems, which prevents long range phase coherence [1] and makes 2D the marginal dimension for the existence of superfluidity [2]. Hence it is quite surprising that in all known ambient-pressure high-$\mathrm{T_c}$ materials superconductivity occurs in two-dimensional structures, such as the copper-oxide layers in cuprates. Three decades after their discovery, the mechanism giving rise to superconductivity and the role of the reduced dimensionality in these systems are still under debate [3].

Over the last years, ultracold 2D Fermi gases [4–9] have been established as model systems that can provide insight into the interplay of strong correlations and reduced dimensionality [10–15]. Recent experiments have observed pair condensation [16] and phase coherence [17] at low temperatures. While these results suggest the presence of a superfluid, this has not been directly observed so far.

In this work, we obtain definitive evidence for superfluidity in a 2D Fermi gas by observing frictionless flow below a critical velocity v_c. We study the temperature-dependence of the critical velocity and observe the phase transition from the superfluid to the normal state at a critical temperature T_c. Finally, we measure the critical velocity as a function of interaction strength and show that the 2D Fermi gas is superfluid throughout the BEC-BCS crossover from deeply bound dimers to weakly bound Cooper pairs.

For our experiments, we use a Fermi gas of $N \approx 6000$ ultracold ^{6}Li atoms in the lowest two hyperfine states, trapped in a box potential [18]. The gas is tightly confined along the z-direction with a level spacing $\hbar\omega_\mathrm{z} \approx h \cdot 9.2\,\mathrm{kHz}$ that is larger than the thermal energy $k_\mathrm{B}T$ and the chemical potential μ of the gas, which places our system in the quasi-2D regime [19].

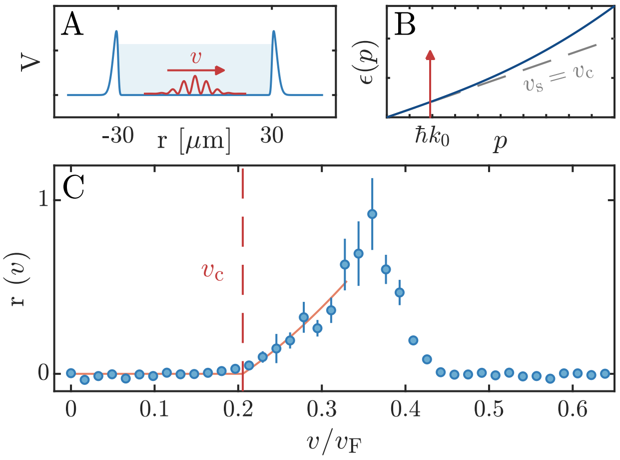

FIG. 1. **Measuring the critical velocity of a two-dimensional Fermi gas.** (A) Sketch of the trapping potential. A 2D Fermi gas is trapped in a box potential (blue) projected through a high-resolution microscope objective. A periodic potential (red) can be moved through the gas at a variable velocity v. (B) Sketch of the Bogoliubov dispersion of a superfluid Bose gas. At small momentum transfer $\hbar q$, excitations are phononic and the dispersion has a linear slope given by the speed of sound v_s, while for higher momentum transfers single-particle excitations become dominant and the dispersion becomes quadratic. (C) Response $r(v)$ of a system at an interaction strength of $\ln(k_\mathrm{F}a_\mathrm{2D}) = -0.8$ to a moving optical lattice with wavevector $k_0 \approx 0.15\,k_\mathrm{F}$. While no dissipation occurs at low lattice velocities, there is a sharp increase in the response of the system above a critical velocity v_c. Note that the moving lattice probes the dispersion relation of the system along a vertical line, as visualized by the red arrow in (B). This results in a decrease of the response at high lattice velocities. The critical velocity is extracted by a fit (red solid line) according to $r(v) = A\max(0, v^2 - v_\mathrm{c}^2)$ [20].

To show that the system is superfluid, we verify that it fulfills the Landau criterion [21–26], which states that the dispersion $\epsilon(p)$ of a superfluid does not allow for the creation of excitations at velocities smaller than a nonzero critical velocity $v_\mathrm{c} = \min_p(\frac{\epsilon(p)}{p})$. Thus, an impurity moving through a superfluid with a velocity $v < v_\mathrm{c}$ creates no excitations, and the superfluid flows around it without friction. We create such an impurity by interfering two red-detuned laser beams in the center of the trap, resulting in a sinusoidal potential whose wavelength can be tuned by adjusting the crossing angle of the two beams. A frequency detuning $\Delta\nu$ between the two laser beams causes this optical lattice to move at a constant speed $v = L\Delta\nu$, where L is the spacing between two maxima of the periodic potential.

To measure the critical velocity in our system, we move the optical lattice through the gas at different velocities and observe the response of the system by measuring its momentum distribution $n(k)$. To obtain $n(k)$, we ramp the interaction strength to a value of $\ln(k_\mathrm{F} a_\mathrm{2D}) = -2.8$, where $k_\mathrm{F} = \sqrt{4\pi n} = m v_\mathrm{F}/\hbar$ is the Fermi wavevector of a gas with density n per spin state and a_2D is the 2D scattering length [27]. At this interaction strength, the system is deep in the BEC regime, where the gas consists of weakly interacting dimers and it is straightforward to measure $n(k)$ using matter wave focusing [28]. As the occupation of the lowest momentum modes decreases with increasing temperature, we define the response $r(v) = (n(k = 0, v = 0)/n(k = 0, v)) - 1$ as a robust measure for the amount of energy that was imparted to the system by the moving potential [19].

A typical measurement of the response of the system as a function of lattice velocity is shown in Fig 1 C. We observe that as the velocity of the optical lattice is increased, the gas is unaffected until a critical velocity is reached and a sharp onset of dissipation occurs. In contrast to previous experiments [22–25], we observe that the response decreases again at higher velocities. This is due to the fact that the optical lattice transfers a specific momentum $\hbar k_0 = \hbar 2\pi/L$ to the superfluid, whereas the impurity in Landau's gedankenexperiment can excite the system at all momenta. Therefore, a moving optical lattice with varying velocity probes the dispersion relation of the gas on a vertical line of constant $p = \hbar k_0$. This is visualized in Fig. 1 B.

We hence perform measurements at different spacings L of the periodic potential, and thereby determine the response $r(v, k_0)$ as a function of both the lattice velocity v and the lattice wavevector k_0. In bosonic superfluids, the lowest velocity at which excitations can be created is found at small wavevectors. These long-wavelength excitations are phononic modes that are excited by an obstacle moving at a velocity close to the speed of sound of the system. In BCS superfluids, phononic excitations at low k_0 can still be created, but the lowest onset velocity is found at $k_0 \approx 2\,k_\mathrm{F}$. This is due to pair breaking excitations, which can occur at all momenta but according to BCS theory can be excited with the lowest velocites at a wavevector of $2\,k_\mathrm{F}$. Our measurements in the BEC (see Fig. 2 A) and BCS (see Fig. 2 B) regimes directly show this difference in the excitation spectra of bosonic and fermionic superfluids. For both interaction strengths, we clearly observe a critical velocity below which no excitations are created, which constitutes conclusive evidence of superfluidity.

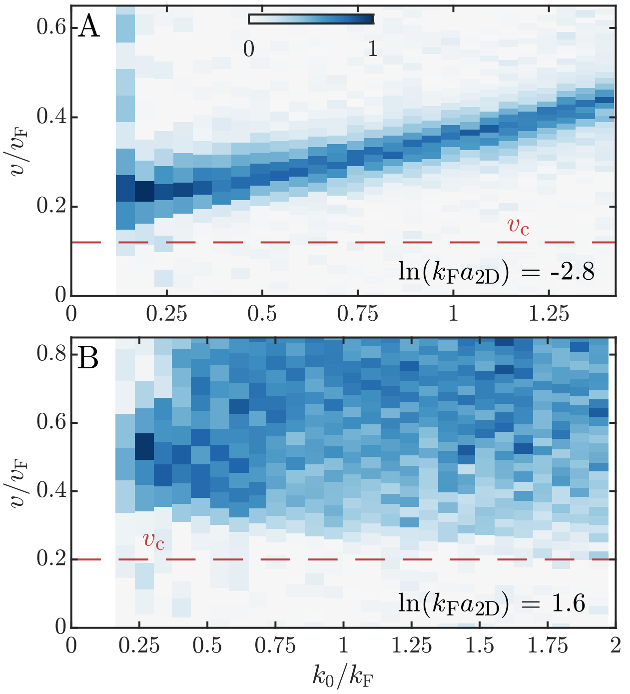

FIG. 2. **Phononic and pair breaking excitations in a 2D Fermi gas.** (A) Response of a gas in the BEC regime to excitations with lattice wavevector k_0 and velocity v. For small wavevectors, the moving lattice excites phononic modes at the sound velocity v_s. For larger wavevectors, the peak in the heating rate moves to higher velocities as the dispersion deviates from the linear phononic branch and single-particle excitations become dominant. (B) In the BCS regime, we observe a continuum of pair breaking excitations with a minimum of the onset velocity at $k_0 = 2\,k_\mathrm{F}$. In both regimes, the heating rate is negligible for excitations that move slower than the critical velocity (red dashed lines, taken from Fig. 4 C). To enhance the visibility of weaker excitations, each column has been linearly rescaled to range from 0 to 1.

Having established a measurement of the critical velocity, we now go on to determine the critical temperature T_c of a gas in the BEC regime ($\ln(k_\mathrm{F} a_\mathrm{2D}) = -2.9$). We achieve this by preparing gases at different temperatures [19] and measuring the response of the system to the moving periodic potential. With increasing temperature, we expect the phononic branch of the dispersion to broaden, and eventually become broad enough that excitations at arbitrarily small velocities can heat the gas. This causes the critical velocity to decrease with temperature and vanish at $T = T_\mathrm{c}$. Measurements of the

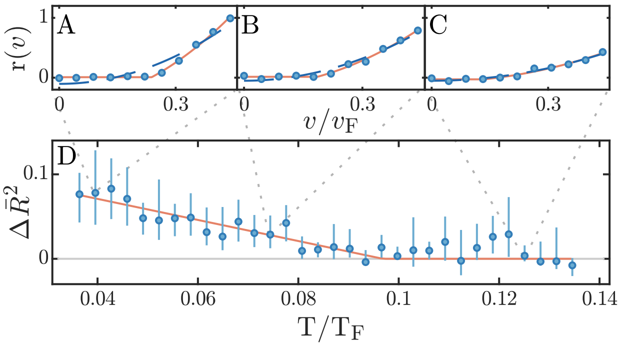

FIG. 3. **Observing the superfluid phase transition.** (A,B,C) We determine the critical temperature of a gas in the BEC regime ($\ln(k_{\mathrm{F}}a_{2\mathrm{D}}) = -2.9$) by measuring the response of the system to a moving periodic potential at different temperatures. For a cold gas (A), the absence of dissipation at low velocities is followed by a sharp rise in the response of the gas at the critical velocity. As the temperature increases, the critical velocity is reduced (B) until dissipation occurs at arbitrarily small velocities once the temperature is above T_{c} (C). The red solid lines are fits of the response $r(v)$ according to $r(v) = A\max(C, v^2 - v_{\mathrm{c}}^2)$. The blue dashed lines show fits where v_{c} is fixed to 0. (D) Difference $\Delta\bar{R}^2 = \bar{R}^2_{v_{\mathrm{c}}>0} - \bar{R}^2_{v_{\mathrm{c}}=0}$ of the adjusted coefficients of determination of the two fits. For low temperature gases, allowing a finite critical velocity significantly improves the fit beyond the trivial effect of adding a free parameter and hence $\Delta\bar{R}^2 > 0$. In contrast, this is not the case for high temperature systems above T_{c}. We can therefore estimate T_{c} by extracting the temperature at which a nonzero v_{c} no longer improves the fit. For the measurement shown in this figure, we find that the phase transition to the normal state occurs at $T_{\mathrm{c}}/T_{\mathrm{F}} = 0.094 \pm 0.004_{\mathrm{stat}} \pm 0.02_{\mathrm{sys}}$ [19]. The errorbars show 1σ confidence intervals obtained by bootstrapping.

response of the system for three different initial temperatures are shown in Fig. 3 A-C. While the sharp onset of dissipation at the critical velocity is clearly visible in the colder data, it disappears at higher temperatures, signalling the phase transition from a superfluid to a normal state. We extract a critical temperature of $T_{\mathrm{c}}/T_{\mathrm{F}} = 0.094 \pm 0.004_{\mathrm{stat}} \pm 0.02_{\mathrm{sys}}$ [19], which is in very good agreement with theoretical predictions [8] and the observed onset of pair condensation [16][29].

In our final set of measurements, we study the evolution of the critical velocity in the crossover from a condensate of bosonic dimers to a BCS superfluid. As shown in Fig. 2, the lowest-lying excitations on the BEC side of the resonance are sound modes at small values of k_0, while for a BCS superfluid the minimum velocity for pair breaking occurs for excitations around $2\,k_{\mathrm{F}}$. Hence, we measure the interaction dependence of the response $r(v)$ at two different lattice wavevectors of $k_0 \approx 0.3\,k_{\mathrm{F}}$ and $k_0 \approx 2\,k_{\mathrm{F}}$. The results are shown in Fig. 4 A and B.

For a lattice wavevector of $k_0 \approx 0.3\,k_{\mathrm{F}}$, we clearly observe the presence of a well defined sound mode with an onset velocity that increases as a function of interaction strength. In the crossover region ($\ln(k_{\mathrm{F}}a_{2\mathrm{D}}) \approx 0.5$), the peak smoothly broadens into a continuum as pair breaking becomes the dominant excitation in the system. For $k_0 \approx 2\,k_{\mathrm{F}}$, the excitations on the BEC side are single particle excitations, with pair breaking taking over towards the BCS side of the resonance. We fit the onset velocities for both data sets and use the smaller of the two values as the critical velocity of the system (see Fig. 4 C).

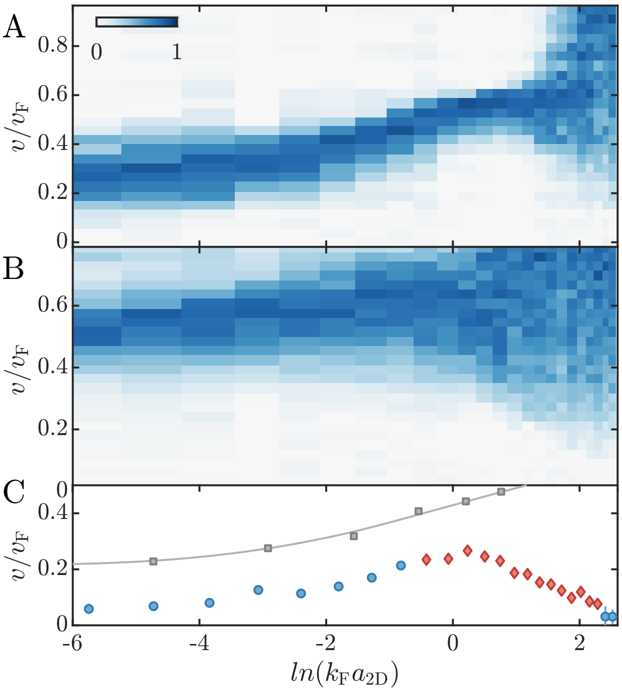

FIG. 4. **Interaction dependence of the critical velocity.** (A,B) Response of a 2D Fermi gas to a moving lattice with wavevectors $k_0 \approx 0.3\,k_{\mathrm{F}}$ (A) and $k_0 \approx 2\,k_{\mathrm{F}}$ (B) at different interaction strengths. In the BEC regime ($\ln(k_{\mathrm{F}}a_{2\mathrm{D}}) < -1$), we observe a well defined excitation that corresponds to a sound mode for $k_0 \approx 0.3\,k_{\mathrm{F}}$ and single particle excitations for $k_0 \approx 2\,k_{\mathrm{F}}$. When going to the BCS side of the crossover, the peak broadens into a continuum of pair breaking excitations. To enhance the visibility of weaker excitations, each column has been linearly rescaled to range from 0 to 1. (C) We determine the critical velocity as a function of interaction strength as the lower of the two onset velocities obtained from the data shown in (A,B). In the BEC regime, the critical velocity is limited by excitations at small wavevectors (blue dots), while in the crossover the lowest onset velocities occur at $2\,k_{\mathrm{F}}$ (red diamonds). We find that the 2D Fermi gas is superfluid throughout the 2D BEC-BCS crossover with the highest critical velocities found in the crossover regime at $\ln(k_{\mathrm{F}}a_{2\mathrm{D}}) \approx 0$. For comparison, we show the speed of sound v_{s} (grey squares) as measured in [30], the grey line is a guide to the eye. The error bars denote the 1σ confidence intervals of the fit and are mostly smaller than the symbol size.

The measured critical velocities scale with the speed of sound on the BEC side of the resonance, show a maximum in the crossover and decrease again as pair breaking becomes dominant in the BCS regime. The maximum of v_c at an interaction strength of $\ln(k_\mathrm{F}a_\mathrm{2D}) \approx 0$ furthermore indicates that fermionic 2D superfluids are most stable in the strongly correlated crossover regime, in good agreement with the maximum of the critical temperature for pair condensation reported in [16].

Our results establish 2D Fermi gases as ideal model systems to study how superfluidity is affected by the interplay of strong correlations and reduced dimensionality. In particular, they can be used to study the transition from a superfluid to a strongly correlated pseudogap state above T_c in a much simpler and more accessible system than high-T_c superconductors. Finally, the dimensionality of ultracold Fermi gases can be tuned continuously, making them uniquely suited to study the remarkable stability of the superfluid phase in the crossover from two to three dimensions.

We thank L. Mathey and V. Singh for valuable insights and stimulating discussions. This work is supported by the European Union's Seventh Framework Programme (FP7/2007-2013) under grant agreement No. 335431 and by the Deutsche Forschungsgemeinschaft (DFG, German Research Foundation) in the framework of SFB 925 and the excellence cluster 'Advanced Imaging of Matter' - EXC 2056 - project ID 390715994. M. Bohlen acknowledges support by Labex ICFP of École Normale Supérieure Paris.

---

[*] lsobirey@physnet.uni-hamburg.de

[1] N. D. Mermin and H. Wagner, Physical Review Letters **17**, 1133 (1966).
[2] J. M. Kosterlitz and D. J. Thouless, Journal of Physics C: Solid State Physics **6**, 1181 (1973).
[3] B. Keimer, S. A. Kivelson, M. R. Norman, S. Uchida, and J. Zaanen, Nature **518**, 179 (2015).
[4] B. Fröhlich, M. Feld, E. Vogt, M. Koschorreck, W. Zwerger, and M. Köhl, Physical review letters **106**, 105301 (2011).
[5] A. T. Sommer, L. W. Cheuk, M. J. Ku, W. S. Bakr, and M. W. Zwierlein, Physical review letters **108**, 045302 (2012).
[6] V. Makhalov, K. Martiyanov, and A. Turlapov, Physical review letters **112**, 045301 (2014).
[7] W. Ong, C. Cheng, I. Arakelyan, and J. Thomas, Physical review letters **114**, 110403 (2015).
[8] J. Levinsen and M. M. Parish, in *Annual review of cold atoms and molecules* (World Scientific, 2015) pp. 1–75.
[9] A. Turlapov and M. Y. Kagan, Journal of Physics: Condensed Matter **29**, 383004 (2017).
[10] P. A. Murthy, M. Neidig, R. Klemt, L. Bayha, I. Boettcher, T. Enss, M. Holten, G. Zürn, P. M. Preiss, and S. Jochim, Science **359**, 452 (2018).
[11] T. Peppler, P. Dyke, M. Zamorano, I. Herrera, S. Hoinka, and C. Vale, Physical review letters **121**, 120402 (2018).
[12] M. Holten, L. Bayha, A. C. Klein, P. A. Murthy, P. M. Preiss, and S. Jochim, Physical review letters **121**, 120401 (2018).
[13] D. Mitra, P. T. Brown, P. Schauß, S. S. Kondov, and W. S. Bakr, Physical review letters **117**, 093601 (2016).
[14] K. Fenech, P. Dyke, T. Peppler, M. Lingham, S. Hoinka, H. Hu, and C. Vale, Physical review letters **116**, 045302 (2016).
[15] I. Boettcher, L. Bayha, D. Kedar, P. Murthy, M. Neidig, M. Ries, A. Wenz, G. Zuern, S. Jochim, and T. Enss, Physical review letters **116**, 045303 (2016).
[16] M. Ries, A. Wenz, G. Zürn, L. Bayha, I. Boettcher, D. Kedar, P. Murthy, M. Neidig, T. Lompe, and S. Jochim, Physical review letters **114**, 230401 (2015).
[17] N. Luick, L. Sobirey, M. Bohlen, V. P. Singh, L. Mathey, T. Lompe, and H. Moritz, arXiv preprint arXiv:1908.09776 (2019).
[18] K. Hueck, N. Luick, L. Sobirey, J. Siegl, T. Lompe, and H. Moritz, Physical review letters **120**, 060402 (2018).
[19] See Supplementary Materials.
[20] G. Astrakharchik and L. Pitaevskii, Physical Review A **70**, 013608 (2004).
[21] L. Landau, Physical Review **60**, 356 (1941).
[22] C. Raman, M. Köhl, R. Onofrio, D. Durfee, C. Kuklewicz, Z. Hadzibabic, and W. Ketterle, Physical Review Letters **83**, 2502 (1999).
[23] R. Desbuquois, L. Chomaz, T. Yefsah, J. Léonard, J. Beugnon, C. Weitenberg, and J. Dalibard, Nature Physics **8**, 645 (2012).
[24] W. Weimer, K. Morgener, V. P. Singh, J. Siegl, K. Hueck, N. Luick, L. Mathey, and H. Moritz, Physical review letters **114**, 095301 (2015).
[25] D. Miller, J. Chin, C. Stan, Y. Liu, W. Setiawan, C. Sanner, and W. Ketterle, Physical review letters **99**, 070402 (2007).
[26] L.-C. Ha, L. W. Clark, C. V. Parker, B. M. Anderson, and C. Chin, Physical review letters **114**, 055301 (2015).
[27] D. Petrov and G. Shlyapnikov, Physical Review A **64**, 012706 (2001).
[28] P. Murthy, D. Kedar, T. Lompe, M. Neidig, M. Ries, A. Wenz, G. Zürn, and S. Jochim, Physical Review A **90**, 043611 (2014).
[29] Measurements performed at interaction strengths of up to $\ln(k_\mathrm{F}a_\mathrm{2D}) = 1.1$ show the same qualitative behaviour [19], but we currently do not have a quantitatively accurate temperature determination for our homogenous system at these interaction strengths.
[30] M. Bohlen, L. Sobirey, N. Luick, H. Biss, T. Enss, T. Lompe, and H. Moritz, arXiv preprint arXiv:2003.02713 (2020).
[31] K. Hueck, N. Luick, L. Sobirey, J. Siegl, T. Lompe, H. Moritz, L. W. Clark, and C. Chin, Optics express **25**, 8670 (2017).
[32] G. Zürn, T. Lompe, A. N. Wenz, S. Jochim, P. Julienne, and J. Hutson, Physical review letters **110**, 135301 (2013).
[33] H. Shi, S. Chiesa, and S. Zhang, Physical Review A **92**, 033603 (2015).

Supplementary materials

Preparation Scheme and Tuning of Interactions

We perform our experiments with a balanced spin mixture of ^{6}Li atoms in the $|F=1/2, m_F=1/2\rangle$ and $|F=1/2, m_F=-1/2\rangle$ hyperfine states. The atoms are trapped in a box potential, resulting in a homogeneous density distribution as shown in Fig. S1. As the critical velocity depends on the density of the gas, this homogenous density is critical for observing a sharp onset of dissipation at v_c.

The experimental setup and the procedure used to prepare homogeneous 2D Fermi gases are described in detail in [18]. In brief, we first prepare an ultracold gas of ^{6}Li atoms in a highly elliptical optical dipole trap. We then perform further evaporative cooling and transfer the remaining $4000-8000$ atoms into a circular box potential with a diameter of $D \approx 60\,\mu$m.

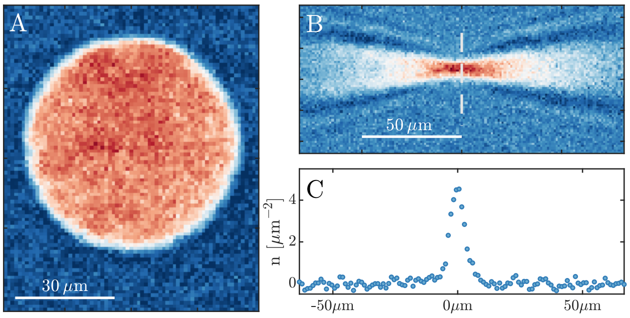

FIG. S1. **Imaging a homogeneous 2D Fermi gas** (A) In-situ absorption image of the density distribution in our box potential [31]. (B) Momentum distribution after performing matter wave focusing by letting the gas expand into a harmonic potential for a quarter of the trap period. The tight confinement in the z-axis leads to a rapid expansion of the gas in this direction, which causes the gas to expand far outside the depth of field of the imaging system. By tilting the imaging beam relative to the z-axis, the image of the gas at different z-positions is displaced laterally, with the gas being in focus in the center and imaging aberrations increasing to the sides. (C) In-focus part of the momentum distribution along the dashed grey line in (B). The condensate peak at low momenta is clearly visible. All images are the result of averaging over 8 individual measurements. Note that resolving thermal wings in the momentum distribution (C) requires averaging over a significantly higher number of images.

To bring the system into the 2D regime, the atoms are confined in the z-direction in a single antinode of an optical standing wave potential. This potential is created by two blue-detuned ($\lambda = 532\,$nm) laser beams interfering under a shallow angle, resulting in an optical lattice with a lattice spacing of approximately $3\,\mu$m and a harmonic oscillator spacing of $\hbar\omega_z \approx h\,9.2\,$kHz. For all measurements shown in this work, both the chemical potential μ and the thermal energy $k_\mathrm{B}T$ of the gas were kept well below the level spacing $\hbar\omega_z$, thus avoiding population of excited states in the z-direction. Therefore, we can parametrize the interparticle interactions by an effective 2D scattering length $a_{2\mathrm{D}}$ and treat the gas as an effective 2D system. The 2D scattering length depends on the harmonic oscillator length in z-direction $l_\mathrm{z} = \sqrt{\hbar/m\omega_\mathrm{z}}$ and the 3D scattering length $a_{3\mathrm{D}}$ according to $a_{2\mathrm{D}} = l_\mathrm{z}\sqrt{\pi/0.905}\exp(-\sqrt{\pi/2}\cdot l_\mathrm{z}/a_{3\mathrm{D}})\exp(-\frac{1}{2}\Delta w)$ [27], where $\Delta w(\mu/\hbar\omega_z)$ is a momentum-scale correction that becomes relevant on the BCS side of the crossover. In our experiments we tune the 2D scattering length $a_{2\mathrm{D}}$ by varying $a_{3\mathrm{D}}$ using a broad Feshbach resonance located at a magnetic field of $B = 832\,$G [32]. This allows us to continuously tune the system from a gas of deeply bound dimers to a BCS superfluid.

	μ/h [kHz]	n [μm^{-2}]	V_Latt/h [kHz]
Fig. 2A	0.96	1.5	0.36
Fig. 2B	5.1	0.80	0.58
Fig. 3	0.66	1.1	0.24
Fig. 4	-	0.80	0.49

TABLE S1. **Experimental parameters.** Chemical potential μ, density n and lattice power V_Latt used to obtain the data shown in Figs. 2-4. The value of the chemical potential was calculated from the measured density using the equation of state published in [33]. The height of the lattice potential is determined from the laser power of the lattice beams using the mean of the two calibration results described in the text.

Lattice Calibration

To observe frictionless flow in our 2D Fermi gas, we realize Landau's gedankenexperiment of a mobile impurity moving through the system without dissipation. In Landau's scenario, this disturbance is point-like and can excite the system at all momenta. However, when trying to experimentally realize this with a focused laser beam, the shape and finite size of the focus introduce a momentum scale that is difficult to control. Hence, we use a moving optical lattice as our impurity, since it has a well-defined and tunable momentum transfer that is determined by the lattice wavevector k_0.

The moving optical lattice is created by interfering two red-detuned ($\lambda = 780\,$nm) laser beams with a controllable frequency difference. To obtain these beams, we use light from an extended-cavity diode laser (Toptica DL PRO 780), split it into two paths and route each beam through an independently controlled acousto-optical modulator (AOM). This allows us to create an optical lattice moving at a speed of $v = L\Delta\nu$ by setting the frequency difference $\Delta\nu$ between the two AOMs. We can also tune the momentum transfer $\hbar k_0 \propto 1/L$ of the lattice by varying the distance of the two beams on the entrance aperture of the high-resolution objective that focuses them onto the atoms. This changes the crossing angle α of the interfering beams and thus the lattice spacing $L = \frac{\lambda}{2\sin\alpha/2}$.

To determine the lattice spacing, we image the potential directly onto a camera using a second high-resolution objective. The height of the lattice potential is calibrated by projecting each beam onto the gas individually and measuring the change in the density distribution as a function of laser power. We observe a linear dependence of the change in density on the laser power and use the known equation of state of the system to extract the potential height as a function of laser power for both beams. We find potential heights V/h of 108 Hz/mW and 122 Hz/mW for the two beams. As the contrast of the interference pattern can be extracted from the images of the intensity distribution and is $\gtrsim 0.95$, the potential height is computed to be $V_{\mathrm{Latt}}/h \approx 460\,\mathrm{Hz/mW}$.

Alternatively, we can project the optical lattice at the widest lattice spacing onto the atoms at variable laser power and directly measure the amplitude of the resulting density modulation. Using this method, we obtain $V_{\mathrm{Latt}}/h \approx 510\,\mathrm{Hz/mW}$, showing reasonable agreement between the two methods. Thus, the lattice heights used in this work are a small fraction of the chemical potential of the gas for all but the lowest values of $\ln(\mathrm{k_F a_{2D}})$ (see Table S1).

Thermometry and Controlled Heating

Performing thermometry on strongly interacting degenerate 2D Fermi gases is challenging, as there is only very limited theory available for these systems. For harmonically trapped gases, this problem can be circumvented since a significant fraction of the atoms is in the low density region at the edge of the trap where the gas is non-degenerate and can be reasonably well described by a Boltzmann distribution. This allows the extraction of the temperature of the gas from the *in situ* density distribution as done for example in [15]. For our homogeneous system, however, such low density wings do not exist.

An alternative approach is to use matter wave focusing, where a weak harmonic confinement is used to perform a rotation in phase space [18, 28] to extract the momentum distribution of the system. In our case, the harmonic confinement has a trap frequency of $\omega_{\mathrm{mag}} \approx 2\pi \cdot 28\,\mathrm{Hz}$ and is provided by the curvature of the magnetic offset field. Since this technique requires ballistic expansion of the sample, we can only use it in the BEC regime, where the interactions are weak enough that the effect of collisions during the time of flight can be neglected.

As shown in [15], the high-momentum tail of the momentum distribution is well described by a Boltzmann equation of state $n\lambda_T^2 = e^{\mu_d/kT}$, where $\lambda_T = \sqrt{\frac{2\pi\hbar^2}{m_d k_{\mathrm{B}} T}}$ is the thermal wavelength of dimers with mass m_d and μ_d is the chemical potential of the dimers. Hence we can extract the temperature of a gas in the BEC regime by performing matter wave focusing and fitting the high-momentum part of the momentum distribution. However, since the signal-to-noise ratio for this high-momentum part is quite low in our measurements, this method requires considerable averaging and is not suitable as a single-shot thermometer. We therefore use the change of the height of the condensate peak, which can be determined with a much higher signal-to-noise ratio, to quantify the response of the system to the moving periodic potential.

To increase the temperature of the gas in a controlled manner, we move the periodic potential through the system for a variable heating time τ at a velocity larger than the critical velocity. The resulting change in the momentum distribution of the system is shown in Fig. S2 A-C, with the extracted temperatures shown in Fig. S2 D. For comparison, we show the change in the height of the condensate peak, plotted as $r(\tau) = (n(k=0,\tau=0)/n(k=0,\tau)) - 1$ in Fig. S2 E. We use this measurement to calibrate the heating procedure and thereby the temperature axis shown in Fig. 3 D.

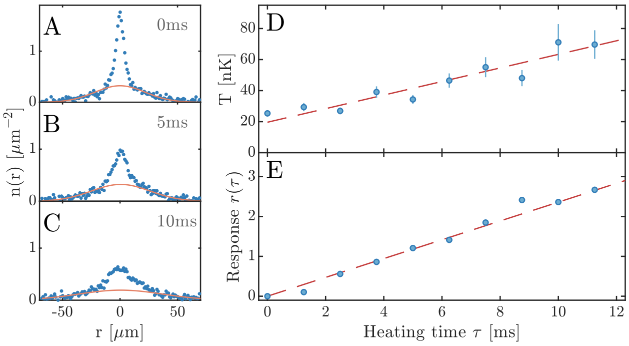

FIG. S2. **Calibration of the heating procedure.** (A-C) Measurements of the momentum distribution of the gas after applying the moving lattice to the system for different heating times τ. The red solid lines show the Boltzmann fits to the wings of the distribution from which the temperature is extracted. (D) Temperature T of the gas as a function of heating time. We observe that the temperature of the gas increases roughly linearly with the heating time (red dashed line). (E) Response $r(\tau)$ as a function of heating time. The response shows a very similar behavior to the temperature, but can be measured with a much higher signal-to-noise ratio. All data points are obtained from an average of 55 individual measurements. The error bars in (D) denote the 1σ confidence interval of the fit.

To obtain an estimate of the systematic uncertainty of our determination of T_{c}, we performed a second set of measurements with a homogeneous 2D Fermi gas in a different potential: Using a red-detuned ($\lambda = 770\,\mathrm{nm}$) flat-bottom potential shaped by a digital micromirror device (DMD) instead of blue-detuned walls creates a box trap of the same dimensions as in the previous measurement, but with a weak ($\omega_{\mathrm{mag}} \approx 2\pi \cdot 28\,\mathrm{Hz}$) harmonic confinement outside the trap volume that is populated by a small number of thermal atoms. While the lowest temperatures we achieved in this red-detuned potential were significantly higher than in the blue-detuned trap, we were able to perform a measurement of the critical temperature at comparable interaction strength and density to the data shown in Fig. 3 of the main text. For this measurement, thermometry was performed using a Boltzmann fit to the low density part of the *in situ* density distribution, from which we obtain a critical temperature of $T_\mathrm{c} = 0.116(2)\,T_\mathrm{F}$ using the same evaluation as for the data shown in Fig. 3. A source of error on the temperatures extracted using these *in situ* fits are inhomogeneities of the harmonic potential, for example due to the optical lattice used for the 2D confinement, as well as small offsets in the absorption imaging, which most likely lead to an overestimation of the temperature of the gas. As a rough approximation for the systematic error of our determination of T_c we use the difference between the values obtained using time-of-flight thermometry ($T_\mathrm{c}/T_\mathrm{F} = 0.094(4)$) and *in situ* thermometry ($T_\mathrm{c}/T_\mathrm{F} = 0.116(2)$). This then yields a critical temperature of $T_\mathrm{c}/T_\mathrm{F} = 0.094 \pm 0.004_{\mathrm{stat}} \pm 0.02_{\mathrm{sys}}$ for a bosonic system at an interaction parameter of $\ln(\mathrm{k_F a_{2D}}) = -2.9$.

Critical Temperature in the BEC-BCS Crossover

To observe the phase transition from a superfluid to a normal state across the BEC-BCS crossover, we performed measurements similar to the one shown in Fig. 3 for interaction strengths ranging from $\ln(\mathrm{k_F a_{2D}}) = -4.1$ deep in the molecular regime to $\ln(\mathrm{k_F a_{2D}}) = 1.1$ on the BCS side of the resonance (Fig. S3). For these measurements, we prepare and heat the system at the same interaction strength of $\ln(\mathrm{k_F a_{2D}}) = -2.9$ as for the measurements shown in Fig. 3, ramp to different magnetic fields to tune the interaction strength to the desired value, and perform measurements of v_c at these interaction strengths. We observe a clear qualitative difference in the response to the moving lattice between cold and hot systems at all measured interaction strengths, showing the presence of a critical temperature. However, as the temperature of the gas changes during the interaction ramp and we cannot use matter wave focusing to determine the temperature at higher interaction strengths, we are currently unable to quantitatively determine the critical temperatures of these systems. Nevertheless, these results present a promising starting point for a future measurement of the critical temperature for superfluidity in 2D Fermi gases across the BEC-BCS crossover.

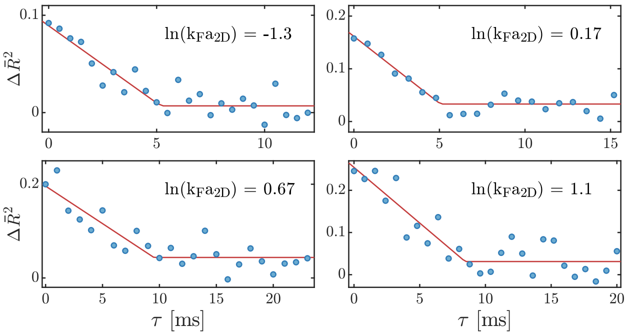

FIG. S3. **Superfluid phase transition at different interaction strengths.** Difference $\Delta\bar{R}^2$ of the adjusted coefficients of determination between fits to $r(v,T)$ with zero and non-zero v_c as a function of heating time τ for different interaction strengths. Linear fits of $\Delta\bar{R}^2$ with a threshold at a critical heating time (red lines) clearly show the appearance of a non-zero critical velocity below a critical temperature for systems across the crossover (A,B,C) and into the BCS regime (D). However, due to the challenges involved in measuring the temperature of strongly interacting homogenous Fermi gases discussed in the text we are currently not able to quantitatively determine the relation between the heating time and the temperature for these systems and hence cannot give a value for T_c.

B. Calculations

B.1. Heat equation

Derivation of equation 6.24

We want to calculate the change in energy in a given volume, given by

$$\frac{\partial}{\partial t}\left(\frac{\varrho v^2}{2}+\varrho\varepsilon\right). \tag{B.1}$$

We first have a look at the kinetic energy term. The change of kinetic energy can be rewritten using the continuity and Euler equations (eqs. 6.1 and 6.9):

$$\begin{aligned}\frac{\partial}{\partial t}\left(\frac{\varrho v^2}{2}\right) &= \frac{v^2}{2}\frac{\partial \varrho}{\partial t}+\frac{\varrho}{2}\frac{\partial \mathbf{v}^2}{\partial t}\\ &= -\frac{v^2}{2}\boldsymbol{\nabla}\cdot(\varrho\mathbf{v})-\mathbf{v}\cdot\boldsymbol{\nabla}p-\varrho\mathbf{v}\cdot(\mathbf{v}\cdot\boldsymbol{\nabla})\mathbf{v}\\ &= -\frac{v^2}{2}\boldsymbol{\nabla}\cdot(\varrho\mathbf{v})-\mathbf{v}\cdot\boldsymbol{\nabla}p-\frac{\varrho}{2}\mathbf{v}\cdot\boldsymbol{\nabla}v^2. \end{aligned}\tag{B.2}$$

The pressure gradient is then eliminated by introducing the enthalpy density $w=\varepsilon+pV/Nm=\varepsilon+p/\varrho$. The change in enthalpy is given by changes in entropy and volume: $dw=Tds+dp/\varrho$. Thus, we have $\boldsymbol{\nabla}p=\varrho\boldsymbol{\nabla}w-\varrho T\boldsymbol{\nabla}s$, and then

$$\frac{\partial}{\partial t}\left(\frac{\varrho v^2}{2}\right)=-\frac{v^2}{2}\boldsymbol{\nabla}\cdot(\varrho\mathbf{v})-\varrho\mathbf{v}\cdot\boldsymbol{\nabla}\left(\frac{v^2}{2}+w\right)+\varrho T\mathbf{v}\cdot\boldsymbol{\nabla}s. \tag{B.3}$$

For the change in internal energy, we use $dV=-d\varrho/\varrho^2$ to write $d(\varrho\varepsilon)=\varepsilon d\varrho+\varrho d\varepsilon=\varepsilon d\varrho+\varrho Tds+(p/\varrho)d\varrho=wd\varrho+\varrho Tds$. The change in internal energy in the volume is then given by

$$\frac{\partial(\varrho\varepsilon)}{\partial t}=w\frac{\partial\varrho}{\partial t}+\varrho T\frac{\partial s}{\partial t}=-w\boldsymbol{\nabla}\cdot(\varrho\mathbf{v})-\varrho T\mathbf{v}\cdot\boldsymbol{\nabla}s, \tag{B.4}$$

where we have used the continuity equation for particle (eq. 6.1) and entropy density (eq. 6.6). The energy balance equation (eq. 6.24) is obtained by combining equations B.3 and B.4.

$$\begin{aligned}\frac{\partial}{\partial t}\left(\frac{\varrho v^2}{2}+\varrho\varepsilon\right) &= -\frac{v^2}{2}\boldsymbol{\nabla}\cdot(\varrho\mathbf{v})-\varrho\mathbf{v}\cdot\boldsymbol{\nabla}\left(\frac{v^2}{2}+w\right)\\ &\qquad+\varrho T\mathbf{v}\cdot\boldsymbol{\nabla}s-w\boldsymbol{\nabla}\cdot(\varrho\mathbf{v})-\varrho T\mathbf{v}\cdot\boldsymbol{\nabla}s\\ &= -\boldsymbol{\nabla}\cdot\left[\varrho\mathbf{v}\left(\frac{v^2}{2}+w\right)\right]. \end{aligned}\tag{B.5}$$

Derivation of equation 6.26

To derive equation 6.26 we expand the left-hand side of equation 6.24:

$$\frac{\partial}{\partial t}\left(\frac{\varrho v^2}{2}+\varrho\varepsilon\right)=\frac{v^2}{2}\frac{\partial\varrho}{\partial t}+\varrho\mathbf{v}\frac{\partial\mathbf{v}}{\partial t}+\varrho\frac{\partial\varepsilon}{\partial t}+\varepsilon\frac{\partial\varrho}{\partial t}. \tag{B.6}$$

The continuity equation is used to eliminate $\partial\varrho/\partial t$ and inserting $\partial\mathbf{v}/\partial t$ from equation 6.20, one obtains

$$\frac{\partial}{\partial t}\left(\frac{\varrho v^2}{2}+\varrho\varepsilon\right)=-\frac{v^2}{2}\boldsymbol{\nabla}(\varrho\mathbf{v})-\varrho(\mathbf{v}\boldsymbol{\nabla})\frac{v^2}{2}-\mathbf{v}\boldsymbol{\nabla}p+v_i\frac{\partial\sigma'_{ik}}{\partial x_k}+\varrho\frac{\partial\varepsilon}{\partial t}-\varepsilon\boldsymbol{\nabla}(\varrho\mathbf{v}). \tag{B.7}$$

With $d\varepsilon=Tds+p/\varrho^2d\varrho$ and the continuity equation (eq. 6.1), we have

$$\frac{\partial\varepsilon}{\partial t}=T\frac{\partial s}{\partial t}+\frac{p}{\varrho^2}\frac{\partial\varrho}{\partial t}=T\frac{\partial s}{\partial t}-\frac{p}{\varrho^2}\boldsymbol{\nabla}\cdot(\varrho\mathbf{v}), \tag{B.8}$$

and since $w=\varepsilon+p/\varrho$, this yields:

$$\begin{aligned}\frac{\partial}{\partial t}\left(\frac{\varrho v^2}{2}+\varrho\varepsilon\right)=&-\left(\frac{v^2}{2}+w\right)\boldsymbol{\nabla}\cdot(\varrho\mathbf{v})-\varrho(\mathbf{v}\cdot\boldsymbol{\nabla})\frac{v^2}{2}\\&-\mathbf{v}\cdot\boldsymbol{\nabla}p+\varrho T\frac{\partial s}{\partial t}+v_i\frac{\partial\sigma'_{ik}}{\partial x_k}.\end{aligned} \tag{B.9}$$

We then replace $\boldsymbol{\nabla}p=\varrho\boldsymbol{\nabla}w-\varrho T\boldsymbol{\nabla}s$ and for the rightmost term, one can write

$$v_i\frac{\partial\sigma'_{ik}}{\partial x_k}=\frac{\partial}{\partial x_k}(v_i\sigma'_{ik})-\sigma'_{ik}\frac{\partial v_i}{\partial x_k}=\boldsymbol{\nabla}\cdot(\mathbf{v}\sigma')-\sigma'_{ik}\frac{\partial v_i}{\partial x_k}. \tag{B.10}$$

Together, this yields equation 6.26.

B.2. Calculation of the sound dispersion

B.2.1. Classical gas

Setting up the system of equations

In order to derive the sound dispersion, one assumes that the particles oscillate harmonically around their rest position and that this movement causes small fluctuations in the thermodynamic quantities

$$\mathbf{v}(\mathbf{r},t) = \mathbf{v}\exp[i(\mathbf{q}\cdot\mathbf{r}-\omega t)], \text{ and} \tag{B.11}$$

$$\begin{pmatrix} \varrho(\mathbf{r},t) \\ p(\mathbf{r},t) \\ T(\mathbf{r},t) \\ s(\mathbf{r},t) \end{pmatrix} = \begin{pmatrix} \varrho_0 \\ p_0 \\ T_0 \\ s_0 \end{pmatrix} + \begin{pmatrix} \varrho' \\ p' \\ T' \\ s' \end{pmatrix} \times \exp[i(\mathbf{q}\cdot\mathbf{r}-\omega t)]. \tag{B.12}$$

The first step is to linearize the hydrodynamic equations in $\mathbf{v}$ the small variations ϱ', p', T' and s'.

We start out with the continuity equation 6.1. In component notation, it reads

$$0 = \frac{\partial \varrho}{\partial t} + \frac{\partial}{\partial x_i}(\varrho v_i) \tag{B.13}$$

$$= \left[-i\omega\varrho' + \varrho(iq_i)v_i + \cancel{v_i(iq_i)\varrho'}\right]\exp[i(\mathbf{q}\cdot\mathbf{r}-\omega t)]. \tag{B.14}$$

The third term is nonlinear and drops out, since v_i and ϱ' are multiplied. Writing this equation in vector notation, this yields

$$\omega\varrho' - \varrho\mathbf{q}\cdot\mathbf{v} = 0. \tag{B.15}$$

Next, the momentum balance equation is written in component notation as

$$0 = \frac{\partial}{\partial t}(\varrho v_i) + \frac{\partial}{\partial x_k}\Pi_{ik} \tag{B.16}$$

$$= \frac{\partial}{\partial t}(\varrho v_i) + \frac{\partial}{\partial x_k}(p\delta_{ik} + \cancel{\varrho v_i v_k} - \sigma'_{ik}). \tag{B.17}$$

The first two terms yield

$$\frac{\partial}{\partial t}(\varrho v_i) + \frac{\partial}{\partial x_k}(p\delta_{ik}) = (-\cancel{i\omega v_i\varrho'} - i\varrho\omega v_i + iq_i p')\exp[i(\mathbf{q}\cdot\mathbf{r}-\omega t)] \tag{B.18}$$

Again, the crossed term drop out since $\varrho v_i v_k$ and $v_i\varrho'$ are nonlinear contributions. The term containing the viscous stress tensor results in

$$\frac{\partial}{\partial x_k}\sigma'_{ik} = \frac{\partial}{\partial x_k}\eta\left(\frac{\partial v_i}{\partial x_k} + \frac{\partial v_k}{\partial x_i} - \frac{2}{d}\delta_{ik}\frac{\partial v_l}{\partial x_l}\right) + \zeta\delta_{ik}\frac{\partial v_l}{\partial x_l} \tag{B.19}$$

$$= \left[-\eta q_k^2 v_i - \eta q_i q_k v_k + \frac{2}{d}\eta q_i q_l v_l - \zeta q_i q_l v_l\right]\exp[i(\mathbf{q}\cdot\mathbf{r}-\omega t)] \tag{B.20}$$

$$= \left[-\eta q^2 v_i - \left(\frac{d-2}{d}\eta + \zeta\right)(\mathbf{q}\mathbf{v})q_i\right]\exp[i(\mathbf{q}\cdot\mathbf{r}-\omega t)]. \tag{B.21}$$

Putting B.18 and B.21 together, one obtains in vector notation

$$\omega\varrho\mathbf{v} + i\eta q^2\mathbf{v} + i\left(\frac{d-2}{d}\eta + \zeta\right)(\mathbf{q}\cdot\mathbf{v})\mathbf{q} - p'\mathbf{q} = 0. \tag{B.22}$$

In this equation, vectors proportional to $\mathbf{v}$ and $\mathbf{q}$ have to add up to zero. Therefore, $\mathbf{v}$ and $\mathbf{q}$ have to be collinear. We can thus write $(\mathbf{q}\cdot\mathbf{v})\mathbf{q} = q^2\mathbf{v}$ and obtain

$$\left[\omega\varrho + i\left(\frac{2d-2}{d}\eta + \zeta\right)q^2\right]\mathbf{v} - p'\mathbf{q} = 0. \tag{B.23}$$

The third equation is the heat equation, which takes on the following form

$$\varrho T\left(\frac{\partial s}{\partial t} + \mathbf{v}\cdot\boldsymbol{\nabla}s\right) = \sigma'_{ik}\frac{\partial v_i}{\partial x_k} + \boldsymbol{\nabla}\cdot(\varkappa\boldsymbol{\nabla}T). \tag{B.24}$$

Since the viscous stress tensor is already a combination of derivatives of the velocity, the first term on the right hand side is nonlinear and does not contribute to the linearized version of this equation. Similarly, $\mathbf{v}\boldsymbol{\nabla}s$ will be nonlinear, since $\mathbf{v}$ and s' are multiplied. We then are left with

$$\varrho T\omega s' + i\varkappa q^2 T' = 0. \tag{B.25}$$

Simplifying the expressions

In order to simplify eqs. B.15, B.23 and B.25, we note that the thermodynamic variables are not independent but are related via

$$\varrho' = \left(\frac{\partial\varrho}{\partial p}\right)_T p' + \left(\frac{\partial\varrho}{\partial T}\right)_p T' \quad \text{and} \quad s' = \left(\frac{\partial s}{\partial p}\right)_T p' + \left(\frac{\partial s}{\partial T}\right)_p T'. \tag{B.26}$$

This allows us to eliminate ϱ' and s', resulting in the following system of equations

$$\begin{pmatrix} \omega\left(\partial\varrho/\partial T\right)_p & -\varrho\mathbf{q} & \omega\left(\partial\varrho/\partial p\right)_T \\ 0 & \omega\varrho + iaq^2 & -\mathbf{q} \\ \omega\varrho T\left(\partial s/\partial T\right)_p + i\varkappa q^2 & 0 & \omega\varrho T\left(\partial s/\partial p\right)_T \end{pmatrix} \cdot \begin{pmatrix} T' \\ \mathbf{v} \\ p' \end{pmatrix} = \begin{pmatrix} 0 \\ 0 \\ 0 \end{pmatrix}, \tag{B.27}$$

where we have written $a = \frac{2d-2}{d}\eta + \zeta$ for convenience.

We now introduce the adiabatic and isothermal sound velocities

$$c^2 = \left(\frac{\partial p}{\partial\varrho}\right)_s \quad \text{and} \quad c_T^2 = \left(\frac{\partial p}{\partial\varrho}\right)_T, \tag{B.28}$$

which for now are just notational shortcuts, as well as the heat capacities at constant pressure and volume

$$C_p = \varrho T\left(\frac{\partial s}{\partial T}\right)_p \quad \text{and} \quad C_v = \varrho T\left(\frac{\partial s}{\partial T}\right)_v. \tag{B.29}$$

We further simplify the equations by making use of the relation

$$c^2 = \frac{C_p}{C_v} c_T^2 \tag{B.30}$$

between the sound velocities and the heat capacities. With equations B.28 to B.30, the system of equations reads

$$\begin{pmatrix} \omega\left(\partial\varrho/\partial T\right)_p & -\varrho\mathbf{q} & \omega C_p/(C_v c^2) \\ 0 & \omega\varrho + iaq^2 & -\mathbf{q} \\ \omega C_p + i\varkappa q^2 & 0 & \omega\varrho T\left(\partial s/\partial p\right)_T \end{pmatrix} \cdot \begin{pmatrix} T' \\ \mathbf{v} \\ p' \end{pmatrix} = \begin{pmatrix} 0 \\ 0 \\ 0 \end{pmatrix}. \tag{B.31}$$

The solution to this system is obtained by setting the determinant of the coefficient matrix to zero. With

$$\varrho T \left(\frac{\partial\varrho}{\partial T}\right)_p \left(\frac{\partial s}{\partial p}\right)_T = \frac{C_p}{c^2}\frac{C_p - C_v}{C_v}, \tag{B.32}$$

this leads to

$$\begin{aligned} 0 = {} & \omega^2 \frac{C_p}{c^2}\frac{C_p - C_v}{C_v}(\omega\varrho + iaq^2) \\ & + \varrho q^2(\omega C_p + i\varkappa q^2) - \frac{\omega}{c^2}\frac{C_p}{C_v^2}(\omega\varrho + iaq^2)(\omega C_p + i\varkappa q^2), \end{aligned} \tag{B.33}$$

After reordering in powers of ω, we finally arrive at eq. 6.34:

$$\omega^3 + i\frac{\omega^2 q^2}{\varrho}\left(\eta + \zeta + \varkappa\varrho\frac{C_p - C_v}{C_p C_v}\right) - \omega q^2 c^2 - \frac{\omega q^4 \varkappa}{\varrho C_v}(\eta + \zeta) = 0 \tag{B.34}$$

All that is left is to prove equations B.30 and B.32. B.32 can be shown by setting $\varrho' = 0$ in B.26 and replacing p' in the equation for s' in order to obtain an expression for the entropy change $s'(T', \varrho')_{\varrho'=0}$ at constant volume. The heat capacity at constant volume is then given by

$$C_v = \varrho T \left(\frac{\partial s}{\partial T}\right)_v = \varrho T \left(\frac{\partial s'}{\partial T'}\right)_{\varrho'=0} \tag{B.35}$$

$$= C_p - \varrho T \left(\frac{\partial s}{\partial p}\right)_T \left(\frac{\partial\varrho}{\partial T}\right)_p \left(\frac{\partial p}{\partial\varrho}\right)_T, \tag{B.36}$$

And therefore

$$\frac{C_v}{C_p} = 1 - \frac{(\partial\varrho/\partial T)_p(\partial s/\partial p)_T}{(\partial s/\partial T)_p(\partial\varrho/\partial p)_T} \tag{B.37}$$

Eq. B.30 can be shown analogously by setting $s' = 0$ and replacing T' in the formula for ϱ', resulting in $\varrho'(p')$. Then

$$\frac{1}{c_s^2} = \left(\frac{\partial\varrho}{\partial p}\right)_s = \frac{\varrho'}{p'} = \left(\frac{\partial\varrho}{\partial p}\right)_T - \left(\frac{\partial\varrho}{\partial T}\right)_p \left(\frac{\partial s}{\partial p}\right)_T \left(\frac{\partial T}{\partial s}\right)_p \tag{B.38}$$

$$= \frac{1}{c_T^2}\left[1 - \frac{(\partial\varrho/\partial T)_p(\partial s/\partial p)_T}{(\partial s/\partial T)_p(\partial\varrho/\partial p)_T}\right] = \frac{1}{c_T^2}\frac{C_v}{C_p}. \tag{B.39}$$

B.2.2. Superfluid

We start out with equations 6.47 and 6.46. These are

$$\frac{\partial^2 \varrho}{\partial t^2} = \Delta p \tag{B.40}$$

$$\frac{\partial^2 s}{\partial t^2} = s^2 \frac{\varrho_s}{\varrho_n} \Delta T. \tag{B.41}$$

We now choose the density and temperature as independent variables and allow for small fluctuations of the form $\sim \exp\left(i\mathbf{q}\cdot\mathbf{r} - i\omega t\right)$. Omitting second order terms in the perturbations, this yields

$$\frac{\partial^2 \varrho}{\partial t^2} = -\omega^2 \varrho' \exp\left(i\mathbf{q}\cdot\mathbf{r} - i\omega t\right) \tag{B.42}$$

$$\begin{aligned}\Delta p &= \left(\frac{\partial p}{\partial \varrho}\right)_T \Delta\rho + \left(\frac{\partial p}{\partial T}\right)_\varrho \Delta T \\ &= -q^2 \exp\left(i\mathbf{q}\cdot\mathbf{r} - i\omega t\right) \left[\left(\frac{\partial p}{\partial \varrho}\right)_T \varrho' + \left(\frac{\partial p}{\partial T}\right)_\varrho T'\right]\end{aligned} \tag{B.43}$$

And thus from equation 6.47:

$$\omega^2 \varrho' - q^2 \left[\left(\frac{\partial p}{\partial \varrho}\right)_T \varrho' + \left(\frac{\partial p}{\partial T}\right)_\varrho T'\right] = 0 \tag{B.44}$$

Analogously, we obtain from equation 6.46

$$\omega^2 \left[\left(\frac{\partial s}{\partial \varrho}\right)_T \varrho' + \left(\frac{\partial s}{\partial T}\right)_\varrho T'\right] - q^2 \frac{\rho_s}{\rho_n} s^2 T' = 0. \tag{B.45}$$

Simplifying these equations

We now want to simplify these equations. For this, we first introduce the following quantities:

$$c^2 = \left(\frac{\partial p}{\partial \varrho}\right)_s, c_T^2 = \left(\frac{\partial p}{\partial \varrho}\right)_T, C_v = \varrho T \left(\frac{\partial s}{\partial T}\right)_\varrho, \text{ and } c_2^2 = \frac{\varrho_s}{\varrho_n} s^2 \frac{\varrho T}{C_v}. \tag{B.46}$$

Setting $u = \omega/q$, we immediately find equation 6.51:

$$(u^2 - c_T^2)\varrho' - \left(\frac{\partial p}{\partial T}\right)_\varrho T' = 0. \tag{B.47}$$

Equation B.45 transforms to

$$u^2 \frac{\varrho T}{C_v} \left(\frac{\partial s}{\partial \varrho}\right)_T \varrho' + (u^2 - c_2^2) T' = 0. \tag{B.48}$$

Using thermodynamic relations, one can derive the following equality:

$$\frac{\varrho T}{C_v} \left(\frac{\partial s}{\partial \varrho}\right)_T = -(c_T^2 - c^2) \frac{1}{\varrho^2} \left(\frac{\partial \varrho}{\partial s}\right)_T. \tag{B.49}$$

We insert this into equation B.48 and using $\left(\frac{\partial p}{\partial T}\right)_\varrho = \left(\frac{\partial S}{\partial V}\right)_T = -\varrho^2 \left(\frac{\partial s}{\partial \varrho}\right)_T$, we finally arrive at equation 6.52:

$$u^2 (c_T^2 - c^2) \left(\frac{\partial p}{\partial T}\right)_\varrho^{-1} \varrho' + (u^2 - c_2^2) T' = 0. \tag{B.50}$$

Derivation of eq. B.49

Here I show how to derive equation B.49. To obtain this result, we have to do a bit more work and play with thermodynamic partial derivatives. The variation of the internal energy is given by $dU = TdS - pdV$. We can differentiate this with respect to two quantities X and Y:

$$\frac{\partial U}{\partial X} = T\left(\frac{\partial S}{\partial X}\right)_Y - p\left(\frac{\partial V}{\partial X}\right)_Y \tag{B.51}$$

$$\frac{\partial U}{\partial Y} = T\left(\frac{\partial S}{\partial Y}\right)_X - p\left(\frac{\partial V}{\partial Y}\right)_X \tag{B.52}$$

We now differentiate with respect to the other quantities:

$$\frac{\partial^2 U}{\partial Y \partial X} = \left(\frac{\partial T}{\partial Y}\right)_X \left(\frac{\partial S}{\partial X}\right)_Y - \left(\frac{\partial p}{\partial Y}\right)_X \left(\frac{\partial V}{\partial X}\right)_Y \tag{B.53}$$

$$\frac{\partial^2 U}{\partial X \partial Y} = \left(\frac{\partial T}{\partial X}\right)_Y \left(\frac{\partial S}{\partial Y}\right)_X - \left(\frac{\partial p}{\partial X}\right)_Y \left(\frac{\partial V}{\partial Y}\right)_X \tag{B.54}$$

Both quantities on the left hand sides are equal (Schwarz's theorem), which gives us the general form of Maxwell's relations:

$$\begin{aligned}&\left(\frac{\partial T}{\partial Y}\right)_X \left(\frac{\partial S}{\partial X}\right)_Y - \left(\frac{\partial p}{\partial Y}\right)_X \left(\frac{\partial V}{\partial X}\right)_Y \\ &\qquad = \left(\frac{\partial T}{\partial X}\right)_Y \left(\frac{\partial S}{\partial Y}\right)_X - \left(\frac{\partial p}{\partial X}\right)_Y \left(\frac{\partial V}{\partial Y}\right)_X\end{aligned} \tag{B.55}$$

Now, X and Y can be any variables out of T, S, p and V. Choosing $X = p$ and $Y = V$, we get

$$\left(\frac{\partial S}{\partial V}\right)_p = \left(\frac{\partial p}{\partial T}\right)_V + \left(\frac{\partial T}{\partial V}\right)_p \left(\frac{\partial S}{\partial T}\right)_V . \tag{B.56}$$

This gives us

$$\begin{aligned}-\left(\frac{\partial p}{\partial V}\right)_S &= \left(\frac{\partial p}{\partial S}\right)_V \left(\frac{\partial S}{\partial V}\right)_p \\ &= \left(\frac{\partial p}{\partial S}\right)_V \left[\left(\frac{\partial T}{\partial V}\right)_p \left(\frac{\partial S}{\partial T}\right)_V + \left(\frac{\partial p}{\partial T}\right)_V\right] \\ &= \left(\frac{\partial p}{\partial T}\right)_V \left(\frac{\partial T}{\partial V}\right)_p + \left(\frac{\partial T}{\partial S}\right)_V \left(\frac{\partial p}{\partial T}\right)_V^2 \\ &= -\left(\frac{\partial p}{\partial V}\right)_T + \left(\frac{\partial T}{\partial S}\right)_V \left(\frac{\partial S}{\partial V}\right)_T^2 .\end{aligned} \tag{B.57}$$

With $\partial/\partial\varrho = -Nm\partial/\varrho^2\partial V$, we finally arrive at

$$\left(\frac{\partial p}{\partial \varrho}\right)_T - \left(\frac{\partial p}{\partial \varrho}\right)_s = -\varrho^2 \left(\frac{\partial s}{\partial \varrho}\right)_T^2 \left(\frac{\partial T}{\partial s}\right)_V , \tag{B.58}$$

which we only need to rearrange as:

$$\frac{\varrho T}{C_v}\left(\frac{\partial s}{\partial \varrho}\right)_T = -(c_T^2 - c^2)\frac{1}{\varrho^2}\left(\frac{\partial \varrho}{\partial s}\right)_T . \tag{B.59}$$

B.3. Derivation of the inverse AC - Josephson effect

The Josephson junction is driven with a voltage of the form

$$V(t) = V_{\mathrm{DC}} + V_{\mathrm{AC}} \cos(\omega t). \tag{B.60}$$

The dynamics of the Josephson junction are given by the equations

$$I(\varphi) = I_c \sin(\varphi) \text{ and} \tag{B.61}$$

$$\frac{\partial}{\partial t}\varphi = \frac{2eV}{\hbar}. \tag{B.62}$$

The phase difference across the junction thus evolves in time as

$$\varphi(t) = \varphi_0 + \frac{2e}{\hbar} V_{\mathrm{DC}} t + \frac{2e}{\hbar\omega} V_{\mathrm{AC}} t \sin(\omega t), \tag{B.63}$$

which yields a current of

$$I(t) = I_c \sin\left(\varphi_0 + \frac{2e}{\hbar} V_{\mathrm{DC}} t + \frac{2e}{\hbar\omega} V_{\mathrm{AC}} t \sin(\omega t)\right). \tag{B.64}$$

We now use the following identities:

$$\sin(a \sin(x)) = \sum_{n \text{ odd}} J_n(a) \sin(nx), \tag{B.65}$$

$$\cos(a \sin(x)) = \sum_{n \text{ even}} J_n(a) \cos(nx), \text{ and} \tag{B.66}$$

$$J_{\text{-n}}(x) = (-1)^n J_n(x), \tag{B.67}$$

which involve the Bessel functions $J_n(x)$ of first kind. With these, we can expand the current in the form

$$I(t) = I_c \sum_{n=-\infty}^{\infty} (-1)^n J_n\left(\frac{2e}{\hbar\omega} V_{\mathrm{AC}}\right) \sin\left[\varphi_0 + \left(\frac{2e}{\hbar} V_{\mathrm{DC}} - n\omega\right) t\right],$$

which is an infinite sum of oscillating terms, whose amplitude is fixed by the alternating voltage V_{AC} and whose frequency is fixed by the term $\frac{2e}{\hbar} V_{\mathrm{DC}} - n\omega$.

We see that the time-dependent parts indeed drop out for

$$V_{\mathrm{DC}} = n\frac{\hbar\omega}{2e}. \tag{B.68}$$

B.4. Derivation of the effective current phase relation eq. 7.12

To show the effective current phase relation 7.12 of an ideal Josephson junction, we assume that we are in a regime in which the dynamics are dominated by the barrier ($L_{\mathrm{J}} \gg L_{\mathrm{B}}$). We can then neglect the bulk inductance and write Kirchhoff's law for the voltages in the LC circuit as

$$U_\mathrm{C} + U_\mathrm{J} = \frac{\Delta N}{2C} + \hbar\dot{\varphi} = 0. \tag{B.69}$$

By differentiating this equation with respect to time, we obtain

$$\frac{I}{C} + \hbar\ddot{\varphi} = 0, \tag{B.70}$$

in which we can insert the current phase relation of an ideal Josephson junction $I(\varphi) = I_c \sin(\varphi)$. This yields

$$\ddot{\varphi} + \frac{I_c}{\hbar C}\sin(\varphi), \tag{B.71}$$

which is the equation of motion of a mathematical pendulum.

The oscillation frequency of the pendulum in terms of the maximum excursion φ_0 is given by the expansion $\omega(\varphi_0)^2 \approx \frac{I_c}{\hbar C}(1 - \varphi_0^2/8 + \dots) \approx \frac{I_c}{\hbar C}\cos(\frac{\varphi_0}{2})$.

Since $\omega^2 = 1/L_\mathrm{J}C$, we can then extract the effective inductance $L_{\mathrm{J},0}(\varphi_0)$ at large φ_0 from the frequency shift with respect to very small oscillations:

$$L_{\mathrm{J},0}(\varphi_0) \approx L_{\mathrm{J},0}(\varphi_0 \to 0)\left(\frac{\omega(\varphi_0 \to 0)}{\omega(\varphi_0)}\right)^2 \approx \frac{\hbar}{I_c\cos(\varphi_0/2)}. \tag{B.72}$$

We now rearrange eq. 7.8 to obtain

$$I_0(\varphi_0) \approx \int_0^{\varphi_0} \frac{\hbar}{L_{\mathrm{J},0}(\varphi_0')}d\varphi_0' = \int_0^{\varphi_0} I_c\cos(\varphi_0'/2)d\varphi_0' \tag{B.73}$$

$$= 2I_c\sin\left(\frac{\varphi_0}{2}\right), \tag{B.74}$$

which is the simple rescaled expression for the effective current that we wanted to derive.

C. Acknowledgments

The completion of this thesis would not have been possible were it not for a multitude of people who helped and encouraged me along the way. I would like to take this opportunity to express my gratitude to all of you.

First, I would like to thank Christophe and Fred for having welcomed me into their group. It is clearly not evident to employ a PhD student who will leave the group after two years, soon after the learning period is over. Your generosity has made it possible for me to continue on my German-French path even during the PhD time and has made it much easier to reconcile it with friends and family abroad.

My second thanks go out to Henning, who in a similar way agreed to take over a PhD student who would soon have to begin writing his thesis. I am grateful that you introduced me to the fascinating field of ultracold atoms seven years ago. You always gave me the feeling that you care about your team, their strengths and worries, as well as their plans for the future. It is inspiring to see how you manage to create this sense of appreciation within your group while staying on top of what happens in the labs all the while juggling your many obligations.

I also want to express my heartfelt thanks to the two teams I had the pleasure of working with. Without a good atmosphere in the lab and office, four years of PhD work could easily feel like many more. This was not at all the case. Thank you to Tom, Cédric and Clément for showing me the ins and outs, for going to Chez Gladines with me and for your good mood, all the laughs as well as the fun evenings. Thank you to Lennart, Niclas and Hauke for a relaxed, friendly and productive work environment and for accepting me so warmly into the group. Thank you to Misha for musical evenings and to Chayma for the spatula. Thank you also to Alex and Martin, whose calm presence often provided a welcome counterpoint of sorts.

Thomas, a big thank you to you as well. Your impressive experimental and technical knowledge and your readiness to help wherever needed have been invaluable for me in the past two years. I am very much looking forward to my return to the lab and having interesting discussions with you over lunch from time to time again!

Thank you as well to Tarik and Julian. Both of you showed an incredible commitment to improve on the conditions both in the lab, in the office and sometimes even off work. Your drive to get things done caused many things to happen that would not have otherwise and it is something I find admirable.

Special thanks are due to Tilman Enss, whose patient explanations of hydrodynamics and transport have helped me and the entire group immensely during the writing period of the sound article.

Furthermore, I would like to thank all those who I unfortunately cannot give more room at this place. In particular, I'd like to mention the lithium team at LKB, the administrative and technical staff of ILP and LKB as well as the members of the mechanics and electronics workshops.

Finally, I thank my friends and family, for believing in me, for saving the world with me (at least most of the times) on Sunday afternoons, and for giving me support in tougher times.

And last but not least, thank you so so much, Alina! You stuck with me through many years of travel, video calls and much-too-short visits, through stressful and scary times, but also during fun and truly wonderful times. I am so glad to have you in my life. With you, everything seems easier.

List of Figures

Bibliography

[1] N. D. Mermin and H. Wagner. Absence of Ferromagnetism or Antiferromagnetism in One- or Two-Dimensional Isotropic Heisenberg Models. *Phys. Rev. Lett.* **17**, 1133 (1966). [Cited on pages 1, 9, and 109.]

[2] P. C. Hohenberg. Existence of Long-Range Order in One and Two Dimensions. *Phys. Rev.* **158**, 383 (1967). [Cited on pages 1, 9, and 109.]

[3] V. L. Berezinskii. Destruction of Long-range Order in One-dimensional and Two-dimensional Systems Having a Continuous Symmetry Group. I. Classical systems. *Sov. Phys. JETP* **32**(3), 493–500 (1971). (english translation). [Cited on pages 1 and 9.]

[4] V. L. Berezinskii. Destruction of Long-range Order in One-dimensional and Two-dimensional Systems Possessing a Continuous Symmetry Group. II. quantum systems. *Sov. Phys. JETP* **34**(3), 610–616 (1972). (english translation). [Cited on pages 1 and 9.]

[5] J. M. Kosterlitz and D. J. Thouless. Ordering, metastability and phase transitions in two-dimensional systems. *Journal of Physics C: Solid State Physics* **6**(7), 1181–1203 (1973). [Cited on pages 1 and 9.]

[6] C. C. Tsuei and J. R. Kirtley. Pairing symmetry in cuprate superconductors. *Rev. Mod. Phys.* **72**, 969 (2000). [Cited on pages 1 and 43.]

[7] Q. Si, R. Yu, and E. Abrahams. High-temperature superconductivity in iron pnictides and chalcogenides. *Nature Reviews Materials* **1**, 16017 (2016). [Cited on pages 1 and 43.]

[8] Y. Cao, V. Fatemi, S. Fang, K. Watanabe, T. Taniguchi, E. Kaxiras, and P. Jarillo-Herrero. Unconventional superconductivity in magic-angle graphene superlattices. *Nature* **556**, 43–50 (2018). [Cited on pages 1, 43, 109, and 110.]

[9] K. Maki and F. Mancini. Introduction to d-wave superconductivity. *AIP Conference Proceedings* **438**, 83 (1998). [Cited on pages 1 and 43.]

[10] E. Y. Loh, J. E. Gubernatis, R. T. Scalettar, S. R. White, D. J. Scalapino, and R. L. Sugar. Sign problem in the numerical simulation of many-electron systems. *Phys. Rev. B* **41**, 9301 (1990). [Cited on page 1.]

[11] M. Troyer and U.-J. Wiese. Computational Complexity and Fundamental Limitations to Fermionic Quantum Monte Carlo Simulations. *Phys. Rev. Lett.* **94**, 170201 (2005). [Cited on page 1.]

[12] A. P. Lyubartsev. Simulation of excited states and the sign problem in the path integral Monte Carlo method. *Journal of Physics A: Mathematical and General* **38**(30), 6659–6674 (2005). [Cited on page 1.]

[13] I. Bloch, J. Dalibard, and S. Nascimbène. Quantum simulations with ultracold quantum gases. *Nature Physics* **8**, 267–276 (2012). [Cited on page 2.]

[14] R. P. Feynman. Simulating physics with computers. *International Journal of Theoretical Physics* **21**, 467–488 (1982). [Cited on page 2.]

[15] A. Ashkin. Acceleration and Trapping of Particles by Radiation Pressure. *Phys. Rev. Lett.* **24**, 156 (1970). [Cited on page 2.]

[16] T. W. Hänsch and A. L. Schawlow. Cooling of gases by laser radiation. *Optics Communications* **13**(1), 68–69 (1975). [Cited on page 2.]

[17] W. D. Phillips and H. Metcalf. Laser Deceleration of an Atomic Beam. *Phys. Rev. Lett.* **48**, 596 (1982). [Cited on pages 2, 26, and 59.]

[18] S. Chu, J. E. Bjorkholm, A. Ashkin, and A. Cable. Experimental Observation of Optically Trapped Atoms. *Phys. Rev. Lett.* **57**, 314 (1986). [Cited on page 2.]

[19] E. L. Raab, M. Prentiss, Alex Cable, Steven Chu, and D. E. Pritchard. Trapping of Neutral Sodium Atoms with Radiation Pressure. *Phys. Rev. Lett.* **59**, 2631 (1987). [Cited on pages 2, 26, 28, and 59.]

[20] M. H. Anderson, J. R. Ensher, M. R. Matthews, C. E. Wieman, and E. A. Cornell. Observation of Bose-Einstein Condensation in a Dilute Atomic Vapor. *Science* **269**(5221), 198–201 (1995). [Cited on pages 2, 5, and 115.]

[21] K. B. Davis, M. O. Mewes, M. R. Andrews, N. J. van Druten, D. S. Durfee, D. M. Kurn, and W. Ketterle. Bose-Einstein Condensation in a Gas of Sodium Atoms. *Phys. Rev. Lett.* **75**, 3969 (1995). [Cited on pages 2, 5, and 115.]

[22] B. DeMarco and D. S. Jin. Onset of Fermi Degeneracy in a Trapped Atomic Gas. *Science* **285**(5434), 1703–1706 (1999). [Cited on pages 2 and 5.]

[23] W. Ketterle, D. S. Durfee, and D. M. Stamper-Kurn. Making, probing and understanding Bose-Einstein condensates. In M. Inguscio, S. Stringari, and C. E. Wieman, editors: *Bose-Einstein Condensation in Atomic Gases*, volume 140 of *Proceedings of the International School of Physics "Enrico Fermi"*. IOS Press, Amsterdam, 1999. [Cited on pages 2 and 5.]

[24] W. Ketterle and M. W. Zwierlein. Making, probing and understanding ultracold Fermi gases. In M. Inguscio, W. Ketterle, and C. Salomon, editors: *Ultracold Fermi Gases*, volume 164 of *Proceedings of the International School of Physics "Enrico Fermi"*. IOS Press, Amsterdam, 2007. [Cited on pages 2, 5, and 16.]

[25] I. Bloch, J. Dalibard, and W. Zwerger. Many-body physics with ultracold gases. *Rev. Mod. Phys.* **80**, 885 (2008). [Cited on pages 2, 13, 17, and 19.]

[26] W. Hofstetter and T. Qin. Quantum simulation of strongly correlated condensed matter systems. *Journal of Physics B: Atomic, Molecular and Optical Physics* **51**(8), 082001 (2018). [Cited on pages 2 and 5.]

[27] Ch. Gross and I. Bloch. Quantum simulations with ultracold atoms in optical lattices. *Science* **357**(6355), 995–1001 (2017). [Cited on page 2.]

[28] G. Jotzu, M. Messer, R. Desbuquois, M. Lebrat, T. Uehlinger, D. Greif, and T. Esslinger. Experimental realization of the topological Haldane model with ultracold fermions. *Nature* **515**, 237–240 (2014). [Cited on page 2.]

[29] A. L. Gaunt, T. F. Schmidutz, I. Gotlibovych, R. P. Smith, and Z. Hadzibabic. Bose-Einstein Condensation of Atoms in a Uniform Potential. *Phys. Rev. Lett.* **110**, 200406 (2013). [Cited on page 2.]

[30] B. Mukherjee, Z. Yan, P. B. Patel, Z. Hadzibabic, T. Yefsah, J. Struck, and M. W. Zwierlein. Homogeneous Atomic Fermi Gases. *Phys. Rev. Lett.* **118**, 123401 (2017). [Cited on page 2.]

[31] J. Billy, V. Josse, Z. Zuo, A. Bernard, B. Hambrecht, P. Lugan, D. Clément, L. Sanchez-Palencia, P. Bouyer, and A. Aspect. Direct observation of Anderson localization of matter waves in a controlled disorder. *Nature* **453**, 891–894 (2008). [Cited on page 2.]

[32] S. Krinner, T. Esslinger, and J.-P. Brantut. Two-terminal transport measurements with cold atoms. *Journal of Physics: Condensed Matter* **29**, 343003 (2017). [Cited on page 2.]

[33] N. B. Jørgensen, L. Wacker, K. T. Skalmstang, M. M. Parish, J. Levinsen, R. S. Christensen, G. M. Bruun, and J. J. Arlt. Observation of Attractive and Repulsive Polarons in a Bose-Einstein Condensate. *Phys. Rev. Lett.* **117**, 055302 (2016). [Cited on page 2.]

[34] M.-G. Hu, M. J. Van de Graaff, D. Kedar, J. P. Corson, E. A. Cornell, and D. S. Jin. Bose Polarons in the Strongly Interacting Regime. *Phys. Rev. Lett.* **117**, 055301 (2016). [Cited on page 2.]

[35] C. Zipkes, S. Palzer, C. Sias, and M. Köhl. A trapped single ion inside a Bose–Einstein condensate. *Nature* **464**, 388–391 (2010). [Cited on page 2.]

[36] R. Löw, H. Weimer, J. Nipper, J. B. Balewski, B. Butscher, H. P. Büchler, and T. Pfau. An experimental and theoretical guide to strongly interacting Rydberg gases. *Journal of Physics B: Atomic, Molecular and Optical Physics* **45**(11), 113001 (2012). [Cited on page 2.]

[37] A. Mazurenko, C. S. Chiu, G. Ji, M. F. Parsons, M. Kanász-Nagy, R. Schmidt, F. Grusdt, E. Demler, D. Greif, and M. Greiner. A cold-atom Fermi–Hubbard antiferromagnet. *Nature* **545**, 462–466 (2017). [Cited on page 2.]

[38] M. A. Nichols, L. W. Cheuk, M. Okan, T. R. Hartke, E. Mendez, T. Senthil, E. Khatami, H. Zhang, and M. W. Zwierlein. Spin transport in a Mott insulator of ultracold fermions. *Science* **363** (6425), 383–387 (2019). [Cited on page 2.]

[39] P. T. Brown, D. Mitra, E. Guardado-Sanchez, R. Nourafkan, A. Reymbaut, Ch.-D. Hébert, S. Bergeron, A.-M. S. Tremblay, J. Kokalj, D. A. Huse, P. Schauß, and W. S. Bakr. Bad metallic transport in a cold atom Fermi-Hubbard system. *Science* **363** (6425), 379–382 (2019). [Cited on page 2.]

[40] J. Koepsell, J. Vijayan, P. Sompet, F. Grusdt, T. A. Hilker, E. Demler, G. Salomon, I. Bloch, and Ch. Gross. Imaging magnetic polarons in the doped Fermi–Hubbard model. *Nature* **572**, 358–362 (2019). [Cited on page 2.]

[41] K. Martiyanov, V. Makhalov, and A. Turlapov. Observation of a Two-Dimensional Fermi Gas of Atoms. *Phys. Rev. Lett.* **105**, 030404 (2010). [Cited on page 2.]

[42] P. Dyke, E. D. Kuhnle, S. Whitlock, H. Hu, M. Mark, S. Hoinka, M. Lingham, P. Hannaford, and C. J. Vale. Crossover from 2D to 3D in a Weakly Interacting Fermi Gas. *Phys. Rev. Lett.* **106**, 105304 (2011). [Cited on page 2.]

[43] W. Ong, C. Cheng, I. Arakelyan, and J. E. Thomas. Spin-Imbalanced Quasi-Two-Dimensional Fermi Gases. *Phys. Rev. Lett.* **114**, 110403 (2015). [Cited on page 2.]

[44] D. Mitra, P. T. Brown, P. Schauß, S. S. Kondov, and W. S. Bakr. Phase Separation and Pair Condensation in a Spin-Imbalanced 2D Fermi Gas. *Phys. Rev. Lett.* **117**, 093601 (2016). [Cited on page 2.]

[45] B. Fröhlich, M. Feld, E. Vogt, M. Koschorreck, W. Zwerger, and M. Köhl. Radio-Frequency Spectroscopy of a Strongly Interacting Two-Dimensional Fermi Gas. *Phys. Rev. Lett.* **106**, 105301 (2011). [Cited on page 2.]

[46] M. Feld, B. Fröhlich, E. Vogt, M. Koschorreck, and M. Köhl. Observation of a pairing pseudogap in a two-dimensional Fermi gas. *Nature* **480**, 75–78 (2011). [Cited on page 2.]

[47] A. T. Sommer, L. W. Cheuk, M. J. H. Ku, W. S. Bakr, and M. W. Zwierlein. Evolution of Fermion Pairing from Three to Two Dimensions. *Phys. Rev. Lett.* **108**, 045302 (2012). [Cited on page 2.]

[48] C. Cheng, J. Kangara, I. Arakelyan, and J. E. Thomas. Fermi gases in the two-dimensional to quasi-two-dimensional crossover. *Phys. Rev. A* **94**, 031606(R) (2016). [Cited on page 2.]

[49] M. G. Ries, A. N. Wenz, G. Zürn, L. Bayha, I. Boettcher, D. Kedar, P. A. Murthy, M. Neidig, T. Lompe, and S. Jochim. Observation of Pair Condensation in the Quasi-2D BEC-BCS Crossover. *Phys. Rev. Lett.* **114**, 230401 (2015). [Cited on pages 2, 109, and 110.]

[50] P. A. Murthy, I. Boettcher, L. Bayha, M. Holzmann, D. Kedar, M. Neidig, M. G. Ries, A. N. Wenz, G. Zürn, and S. Jochim. Observation of the Berezinskii-Kosterlitz-Thouless Phase Transition in an Ultracold Fermi Gas. *Phys. Rev. Lett.* **115**, 010401 (2015). [Cited on page 2.]

[51] M. Koschorreck, D. Pertot, E. Vogt, B. Fröhlich, M. Feld, and M. Köhl. Attractive and repulsive Fermi polarons in two dimensions. *Nature* **485**, 619–622 (2012). [Cited on page 2.]

[52] Y. Zhang, W. Ong, I. Arakelyan, and J. E. Thomas. Polaron-to-Polaron Transitions in the Radio-Frequency Spectrum of a Quasi-Two-Dimensional Fermi Gas. *Phys. Rev. Lett.* **108**, 235302 (2012). [Cited on page 2.]

[53] B. Fröhlich, M. Feld, E. Vogt, M. Koschorreck, M. Köhl, C. Berthod, and T. Giamarchi. Two-Dimensional Fermi Liquid with Attractive Interactions. *Phys. Rev. Lett.* **109**, 130403 (2012). [Cited on page 2.]

[54] V. Makhalov, K. Martiyanov, and A. Turlapov. Ground-State Pressure of Quasi-2D Fermi and Bose Gases. *Phys. Rev. Lett.* **112**, 045301 (2014). [Cited on pages 3 and 103.]

[55] K. Fenech, P. Dyke, T. Peppler, M. G. Lingham, S. Hoinka, H. Hu, and C. J. Vale. Thermodynamics of an Attractive 2D Fermi Gas. *Phys. Rev. Lett.* **116**, 045302 (2016). [Cited on pages 3 and 103.]

[56] I. Boettcher, L. Bayha, D. Kedar, P. A. Murthy, M. Neidig, M. G. Ries, A. N. Wenz, G. Zürn, S. Jochim, and T. Enss. Equation of

State of Ultracold Fermions in the 2D BEC-BCS Crossover Region. *Phys. Rev. Lett.* **116**, 045303 (2016). [Cited on pages 3, 21, 98, 103, and 105.]

[57] E. Vogt, M. Feld, B. Fröhlich, D. Pertot, M. Koschorreck, and M. Köhl. Scale Invariance and Viscosity of a Two-Dimensional Fermi Gas. *Phys. Rev. Lett.* **108**, 070404 (2012). [Cited on pages 3, 96, and 107.]

[58] M. Koschorreck, D. Pertot, E. Vogt, and M. Köhl. Universal spin dynamics in two-dimensional Fermi gases. *Nature Physics* **9**, 405–409 (2013). [Cited on pages 3, 96, and 107.]

[59] C. Luciuk, S. Smale, F. Böttcher, H. Sharum, B. A. Olsen, S. Trotzky, T. Enss, and J. H. Thywissen. Observation of Quantum-Limited Spin Transport in Strongly Interacting Two-Dimensional Fermi Gases. *Phys. Rev. Lett.* **118**, 130405 (2017). [Cited on pages 3, 96, and 107.]

[60] K. Hueck, N. Luick, L. Sobirey, J. Siegl, T. Lompe, and H. Moritz. Two-Dimensional Homogeneous Fermi Gases. *Phys. Rev. Lett.* **120**, 060402 (2018). [Cited on pages 3, 60, 62, 65, 69, 70, 71, 97, 103, 118, and 125.]

[61] C. Chin, R. Grimm, P. Julienne, and E. Tiesinga. Feshbach resonances in ultracold gases. *Rev. Mod. Phys.* **82**, 1225 (2010). [Cited on pages 3 and 45.]

[62] S. Kokkelmans. Feshbach Resonances in Ultracold Gases. In P. Törmä and K. Sengstock, editors: *Quantum Gas Experiments - Exploring Many-Body States*, volume 3 of *Cold Atoms (series ed. C. Salomon)*. Imperial College Press, London, 2015. [Cited on pages 3, 17, and 46.]

[63] W. Zwerger, editor: *The BCS-BEC Crossover and the Unitary Fermi Gas*, volume 836 of *Lecture Notes in Physics*. Springer, Berlin, 2012. [Cited on page 3.]

[64] M. M. Parish. The BCS–BEC Crossover. In P. Törmä and K. Sengstock, editors: *Quantum Gas Experiments - Exploring Many-Body States*, volume 3 of *Cold Atoms (series ed. C. Salomon)*. Imperial College Press, London, 2015. [Cited on pages 3, 12, 13, and 14.]

[65] T. Schäfer and D. Teaney. Nearly perfect fluidity: from cold atomic gases to hot quark gluon plasmas. *Reports on Progress in Physics* **72**(12), 126001 (2009). [Cited on pages 4 and 96.]

[66] P. Törmä and K. Sengstock, editors: *Quantum Gas Experiments - Exploring Many-Body States*, volume 3 of *Cold Atoms (series ed. C. Salomon)*. Imperial College Press, London, 2015. [Cited on page 5.]

[67] D. Jervis and J. H. Thywissen. Making an Ultracold Gas. In P. Törmä and K. Sengstock, editors: *Quantum Gas Experiments - Exploring Many-Body States*, volume 3 of *Cold Atoms (series ed. C. Salomon)*. Imperial College Press, London, 2015. [Cited on page 6.]

[68] S. Stellmer, M. K. Tey, B. Huang, R. Grimm, and F. Schreck. Bose-Einstein Condensation of Strontium. *Phys. Rev. Lett.* **103**, 200401 (2009). [Cited on page 6.]

[69] S. Kraft, F. Vogt, O. Appel, F. Riehle, and U. Sterr. Bose-Einstein Condensation of Alkaline Earth Atoms: ^{40}Ca. *Phys. Rev. Lett.* **103**, 130401 (2009). [Cited on page 6.]

[70] A. Griesmaier, J. Stuhler, and T. Pfau. Production of a chromium Bose–Einstein condensate. *Applied Physics B* **82**, 211–216 (2006). [Cited on page 6.]

[71] S. Baier, D. Petter, J. H. Becher, A. Patscheider, G. Natale, L. Chomaz, M. J. Mark, and F. Ferlaino. Realization of a Strongly Interacting Fermi Gas of Dipolar Atoms. *Phys. Rev. Lett.* **121**, 093602 (2018). [Cited on page 6.]

[72] Y. Takasu, K. Maki, K. Komori, T. Takano, K. Honda, M. Kumakura, T. Yabuzaki, and Y. Takahashi. Spin-Singlet Bose-Einstein Condensation of Two-Electron Atoms. *Phys. Rev. Lett.* **91**, 040404 (2003). [Cited on page 6.]

[73] J. W. Park, S. A. Will, and M. W. Zwierlein. Ultracold Dipolar Gas of Fermionic ^{23}Na^{40}K Molecules in Their Absolute Ground State. *Phys. Rev. Lett.* **114**, 205302 (2015). [Cited on page 7.]

[74] S. de Léséleuc, D. Barredo, V. Lienhard, A. Browaeys, and T. Lahaye. Optical Control of the Resonant Dipole-Dipole Interaction between Rydberg Atoms. *Phys. Rev. Lett.* **119**, 053202 (2017). [Cited on page 7.]

[75] E. A. L. Henn, J. Billy, and T. Pfau. Dipolar Gases - Experiment. In P. Törmä and K. Sengstock, editors: *Quantum Gas Experiments - Exploring Many-Body States*, volume 3 of *Cold Atoms (series ed. C. Salomon)*. Imperial College Press, London, 2015. [Cited on page 7.]

[76] C. A. Regal, M. Greiner, and D. S. Jin. Observation of Resonance Condensation of Fermionic Atom Pairs. *Phys. Rev. Lett.* **92**, 040403 (2004). [Cited on page 7.]

[77] M. W. Zwierlein, C. A. Stan, C. H. Schunck, S. M. F. Raupach, A. J. Kerman, and W. Ketterle. Condensation of Pairs of Fermionic Atoms near a Feshbach Resonance. *Phys. Rev. Lett.* **92**, 120403 (2004). [Cited on page 7.]

[78] J. Bardeen, L. N. Cooper, and J. R. Schrieffer. Microscopic Theory of Superconductivity. *Phys. Rev.* **106**, 162 (1957). [Cited on pages 7 and 12.]

[79] M. W. Zwierlein. Thermodynamics of Strongly Interacting Fermi Gases. In *Quantum Matter at Ultralow Temperatures*, volume 191 of *Proceedings of the International School of Physics "Enrico Fermi"*. IOS Press, Amsterdam, 2016. [Cited on page 8.]

[80] S.-I. Tomonaga. Remarks on Bloch's Method of Sound Waves applied to Many-Fermion Problems. *Progress of Theoretical Physics* **5**(4), 544–569 (1950). [Cited on page 8.]

[81] J. M. Luttinger. An Exactly Soluble Model of a Many-Fermion System. *Journal of Mathematical Physics* **4**, 1154 (1963). [Cited on page 8.]

[82] D. C. Mattis and E. H. Lieb. Exact Solution of a Many-Fermion System and Its Associated Boson Field. *Journal of Mathematical Physics* **6**, 304 (1965). [Cited on page 8.]

[83] Z. Hadzibabic and J. Dalibard. Two-dimensional Bose fluids: An atomic physics perspective. *La Rivista del Nuovo Cimento* **34**, 389–434 (2011). [Cited on pages 8, 9, 10, 11, and 102.]

[84] D. S. Petrov and G. V. Shlyapnikov. Interatomic collisions in a tightly confined Bose gas. *Phys. Rev. A* **64**, 012706 (2001). [Cited on pages 8, 19, 20, and 68.]

[85] C. J. Pethick and H. Smith. *Microscopic theory of the Bose gas*. Cambridge University Press, Cambridge, 2nd edition, 2008. [Cited on pages 9, 84, and 92.]

[86] E. P. Gross. Structure of a quantized vortex in boson systems. *Il Nuovo Cimento (1955-1965)* **20**, 454–477 (1961). [Cited on page 11.]

[87] L. P. Pitaevskii. Vortex Lines in an Imperfect Bose Gas. *Sov. Phys. JETP* **13**(2), 451–454 (1961). (english translation). [Cited on page 11.]

[88] N. N. Bogoliubov. On a new method in the theory of superconductivity. *Il Nuovo Cimento (1955-1965)* **7**, 794–805 (1958). [Cited on page 12.]

[89] G. Bighin, L. Salasnich, P. A. Marchetti, and F. Toigo. Beliaev damping of the Goldstone mode in atomic Fermi superfluids. *Phys. Rev. A* **92**, 023638 (2015). [Cited on page 12.]

[90] H. Kurkjian, Y. Castin, and A. Sinatra. Landau-Khalatnikov phonon damping in strongly interacting Fermi gases. *Europhysics Letters* **116**, 40002 (2016). [Cited on page 12.]

[91] P. W. Anderson. Random-Phase Approximation in the Theory of Superconductivity. *Phys. Rev.* **112**, 1900 (1958). [Cited on page 13.]

[92] R. Grimm, M. Weidemüller, and Y. B. Ovchinnikov. Optical Dipole Traps for Neutral Atoms. In B. Bederson and H. Walther, editors: *Advances In Atomic, Molecular, and Optical Physics*, volume 42. Academic Press, New York, 2000. [Cited on pages 14, 27, and 59.]

[93] D. S. Petrov, C. Salomon, and G. V. Shlyapnikov. Weakly Bound Dimers of Fermionic Atoms. *Phys. Rev. Lett.* **93**, 090404 (2004). [Cited on pages 19 and 102.]

[94] J. Levinsen and M. M. Parish. Strongly interacting two-dimensional Fermi gases. In K. W. Madison, K. Bongs, L. D. Carr, A. M. Rey, and H. Zhai, editors: *Annual Review of Cold Atoms and Molecules*, volume 3. World Scientific, Singapore, 2015. [Cited on pages 19, 20, 22, 97, and 101.]

[95] M. Randeria, J.-M. Duan, and L.-Y. Shieh. Superconductivity in a two-dimensional Fermi gas: Evolution from Cooper pairing to Bose condensation. *Phys. Rev. B* **41**, 327–343 (1990). [Cited on page 19.]

[96] A. V. Turlapov and M. Y. Kagan. Fermi-to-Bose crossover in a trapped quasi-2D gas of fermionic atoms. *Journal of Physics: Condensed Matter* **29**, 383004 (2017). [Cited on pages 21 and 102.]

[97] A. Ridinger. *Towards quantum degenerate Fermi mixtures: Photoassociation of weakly bound* $^6Li^{40}K$ *molecules.* PhD thesis, École Normale Supérieure Paris, Université Paris VI, 2011. [Cited on pages 25, 27, and 41.]

[98] T. Salez. *Towards quantum degerate atomic Fermi mixtures.* PhD thesis, École Normale Supérieure Paris, Université Paris VI, 2011. [Cited on pages 25, 27, and 31.]

[99] F. Sievers. *Ultracold Fermi mixtures and simultaneous sub-Doppler laser cooling of fermionic* ^6Li *and* ^{40}K*.* PhD thesis, École Normale Supérieure Paris, Université Paris VI, 2014. [Cited on pages 25 and 27.]

[100] D. Rio Fernandez. *Trapping and cooling of fermionic alkali atoms to quantum degeneracy. Sub-Doppler cooling of Potassium-40 and Lithium-6 in gray molasses.* PhD thesis, École Normale Supérieure Paris, Université Paris VI, 2014. [Cited on pages 25, 27, and 39.]

[101] N. Kretzschmar. *Experiments with Ultracold Fermi Gases: Quantum Degeneracy of Potassium-40 and All-solid-state Laser Sources for Lithium.* PhD thesis, École Normale Supérieure Paris, Université Paris VI, 2015. [Cited on pages 25 and 27.]

[102] D. Suchet. *Simulating the dynamics of harmonically trapped Weyl particles with cold atoms.* PhD thesis, École Normale Supérieure Paris, Université Paris VI, 2016. [Cited on pages 25, 27, and 39.]

[103] M. Rabinovic. *Quasithermalization of Fermions in a Quadrupole Potential and Evaporative Cooling of ^{40}K to Quantum Degeneracy.* PhD thesis, École Normale Supérieure Paris, PSL Research University, 2017. [Cited on pages 25, 27, 43, and 44.]

[104] T. Reimann. *Resonant spin dynamics and 3D-1D dimensional crossovers in ultracold Fermi gases.* PhD thesis, École Normale Supérieure Paris, Université PSL - PSL Research University, 2018. [Cited on pages 25, 26, 27, 29, 34, 36, 37, 38, 39, 44, 46, 49, 50, 51, 52, and 55.]

[105] C. Enesa. *Experimental realization of a strongly interacting 2D Fermi gas.* PhD thesis, École Normale Supérieure Paris, Université PSL - PSL Research University, 2019. [Cited on pages 25, 37, and 38.]

[106] M. E. Gehm. Properties of ^{6}Lithium. `https://www.physics.ncsu.edu/jet/techdocs/pdf/PropertiesOfLi.pdf`, 2003. Accessed on 2020-08-28. [Cited on page 26.]

[107] H. J. Metcalf and P. van der Straten. *Laser Cooling and Trapping.* Graduate Texts in Contemporary Physics. Springer, New York, 1999. [Cited on pages 26 and 27.]

[108] T. G. Tiecke. Properties of Potassium. `https://tobiastiecke.nl/archive/PotassiumProperties.pdf`, 2019. Accessed on 2020-09-10. [Cited on page 26.]

[109] J. Dalibard and C. Cohen-Tannoudji. Laser cooling below the Doppler limit by polarization gradients: simple theoretical models. *J. Opt. Soc. Am. B* **6**(11), 2023–2045 (1989). [Cited on page 26.]

[110] A. Aspect, E. Arimondo, R. Kaiser, N. Vansteenkiste, and C. Cohen-Tannoudji. Laser Cooling below the One-Photon Recoil Energy by Velocity-Selective Coherent Population Trapping. *Phys. Rev. Lett.* **61**, 826 (1988). [Cited on page 26.]

[111] M. Kasevich and S. Chu. Laser cooling below a photon recoil with three-level atoms. *Phys. Rev. Lett.* **69**, 1741 (1992). [Cited on page 26.]

[112] M. Weidemüller and T. Esslinger and M. A. Ol'shanii and A. Hemmerich and T. W. Hänsch. A Novel Scheme for Efficient Cooling below the Photon Recoil Limit. *Europhysics Letters* **27**, 109 (1994). [Cited on page 26.]

[113] D. Rio Fernandes, F. Sievers, N. Kretzschmar, S. Wu, C. Salomon, and F. Chevy. Sub-Doppler laser cooling of fermionic ^{40}K atoms in three-dimensional gray optical molasses. *Europhysics Letters* **100**, 63001 (2012). [Cited on pages 26, 30, and 62.]

[114] N. Masuhara, J. M. Doyle, J. C. Sandberg, D. Kleppner, T. J. Greytak, H. F. Hess, and G. P. Kochanski. Evaporative Cooling of Spin-Polarized Atomic Hydrogen. *Phys. Rev. Lett.* **61**, 935 (1988). [Cited on pages 27 and 59.]

[115] K. Hueck, N. Luick, L. Sobirey, J. Siegl, T. Lompe, H. Moritz, L. W. Clark, and C. Chin. Calibrating high intensity absorption imaging of ultracold atoms. *Opt. Express* **25**(8), 8670–8679 (2017). [Cited on pages 27, 60, 66, and 67.]

[116] K. Hueck. *A homogeneous, two-dimensional Fermi gas.* PhD thesis, Universität Hamburg, 2017. [Cited on pages 27, 59, 60, 62, 65, 67, 68, 69, and 70.]

[117] M. Berglund and M. E. Wieser. Isotopic compositions of the elements 2009 (IUPAC Technical Report). *Pure Appl. Chem.* **83**(2), 397–410 (2011). [Cited on page 28.]

[118] A. Ridinger, S. Chaudhuri, T. Salez, U. Eismann, D. Rio Fernandes, K. Magalhães, D. Wilkowski, C. Salomon, and F. Chevy. Large atom number dual-species magneto-optical trap for fermionic ^{6}Li and ^{40}K atoms. *The European Physical Journal D* **65**, 223–242 (2011). [Cited on pages 28 and 29.]

[119] G. Grynberg and J.-Y. Courtois. Proposal for a Magneto-Optical Lattice for Trapping Atoms in Nearly-Dark States. *Europhysics Letters* **27**, 41 (1994). [Cited on page 30.]

[120] A. T. Grier, I. Ferrier-Barbut, B. S. Rem, M. Delehaye, L. Khaykovich, F. Chevy, and C. Salomon. Λ-enhanced sub-Doppler cooling of lithium atoms in D_1 gray molasses. *Phys. Rev. A* **87**, 063411 (2013). [Cited on page 31.]

[121] H. J. Lewandowski, D. M. Harber, D. L. Whitaker, and E. A. Cornell. Simplified System for Creating a Bose–Einstein Condensate. *Journal of Low Temperature Physics* **132**, 309–367 (2003). [Cited on page 31.]

[122] K. Nakagawa, Y. Suzuki, M. Horikoshi, and J.B. Kim. Simple and efficient magnetic transport of cold atoms using moving coils for the production of Bose–Einstein condensation. *Applied Physics B* **81**, 791–794 (2005). [Cited on page 31.]

[123] M. Greiner, I. Bloch, T. W. Hänsch, and T. Esslinger. Magnetic transport of trapped cold atoms over a large distance. *Phys. Rev. A* **63**, 031401(R) (2001). [Cited on page 31.]

[124] L. Mudarikwa, K. Pahwa, and J. Goldwin. Sub-doppler modulation spectroscopy of potassium for laser stabilization. *Journal of Physics B: Atomic, Molecular and Optical Physics* **45**, 065002 (2012). [Cited on page 39.]

[125] T. G. Tiecke, M. R. Goosen, A. Ludewig, S. D. Gensemer, S. Kraft, S. J. J. M. F. Kokkelmans, and J. T. M. Walraven. Broad Feshbach Resonance in the ^{6}Li$-^{40}$K Mixture. *Phys. Rev. Lett.* **104**, 053202 (2010). [Cited on page 43.]

[126] T. G. Tiecke. *Feshbach resonances in ultracold mixtures of the fermionic quantum gases 6Li and 40K.* PhD thesis, Universiteit van Amsterdam, 2010. [Cited on page 43.]

[127] A. Ludewig. *Feshbach resonances in* ^{40}K. PhD thesis, Universiteit van Amsterdam, 2012. [Cited on page 43.]

[128] J. S. Krauser, J. Heinze, S. Götze, M. Langbecker, N. Fläschner, L. Cook, T. M. Hanna, E. Tiesinga, K. Sengstock, and C. Becker. Investigation of Feshbach resonances in ultracold $^{40}\mathbf{K}$ spin mixtures. *Phys. Rev. A* **95**, 042701 (2017). [Cited on page 43.]

[129] A. Zenesini, B. Huang, M. Berninger, S. Besler, H.-C. Nägerl, F. Ferlaino, R. Grimm, C. H. Greene, and J. von Stecher. Resonant five-body recombination in an ultracold gas of bosonic atoms. *New Journal of Physics* **15**, 043040 (2013). [Cited on page 49.]

[130] C. Ticknor, C. A. Regal, D. S. Jin, and J. L. Bohn. Multiplet structure of Feshbach resonances in nonzero partial waves. *Phys. Rev. A* **69**, 042712 (2004). [Cited on page 52.]

[131] Y. Cui, C. Shen, M. Deng, S. Dong, C. Chen, R. Lü, B. Gao, M. K. Tey, and L. You. Observation of Broad d-Wave Feshbach Resonances with a Triplet Structure. *Phys. Rev. Lett.* **119**, 203402 (2017). [Cited on page 52.]

[132] Q. Beaufils, A. Crubellier, T. Zanon, B. Laburthe-Tolra, E. Maréchal, L. Vernac, and O. Gorceix. Feshbach resonance in d-wave collisions. *Phys. Rev. A* **79**, 032706 (2009). [Cited on page 52.]

[133] W. Weimer. *Probing superfluid properties in strongly correlated Fermi gases with high spatial resolution.* PhD thesis, Universität Hamburg, 2014. [Cited on pages 59, 60, and 62.]

[134] K. Morgener. *Microscopy of 2D Fermi gases - Exploring excitations and thermodynamics.* PhD thesis, Universität Hamburg, 2014. [Cited on pages 59, 60, 61, 62, 63, 68, 72, and 74.]

[135] N. Luick. *An ideal Josephson junction in an ultracold two-dimensional Fermi gas.* PhD thesis, Universität Hamburg, 2020. [Cited on pages 59, 60, 62, 63, 65, 67, 71, 109, 110, 111, 117, 123, and 129.]

[136] G. Reinaudi, T. Lahaye, Z. Wang, and D. Guéry-Odelin. Strong saturation absorption imaging of dense clouds of ultracold atoms. *Opt. Lett.* **32**(21), 3143–3145 (2007). [Cited on pages 60 and 66.]

[137] I. Shvarchuck, Ch. Buggle, D. S. Petrov, K. Dieckmann, M. Zielonkowski, M. Kemmann, T. G. Tiecke, W. von Klitzing, G. V. Shlyapnikov, and J. T. M. Walraven. Bose-Einstein Condensation into Nonequilibrium States Studied by Condensate Focusing. *Phys. Rev. Lett.* **89**, 270404 (2002). [Cited on page 60.]

[138] P. A. Murthy, D. Kedar, T. Lompe, M. Neidig, M. G. Ries, A. N. Wenz, G. Zürn, and S. Jochim. Matter-wave Fourier optics with a strongly interacting two-dimensional Fermi gas. *Phys. Rev. A* **90**, 043611 (2014). [Cited on pages 60 and 118.]

[139] J. Léonard, M. Lee, A. Morales, T. M. Karg, T. Esslinger, and T. Donner. Optical transport and manipulation of an ultracold atomic cloud using focus-tunable lenses. *New Journal of Physics* **16**, 093028 (2014). [Cited on page 62.]

[140] J. H. Drewes. Aufbau eines hochauflösenden optischen Systems zur Untersuchung ultrakalter Quantengase. (german), Master thesis, Universität Hamburg, 2012. [Cited on page 62.]

[141] J. Siegl. *Probing coherence properties of strongly interacting Bose gases.* PhD thesis, Universität Hamburg, 2018. [Cited on pages 63 and 68.]

[142] R. W. P. Drever, J. L. Hall, F. V. Kowalski, J. Hough, G. M. Ford, A. J. Munley, and H. Ward. Laser phase and frequency stabilization using an optical resonator. *Applied Physics B* **31**, 97–105 (1983). [Cited on page 64.]

[143] E. D. Black. An introduction to Pound–Drever–Hall laser frequency stabilization. *American Journal of Physics* **69**, 79 (2001). [Cited on page 64.]

[144] U. Schünemann, H. Engler, R. Grimm, M. Weidemüller, and M. Zielonkowski. Simple scheme for tunable frequency offset locking of two lasers. *Review of Scientific Instruments* **70**, 242 (1999). [Cited on page 64.]

[145] L. D. Landau. The Theory of a Fermi liquid. *Sov. Phys. JETP* **3** (6), 920–925 (1957). [Cited on page 82.]

[146] H. J. Schulz. Fermi liquids and non–fermi liquids. In E. Akkermans, G. Montambaux, J. Pichard, and J. Zinn-Justin, editors: *Proceedings of Les Houches Summer School LXI.* Elsevier, Amsterdam, 1995. [Cited on page 82.]

[147] S. Hoefner. The equations of fluid dynamics and their connection with the Boltzmann equation. `https://www.astro.uu.se/~hoefner/astro/teach/adp08_L3_notes.pdf`, 2008. Lecture notes, Department of physics and astronomy, Uppsala university. Accessed on 2020-09-09. [Cited on page 82.]

[148] H. Smith and H. H. Jensen. *Transport Phenomena.* Oxford science publications. Clarendon Press, Oxford, 1989. [Cited on pages 83, 84, 90, 92, 94, and 105.]

[149] L. D. Landau and E. M. Lifshitz. *Hydrodynamik.* Lehrbuch der Theoretischen Physik, Band VI. Akademie-Verlag, Berlin, 3rd edition, 1974. (german, ed: W. Weller). [Cited on pages 84, 85, 90, and 105.]

[150] P. L. Kapitza. Heat Transfer and Superfluidity of Helium II. *Phys. Rev.* **60**, 354 (1941). [Cited on page 92.]

[151] L. Tisza. Transport Phenomena in Helium II. *Nature* **141**, 913 (1938). [Cited on page 94.]

[152] L. Landau. Theory of the Superfluidity of Helium II. *Phys. Rev.* **60**, 356 (1941). [Cited on page 94.]

[153] S. Balibar. The Discovery of Superfluidity. *Journal of Low Temperature Physics* **146**, 441–470 (2007). [Cited on page 94.]

[154] V. Peshkov. Determination of the velocity of propagation of the second sound in helium ii. *Journal of Physics (Moscow)* **10**, 389–398 (1946). [Cited on page 94.]

[155] L. A. Sidorenkov, M. K. Tey, R. Grimm, Y. H. Hou, L. Pitaevskii, and S. Stringari. Second sound and the superfluid fraction in a Fermi gas with resonant interactions. *Nature* **498**, 78–81 (2013). [Cited on pages 94 and 101.]

[156] P. K. Kovtun, D. T. Son, and A. O. Starinets. Viscosity in Strongly Interacting Quantum Field Theories from Black Hole Physics. *Phys. Rev. Lett.* **94**, 111601 (2005). [Cited on page 96.]

[157] T. Enss, R. Haussmann, and W. Zwerger. Viscosity and scale invariance in the unitary Fermi gas. *Annals of Physics* **326**(3), 770 – 796 (2011). [Cited on pages 96 and 107.]

[158] G. M. Bruun. Shear viscosity and spin-diffusion coefficient of a two-dimensional Fermi gas. *Phys. Rev. A* **85**, 013636 (2012). [Cited on pages 96, 105, and 107.]

[159] T. Schäfer. Shear viscosity and damping of collective modes in a two-dimensional Fermi gas. *Phys. Rev. A* **85**, 033623 (2012). [Cited on pages 96, 105, and 107.]

[160] T. Enss, C. Küppersbusch, and L. Fritz. Shear viscosity and spin diffusion in a two-dimensional Fermi gas. *Phys. Rev. A* **86**, 013617 (2012). [Cited on pages 96, 105, and 107.]

[161] P. Massignan, G. M. Bruun, and H. Smith. Viscous relaxation and collective oscillations in a trapped Fermi gas near the unitarity limit. *Phys. Rev. A* **71**, 033607 (2005). [Cited on pages 96 and 107.]

[162] C. Cao, E. Elliott, J. Joseph, H. Wu, J. Petricka, T. Schäfer, and J. E. Thomas. Universal Quantum Viscosity in a Unitary Fermi Gas. *Science* **331**(6013), 58–61 (2011). [Cited on pages 96 and 107.]

[163] A. Sommer, M. Ku, G. Roati, and M. W. Zwierlein. Universal spin transport in a strongly interacting Fermi gas. *Nature* **472**, 201–204 (2011). [Cited on pages 96 and 107.]

[164] G. M. Bruun. Spin diffusion in Fermi gases. *New Journal of Physics* **13**, 035005 (2011). [Cited on pages 96 and 107.]

[165] T. Enss and R. Haussmann. Quantum Mechanical Limitations to Spin Diffusion in the Unitary Fermi Gas. *Phys. Rev. Lett.* **109**, 195303 (2012). [Cited on pages 96 and 107.]

[166] A. B. Bardon, S. Beattie, C. Luciuk, W. Cairncross, D. Fine, N. S. Cheng, G. J. A. Edge, E. Taylor, S. Zhang, S. Trotzky, and J. H. Thywissen. Transverse Demagnetization Dynamics of a Unitary Fermi Gas. *Science* **344**(6185), 722–724 (2014). [Cited on pages 96 and 107.]

[167] G. Valtolina, F. Scazza, A. Amico, A. Burchianti, A. Recati, T. Enss, M. Inguscio, M. Zaccanti, and G. Roati. Exploring the ferromagnetic behaviour of a repulsive Fermi gas through spin dynamics. *Nature Physics* **13**, 704–709 (2017). [Cited on pages 96 and 107.]

[168] P. B. Patel, Z. Yan, B. Mukherjee, R. J. Fletcher, J. Struck, and M. W. Zwierlein. Universal Sound Diffusion in a Strongly Interacting Fermi Gas (2019). Preprint: arXiv:1909.02555v2. [Cited on pages 96 and 107.]

[169] T. Enss and J. H. Thywissen. Universal Spin Transport and Quantum Bounds for Unitary Fermions. *Annual Review of Condensed Matter Physics* **10**, 85–106 (2019). [Cited on page 96.]

[170] M. Olshanii, H. Perrin, and V. Lorent. Example of a Quantum Anomaly in the Physics of Ultracold Gases. *Phys. Rev. Lett.* **105**, 095302 (2010). [Cited on page 96.]

[171] M. Holten, L. Bayha, A. C. Klein, P. A. Murthy, P. M. Preiss, and S. Jochim. Anomalous Breaking of Scale Invariance in a Two-Dimensional Fermi Gas. *Phys. Rev. Lett.* **121**, 120401 (2018). [Cited on page 96.]

[172] T. Peppler, P. Dyke, M. Zamorano, I. Herrera, S. Hoinka, and C. J. Vale. Quantum Anomaly and 2D-3D Crossover in Strongly Interacting Fermi Gases. *Phys. Rev. Lett.* **121**, 120402 (2018). [Cited on page 96.]

[173] P. A. Murthy, N. Defenu, L. Bayha, M. Holten, P. M. Preiss, T. Enss, and S. Jochim. Quantum scale anomaly and spatial coherence in a 2D Fermi superfluid. *Science* **365**(6450), 268–272 (2019). [Cited on page 96.]

[174] J. A. N. Bruin, H. Sakai, R. S. Perry, and A. P. Mackenzie. Similarity of Scattering Rates in Metals Showing T-Linear Resistivity. *Science* **339**(6121), 804–807 (2013). [Cited on page 97.]

[175] S. A. Hartnoll. Theory of universal incoherent metallic transport. *Nature Physics* **11**, 54–61 (2015). [Cited on page 97.]

[176] S. A. Hartnoll, A. Lucas, and S. Sachdev. *Holographic Quantum Matter*. MIT Press, Cambridge, MA, 2018. [Cited on page 97.]

[177] N. Luick, L. Sobirey, M. Bohlen, V. P. Singh, L. Mathey, T. Lompe, and H. Moritz. An ideal Josephson junction in an ultracold two-dimensional Fermi gas. *Science* **369**(6499), 89–91 (2020). [Cited on pages 97, 98, 102, 111, 115, 117, 119, 121, 122, and 129.]

[178] N. Prokof'ev, O. Ruebenacker, and B. Svistunov. Critical Point of a Weakly Interacting Two-Dimensional Bose Gas. *Phys. Rev. Lett.* **87**, 270402 (2001). [Cited on page 97.]

[179] M. Bohlen, L. Sobirey, N. Luick, H. Biss, T. Enss, T. Lompe, and H. Moritz. Sound Propagation and Quantum-Limited Damping in a Two-Dimensional Fermi Gas. *Phys. Rev. Lett.* **124**, 240403 (2020). [Cited on pages 99, 126, and 127.]

[180] J. L. Ville, R. Saint-Jalm, É. Le Cerf, M. Aidelsburger, S. Nascimbène, J. Dalibard, and J. Beugnon. Sound Propagation in a Uniform Superfluid Two-Dimensional Bose Gas. *Phys. Rev. Lett.* **121**, 145301 (2018). [Cited on page 98.]

[181] E. Taylor, H. Hu, X.-J. Liu, L. P. Pitaevskii, A. Griffin, and S. Stringari. First and second sound in a strongly interacting Fermi gas. *Phys. Rev. A* **80**, 053601 (2009). [Cited on page 101.]

[182] H. Hu, P. Dyke, C. J. Vale, and X.-J. Liu. First and second sound of a unitary Fermi gas in highly oblate harmonic traps. *New Journal of Physics* **16**, 083023 (2014). [Cited on page 101.]

[183] M. Ota and S. Stringari. Second sound in a two-dimensional Bose gas: From the weakly to the strongly interacting regime. *Phys. Rev. A* **97**, 033604 (2018). [Cited on pages 101 and 107.]

[184] V. P. Singh and L. Mathey. Sound propagation in a two-dimensional Bose gas across the superfluid transition. *Phys. Rev. Research* **2**, 023336 (2020). [Cited on pages 102 and 107.]

[185] D. S. Petrov, C. Salomon, and G. V. Shlyapnikov. Scattering properties of weakly bound dimers of fermionic atoms. *Phys. Rev. A* **71**, 012708 (2005). [Cited on page 102.]

[186] L. Salasnich, P. A. Marchetti, and F. Toigo. Superfluidity, sound velocity, and quasicondensation in the two-dimensional BCS-BEC crossover. *Phys. Rev. A* **88**, 053612 (2013). [Cited on page 102.]

[187] H. Shi, S. Chiesa, and S. Zhang. Ground-state properties of strongly interacting Fermi gases in two dimensions. *Phys. Rev. A* **92**, 033603 (2015). [Cited on pages 103 and 104.]

[188] G. Bighin and L. Salasnich. Finite-temperature quantum fluctuations in two-dimensional Fermi superfluids. *Phys. Rev. B* **93**, 014519 (2016). [Cited on page 104.]

[189] F. Wu, J. Hu, L. He, X.-J. Liu, and H. Hu. Effective theory for ultracold strongly interacting fermionic atoms in two dimensions. *Phys. Rev. A* **101**, 043607 (2020). [Cited on page 105.]

[190] T. Enss. Bulk Viscosity and Contact Correlations in Attractive Fermi Gases. *Phys. Rev. Lett.* **123**, 205301 (2019). [Cited on page 105.]

[191] Y. Nishida. Viscosity spectral functions of resonating fermions in the quantum virial expansion. *Annals of Physics* **410**, 167949 (2019). [Cited on page 105.]

[192] J. Hofmann. High-temperature expansion of the viscosity in interacting quantum gases. *Phys. Rev. A* **101**, 013620 (2020). [Cited on page 105.]

[193] A. Tononi, A. Cappellaro, G. Bighin, and L. Salasnich. Propagation of first and second sound in a two-dimensional Fermi superfluid (2020). Preprint: arXiv:2005.07607. [Cited on pages 107 and 129.]

[194] G. Eska, K. Neumaier, W. Schoepe, K. Uhlig, W. Wiedemann, and P. Wölfle. First-Sound Attenuation and Viscosity of Superfluid ^{3}He-*B*. *Phys. Rev. Lett.* **44**, 1337 (1980). [Cited on page 107.]

[195] R. Peierls. Remarks on transition temperatures. *Helv. Phys. Acta* **7**, 81–83 (1934). [Cited on page 109.]

[196] J. Dalibard. Fluides quantiques de basse dimension et transition de Kosterlitz-Thouless. `https://www.college-de-france.fr/media/jean-dalibard/UPL6519324985816302006_notes_cours_total.compressed.pdf`, 2017. Lecture notes (french), Collège de France, Paris. Accessed on 2020-06-21. [Cited on page 109.]

[197] Y. J. Uemura, L. P. Le, G. M. Luke, B. J. Sternlieb, W. D. Wu, J. H. Brewer, T. M. Riseman, C. L. Seaman, M. B. Maple, M. Ishikawa, D. G. Hinks, J. D. Jorgensen, G. Saito, and H. Yamochi. Basic similarities among cuprate, bismuthate, organic, Chevrel-phase, and heavy-fermion superconductors shown by penetration-depth measurements. *Phys. Rev. Lett.* **66**, 2665 (1991). [Cited on page 109.]

[198] Y. J. Uemura, L. P. Le, G. M. Luke, B. J. Sternlieb, W. D. Wu, J. H. Brewer, T. M. Riseman, C. L. Seaman, M. B. Maple, M. Ishikawa, D. G. Hinks, J. D. Jorgensen, G. Saito, and H. Yamochi. Basic Similarities among Cuprate, Bismuthate, Organic, Chevrel-Phase, and Heavy-Fermion Superconductors Shown by Penetration-Depth Measurements. *Phys. Rev. Lett.* **68**, 2712 (1992). [Cited on page 109.]

[199] D. S. Petrov, M. A. Baranov, and G. V. Shlyapnikov. Superfluid transition in quasi-two-dimensional Fermi gases. *Phys. Rev. A* **67**, 031601 (2003). [Cited on page 109.]

[200] B. D. Josephson. Possible new effects in superconductive tunnelling. *Physics Letters* **1**(7), 251–253 (1962). [Cited on page 111.]

[201] P. W. Anderson and J. M. Rowell. Probable Observation of the Josephson Superconducting Tunneling Effect. *Phys. Rev. Lett.* **10**, 230 (1963). [Cited on page 111.]

[202] M. Buchner, K. Höfler, B. Henne, V. Ney, and A. Ney. Tutorial: Basic principles, limits of detection, and pitfalls of highly sensitive SQUID magnetometry for nanomagnetism and spintronics. *Journal of Applied Physics* **124**, 161101 (2018). [Cited on page 113.]

[203] S. Shapiro. Josephson Currents in Superconducting Tunneling: The Effect of Microwaves and Other Observations. *Phys. Rev. Lett.* **11**, 80 (1963). [Cited on page 114.]

[204] C. A. Hamilton, C. J. Burroughs, and S. P. Benz. Josephson voltage standard-a review. *IEEE Transactions on Applied Superconductivity* **7**(2), 3756–3761 (1997). [Cited on page 114.]

[205] A. Rüfenacht, N. E. Flowers-Jacobs, and S. P. Benz. Impact of the latest generation of Josephson voltage standards in ac and dc electric metrology. *Metrologia* **55**(5), 152–173 (2018). [Cited on page 114.]

[206] J. Koch, T. M. Yu, J. Gambetta, A. A. Houck, D. I. Schuster, J. Majer, A. Blais, M. H. Devoret, S. M. Girvin, and R. J. Schoelkopf. Charge-insensitive qubit design derived from the Cooper pair box. *Phys. Rev. A* **76**, 042319 (2007). [Cited on page 114.]

[207] F. Arute, K. Arya, R. Babbush, D. Bacon, J. C. Bardin, R. Barends, R. Biswas, S. Boixo, F. G. S. L. Brandao, D. A. Buell, B. Burkett, Y. Chen, Z. Chen, B. Chiaro, R. Collins, W. Courtney, A. Dunsworth, E. Farhi, B. Foxen, A. Fowler, C. Gidney, M. Giustina, R. Graff, K. Guerin, S. Habegger, M. P. Harrigan, M. J. Hartmann, A. Ho, M. Hoffmann, T. Huang, T. S. Humble, S. V. Isakov, E. Jeffrey, Z. Jiang, D. Kafri, K. Kechedzhi, J. Kelly, P. V. Klimov, S. Knysh, A. Korotkov, F. Kostritsa, D. Landhuis, M. Lindmark, E. Lucero, D. Lyakh, S. Mandrà, J. R. McClean,

M. McEwen, A. Megrant, X. Mi, K. Michielsen, M. Mohseni, J. Mutus, O. Naaman, M. Neeley, C. Neill, M. Y. Niu, E. Ostby, A. Petukhov, J. C. Platt, C. Quintana, E. G. Rieffel, P. Roushan, N. C. Rubin, D. Sank, K. J. Satzinger, V. Smelyanskiy, K. J. Sung, M. D. Trevithick, A. Vainsencher, B. Villalonga, T. White, Z. J. Yao, P. Yeh, A. Zalcman, H. Neven, and J. M. Martinis. Quantum supremacy using a programmable superconducting processor. *Nature* **574**, 505–510 (2019). [Cited on page 114.]

[208] P. Krantz, M. Kjaergaard, F. Yan, T. P. Orlando, S. Gustavsson, and W. D. Oliver. A quantum engineer's guide to superconducting qubits. *Applied Physics Reviews* **6**, 021318 (2019). [Cited on pages 114 and 115.]

[209] V. Bouchiat, D. Vion, P. Joyez, D. Esteve, and M. H. Devoret. Quantum coherence with a single Cooper pair. *Physica Scripta* **1998**, 165 (1998). [Cited on page 115.]

[210] J. Javanainen. Oscillatory exchange of atoms between traps containing Bose condensates. *Phys. Rev. Lett.* **57**, 3164 (1986). [Cited on page 115.]

[211] F. S. Cataliotti, S. Burger, C. Fort, P. Maddaloni, F. Minardi, A. Trombettoni, A. Smerzi, and M. Inguscio. Josephson Junction Arrays with Bose-Einstein Condensates. *Science* **293**(5531), 843–846 (2001). [Cited on page 115.]

[212] M. Albiez, R. Gati, J. Fölling, S. Hunsmann, M. Cristiani, and M. K. Oberthaler. Direct Observation of Tunneling and Nonlinear Self-Trapping in a Single Bosonic Josephson Junction. *Phys. Rev. Lett.* **95**, 010402 (2005). [Cited on pages 115 and 116.]

[213] S. Levy, E. Lahoud, I. Shomroni, and J. Steinhauer. The a.c. and d.c. Josephson effects in a Bose–Einstein condensate. *Nature* **449**, 579–583 (2007). [Cited on page 115.]

[214] T. Betz, S. Manz, R. Bücker, T. Berrada, Ch. Koller, G. Kazakov, I. E. Mazets, H.-P. Stimming, A. Perrin, T. Schumm, and J. Schmiedmayer. Two-Point Phase Correlations of a One-Dimensional Bosonic Josephson Junction. *Phys. Rev. Lett.* **106**, 020407 (2011). [Cited on page 115.]

[215] G. Valtolina, A. Burchianti, A. Amico, E. Neri, K. Xhani, J. A. Seman, A. Trombettoni, A. Smerzi, M. Zaccanti, M. Inguscio, and G. Roati. Josephson effect in fermionic superfluids across the BEC-BCS crossover. *Science* **350**(6267), 1505–1508 (2015). [Cited on page 115.]

[216] G. Spagnolli, G. Semeghini, L. Masi, G. Ferioli, A. Trenkwalder, S. Coop, M. Landini, L. Pezzè, G. Modugno, M. Inguscio, A. Smerzi, and M. Fattori. Crossing Over from Attractive to Repulsive Interactions in a Tunneling Bosonic Josephson Junction. *Phys. Rev. Lett.* **118**, 230403 (2017). [Cited on pages 115 and 121.]

[217] C. Ryu, P. W. Blackburn, A. A. Blinova, and M. G. Boshier. Experimental Realization of Josephson Junctions for an Atom SQUID. *Phys. Rev. Lett.* **111**, 205301 (2013). [Cited on page 115.]

[218] A. Burchianti, F. Scazza, A. Amico, G. Valtolina, J. A. Seman, C. Fort, M. Zaccanti, M. Inguscio, and G. Roati. Connecting Dissipation and Phase Slips in a Josephson Junction between Fermionic Superfluids. *Phys. Rev. Lett.* **120**, 025302 (2018). [Cited on pages 115 and 119.]

[219] K. Xhani, E. Neri, L. Galantucci, F. Scazza, A. Burchianti, K.-L. Lee, C. F. Barenghi, A. Trombettoni, M. Inguscio, M. Zaccanti, G. Roati, and N. P. Proukakis. Critical Transport and Vortex Dynamics in a Thin Atomic Josephson Junction. *Phys. Rev. Lett.* **124**, 045301 (2020). [Cited on pages 115 and 117.]

[220] W. J. Kwon, G. Del Pace, R. Panza, M. Inguscio, W. Zwerger, M. Zaccanti, F. Scazza, and G. Roati. Strongly correlated superfluid order parameters from dc Josephson supercurrents. *Science* **369**(6499), 84–88 (2020). [Cited on pages 115 and 124.]

[221] A. Smerzi, S. Fantoni, S. Giovanazzi, and S. R. Shenoy. Quantum Coherent Atomic Tunneling between Two Trapped Bose-Einstein Condensates. *Phys. Rev. Lett.* **79**, 4950 (1997). [Cited on page 116.]

[222] S. Raghavan, A. Smerzi, S. Fantoni, and S. R. Shenoy. Coherent oscillations between two weakly coupled Bose-Einstein condensates: Josephson effects, π oscillations, and macroscopic quantum self-trapping. *Phys. Rev. A* **59**, 620 (1999). [Cited on pages 117 and 121.]

[223] V. P. Singh, N. Luick, L. Sobirey, and L. Mathey. Josephson junction dynamics in a two-dimensional ultracold Bose gas. *Phys. Rev. Research* **2**, 033298 (2020). [Cited on pages 117 and 119.]

[224] J. G. Lee, B. J. McIlvain, C. J. Lobb, and W. T. Hill III. Analogs of Basic Electronic Circuit Elements in a Free-Space Atom Chip. *Scientific Reports* **3**, 1034 (2013). [Cited on page 119.]

[225] S. Eckel, J. G. Lee, F. Jendrzejewski, C. J. Lobb, G. K. Campbell, and W. T. Hill III. Contact resistance and phase slips in mesoscopic superfluid-atom transport. *Phys. Rev. A* **93**, 063619 (2016). [Cited on page 119.]

[226] L. Sobirey, N. Luick, M. Bohlen, H. Biss, H. Moritz, and T. Lompe. Observation of superfluidity in a strongly correlated two-dimensional Fermi gas (2020). In preparation. Eprint: arXiv:2005.07607. [Cited on pages 123, 124, 125, 126, and 127.]

[227] C. Raman, M. Köhl, R. Onofrio, D. S. Durfee, C. E. Kuklewicz, Z. Hadzibabic, and W. Ketterle. Evidence for a Critical Velocity in

a Bose-Einstein Condensed Gas. *Phys. Rev. Lett.* **83**, 2502 (1999). [Cited on page 124.]

[228] P. Engels and C. Atherton. Stationary and Nonstationary Fluid Flow of a Bose-Einstein Condensate Through a Penetrable Barrier. *Phys. Rev. Lett.* **99**, 160405 (2007). [Cited on page 124.]

[229] T. W. Neely, E. C. Samson, A. S. Bradley, M. J. Davis, and B. P. Anderson. Observation of Vortex Dipoles in an Oblate Bose-Einstein Condensate. *Phys. Rev. Lett.* **104**, 160401 (2010). [Cited on page 124.]

[230] L.-C. Ha, L. W. Clark, C. V. Parker, B. M. Anderson, and C. Chin. Roton-Maxon Excitation Spectrum of Bose Condensates in a Shaken Optical Lattice. *Phys. Rev. Lett.* **114**, 055301 (2015). [Cited on page 124.]

[231] R. Desbuquois, L. Chomaz, T. Yefsah, J. Léonard, J. Beugnon, C. Weitenberg, and J. Dalibard. Superfluid behaviour of a two-dimensional Bose gas. *Nature Physics* **8**, 645–648 (2012). [Cited on page 124.]

[232] D. E. Miller, J. K. Chin, C. A. Stan, Y. Liu, W. Setiawan, C. Sanner, and W. Ketterle. Critical Velocity for Superfluid Flow across the BEC-BCS Crossover. *Phys. Rev. Lett.* **99**, 070402 (2007). [Cited on page 124.]

[233] W. Weimer, K. Morgener, V. P. Singh, J. Siegl, K. Hueck, N. Luick, L. Mathey, and H. Moritz. Critical Velocity in the BEC-BCS Crossover. *Phys. Rev. Lett.* **114**, 095301 (2015). [Cited on page 124.]

RÉSUMÉ

Les systèmes bi-dimensionnels fortement corrélés sont captivants. À cause de la dimensionnalité réduite, des fluctuations thermiques empêchent un vrai ordre à longue portée et devraient donc entraver des phénomènes comme la condensation Bose-Einstein ou la superfluidité. Malgré cela, la superfluditié et la supraconductivité semblent particulièrement robustes en 2D : Dans presque tous les supraconducteurs à haute température critique les structures 2D ainsi que le couplage en onde d semblent jouer un rôle central. Dans cette thèse, nous utilisons des gaz de lithium 6 ultrafroids et homogènes avec des interactions ajustables pour effectuer des simulations quantiques explorant certaines propriétés de ces systèmes fascinants.

Comme résultat principal, je présente les premières mesures de la vitesse et de l'atténuation du son dans un gaz de Fermi 2D ultrafroid, que nous utilisons pour étudier des propriétés thermodynamiques et les coefficients de transport du gaz. La vitesse du son nous permet d'extraire la compressibilité du gaz et nous obtenons un accord raisonnable avec la valeur mesurée indépendamment dans un système statique ou calculée à partir de simulations Monte-Carlo quantiques. L'atténuation des ondes sonores est déterminée par la viscosité et la conductivité thermique du gaz, et approche un minimum dans le régime fortement corrélé. Ce minimum correspond à une limite quantique universelle $\hbar/m$ pour la diffusivité du son. Le gaz de Fermi 2D fortement corrélé représente donc un fluide quasi-parfait.

En outre, je rends compte de deux autres expériences qui ont été réalisées dans le cadre de cette thèse, menées principalement par mes collègues N. Luick et L. Sobirey. Premièrement, nous réalisons une jonction de Josephson en séparant le gaz en deux réservoirs à l'aide d'un laser induisant une fine barrière de potentiel répulsive. Nous observons des oscillations de Josephson entre les deux réservoirs démontrant la cohérence de phase du gaz de Fermi 2D. En réduisant la hauteur de la barrière, ces oscillations sont progressivement transformées en ondes sonores. Dans la deuxième expérience, nous déplaçons un réseau optique à travers le gaz à des vitesses ajustables. Nous observons une vitesse critique pour la création d'excitations, prouvant que le gaz de Fermi 2D est superfluide. La vitesse critique est déterminée par la vitesse du son sur un grand domaine d'interactions.

Finalement, je présente la caractérisation d'une nouvelle résonance Feshbach en onde d dans du potassium 40 ultrafroid, un projet qui a été mené principalement par mon collègue T. Reimann. Nous mesurons le taux de pertes inélastiques $L^{(2)}$ et l'évolution des populations de spins et nous les comparons à des prédictions théoriques. Nous trouvons un bon accord entre théorie et expérience pour le taux de pertes. L'évolution des populations des spins est compatible avec le comportement prédit par la théorie.

MOTS CLÉS

Gaz de Fermi ultrafroids - Dimensions réduites - Ondes sonores

ABSTRACT

Strongly correlated two-dimensional (2D) systems are a fascinating field of study. The reduced dimensionality should in principle impede phenomena such as Bose-Einstein condensation or superfluidity. Yet, evidence suggests that superfluidity and superconductivity are especially robust in 2D: In almost all known high T_c-supercondcutors, strongly correlated 2D structures and higher-partial-wave coupling seem to play a crucial role. In this thesis, we use ultracold homogeneous gases of lithium 6 with tunable interactions to perform analog quantum simulation of these captivating systems.

As the main result of this thesis, I present the first measurements of the speed and attenuation of sound waves in ultracold 2D Fermi gases, which we use to probe the thermodynamic and transport properties of the gas. From the speed of sound, we extract the compressibility equation of state and compare it both to an independent static measurement and to quantum Monte Carlo calculations and find reasonable agreement between the three. The damping of the sound waves, which is determined by the shear and bulk viscosities as well as the thermal conductivity of the gas, exhibits a minimum in the strongly correlated regime. Here, the sound diffusivity approaches a universal quantum bound $\hbar/m$ and the strongly correlated 2D Fermi gas thus realizes a nearly perfect fluid.

In addition, I report on further related measurements performed in the course of this thesis, which were led by my coworkers N. Luick and L. Sobirey. We show that the 2D Fermi gas is phase coherent by realizing a Josephson junction in the homogeneous gas and observing Josephson oscillations between two reservoirs separated by a thin barrier. When the barrier height is reduced to zero, these oscillations transform smoothly into sound waves. By dragging a lattice though the homogeneous system at variable velocities, we observe a critical velocity for the creation of excitations, proving that the system is superfluid. Here, the sound velocity determines the critical velocity for a large range of interaction strengths.

Finally, I present the characterization of a novel d-wave Feshbach resonance in ultracold potassium 40 via measurements of the inelastic loss rate $L^{(2)}$ and via the dynamics of spin populations, led by my coworker T. Reimann. The experimental results are compared to theoretical predictions and we observe good agreement between the theoretical and experimental loss rates. The evolution of the spin populations is found to be consistent with the expected behavior for the theoretically predicted exit channel.

KEYWORDS

Ultracold Fermi gases - Reduced dimensions - Sound waves